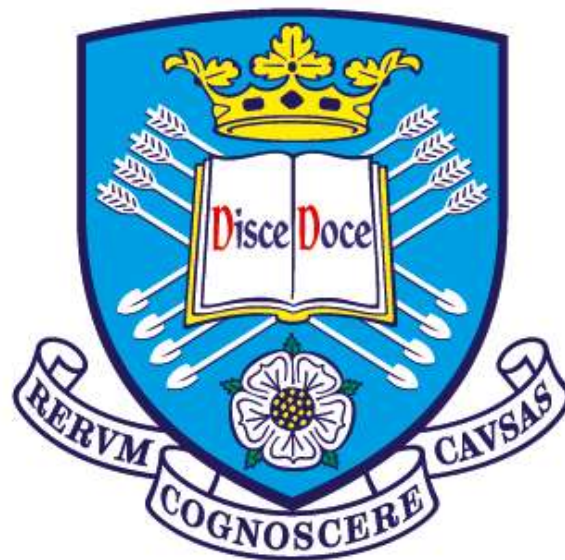


Accident Tolerant Barriers for Fuel Rod Cladding in Nuclear Reactors

A Thesis Submitted in Fulfilment of the Requirements for the Degree
of Doctor of Philosophy

by

Dilwar Hussain



Department of Materials Science and Engineering

The University of Sheffield, UK

July 2020

© 2020, D. Hussain

بِسْمِ اللَّهِ الرَّحْمَنِ الرَّحِيمِ

In The Name of Allah, The Most Gracious, The Most Merciful

Acknowledgements

All praises and thanks be to Allah, the Lord of the Worlds. I thank Allah, the All-Mighty for giving me this opportunity to study for a PhD in a subject, that I love, cherish and am truly passionate about. I testify that there is no god but Allah, and that Muhammad (pbuh) is His last and final Messenger. As for what follows:

I would like to express my sincere gratitude to my supervisor Dr Adrian Leyland for his guidance as my supervisor over the years it took me to reach this stage. This project would not have been accomplished without his expert advice and knowledge. The past years in Sheffield have become one of the most important and formative experiences in my life. This project is sponsored by the Engineering and Physical Sciences Research Council (EPSRC), through the Nuclear FiRST DTC (Fission, Research, Science and Technology Doctoral Training Centre) in collaboration with Westinghouse Electric Co.

I would like to extend my gratitude to many people, including my co-supervisor Prof. Michael Preuss (The University of Manchester) for his knowledge and advice. Dr Nik Reeves McLaren (The University of Sheffield), for providing his extensive knowledge and help on using X-ray Diffraction machines and Raman Spectroscopy; Miss Dawn Bussey (The University of Sheffield) for her unwavering support in collecting nanoindentation data; Mr Michael Bell (The University of Sheffield), for his expert knowledge on micropreparation of samples; Dr Jonna M. Partezana (Westinghouse, USA) for carrying out corrosion testing of samples and Mr David Eaves (Springfields Fuels Ltd.) for helping with the scratch adhesion tests.

I would like to extend a special thanks to my family, especially my parents Fathama Perven and Harun Rashid for having raised me, helped me and guided me throughout my entire life. It is through their inspiration, unconditional love, dedication, their unshakable belief in me and their duas (prayers) and that of my late grandparents Sajjad Ali and Khadeja Bibi that has allowed me to reach this stage. I would like to thank my siblings Zahurah Yasmin-Ahmed (who was instrumental in helping me prepare for the viva), Hajarah Banu, Hasan Abdullah, Sumayya Tasnim and last but not least Maryam Firdaws for always being there for me, for being the best siblings a brother could have. Most of all, I wholeheartedly thank my wife Mazedra Sultana Sabur. Her humour and optimism eased the pressure off me during difficult & challenging times and had inspired confidence in me, reaching the light at the end of the tunnel. To my family I dedicate this work.

I ask Allah (SWT), to continue to shower His Mercy and Blessings on me and my family and to use my skills for the sake of Allah to benefit the Ummah. Ameen.

Abstract

Zirconium-based alloys are currently used as fuel rod cladding in nuclear power reactors because of their low neutron absorption cross-section and adequate oxidation resistance. However, zirconium (Zr) alloys undergo waterside corrosion by the primary coolant water under normal operating conditions (300-330°C) and at high temperature, especially during loss of coolant accident conditions. During the oxidation reaction, hydrogen generated which can lead to the formation of zirconium hydride precipitates in the Zr alloy cladding - and is detrimental to the mechanical integrity of the fuel rods. The principal objective of this work was to develop a surface-treated layer/coating for pure Zr in order to improve its oxidation resistance (and to determine the feasibility of such surface-treated layers/coatings being used on Zr alloys) - and thereby increase its operational longevity under both normal and abnormal operating conditions.

Triode Plasma Nitriding (TPN) diffusion treatments were used to develop diffusion-treated nitride layers intended to enhance load-bearing capacity of bulk Zr while allowing for good adhesion properties to the substrate. Physical Vapour Deposition (PVD) was also used to fabricate magnesium-containing zirconium coatings with a range of magnesium concentrations to study the solubility magnesium and zirconium in a Zr-Mg coating intended to enhance hydrothermal oxidation resistance. Various characterisation techniques were used to investigate the effects of diffusion treatments and sputter deposition on surface morphology, topology and bulk substrate microstructure. The hardness, adhesion and oxidation resistance of the nitrided layers and sputter-deposited coatings were assessed. The hardness of the diffusion-treated surface of pure Zr metal was found to have been significantly improved and a higher load-bearing capacity was achieved after TPN-treatment compared to untreated pure zirconium. This was due to a 'deep' hardened case which was achieved at moderately low temperatures at short processing times, allowing significantly higher loads to be applied before failure occurred.

TPN treatment of pure zirconium metal was found to have improved the oxidation resistance compared to untreated pure zirconium in aqueous conditions. The Zr-Mg coatings produced by PVD showed that magnesium can remain in substitutional solid solution with zirconium at high magnesium concentration and showed no evidence of phase separation. Hydrothermal oxidation tests of the Zr-Mg coatings revealed the formation of a (metastable) tetragonal zirconia phase throughout the oxide scale which plays an important role in stabilising of the oxide. The evidence presented suggests that both the diffusion treatments and sputter co-deposition process need to be optimised in order to improve oxidation resistance under aqueous conditions and abnormal reactor operating conditions.

Table of Contents

Acknowledgements.....	iii
Abstract.....	iv
List of Figures	ix
List of Tables	xv
Chapter 1 – Introduction, Background and Literature Review	1
1.1 Introduction and Objectives	1
1.2 Fukushima Nuclear Accident Issues with Zr Alloys under High Temperature Conditions.....	3
1.3 The Demand for Nuclear Energy.....	5
1.4 Overview of Zirconium.....	7
1.4.1 Crystal Structure of Zirconium	8
1.5 The Use of Zirconium Alloys in the Nuclear Industry.....	8
1.6 A Brief History of Cladding Materials used in the Nuclear Industry	9
1.7 The Fabrication and Manufacture of Zr Alloys for Nuclear Reactors	10
1.7.1 The Kroll Process	11
1.7.2 The Manufacture of Zircaloy Fuel Cladding	13
1.8 Oxidation Behaviour of Zr Alloys.....	14
1.8.1 Polymorphs of Zirconium Oxide.....	16
1.8.2 The Pre-Transition Period	21
1.8.3 The Post-Transition Period.....	24
1.8.4 Determining Oxidation Resistance.....	25
1.8.5 Volume Fraction Determination of the Monoclinic and Tetragonal Zirconia Phase	26
1.8.6 Determination of Pilling-Bedworth Ratio for Zirconia Polymorphs.....	27
1.8.7 The Effects of Hydrogen Evolution and Hydrogen Precipitates.....	31
1.8.8 Issues Surrounding Modification of Alloying Elements in Zircalloys	35
1.9 Plasma Nitriding.....	37
1.9.1 Surface Treatments.....	37
1.9.2 Enhanced Plasma Diffusion Processes: Nitriding.....	38

1.9.3 The Issues with Diode Plasmas	40
1.9.4 The Case for Triode Discharge Systems	40
1.9.5 Triode Plasma Nitriding.....	43
1.9.6 The Role of Argon Gas in Triode Systems	44
1.9.7 The Use of Triode Plasma Nitriding in Diffusion Treatments.....	45
1.10 Motivation Behind the Use of Zirconium Nitride (ZrN) Coatings.....	47
1.11 Current Coating Trends in Nuclear Applications.....	48
1.12 Stabilisation of the Oxide Layer	49
1.13 Hume-Rothery Rules for Substitutional Solid Solution	55
1.14 Structure Zone Model for Coating Growth.....	57
Chapter 2 – Experimental Methodology.....	62
2.1 Micro-preparation of Samples	62
2.2 Optical Light Microscopy Imaging.....	63
2.3 Ion Beam Polishing.....	63
2.4 Triode Plasma Nitriding Diffusion Treatment	63
2.5 Sputter Deposition	65
2.6 Fundamental Concepts in X-ray Diffraction (XRD).....	68
2.6.1 Diffractometer Geometry	69
2.6.2 Glancing Angle X-ray Diffraction.....	70
2.7 Vibrational Modes using Raman Spectroscopy	72
2.8 Determination of Surface Roughness	74
2.9 Determining Surface Morphology and Elemental Composition using Scanning Electron Microscopy (SEM) and Energy Dispersive X-ray Spectroscopy (EDX)	75
2.10 Nanoindentation	77
2.11 Scratch Adhesion Testing.....	79
2.12 Hydrothermal Oxidation Testing.....	81
Chapter 3 – Triode Plasma Nitriding Diffusion Treatments.....	83
3.1 Plasma-nitriding of Zr: Trial Runs.....	83

3.2 Microstructure of TPN-treated Zirconium	89
3.3 Surface Roughness of the TPN-treated Surface.....	94
3.4 Determining Nitrided Layer Thickness in Cross-section	95
3.5 The Use of Ion Polishing to Observe the Nitrogen Diffusion Zone	97
3.6 Determining Crystallographic phases Using Glancing-Angle XRD	100
3.7 Determining Vibrational Modes of the Plasma-Nitrided Zr Layer Using Raman Spectroscopy	105
3.8 Hardness Measurements Using Nanoindentation.....	107
3.8.1 Nanoindentation of Bulk Zr and ZIRLO Substrates	107
3.8.2 Nanoindentation of TPN-Treated Zr	109
3.9 Scratch Adhesion of the TPN-treated Zirconium Samples.....	112
3.9.1 Adhesion of the 2 hr TPN-treated Zr Sample	113
3.9.2 Adhesion of the 3 hr TPN-treated Zr Sample.....	115
3.9.3 Adhesion of the 4 hr TPN-treated Zr Sample.....	117
3.10 Summary	119
Chapter 4 – Hydrothermal Oxidation Tests	120
4.1 Background	120
4.2 Hydrothermal Oxidation Testing in Water.....	120
4.2.1 Cross-sectional SEM Analysis of the Oxide Scale formed on TPN-treated Zr and Untreated Pure Zr Following Hydrothermal Oxidation	126
4.2.2 Phase Analysis of the Hydrothermally Oxidised TPN-Zr	130
4.2.3 Raman Spectroscopy of the Hydrothermally Oxidised Sample	137
4.2.4 Surface Roughness Measurements of the Hydrothermally Oxidised Samples.....	138
4.3 Nanoindentation Hardness Measurements of Oxide Scales following Hydrothermal Oxidation of Plasma Nitrided Diffusion-Treated Layers	139
4.3.1 Hardness Measurements of Hydrothermally Oxidised Samples	139
4.4 Scratch Adhesion of Oxide scales following Hydrothermal Oxidation of Plasma Nitrided Diffusion-Treated Layers.....	141
4.4.1 Scratch ‘Adhesion’ Testing of Hydrothermally Oxidised 2h TPN-treated Zr Samples (A_TPN_2hr).....	141

4.4.2 Scratch 'Adhesion' Profiles of Hydrothermally Oxidised 3h TPN-treated Zr Samples (A_TPN_3hr).....	144
4.4.3 Scratch Adhesion Profiles of Hydrothermally Oxidised 4h TPN-treated Zr Samples (A_TPN_4hr).....	146
4.5 Summary	148
Chapter 5 – Sputter-deposited Zirconium-Magnesium Coatings	150
5.1 Fabrication of Zr-Mg Coatings using Magnetron Sputtering	150
5.1.1 Targets with Applied 600W Power	150
5.1.2 SEM/EDX Spectroscopy Analysis of Zr-Mg Coatings	156
5.1.3 Glancing-Angle XRD Analysis of the Sputter Co-deposited Coatings.....	161
5.1.4 Nanoindentation Hardness of Zr-Mg Coatings	171
5.1.5 Scratch Adhesion Tests of Zr-Mg Coatings.....	172
5.2 Hydrothermal Oxidation of Zr-Mg Coatings	177
5.2.1 SEM Analysis of Hydrothermally Oxidised Zr-rich and Mg-rich Coatings	177
5.2.2 GAXRD Analysis of the Hydrothermally Oxidised Zr-rich and Mg-rich Sputter-deposited Coatings.....	186
5.3 Summary	196
Chapter 6 – Conclusions and Recommendations for Future Work	197
6.1 Conclusions	197
6.1.2 Concluding Remarks.....	200
6.2 Recommendations for Future Work	201
References	208
Appendix 1	225

List of Figures

Figure 1.1: Schematic of a Fukushima Dai-Ichi reactor which were GE boiling water reactors known as Mark 1 containment vessels [11].	5
Figure 1.2: Schematic of the zirconium oxidation process [48].	15
Figure 1.3: Zr-O phase diagram showing oxygen solubility in zirconium [54].	16
Figure 1.4: XRD patterns showing reflections of HCP α -Zr [59], m-ZrO ₂ [56], t-ZrO ₂ [57] and c-ZrO ₂ [58].	18
Figure 1.5: Raman spectra of oxidised sample (a) c-ZrO ₂ , (b) t-ZrO ₂ , (c) m-ZrO ₂ [79].	21
Figure 1.6: Optical micrograph show a multi-layered oxide structure formed after aqueous corrosion tests at 360°C for 784 days Zircaloy-4 [63].	23
Figure 1.7: The Zr-H phase diagram [131].	33
Figure 1.8: Optical micrographs of (a) Circumferential and (b) radial microcracks resulting from hydride orientation [18].	34
Figure 1.9: Influence of tin content on oxidation resistance of Zircaloy-4 [41].	35
Figure 1.10 : Schematic diagram of a triode discharge system.	41
Figure 1.11: Changes in L/λ_m ratio show the fraction of the total energy transported by ionic species (-) is greater than the energy fraction of ions arriving at the cathode (---) [161].	41
Figure 1.12: Schematic representation of kinetics of formation and growth of nitride surface layers of zirconium (adapted from [179]).	45
Figure 1.13: Zirconium-Nitrogen binary phase diagram.	46
Figure 1.14: Magnesium-rich region of the Mg-Zr phase diagram [223].	55
Figure 1.15: Structural zone models for coating growth: (a) Model proposed by Movchan and Demchishin [228] and (b) Model proposed by Thornton [169] for metallic coatings deposited by magnetron sputtering.	58
Figure 2.1: Internal view of the chamber showing Zr substrates, and the attached thermocouples in an aura of plasma (purple) during TPN process.	65
Figure 2.2: Schematic of an unbalanced magnetron configuration.	66
Figure 2.3: (a) Schematic drawing target-substrate arrangement in deposition chamber and (b) plasma glow during operation.	67
Figure 2.4: (a) Mg target exhibited high material consumption when power was set to 850 W compared to (b) Zr target. Both targets exhibited 'racetrack' effects during sputter deposition but Mg target segment displayed greater erosion due to having a higher sputtering yield relative to the Zr target segment.	68

Figure 2.5: Schematic of diffraction of X-rays by a crystal lattice (adapted from Pecharky et al [240]).	69
Figure 2.6: Philips Panalytical X’Pert3 (Netherlands) was used to carry out GAXRD experiments at the XRD facility, The University of Sheffield.....	72
Figure 2.7: Schematic of the energy level diagram showing (a) Rayleigh scattering and (b) Raman scattering.	73
Figure 2.8: Schematic of the process for generating an interference image using optical profilometry.	74
Figure 2.9: Philips SEM XL30 was used to analyse the surface morphology.	76
Figure 2.10: An indentation load-displacement curve showing regions that are used to determine hardness [244].	78
Figure 2.11: Schematic of failure modes from scratch adhesion measurements.	81
Figure 2.12: Hydrothermal oxidation test rig showing magnetron sputter-deposited coatings which was performed at 360°C for 3 and 7 days.	82
Figure 3.1: Secondary electron image of (a) as-received HCP α -Zr surface showing impurities and (b) HCP α -Zr after 9 μ m diamond polish is used which shows some scratches.....	84
Figure 3.2: Demarked grain boundaries of Zr grains shows the Zr surface has high resistance to chemical attack after being etched in a HF-based etchant.	85
Figure 3.3: Optical micrographs of (a) bulk HCP α -Zr (ion polished) and (b) TPN diffusion-treated Zr surface which show no observable grain growth of α -Zr.	86
Figure 3.4: SEM micrograph of the TPN-treated Zr surface morphology in SE mode.	87
Figure 3.5: Elemental composition obtained from EDX analysis, shows the presence of Zr and N.	87
Figure 3.6: SEM cross-section of plasma-nitrided Zr and EDX Line-scan from Zr>ZrN layer>Bakelite.	88
Figure 3.7: TPN-treated Zr samples nitrided for (a) 2 hr; (b) 3 hr and (c) 4 hr respectively, showing a shiny reflective golden appearance.	89
Figure 3.8: Optical micrograph of the 4 hr TPN-treated Zr showing more pronounced Zr microstructure towards the edge of the TPN-treated surface due to cathode sheath edge effects.	90
Figure 3.9: (a) SEM micrograph in BSE mode of the 4 hr TPN-treated surface show the 12 μ m grain boundary structure of zirconium grains and (b) EDX elemental maps of the TPN-treated surface show the presence of zirconium (highlighted in red) and nitrogen (highlighted in green).	91
Figure 3.10: Surface topographic maps of the 2 hr, 3 hr and 4 hr TPN-treated Zr samples using (a) AFM imaging of the surface and (b) AFM three-dimensional topographic maps which show protuberances.....	93

Figure 3.11: Optical profilometry images comparing surface roughness of (a) untreated pure Zr and (b) 4 hr TPN-treated Zr show increased surface roughness after diffusion treatment.	95
Figure 3.12: (a) SEM micrograph of the cross-section of the 4h nitrided Zr and (b) EDX spectrum showing where nitride layer was expected to be detected.	96
Figure 3.13: Schematic to prevent edge-rounding during grinding and polishing.	97
Figure 3.14: Cross-sectional optical micrographs of the (a) 2 hr (b) 3 hr and (c) 4 hr TPN-treated Zr sample shows the nitrogen diffusion zone after ion polishing.	99
Figure 3.15: GAXRD of the 4 hr plasma-treated Zr at incident angles 2, 4 and 6° showing the presence of ZrN phase [263] (PDF no. 01-078-1420) and nitrogen-containing Zr phase [59].	101
Figure 3.16: Raman spectra of the plasma diffusion treated Zr showing evolution of ZrN bands with treatment time.	105
Figure 3.17: Raman scattering of ZrN [269].	106
Figure 3.18: Raman Spectrum of ZrN coatings fabricated by magnetron sputtering at 600°C [272].	107
Figure 3.19: AFM image showing indents on (a) Zr and (b) ZIRLO™ substrates used to obtain hardness measurements.	107
Figure 3.20: Load vs Displacement graphs showing nine indents for: (a) bulk Zr and (b) ZIRLO™. ...	108
Figure 3.21: Nanoindentation graph of the 2 hr, 3 hr and 4 hr TPN-treated samples show how apparent hardness of the nitride compound layer decreases with contact depth.	110
Figure 3.22: Scratch test for the 2 hr TPN-treated Zr show optical micrographs of (a) cohesive failure; (b) adhesive failure (c) complete spallation of the treated layer and (d) loading profiles at the points at which L_{C1} , L_{C2} and L_{C3} failure modes occur, identified using a combination of Tangential Force (F_T), Acoustic Emission (AE) and Penetration Depth (P_d) data.	114
Figure 3.23: Scratch test for the 3 hr TPN-treated Zr show optical micrographs of (a) cohesive failure; (b) adhesive failure (c) complete spallation of the treated layer and (d) loading profiles at the points at which L_{C1} , L_{C2} and L_{C3} failure modes occur, identified using a combination of Tangential Force (F_T), Acoustic Emission (AE) and Penetration Depth (P_d) data.	116
Figure 3.24: Scratch test for the 4 hr TPN-treated Zr show optical micrographs of (a) cohesive failure; (b) adhesive failure (c) complete spallation of the treated layer and (d) loading profiles at the points at which L_{C1} , L_{C2} and L_{C3} failure modes occur, identified using a combination of Tangential Force (F_T), Acoustic Emission (AE) and Penetration Depth (P_d) data.	118
Figure 4.1: SEM micrograph in BSE mode of the hydrothermally oxidised 4h TPN-treated sample showing micro-cracks on the oxide surface formed following hydrothermal tests at 360°C for 3 days.	121

Figure 4.2: SEM micrograph in BSE mode shows aluminium and oxygen contamination (highlighted in bright red and grey from EDX analysis) on the surface of the oxide scale following hydrothermal oxidation at 360°C for 3 days.....	122
Figure 4.3: (a) Cross-sectional SEM micrograph of the oxide scale formed on the hydrothermally oxidised TPN-Zr at 360°C, 3 days (A_TPN_4hr) and (b) EDX data show Zr and O elements present in the oxide scale.	127
Figure 4.4: Cross-sectional SEM micrograph of (A_TPN_4hr) sample near the pre-formed outer oxide layer showing spallation of the oxide scale near the oxide surface.	128
Figure 4.5: Cross-sectional SEM micrograph of the oxide scale formed on the hydrothermally oxidised pure zirconium at 360°C, 3 days.....	129
Figure 4.6: GAXRD patterns of the 4 hr TPN-Zr sample following hydrothermal oxidation test at 360°C 3 days show majority of the peaks are identified with the formation monoclinic zirconia. The phases formed and peak positions were compared with HCP α -Zr [59], m-ZrO ₂ [56], t-ZrO ₂ [57] and ZrH _{1.66} [126].....	131
Figure 4.7: Raman spectra showing comparisons of (a) TPN-treated Zr; (b) A_TPN_4hr sample.....	138
Figure 4.8: Surface roughness (R_a) of the hydrothermally oxidised TPN-treated samples was measured to be much higher (more than 2x) compared to TPN-treated samples.	139
Figure 4.9: Hardness (GPa) vs. contact depth (nm) plot shows the hardness of the oxide scale formed on each of the TPN-treated samples decreases with contact depth.....	140
Figure 4.10: Scratch test for the A_TPN_2hr show optical micrographs of (a) cohesive failure; (b) adhesive failure (c) complete spallation of the oxide scale and (d) loading profiles at the points at which L_{C1} , L_{C2} and L_{C3} failure modes occur, identified using a combination of Tangential Force (F_T), Acoustic Emission (AE) and Penetration Depth (P_d) data.	143
Figure 4.11: Optical micrograph of failure of the HCP α -Zr substrate showing a large crack (galling wear) resulting from the indenter load applied.	144
Figure 4.12: Scratch test for the A_TPN_3hr show optical micrographs of (a) cohesive failure; (b) adhesive failure (c) complete spallation of the oxide scale and (d) loading profiles at the points at which L_{C1} , L_{C2} and L_{C3} failure modes occur, identified using a combination of Tangential Force (F_T), Acoustic Emission (AE) and Penetration Depth (P_d) data.	145
Figure 4.13: Scratch test for the A_TPN_4hr show optical micrographs of (a) cohesive failure; (b) adhesive failure (c) complete spallation of the oxide scale and (d) loading profiles at the points at which L_{C1} , L_{C2} and L_{C3} failure modes occur, identified using a combination of Tangential Force (F_T), Acoustic Emission (AE) and Penetration Depth (P_d) data.	147

Figure 5.1: Camera images of sputter co-deposited Zr-Mg coatings on stainless steel substrates (2cm x 2cm) carried out at 600 W at target-substrate distance of 15 cm and negative substrate bias voltage of 150 V which show (a): graded deposition; (b) mostly coated and (c) partial coating of the substrates. SEM micrographs shows the morphology and EDX spectra shows Zr-rich and Mg-rich regions in Figure 5.1(a) and (c) respectively. 152

Figure 5.2: Camera image showing spallation of the Zr-Mg coating on zirconium substrate when the sample was taken out of the deposition chamber following 5 min cooling time. 153

Figure 5.3: Schematic of the configuration of substrates on the substrate holder during sputter deposition at 700 W target power, 3 hours coating duration and one hour cooling time, along with approximate EDX elemental compositions. The Zr-rich (Mg: 25 at%) and Mg-rich (Mg: 53 at%) samples were taken forward for SEM analysis. 154

Figure 5.4: Camera images of the sputter co-deposited Zr-Mg coatings on Zr substrates that were located on (a) lower half and (b) top half of the substrate holder (shown in the schematic configuration in Figure 5.3). The differences in the surface colour is likely to be due to the differences in Mg and Zr concentrations in the coating. 156

Figure 5.5: (a) SEM surface morphology of the Zr-rich sample shows column sizes ranged from 2 μm to about 15 μm in diameter and (b) EDX spectrum of the coated surface revealed a zirconium-rich coating (Mg content 25 at%). 157

Figure 5.6: (a) SEM surface morphology shows column sizes ranged from 2 μm to about 12 μm in diameter and (b) EDX spectrum of the coated surface revealed a magnesium-rich coating (Mg content 53 at%)..... 159

Figure 5.7: Cross-sectional SEM micrographs of the coatings in BSE mode of (a) Zr-rich (25 at%) and (b) Mg-rich (53 at%) samples revealed coating thicknesses of 25.2 μm and 26.5 μm respectively.. 160

Figure 5.8: SEM micrograph of the magnesium-rich coating (Mg content 53 at%) show microcracks on the surface. 161

Figure 5.9: GAXRD pattern of the sputter-deposited Zr-Mg coating on stainless-steel substrates. The patterns are compared to peak positions found in literature: Mg [213], Zr [195], MgO [313] and m-ZrO₂ [56]. 164

Figure 5.10: XRD reference patterns of Zr [195] and Mg [213] Phases show slight differences in the peak positions for some of the peaks such as the (002) and (013). If there was evidence of peak-splitting (in Figure 5.9), separate peaks would have been exhibited which might be indexed to Zr or Mg phases indicating phase separation. However, this was not seen from the GAXRD patterns in Figure 5.9. 165

Figure 5.11: MgO peak reflections..... 166

Figure 5.12: Hardness vs displacement graphs of (a) Zr-rich and (b) Mg-rich sputter-deposited coatings.....	171
Figure 5.13: Scratch adhesion test of the Zr-rich (Mg: 25 at%) coating showing (a) optical micrograph of scratch track and (b) scratch adhesion profiles and the critical loads (L_c) to failure.	174
Figure 5.14: Scratch adhesion test of the Mg-rich (Mg: 53 at%) coating showing (a) optical micrograph of scratch track and (b) scratch adhesion profiles and the critical loads (L_c) to failure..	176
Figure 5.15: SEM micrographs and the associated EDX spectra of the surface of pure Zr following hydrothermal oxidation after (a) 3 days and (b) 7 days.	178
Figure 5.16: SEM micrographs and EDX spectra of the surface of the Zr-rich coatings (Mg: 25 at%) following hydrothermal oxidation after (a) 3 days and (b) 7 days.	179
Figure 5.17: SEM micrographs of the surface of the Mg-rich coatings (Mg: 53 at%) following hydrothermal oxidation after (a) 3 days (with the EDX spectrum of the redeposited material) and (b) 7 days.	180
Figure 5.18: SEM micrograph of the Mg-rich coating hydrothermally oxidised for 7 days showing regions of spallation, microcracks are redeposited material on the oxidised surface.	181
Figure 5.19: Cross-sectional SEM micrographs of hydrothermally-oxidised (a) pure Zr after 3 days; (b) pure Zr after 7 days; (c) Zr-rich coating after 3 days (d) Zr-rich coating after 7 days; (e) Mg-rich coating after 3 days and (f) Mg-rich coating after 7 days.....	185
Figure 5.20: GAXRD patterns of pure zirconium hydrothermally oxidised for (a) 3 days and (b) 7 days. The phases formed and peak positions were compared with HCP α -Zr [59], m-ZrO ₂ [56] and t-ZrO ₂ [57].	187
Figure 5.21: GAXRD patterns of Zr-rich coatings hydrothermally oxidised for (a) 3 days and (b) 7 days. The phases formed and peak positions were compared with HCP α -Zr [59], m-ZrO ₂ [56] and t-ZrO ₂ [57], Mg [213] and MgO [313].	190
Figure 5.22: GAXRD patterns of Mg-rich coatings hydrothermally oxidised for (a) 3 days and (b) 7 days. The phases formed and peak positions were compared with HCP α -Zr [59], m-ZrO ₂ [56] and t-ZrO ₂ [57], Mg [213] and MgO [313].	193

List of Tables

Table 1.1: Properties of HCP α -Zr [20].	7
Table 1.2: Chemical composition of Zr alloys (wt%) used in fuel rod cladding [22].	9
Table 1.3: Lattice parameters for bulk zirconium metal and zirconia polymorphs.	17
Table 1.4: Summary of P-B ratio calculations of the monoclinic zirconia (m-ZrO ₂), tetragonal zirconia (t-ZrO ₂), cubic zirconia (c-ZrO ₂) and HCP α -Zr.	31
Table 2.1: Procedure for grinding and polishing of bulk Zr metal.	62
Table 2.2: Parameters used in scratch adhesion profiles.	80
Table 2.3: Description of failure events, observations and corresponding critical loads [246].	80
Table 3.1: Conditions used during plasma nitriding.	85
Table 3.2: Elemental composition obtained from EDX analysis for the 2 hr, 3 hr and 4 hr TPN-treated surface.	92
Table 3.3: X-ray Penetration Depths for ZrN at 2, 4 and 6° incident angles.	102
Table 3.4: Summary of the critical load values for the 2 hr, 3 hr and 4 hr TPN diffusion-treated Zr samples.	119
Table 4.1: Hydrothermally oxidised TPN-treated Zr samples showed slightly lower weight gains compared to pure Zr under the same conditions.	122
Table 4.2: Average zirconia crystallite size calculated using the Scherrer equation.	133
Table 4.3: Summary of the critical load values for the hydrothermally oxidised 2 hr, 3 hr and 4 hr TPN diffusion-treated Zr samples.	147
Table 5.1: EDX elemental composition of the sputter co-deposited Zr-Mg samples. The Zr-rich (Mg: 25 at%) and Mg-rich (Mg: 53 at%) samples highlighted in grey were taken forward for detailed characterisation.	155
Table 5.2: Average crystallite size determined from GAXRD patterns using Scherrer's equation.	170
Table 5.3: X-ray Penetration Depths into ZrO ₂ at incident angles 2, 4 and 6° determined from AbsorbDX software.	187

Abbreviations

AFM	Atomic Force Microscopy
ASTM	American Society for Testing and Materials
BCC	Body Centred Cubic
BWR	Boiling Water Reactor
CoF	Coefficient of Friction
D.C.	Direct current
EBS	Electron Backscatter Diffraction
EDX	Energy Dispersive X-ray
FCC	Face-Centred Cubic
FP	Fission Product
GAXRD	Glancing Angle X-ray Diffraction
GDOES	Glow Discharge Optical Emission Spectroscopy
HCP	Hexagonal Close Packed
LOCA	Loss of Coolant Accident
PBR	Pilling-Bedworth Ratio
PDF	Powder Diffraction File
PWR	Pressurised Water Reactor
PVD	Physical Vapour Deposition
R.F.	Radio Frequency
RPV	Reactor Pressure Vessel
SEM	Scanning Electron Microscope
TEM	Transmission Electron Microscope
TBC	Thermal Barrier Coating
TPN	Triode Plasma Nitriding
TPO	Triode Plasma Oxidation
YSZ	Yttria-Stabilised Zirconia

Chapter 1 – Introduction, Background and Literature Review

1.1 Introduction and Objectives

Zirconium-based alloys are currently used as fuel rod cladding in nuclear power reactors because of their low neutron absorption cross-section, good corrosion resistance and mechanical strength. They provide the primary containment for fission products generated from nuclear fission reactions and serve as a safety barrier to radionuclide release in the Reactor Pressure Vessel (RPV). However, under normal operating conditions (300-330°C, 15-20 MPa) Zr-alloy fuel cladding undergoes waterside oxidation by the coolant. A significant fraction of the hydrogen generated in the oxidation reaction with moisture is absorbed into the cladding and precipitated as zirconium hydride which can lead to embrittlement of the cladding, thus adversely impacting the mechanical integrity of the fuel rods. During an uncontrolled Loss-Of-Coolant Accident (LOCA), the cladding temperature may rise to above 800°C, in which the oxidation reactions and corresponding hydrogen generation are significantly accelerated. The consequences of this reaction were exemplified during the Fukushima-Daichi accident (after the 2011 Japan earthquake and the subsequent tsunami [1]) which caused explosions of the reactor building, resulting in radioactive release to the environment. Following the accident, the nuclear industry has focused much of its efforts into enhancing safety of its current fleet of reactors and improving safety of future designs. A promising approach that has generated considerable research interest is to fabricate a protective coating or surface-treated layer that would improve/enhance the oxidation resistance of the Zr-alloy cladding to be more damage-tolerant during LOCA conditions, such that cladding failure is delayed and the accident response time to allow external intervention/solutions is increased. Furthermore, this approach could also have the benefit of reducing oxidation rate and hydrogen absorption during normal operation, further enhancing overall reactor safety design.

The current study aims to show whether oxidation-resistant surface-treated layers can be successfully produced using triode plasma-nitriding (TPN) diffusion treatment and/or PVD Zr-Mg coatings, to determine their viability for use on fuel rod cladding in a nuclear reactor with the aim of improving oxidation resistance of zirconium in demanding pressurised-aqueous environments during normal operation and abnormal in-reactor transient scenarios (e.g. loss of coolant accident).

The specific requirements of the surface-treated layer/coating are that:

1. It must reduce oxidation and associated hydrogen precipitation of zirconium.
2. It must have a similar neutron absorption cross-section to the extant Zr alloys (higher neutron absorption requires greater fuel enrichment to achieve the same neutron economy).
3. It must adhere/bond to the Zr-alloy cladding prior to, whilst in and after service (any proposed barrier must not be susceptible to spallation or delamination in the reactor core).
4. It must be stable under the normal thermal cycling conditions during reactor operations.
5. It must be mechanically robust (i.e. resilient to interactions with grid assembly components during fuel rod insertion prior to service).

In order to achieve the overall aim described above, it was necessary to carry out the following objectives:

- A critical assessment of the available knowledge on the properties of zirconium; its oxide polymorphs – particularly behaviour as oxide layers on Zr-metal during oxidation, high temperature corrosion as well as the effects of hydrogen evolution during oxidation of Zr.
- Designing surface-treated nitride layers on bulk zirconium metal to modify the existing surface by inducing a change in its chemical composition through TPN diffusion treatment. This was achieved by taking advantage of the high affinity of nitrogen for zirconium to provide a hardened diffusion layer with a diffusion zone on the substrate surface. Bulk Zirconium metal (98% purity) was chosen for this study because it is a low-cost widely available material and serves as a precursor to reactor-grade zirconium alloys which are difficult to obtain for reasons pertaining to commercial sensitivity.
- Designing a magnesium-containing zirconium PVD coating system to investigate if these elements could be in solid solution with each other and whether magnesium inclusion might stabilise the tetragonal or cubic phase of zirconium oxide (during hydrothermal oxidation) intended to enhance the oxidation resistance of zirconium in aqueous conditions.

The surface-treated layers and coatings were analysed using a series of characterisation techniques including: optical microscopy, optical profilometry, Raman spectroscopy, Glancing-Angle X-ray Diffraction (GAXRD), Scanning Electron Microscopy (SEM), Energy Dispersive X-ray (EDX) spectroscopy, scratch adhesion, nanoindentation hardness and hydrothermal oxidation tests. The combination of these techniques provided information on the oxidation behaviour of the surface-treated layer and coatings in reactor operating conditions.

Following this introduction, the literature review chapter has been compiled to establish the context, background and justification for using surface-treated layers/coatings on zirconium alloys beginning with issues related to the limited corrosion resistance of zirconium alloys in demanding environments and the rationale for using the plasma thermo-chemical diffusion treatment and sputter deposition techniques applied in this work.

1.2 Fukushima Nuclear Accident Issues with Zr Alloys under High Temperature Conditions

On Friday March 11 2011, a powerful earthquake centred 130 km offshore mainland Japan and measuring 9.0 on the Richter scale caused a 15-metre height tsunami on the east coast of Japan [2]. Fukushima Dai-Ichi reactors 1, 2 and 3 shut down automatically and 4, 5 and 6 were not operating at the time. The reactors proved robust seismically but were vulnerable to the tsunami. External electrical power was lost due to earthquake damage and the backup diesel generators (located near the reactors) were flooded following the tsunami. About an hour after shutdown, the reactor cores would still produce 1.5% of their thermal output from fission product decay (22-33 MW). Without a heat removal system by circulation to a heat exchanger, excess steam was generated inside the RPV [3]. As the water level inside the reactor dropped due to the production of steam, this exposed the zirconium alloy fuel rods (encasing the uranium fuel pellets) which reacted with oxygen in the moisture present, to oxidise the Zr-alloy cladding, resulting in the release of hydrogen gas as a by-product of the oxidation reaction which continued to accumulate. Schwantes et al [4] reported that once the coolant water was lost during the earthquake and the subsequent tsunami, the loss of heat removal capability allowed the temperatures within the RPV to rise above 800°C. The zirconium oxidation reaction became autocatalytic, i.e. above a critical temperature the reaction products also form the reactants, acting as a catalyst as the reaction becomes self-sustaining.

Another key reaction that exacerbated the conditions during LOCA was between the boron carbide absorbers, stainless steel control blades and the Zircaloy-2 cladding. In the core of the GE-Hitachi Mark I containment BWR cores (Figure 1.1), cruciform-shaped 304 stainless steel control blades are filled with boron carbide (B_4C) – neutron absorbers (either in powder or pellet form) to aid reactivity control during reactor operation. Although the melting temperature of B_4C is 2450°C, uncooled contact between the 304 stainless steel housing (which has melting temperature of 1530 °C [5]) resulted in a melt formation in the core (due to eutectic reactions) at temperatures of about 1250°C. The 304SS- B_4C melt then relocated to lower parts of the fuel bundle where it reacted with the Zircaloy-2 cladding

producing another, even lower temperature, eutectic reaction between the two metals - at only 850-900°C, which melted the cladding (below its melting temperature of 1850°C). Interestingly, Sepold et al [6] conducted out-of-pile tests a few years before the Fukushima accident and reported that B₄C formed a melt with 304 stainless steel at around 1250°C that then attacked the Zircaloy-2 cladding. The conditions resulted in the rupture of the cladding enabling UO₂ fuel dissolution with the melt which relocated from the bottom of the test bundle. Studies [7, 8] carried out a few decades earlier revealed that reactions 304SS-B₄C start at 800°C and led to a complete failure of the control blade at around 1250°C by rapid liquefaction of the 304 stainless steel by 200°C below its melting temperature. In an experimental study that preceded several years before the Fukushima accident, Steinbruck et al [9] showed that only 1 wt% boron carbide was necessary to completely liquefy the stainless steel at about 1250°C after 1 h. Considering that each control blade in the Fukushima Dai-Ichi nuclear reactors consisted of 7 kg B₄C and 93 kg stainless steel [10], it is likely that these assemblies would have been completely destroyed during the accident, although this has not been visually confirmed due to the high radiation following the accident. Following failure of the stainless steel cladding, the bare B₄C is thought to have reacted with steam in a series of chemical reactions to produce hydrogen, carbon monoxide, carbon dioxide and methane [9].

The high temperature and pressure conditions inside the RPV caused severe degradation and cracking of the fuel rods and together with the exposed uranium fuel, melted steel and cladding which then seeped to the bottom of the reactor where this solidified. These conditions also allowed for the hydrogen to ignite resulting in explosions of reactor units 1, 2 and 3 which occurred 25 hours, 87 hours and 68 hours respectively, following loss of electrical power to the coolant pumps. It is estimated that 770 petabequerels (PBq) were released to the environment [11] which comprised primarily of fission products (i.e. Iodine-131 and Caesium-137).

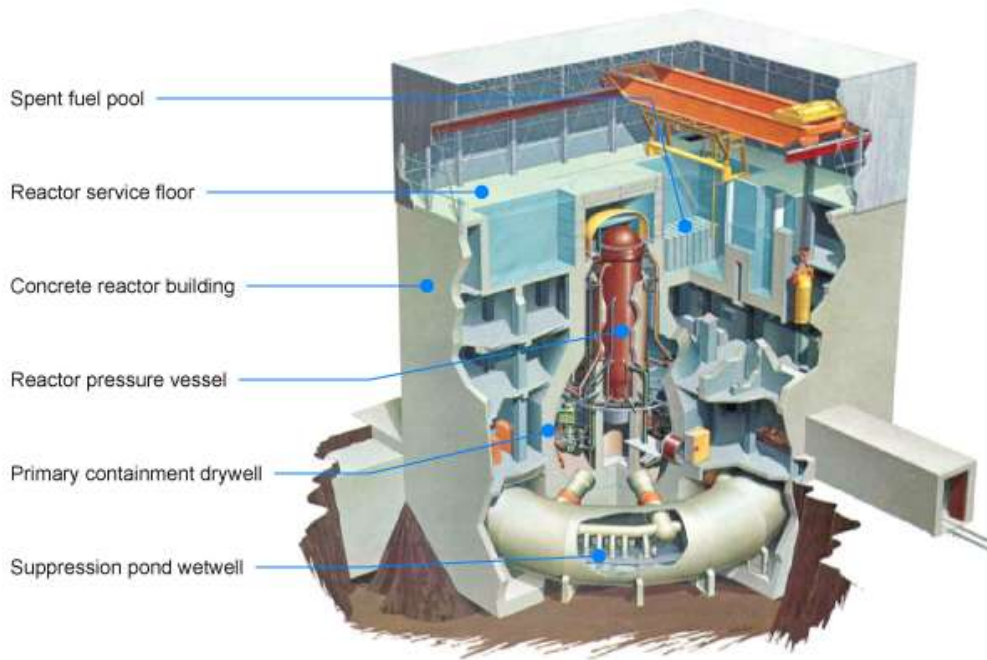


Figure 1.1: Schematic of a Fukushima Dai-Ichi reactor which were GE boiling water reactors known as Mark 1 containment vessels [11].

This further emphasizes the need to limit oxidation rates on zirconium alloy fuel cladding through the use of surface-treated layers to act as an additional safety barrier, long enough for external intervention to facilitate a safe resolution to LOCA.

1.3 The Demand for Nuclear Energy

The Fukushima Dai-Ichi nuclear accident triggered a series of reviews into current nuclear safety practice and multiple regulatory reforms [12, 13] to optimise safety of reactors prior to, during and post-reactor operations. Following the accident, a few countries that use civil nuclear power took the decision to shut down some or most of their reactors [1], until extant regulations were scrutinised, verified, validated and where necessary, improved upon. This decision had detrimental economic consequences on countries such as Japan that have historically relied upon a sizable base load power being produced from nuclear to meet the population's energy requirements [14]. For instance, the shutdown of 48 reactors from a total of 50 in the aftermath of the accident led to a dramatic increase in Liquefied Natural Gas (LNG) imports, in an attempt to replace the energy lost from nuclear. However, this led not only to an increase in carbon footprint due to LNG being a fossil fuel but also resulted in tens of billions of dollars more being spent than if nuclear power stations had been kept operational [14].

The global share of electricity generated from nuclear power is set to increase as environmental policies shift to low-carbon sources of energy. The United Kingdom for instance, is set to close all of its coal-fired power stations (which provide about 40% of its energy needs) by 2025 [15] which would have to be replaced by an alternative energy source. The feasibility of reliance on wind and solar for instance, suffers from intermittency issues for continuous on-demand requirements. Wind turbines and solar panels also occupy a much larger area of land for the equivalent energy output compared to nuclear energy and require frequent replacement and maintenance. The land space occupied by a wind farm is about 133 square miles and for a solar power plant this is about 65 square miles per 1000 Megawatt capacity compared to 1.3 square miles for nuclear [16]. Furthermore, on-site gas power plant would be required should the energy generated from wind and solar not meet demand due to its intermittency. It has been recognised by UK government that nuclear energy will be required to fill this gap, together with renewables and gas, in an 'energy mix' policy. Nuclear power provides 11.5% of the world's electricity, with 65 reactors currently under construction globally, and more being planned or in the pipeline. The rate-limiting factor in the construction of nuclear power plants is the large up-front capital expenditure, however considerable focus and research efforts has recently been given to small modular reactors to: (i) reduce new-build construction costs; (ii) meet the particular needs of industries and consumers, and (iii) ease transport logistics with smaller modular components [17].

For extant reactors, there is also a demand to extend their design life and also to increase reactor burnup from the current 35-45 GWd/tU (gigawatt days per tonne of uranium) [18] to higher than 50 GWd/tU, to meet increasing energy demands from industry and consumers as well as to increase electricity production efficiency and hence profitability for reactor operators. However, higher burn-ups would lead to an accelerated corrosion rate [19]. These issues have driven considerable research into understanding the high temperature oxidation mechanisms of zirconium alloys and has brought a renewed interest to investigate potential avenues to increase the oxidation resistance of fuel rod cladding.

1.4 Overview of Zirconium

Zirconium is a reasonably abundant metal found in the Earth's crust (165 parts per million by weight) [20] and is primarily found in its mineral form as zircon sand ($ZrSiO_4$). It is a transition metal located in the fourth group of the periodic table and is commercially produced by reduction with chloride with magnesium in the Kroll process. Its high melting point places zirconium among the refractory elements – making it attractive for high temperature applications. It is ductile, malleable and has good corrosion resistance below 300°C and its properties (See Table 1.1) have attracted much interest in the nuclear, dental and chemical processing industries.

Table 1.1: Properties of HCP α -Zr [20].

Property	Value
Space Group	P69/mmc
Atomic Weight	91.22
Atomic Number	40
Lattice Parameters (HCP)	$a=b=3.23 \text{ \AA}$, $c=5.14 \text{ \AA}$ $\alpha=\beta=90^\circ$, $\gamma=120^\circ$
Thermal expansion (at RT)	$5.7 \times 10^{-6} \text{ K}^{-1}$
Thermal conductivity	21.5 W/(m.K)
Young's Modulus	64 GPa
Vickers Hardness	0.82-1.80 GPa
Melting Temperature	1850 °C
Density	6.51 g/cm ³
Neutron Absorption Cross-section	0.184 barns

1.4.1 Crystal Structure of Zirconium

Unalloyed zirconium is allotropic. At room temperature, zirconium has a hexagonal close packed (HCP) structure, known as alpha (α)-phase and is anisotropic¹. When this is heated up to 865°C, the Zr atoms rearrange to form a body centred cubic (BCC) structure, referred to as a beta (β)-phase which is stable from 865°C up to the melting point at 1845°C [20]. These two phases have different mechanical properties. The presence of alloying elements changes the transus temperature and allows multiphased alloys to form and in the case of Zr in nuclear applications, enhances oxidation resistance properties. When alloying elements are added in small amounts, they stabilise certain phases by altering the transformation temperature and the regions of stability. The ease of plastic deformation in Zr increases from HCP to BCC due to the limited number of available slip systems² for dislocation movement in the HCP structure – 5 in HCP compared to 12 in BCC. The energy needed for plastic deformation also depends on having the minimum slip distance (i.e. the interatomic distance in the slip direction on the slip plane). For BCC structures, this is $0.866a$ but for HCP structures, this is higher at $1a$ [21] (where a is the lattice parameter of the respective unit cell) – which favours the deformation of BCC over HCP metals.

1.5 The Use of Zirconium Alloys in the Nuclear Industry

Zirconium alloys such as Zircaloy-2 (used in boiling water reactors (BWRs), Zircaloy-4 and ZIRLO™ (used in pressurised water reactors (PWRs) (Table 1.2) are widely used in the nuclear industry as cladding material for fuel rods. The main difference between these two types of light water reactors (LWRs) is PWR has pressurised water at over 300°C in its primary cooling/heat transfer circuit and generates steam in a secondary circuit, while BWR boils water directly to steam in the primary circuit above the reactor core. The use of Zr alloys extends to other major structural parts such as fuel channels, pressure tubes, garter springs and spacer grids [19]. They display favourable properties such as: low neutron absorption cross-section (0.184 barns), resistance to stress corrosion cracking, low hydrogen uptake, radiation tolerance and adequate oxidation/corrosion resistance under reactor operating temperature/pressure conditions.

¹ Anisotropy is the property of being directionally dependent which implies different properties in different directions.

² A slip system describes a set of slip planes and a family of slip directions that allows dislocation motion to occur that lead to plastic deformation.

Table 1.2: Chemical composition of Zr alloys (wt%) used in fuel rod cladding [22].

Element	Zircaloy-2	Zircaloy-4	ZIRLO
Sn	1.20-1.70	1.20-1.70	0.90-1.20
Nb	-	-	0.98-1.0
Fe	0.07-0.20	0.18-0.24	0.1-0.11
Cr	0.05-0.15	0.07-0.13	<0.05
Ni	0.03-0.08	-	-

1.6 A Brief History of Cladding Materials used in the Nuclear Industry

In the 1950's, magnesium (Mg) alloys were selected as cladding material for the Magnox reactor (Calder Hall, Windscale England) – the world's first commercial nuclear power plant (1956) [23]. The obsolete cladding - Magnox (Magnesium non-oxidising) which the reactors are named after, consisted of: A12 alloy (*Mg with 0.7-0.9% Al*) and ZA alloy (*Mg with 0.45-0.65% Zr (in wt%)*) [24]. However, the Mg alloy restricted the maximum coolant temperature to 500°C, which limited the thermal efficiency (heat energy transfer from coolant to the generation of steam) that could be achieved. A second drawback was that spent Mg alloys exhibited high corrosion in water (due to impurities in magnesium) which was not an issue during reactor operation since the coolant used was carbon dioxide gas, but did result in medium to long-term storage issues in spent fuel pools, a legacy which is still present at the storage silos at Sellafield UK [25].

Austenitic 316 stainless steel (20Cr-25Ni-0.70Nb-0.62Mn-0.57Si-0.049C-Fe in wt%) [26] was then adopted as the cladding material for the Generation II Advanced Gas-cooled Reactors (AGRs) in the UK. The advantage of using stainless steel cladding compared to Magnox cans was the capability to reach higher thermal efficiencies due to higher operating temperatures up to 600°C, although using stainless steel cladding increased the neutron absorption cross section relative to the Mg alloys. This necessitated increased uranium enrichment to compensate for the neutrons absorbed during cladding bombardment. Stainless steel cladding was however, found to suffer from inter-granular attack through volatile fission products such as iodine, detrimentally affecting the microstructural properties [27]. Potential cladding failure due to Pellet-Cladding Interaction displayed further deleterious effects on its ductility.

During the 1950's zirconium alloys were developed in the US principally due the low thermal neutron capture cross-section of Zr, which enabled the use of lower enrichment fuels. Zirconium alloys have a thermal conductivity 30% higher (21.5 W/m.K) than stainless steel alloys (16.3 W/m.K) [28, 29], enabling higher thermal efficiencies to be achieved. This is further aided by having a linear coefficient

of thermal expansion almost $1/3$ ($5.3 \times 10^{-6} \text{ K}^{-1}$) the value for stainless steels ($16.0 \times 10^{-6} \text{ K}^{-1}$) [30] giving Zr alloys superior dimensional stability at elevated temperatures. Pure Zr was first used as cladding material in the STR Mark I prototype reactor [31]. The addition of 2.5 wt% tin (Sn) formed the basis for Zircaloy-1 which increased its strength and formability of Kroll sponge Zr. After high temperature water corrosion tests however, it was found that the corrosion rate of Zircaloy-1 had actually increased with time compared to pure Zr [32]. The addition of 1.5% Sn, 0.12% Fe, 0.10% Cr and 0.05% Ni (in wt%) resulted in Zircaloy-2 which was found to have properties similar to those of Zircaloy-1 but much better corrosion resistance. Zircaloy-2 was deployed for use in boiling water reactors (BWRs) and pressure tubes for heavy water reactors. A slight increase in Sn and a reduction in iron (Fe) led to the development of Zircaloy-3. During corrosion testing however, white corrosion artefacts identified as stringers of Fe-Cr intermetallic compounds were observed. These formed during the fabrication process in the $\alpha+\beta$ region (790-950°C) which was found to promote the agglomeration of intermetallic species. This combined with inferior mechanical strength compared to Zircaloy-2 led to its abandonment [33]. The removal of Nickel (Ni) from Zircaloy-2 resulted in lower hydrogen pickup and oxidation resistance was further enhanced when Fe content was increased to 1.5 wt% resulting in the alloy designated as Zircaloy-4. This alloy had good oxidation resistance in water/steam conditions with hydrogen pickup reduced by one half compared to Zircaloy-2 and was thus deployed for use as fuel cladding and associated reactor core components in PWRs. The inclusion of 1 wt% niobium (Nb) added to the cladding resulted in ZIRLO™ whereby the Nb acts as a hardening agent [34]. Other Nb-Zr alloys such as Zr-2.5%Nb, M5® (1Nb-0.01Sn-0.05Fe-0.015Cr-Zr) [34] and E110 (1.04Nb-0.02Sn-0.05-0.01Fe-Zr) [35] (in wt%) were also developed.

1.7 The Fabrication and Manufacture of Zr Alloys for Nuclear Reactors

Zircon is the ore from which zirconium and hafnium (Hf) are produced. It is typically found as beach sand (Zr-HfSiO_2) in many parts of the world. In 1824, Berzelius produced impure Zr powder by the reduction of potassium zirconium fluoride with sodium. Troost was able to obtain Impure Zr metal which involved the reduction of zirconium tetrachloride (ZrCl_4) with magnesium. Later, Van Arkel produced ductile Zr by using an iodine process in which a hot filament was used to decompose zirconium iodide [20], however, this process was expensive.

It wasn't until 1924 that a much higher purity of Zr metal was obtained when Lely and Hamburger [36] reacted zirconium tetrachloride with sodium in an autoclave. The ZrCl_4 was produced by reacting zirconium oxide with chlorine and carbon tetrachloride. The resulting zirconium pellets were washed with concentrated hydrochloric and nitric acid, then washed in solvents and dried. These were treated

in a vacuum furnace to produce Zr metal which was pure, ductile and malleable. They succeeded where others had failed because zirconium tetrachloride was handled in the absence of air [20], preventing oxide formation which having just 0.2% residual oxygen was shown to result in a brittle structure.

But it was Kroll, credited for having developed a magnesium-reduction process for the manufacture of Ti metal [37], who later developed a more economical method for producing ductile Zr by reducing zirconium tetrachloride with molten magnesium in an inert atmosphere [38]. This resulted in the development of 'sponge Zr'. Today, much of the commercial-grade Zr metal is produced via the Kroll process.

A crucial step for the production of reactor-grade Zr is the removal of hafnium from zirconium since this element has a high cross-section for neutron absorption (104 barns) [39] compared to Zr (0.184 barns) which can make the fission process inefficient by absorbing too many neutrons that would otherwise be used in nuclear fission reactions from the uranium oxide (UO₂) fuel pellets encased inside the fuel rods. The Hf separation process is typically conducted after the carbo-chlorination process and before reduction with magnesium. One of the main techniques used for Hf separation involves dissolving the tetrachloride in hydrochloric acid (HCl) and water. The Zr ions are complexed with ammonium thiocyanate and the Hf is preferentially extracted by methyl isobutyl ketone (MIBK), which is an organic solvent, whilst the Zr is in the aqueous phase. This is repeated many times until the Hf content is less than 100 ppm [20] which is then stripped from the solvent. The Zr is precipitated by the reaction of zirconyl-chloride with sulphuric acid and then reacted with ammonium hydroxide and calcined – resulting in (fine) zirconium oxide. After blending to remove impurities, it is reacted with carbon and chlorine gas during chlorination to produce a zirconium tetrachloride [40].

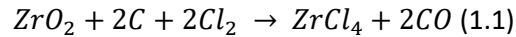
1.7.1 The Kroll Process

The Kroll process is a pyrometallurgical process used to produce zirconium. It consists of a number of key steps that involve zirconium oxide being converted into sponge zirconium [20]:

The Kroll process involves a number of key steps which involve Zircon sand being converted into ZrCl₄ via a carbo-chlorination process in a fluidised bed at 1200°C [20]:

(i) Carbo-chlorination and purification of zirconium oxide

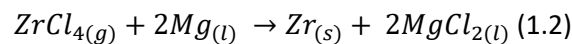
Zirconium oxide and coke³ are fed into a fluidised bed reactor at 1200°C and chlorine gas is also introduced via a separate inlet. The reaction for this is:



The zirconium oxide is stripped of its oxygen and binds with chlorine, forming zirconium tetrachloride which undergoes fractional distillation to remove impurities to produce pure zirconium tetrachloride.

(ii) Reduction of zirconium tetrachloride

Pure zirconium tetrachloride is reduced using molten magnesium at a temperature of 850-850°C to produce zirconium sponge. The reaction for this is:



Magnesium chloride is produced as a by-product of the reaction and settles at the bottom of the reactor due to its heavier density. The reactor is further heated and distilled at 1090°C for 4 days to remove magnesium chloride and any remaining magnesium which is collected in a separation tank leaving zirconium sponge in the reactor.

(iii) Electrolysis of magnesium chloride

The magnesium chloride produced in the reduction process is decomposed into chlorine and magnesium gas by electrolysis. The chlorine gas is returned to the carbo-chlorination process and the magnesium is returned to the reduction process for reuse.

(iv) Crushing and sizing of zirconium sponge and the production of zirconium metal

Zirconium sponge is crushed using a guillotine press machine, shearing machine and a jaw crusher. The crushed zirconium sponge is further pressed then forged into billets. This then undergoes hot rolling then cold rolling steps followed by annealing at 1260°C to produce high purity zirconium metal sheets.

³ Coke is a hard, porous fuel with a high carbon content with few impurities - made by heating coal or oil in the absence of air.

1.7.2 The Manufacture of Zircaloy Fuel Cladding

Cladding tubes for fuel rods house the uranium dioxide (UO_2) fuel pellets and serve to contain the radioactive elements produced due to neutron bombardment during nuclear fission reactions. Zircaloy cladding tubes contain alloying elements including tin (Sn), iron (Fe), chromium (Cr) and nickel (Ni), which are added during the ingot fabrication stage to improve the mechanical and corrosion resistance properties of zirconium. The low solubility of iron, chromium (<150 wt. ppm) [41] and tin (<290 wt. ppm) [42] in HCP α -Zr allow the formation of intermetallic precipitates which are also referred to as secondary phase particles (SPPs). In Zircaloy-2 the precipitates are found as $\text{Zr}(\text{Cr,Fe})_2$ and $\text{Zr}_2(\text{Fe,Ni})$ and in Zircaloy-4, the main precipitates formed are $\text{Zr}(\text{Cr,Fe})_2$ and ZrFe_3 [43]. Whilst the total concentration of the alloying elements is less than 2 wt%, the general oxidation resistance in steam and pressurised aqueous environments (i.e. a nuclear reactor) is substantially improved compared to unalloyed pure Zr [44]. These alloying additions to Zr have low cross-sections for neutron absorption thus preserving neutron economy during reactor operation. Thus, the main function of alloying elements is that they form intermetallic phases within the grains of Zr to precipitate and strengthen the metal by hindering dislocation motion which increases the mechanical strength of the alloy. This improves the corrosion resistance by limiting bulk diffusion of oxygen (via cracks) into the alloy.

The manufacture of Zircaloy cladding tubes involves forging of ingots into rods which are then β -quenched at 1050°C. Initially, the ingots are forged into billets and extruded into a rod with dimensions of 150-200 mm at a temperature of 700-740°C which is in the α -phase region [45]. The rods undergo three cold rolling operations whereby the outer diameter of the tube is about 12.3 mm. Between the first and the second cold rolling the extruded tube is β -quenched to 1050°C for a few seconds at a rate of 200°C per second [46] to room temperature by a water spraying method. β -quenching improves the resistance to accelerated nodular corrosion in water and high-pressure steam. The resistance to the development of nodular corrosion in Zr alloys was attributed to the reduction in particle size and even distribution of the intermetallic compounds in the material. Prior to the last cold-rolling operation, the tube is annealed at a temperature of 575°C [46].

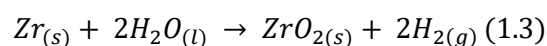
The next section of this chapter will examine the general oxidation mechanisms of zirconium alloys. This is crucial to fully appreciate the challenges that the project presents when attempting to fabricate a surface-treated layer/coating to delay oxidation and prevent hydrogen evolution particularly in abnormal LOCA conditions.

1.8 Oxidation Behaviour of Zr Alloys

Corrosion of metals is the degradation caused by chemical or electrochemical reaction with the environment. The electrochemical process involves two half-cell reactions that involve the transfer of electrons. The two half-cell reactions are oxidation and reduction. Oxidation is the loss of electrons or an increase in oxidation state of an atom. Reduction is the gain of electrons or a decrease in the oxidation state of an atom. The ability of a metal to undergo oxidation and reduction (redox) reactions leads to a potential energy gradient across the system. The ability of a reaction to occur is determined by the Gibbs free energy. A negative free energy corresponds to an increased likelihood of a reaction to occur while a positive free energy requires an external driving force to induce a reaction. The first part of the literature review will outline the oxidation of zirconium.

Zirconium alloys continue to be employed as the primary structural materials for fuel cladding, fuel channels, spacer grids and pressure tubes in most water-cooled nuclear power reactors and forms part of the reactor core. Their most important function is to serve as the first barrier against the release of fission products into the coolant. Reactor grade zirconium alloys are considered to have good corrosion resistance under reactor conditions; however, commercial pressures to achieve higher fuel burnups and thermal efficiencies have resulted in faster oxidation rates and increased corrosion of Zr alloys, which have led to reduced mechanical strength and longevity during operation.

The corrosion reaction of zirconium metal in water is written as [47]:



The products of the reaction in Equation 1.3 are the formation of an oxide layer and the evolution of hydrogen, which is partially absorbed into the metal. A basic schematic of the oxidation process is presented in Figure 1.2.

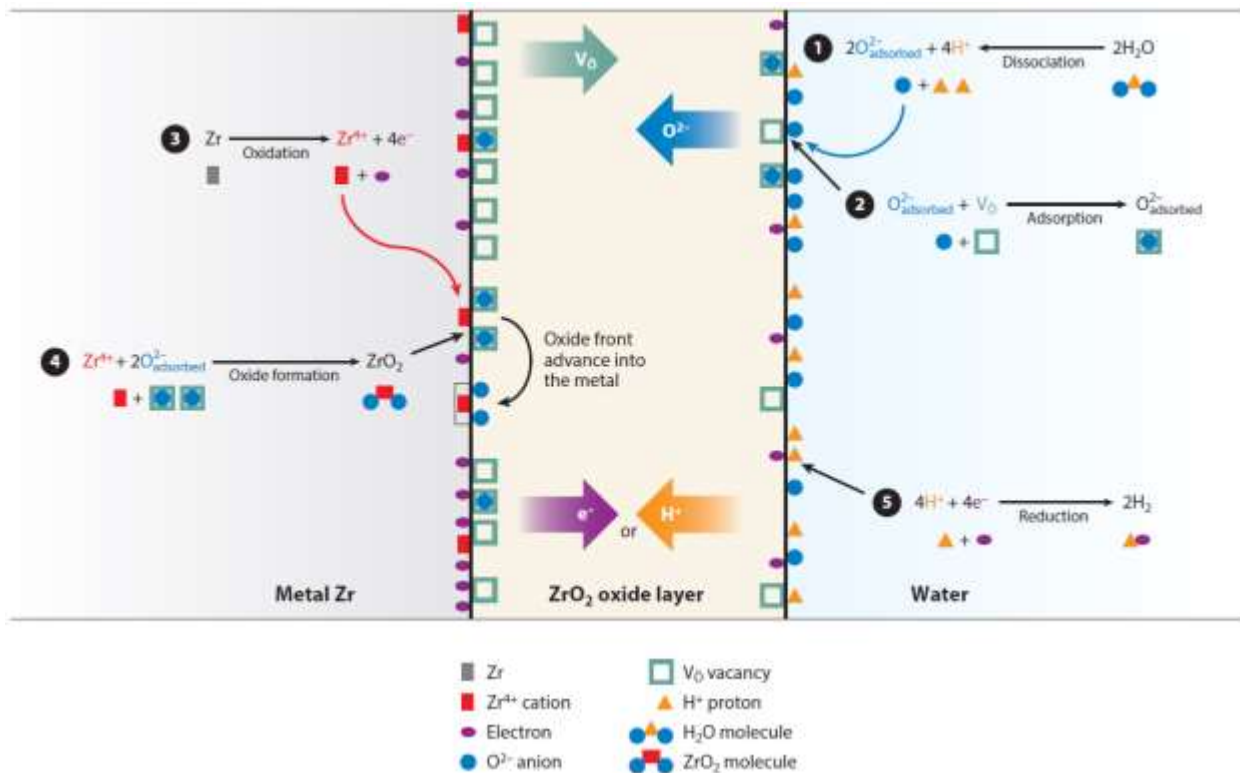


Figure 1.2: Schematic of the zirconium oxidation process [48].

During aqueous corrosion in a reactor, oxygen from the water molecules can dissociate via radiolysis (due to ionising radiation) and is adsorbed onto the oxide layer surface at an oxygen vacancy site (Figure 1.2 Steps (1) and (2)). The oxide is sub-stoichiometric (ZrO_{2-x}) at the metal/oxide interface and since there is a higher oxygen concentration at the oxide/water interface, a concentration gradient exists resulting in an electrochemical potential across the oxide [48]. The oxygen anions (negatively charged ion) diffuse (via solid-state diffusion) either along the grain boundaries or through the cracks and defects of the oxide [49]. When the oxygen anion migrates to the metal/oxide interface region, it reacts with zirconium cations (3) to form new oxide (4). Thus, new oxide growth occurs inwards (towards the bulk metal). The oxidation of zirconium is driven by the low free energy of formation of zirconium oxide (-900 kJ/mol at 360°C [50]) which allows zirconium to easily combine with oxygen. The reaction releases electrons which migrate through the oxide in the opposite direction to oxygen anions, to the oxide/water interface. These electrons then reduce hydrogen ions at the cathodic sites (5). However, some of the hydrogen atoms do not recombine and instead diffuse through the oxide layer and into the metal (commonly referred to as 'hydrogen pickup') where they are typically in solid solution in the α -Zr matrix or precipitate as zirconium hydride upon cooling [51].

Zirconium has a high affinity for oxygen ($\Delta G = -1037$ kJ/mol [52]) and actively absorbs gases such as oxygen. Indeed, fuel rods typically have a nascent 2-5 nm oxide layer [19] in their as-fabricated state which serves to protect the underlying Zr alloy metal from further oxidation. The Zr-O binary phase

diagram in Figure 1.3 shows oxygen solubility in α -Zr to be about 28 at% at 300°C. As the oxide layer thickness increases (due to increased oxidation time), the oxidation rate decreases as direct contact between metal and water is lost due to the formation of the oxide layer. Thus, the diffusion of oxidising species across the oxide layer is a rate-limiting step for the oxidation process [53].

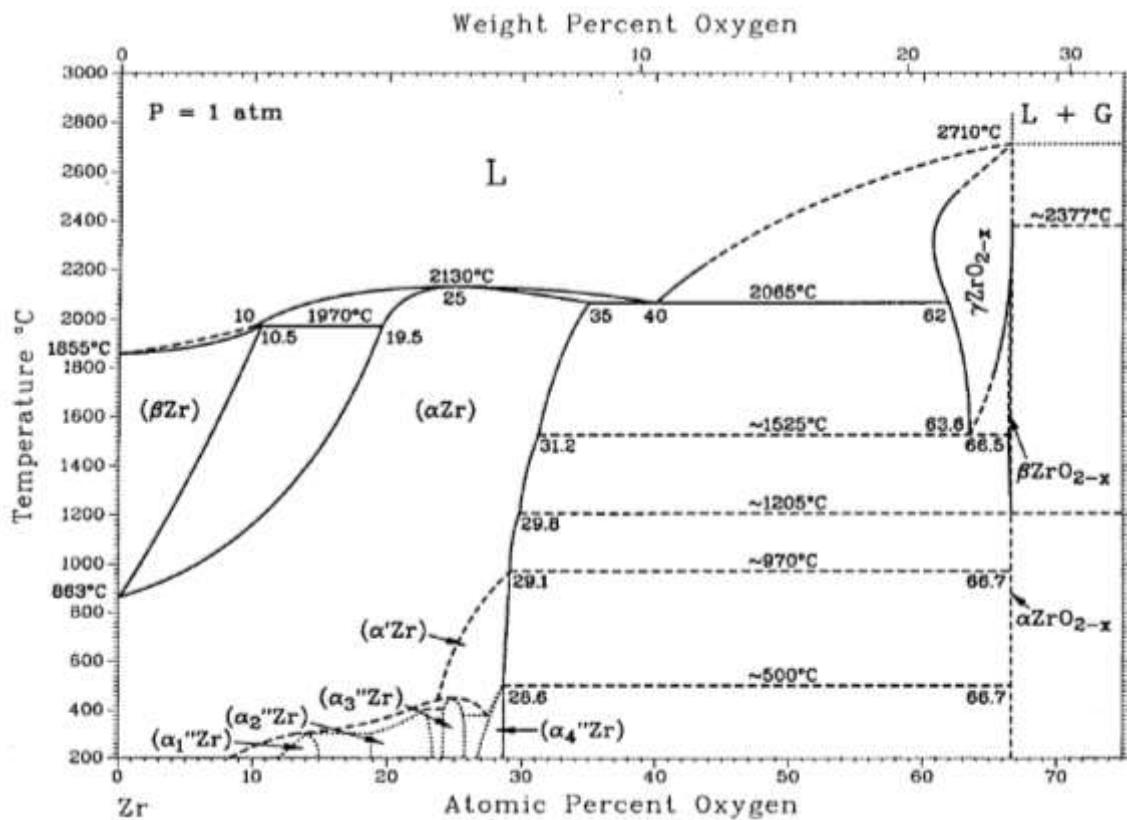


Figure 1.3: Zr-O phase diagram showing oxygen solubility in zirconium [54].

1.8.1 Polymorphs of Zirconium Oxide

Zirconium oxide exists in three crystallographic polymorphs. These are monoclinic (m -ZrO₂), tetragonal (t -ZrO₂) and cubic (c -ZrO₂) zirconia. Monoclinic zirconia is stable from room temperature up to its phase transformation to the tetragonal phase at 1170°C, at which stage the t -ZrO₂ phase is thermodynamically stable until its transformation to the cubic phase at 2370°C [55]. This is a martensitic and reversible process. Given the reactor core temperatures during LOCA in the lead up to the Fukushima disaster were estimated to be above 900°C as mentioned earlier, it is reasonable to assume that the oxide formed on the fuel cladding during oxidation and high temperature corrosion of the Zr alloy fuel cladding comprised predominantly of monoclinic zirconia phase. The lattice parameters for the three polymorphs are summarised in Table 1.3.

Table 1.3: Lattice parameters for bulk zirconium metal and zirconia polymorphs.

Lattice Parameter	Monoclinic [56]	Tetragonal [57]	Cubic [58]	HCP α -Zr [59]
a	5.15 Å	3.59 Å	5.15 Å	3.23 Å
b	5.20 Å	3.59 Å	5.15 Å	3.23 Å
c	5.31 Å	5.18 Å	5.15 Å	5.14 Å
α	90.00°	90.00°	90.00°	90.00°
β	99.22°	90.00°	90.00°	90.00°
γ	90.00°	90.00°	90.00°	90.00°
c/a	1.03	1.44	1.00	1.59

1.8.1.1 Properties of Monoclinic Zirconia

The naturally occurring form of zirconium oxide is the mineral Baddeleyite which has a monoclinic structure (space group P121/c1). XRD studies of zirconia revealed the monoclinic phase has the highest number of peak reflections of the zirconia polymorphs with the main peak reflection in the ($\bar{1}11$) direction at a 2θ angle of $\sim 28^\circ$ [56] (Figure 1.4). This is because of its low symmetry whereby the lattice parameters a , b and c are all different lengths (unlike the tetragonal and cubic zirconia polymorphs) and so there are more planes of the sample for the incident X-ray beam to diffract. For m-ZrO₂, the co-ordination number of Zr⁴⁺ cations is 7, whereas this is 8 for t- and c-ZrO₂ [60]. The strong nature of the Zr-O bond favours a seven-fold co-ordination number and is thermodynamically favourable to form m-ZrO₂ that is stable at lower temperatures (RT to its transformation temperature of 1170°C) compared to t- or c-ZrO₂.

The monoclinic zirconia phase has also been identified using XRD, Raman spectroscopic analysis [61] and Transmission Electron Microscopy (TEM) studies [62]. Oxidation of Zr alloys in aqueous environments typically results in an oxide scale comprised mostly of the m-ZrO₂ phase with an average grain size of 40-60 nm [63]. The monoclinic phase has severe practical implications since its formation during cooling from the high temperature tetragonal phase is associated with an oxide volume expansion of 3-5% [64, 65], followed by crack propagation in the oxide which can lead to increased porosity and accelerated oxidation kinetics compared with oxygen migration to the substrate via grain boundaries. Thus, m-ZrO₂ is regarded as non-protective [66]. This can detrimentally affect the overall mechanical strength of Zr-based components. Furthermore, the monoclinic phase is not stabilised by compressive stresses that develop at the oxide/metal interface. A scrutiny of the available literature revealed that the reason for this has not been clearly identified. A possible reason might be due to the differences in the a and c lattice parameters between monoclinic zirconia (5.15 Å and 5.31 Å respectively) and HCP α -Zr metal (3.23 Å and 5.14 Å). The high lattice mismatch of the a lattice

parameter (*b* & *c* lattice parameters to a lesser extent) of monoclinic zirconia and HCP α -Zr metal may promote the growth of a porous oxide containing defects such as cracks which would allow migration of oxidising species to the host metal resulting in further oxidation.

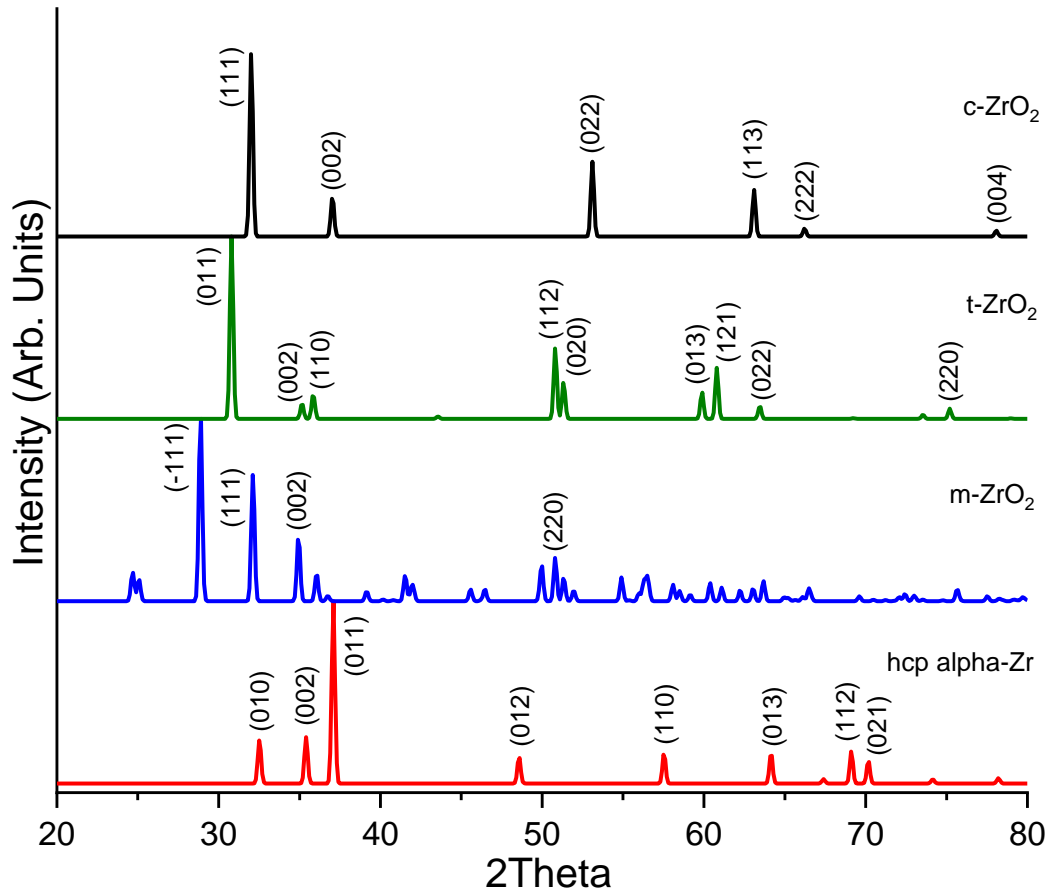


Figure 1.4: XRD patterns showing reflections of HCP α -Zr [59], m-ZrO₂ [56], t-ZrO₂ [57] and c-ZrO₂ [58].

1.8.1.2 Properties of Tetragonal Zirconia

The detection of the tetragonal zirconia phase (space group: P42/nmc) has been commonly reported from XRD studies [67, 68] and the pattern is presented in Figure 1.4 with the predominant peak in the (011) direction at a 2θ angle of $\sim 31^\circ$. During initial oxide growth near the interface region, the oxide scale is comprised of a mixture of tetragonal and (mostly) monoclinic zirconia. The XRD patterns for m- and t-ZrO₂ will play an important role in phase analysis in Chapters 4 and 5. The highest t-ZrO₂ content and stability of this phase during oxide development on Zr (alloys) has been reported to be in the metal/oxide interface region [69] with volume fraction generally reported to be 5-15% [70, 71] but has been reported to be as high as 40% at the oxide/metal interface calculated from residual stress measurements obtained from XRD experiments [70] and decreases with increased distance away from the oxide. It has been suggested that the tetragonal phase promotes a protective role of the oxide

scale due to its stability. A possible reason for this might be due to the similar lattice parameters of the tetragonal phase and the host HCP α -Zr metal. It can be seen from Table 1.3 that the a and c lattice parameters for the tetragonal phase are 3.59 Å and 5.18 Å which is fairly similar to the a and c lattice parameters for HCP α -Zr metal 3.23 Å and 5.14 Å. The slight lattice mismatch is a contributing factor to the growth of compressive stresses which are small during early growth and so the t-ZrO₂ is briefly stabilised by the build-up of these stresses which are highest at the interface. Another reason for t-ZrO₂ stabilisation is due to the smaller crystallite size of about 25-30 nm [72] compared to 40-60 nm for m-ZrO₂. The grain boundaries would act as a barrier to dislocation movement resulting in high strength and this may play a role in its stability. In terms of grain morphology, Petcheur [73] showed that the interface region (comprising high t-ZrO₂ content) tends to exhibit an equiaxed grain structure whilst the preformed outer oxide scale exhibits a columnar grain structure comprising mostly of m-ZrO₂ and low t-ZrO₂ content.

As the oxide thickness increases during growth, a critical point is reached whereby the compressive stress (in the oxide scale) can no longer stabilise the tetragonal phase (due to the diminishing compressive stress with increased distance away from the interface) and transforms to the thermodynamically stable monoclinic zirconia if the temperature range is from RT to its transformation temperature of 1170°C. The question as to why the t-ZrO₂ phase forms in this temperature range in the first place is not clearly defined in the literature but could be due to the process conditions used to carry out oxidation experiments. The pressures used inside the autoclave as well as the smaller grain size of t-ZrO₂ compared to m-ZrO₂ has the effect to influence and lower the monoclinic-tetragonal transformation temperature [60] – allowing metastable t-ZrO₂ to form. As such, the tetragonal zirconia phase has been widely reported in aqueous conditions at about 360°C at a pressure of about 22 MPa in autoclave experiments [74, 75] even though monoclinic to tetragonal zirconia transition temperature is 1170°C at atmospheric pressure.

Other techniques used to identify the tetragonal phase are electron backscatter diffraction (EBSD) and TEM. Garner et al [76] for instance used these techniques to map regions where m- and t-ZrO₂ grains were present in the oxide formed on Zircaloy-4 after hydrothermal oxidation tests at 350°C for 106 days. EBSD is a useful technique as it allows grain-to-grain orientations of specific phases to be measured. The tetragonal phase was shown to form mainly near the metal-oxide interface with equiaxed grain of ~30 nm in diameter and comprised ~1% of the total volume fraction of the oxide which decreased with increasing distance away from the oxide interface. This is much lower than the tetragonal volume fraction reported from X-ray diffraction (XRD) studies of 5-15% [77, 78]. This difference is most probably due to the stress relaxation that occurs during TEM sample preparation, and so there is insufficient compressive stress to stabilise the tetragonal phase which allows

transformation of the metastable tetragonal grains to m-ZrO₂ to take place. In contrast, XRD is a bulk (non-destructive) technique - sampling a comparatively large volume allowing the stress state of the (metastable) tetragonal zirconia to be maintained.

Another technique that has been used to identify tetragonal zirconia is Raman spectroscopy. Iderraga et al [79] performed Raman spectroscopic analysis on oxidised Zr alloys and commercially obtained tetragonal zirconia powder and reported that the peak intensities for t-ZrO₂ were in the 267 and 456 cm⁻¹ regions. This is in good agreement with other Raman spectroscopic analysis carried out to detect tetragonal zirconia phase. Thus, there are a number of characterisation techniques used to detect metastable tetragonal zirconia.

1.8.1.3 Properties of cubic Zirconia

Pure cubic zirconia (space group: Fm-3m) is thermodynamically stable at temperatures above 2370°C. The XRD pattern for cubic zirconia was presented earlier in Figure 1.4 with the predominant peak in the (111) direction at a 2θ angle of ~32°. The lattice parameters are $a = b = c = 5.15 \text{ \AA}$ [80] which differs significantly from the lattice parameters of the HCP α-zirconium bulk metal. The implications of this is that during initial oxidation of the zirconium alloy, any cubic phase formation at temperatures lower than its thermodynamic stability of formation (<2370°C) will only be partially stabilised due to the compressive stress at the metal/oxide interface. However, like the tetragonal zirconia phase, as the oxide thickness increases, the compressive stress is unable to continue to stabilise this phase. Alloying additions such as yttrium (Y), cerium (Ce) and magnesium (Mg) are seen as promising candidates to stabilise the c-ZrO₂ phase due to its high symmetry over a wide temperature range [81] compared to monoclinic zirconia which is low in symmetry. Another technique used to identify cubic zirconia phase was Raman spectroscopy. Idarraga et al [79] studied the oxidation behaviour of Zircaloy-4 at 800-1000°C under air flow and showed Raman peaks that were attributed to the c-ZrO₂ phase presented in the Raman spectrum in Figure 1.5 which can be seen to be distinctly different from the peaks attributed to the m- or t-ZrO₂ phase.

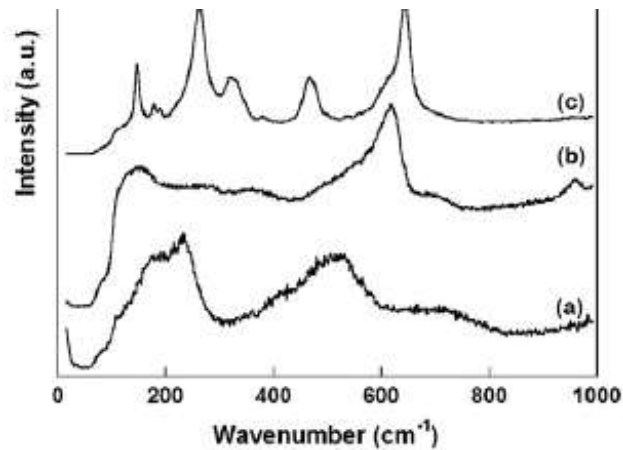


Figure. 1.5: Raman spectra of oxidised sample (a) c-ZrO₂, (b) t-ZrO₂, (c) m-ZrO₂ [79].

Attractive properties include its high hardness and a refractive index of 2.15 which is comparable to that of diamond (2.42) [55] and both therefore share a similar visual appearance. Due to these properties, as well as its low cost and durability, cubic zirconia is used in the synthetic diamond industry and is seen as an important economic competitor for diamonds.

The oxidation kinetics of Zr alloys can be broadly categorised as following the pre-transition and post-transition regimes and are described in the following sections.

1.8.2 The Pre-Transition Period

The early stage of oxidation is characterised by an oxide film which has been commonly reported to grow in accordance with a parabolic rate law⁴ (Equation 1.4) [82-84]:

$$\delta(t) = k_1 t^n \quad (1.4)$$

Where δ is the oxide thickness/weight gain, t is the exposure time, k_1 and n are a constant and a power law exponent respectively [85].

The oxidation process is controlled by oxygen diffusion through the oxide layer [86] or by crystallite boundary diffusion, which is known to be more rapid than bulk diffusion [87]. The process is accompanied by the presence of small grey regions on the black oxide surface [88] which grow larger and spread across the surface, forming a uniform layer of oxide covering the surface of the specimen. The initial oxide layer is comprised of monoclinic and tetragonal grains that are randomly oriented. With increased exposure time, oxide grows inwards into the α -Zr metal. As oxide thickness increases with time, some of the oxide grains grow preferentially in the $(\bar{1}11)$ direction, leading to a columnar

⁴ The oxide weight gain decreases with time. This is because direct contact between the metal and water is lost due to the formation of an oxide layer. Thus, diffusion of oxidising species into the bulk metal is a rate-limiting step for the oxidation process.

oxide structure [89] which is consistent with the predominant peak for the monoclinic phase. TEM studies revealed the formation of columnar grains growing perpendicular to the metal/oxide interface region to a length of ~ 200 nm [48]. The driving force for this has been reported to be the large compressive stresses that develop during early oxide growth due to the Pilling-Bedworth (P-B) ratio of ~ 1.56 [90]. This is the ratio of the volume of the oxide to the volume of the corresponding metal. Since in most autoclave experiments, the metal thickness is much greater than the oxide thickness, the oxide is constrained to accommodate the P-B ratio largely by inward growth into the α -Zr matrix which is why compressive stresses are highest at the metal/oxide interface region. This is able to partially stabilise the t-ZrO₂ phase as it is more dense (5.80 g/cm³) [91] compared to m-ZrO₂ (5.58 g/cm³) [92]. It has been suggested that increase in compressive stress that develops during early oxide growth can affect the oxygen diffusion coefficient by compressing the oxide lattice thereby making oxygen diffusion more difficult [93] resulting in a sub-stoichiometric oxide (ZrO_{2-x}) at the metal/oxide interface region. Indeed, Bryner [94] proposed that the build-up of compressive stress normal to the through-thickness direction of the oxide layer increases with increasing oxide thickness - which indicates the presence of a stress gradient at the oxide/metal interface which may cause the closure of many diffusion paths and was found to reduce the oxidation rate. However, buckling of the oxide film occurs when the compressive stress reaches a critical value, producing cracks and pores that promote paths for oxygen diffusion, further accelerating the oxidation process according to a linear power rate law. It is considered that the tetragonal and monoclinic oxide phases play a protective role against further oxidation to a certain extent, but the reasons of its stabilisation are debatable. Previous studies carried out by Bouvier et al [95], Godlewski et al [66] and Barberis et al [96] concluded that there are three likely factors for stabilisation of the tetragonal phase: i) a smaller crystallite size of t-ZrO₂ compared to m-ZrO₂, ii) point defects in the oxide layer and iii) the compressive stress state of the layer generated during oxidation. Furthermore, Djurado et al [97] demonstrated that crystallite sizes ranging 20-30 nm are responsible for the tetragonal phase stabilisation at the metal/oxide interface. This infers that a nanocolumnar PVD Zr-based metallic coating might also assist in t-ZrO₂ phase stabilisation. Iltis et al [98] proposed that the presence of lattice defects within the oxide layer induced by the sub-stoichiometry of the zirconia stabilises the tetragonal phase beyond the interface region.

During the oxidation process, if the compressive stress generated is below a critical limit, stress relaxation occurs resulting in an instability of the tetragonal phase. A martensitic phase transformation takes place whereby the meta-stable tetragonal phase transforms to the thermodynamically favourable monoclinic phase if the conditions used are below the m \rightarrow t transformation temperature of 1170°C. As mentioned previously, this transformation is associated

with a 3-5% volume expansion of the oxide upon cooling from the tetragonal phase [99]. The transition from equiaxed to columnar oxide growth has been reported to occur at a diameter of 30-40 nm, which has also been reported to be the diameter at which the monoclinic phase is thermodynamically more favourable to form over the tetragonal phase [48]. The diffusion-controlled oxidation rate continues up to a critical oxide thickness reported to be $\sim 2\text{-}3\ \mu\text{m}$ [100] at which point a structural breakdown of the oxide layer occurs (characterised by formation of cracks near the pre-formed outer oxide layer). Yilmazbayhan et al [63] reported a multi-layered oxide structure on Zircaloy-4 was observed using optical microscopy, in the form of light and dark bands (Figure 1.6) after oxidation tests in 360 °C water for 784 days at 18 MPa pressure. This is consistent with the above-mentioned structural transition that occurs every 2-3 μm (due to relaxation of compressive stress, resulting in the breakdown of the oxide layer). What is interesting here is that the oxide band structure is regularly spaced and have similar thicknesses, which is an indication of a linear oxidation rate. The contrast between the bands was speculatively attributed to differences in refractive indices of the t- and m-ZrO₂ phases; grain size variations or possibly due to porosity and cracking although none of these arguments have been confirmed.

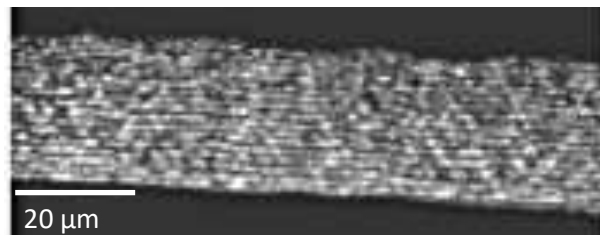


Figure 1.6: Optical micrograph show a multi-layered oxide structure formed after aqueous corrosion tests at 360°C for 784 days Zircaloy-4 [63].

One of the proposed reasons for the breakdown of the oxide layer is due to the diminishing compressive stress across the oxide scale and the resultant volume expansion of the oxide which facilitates the t- to m-ZrO₂ phase transformation. As new oxide formation takes place at the metal/oxide interface region, the oxide formed has higher compressive stress compared to the pre-formed outer oxide layer. As oxide thickness increases with exposure time, the stress at the outer oxide layer become relaxed whilst the compressive stress stabilise the oxide nearest the interface region. Lakshmi et al [101] studied the oxidation of pure zirconium (99% purity) using high temperature in-situ XRD up to 700°C and found the resulting oxide composition to consist overwhelmingly of m-ZrO₂ with one peak associated with t-ZrO₂ at 2 θ reflection of around 30°. The author proposed that the initial oxide formed is highly stressed and, with increased oxidation time, the lattice strain is increased as a new strained layer (comprising of t-ZrO₂/m-ZrO₂ phases) is

continuously formed at the interface between the zirconium metal and the already existing strained oxide layer, where the compressive stress is reduced with increased distance from the interface. As mentioned previously, the stress is relieved and a transformation from t-ZrO₂ to m-ZrO₂ takes place with an associated oxide volume increase. Although the author makes a decent attempt to test the hypothesis that compressive stress gradients and oxygen potential gradients provide the diffusional driving force for describing the oxidation kinetics of zirconium, it is not entirely clear how the oxidation rate varies between the different Zr-O polymorphs.

Successive cycles occur as each new layer of oxide forms which follow oxidation kinetics in accordance with a parabolic rate (or a cubic rate law) until the oxidation rates accelerates, following a linear rate law (Equation 1.5). This is known as the post-transition regime and the oxide scale thickness increases with exposure time until spallation of the oxide occurs. The oxide spallation is attributed to the stress relaxation in the oxide scale.

1.8.3 The Post-Transition Period

The post-transition regime is characterised by an increase in oxidation rate from a parabolic rate law to a linear rate law. This is described by the following expression [19]:

$$\delta(t) = k_2t + C \quad (1.5)$$

Where $\delta(t)$ is the specimen weight gain in mg/dm²; t is the exposure time in days; k_2 is a constant and C is the weight gain at transition.

TEM studies of the pre-formed outer oxide layer show that this region comprises an open network of large pores and cracks perpendicular to the oxide surface [102]; this allows water and oxygen to penetrate the oxide scale. A study by Adamson et al [18] showed that cracks that have formed parallel to the oxide surface provide some resistance to migration of oxidising species to the metal/oxide interface region – limiting the oxidation rate compared to the presence of perpendicular cracks. The formation of these cracks and pores is believed to make the oxide formed in the post-transition stage non-protective. Oxide growth during the post-transition period results in the oxide scale being sufficiently thick (> 2 μm), and the pre-formed oxide layer is stoichiometric (ZrO₂) at the oxide/water interface. This is because oxygen (from the water) is able to diffuse easily through the columnar structure of the oxide scale, unlike at the metal/oxide interface, where the oxide structure is equiaxed, more dense, and the high compressive stress acts also to form a partial barrier to oxygen diffusion – resulting in a sub-stoichiometric oxide being formed. Yoo et al [103] proposed a kinetic model whereby the strain energy gradient is the driving force for oxygen diffusion into the layer, in addition to the

oxygen potential gradient across the oxide layer. The remaining metastable t-ZrO₂ phase continuously transforms to the thermodynamically stable m-ZrO₂ due to the increased thickness of the oxide layer resulting in a relaxation of compressive stress that is no longer sufficient to maintain tetragonal phase (meta)stability. As mentioned in section 1.8.1.1, the low symmetry of the monoclinic phase is also a contributing factor to the inability of the compressive stress to stabilise this phase and cause a stress relaxation following the post-transition stage [71], where the volume fraction of the tetragonal phase is lowest at the pre-formed outer oxide layer - reported to be less than 5% [78]).

1.8.4 Determining Oxidation Resistance

The oxidation kinetics of metals are typically analysed by subjecting a workpiece to high pressure water or steam at elevated temperatures for a defined length of time and calculating the oxide weight gain before and after testing, where the units for weight gain are typically milligrams per decimetre squared (mg/dm²). Literature investigation revealed that a standardised method exists (Standard Test Method for Corrosion Testing of Zirconium Products in Water (360°C) or Steam (400°C) - ASTM-G2 [104]) which many authors use to study oxidation resistance. Although the standard test method is primarily used as an acceptance test for Zr alloys in determining their corrosion resistance, it does not include neutron irradiation effects on the cladding which could be significant in terms of mechanical degradation brought on by the developed oxide.

Zirconium alloys subjected to thermal oxidation (>350°C) in air undergo similar oxidation kinetics to Zr alloys oxidised in aqueous environments. In one example, Suzuki et al [105] carried out oxidation tests of Zircaloy-4 in air from 350-500°C and showed that the oxide weight gain increased dramatically with increasing temperature. What was interesting about this study was the accelerated weight gain during the post-transition stage compared to the pre-transition stage. Accelerated weight gain occurs at higher temperatures, which allows greater transfer of kinetic energy between oxidising species and allows faster migration of oxygen species to the interface region of the developing oxide, as the oxidation kinetics change from parabolic to cubic to eventually a linear rate. Unfortunately, the study did not mention which polymorph was formed at each transition stage. Furthermore, the inner oxide layer was characterised as a wavy undulating appearance indicating a cyclic oxide growth pattern. This was also observed by Bryner [94] who carried out corrosion tests in water at 350°C and showed repeated cycles of new oxide growth at the metal-oxide interface with greater severity of cracks and porosity in the preformed outer oxide layer of the post-transition stage; similar phenomena were also reported by Cox [90].

1.8.5 Volume Fraction Determination of the Monoclinic and Tetragonal Zirconia Phase

Following on from previous discussions, it should become apparent that a litany of studies investigating oxidation of zirconium and its alloys in water/steam environment have been carried out at about 360°C and that high temperature corrosion studies have reported widely the formation of mixtures of monoclinic and tetragonal zirconia. The Garvie-Nicholson expressions in Equations 1.6 and 1.7 are commonly used to quantify the volume fraction of the monoclinic and tetragonal phases in zirconium oxide [106, 107]:

$$X_m = \frac{I_{111}^m + I_{-111}^m}{I_{111}^m + I_{-111}^m + I_{011}^t} \quad (1.6)$$

$$X_t = \frac{I_{011}^t}{I_{111}^m + I_{-111}^m + I_{011}^t} \quad (1.7)$$

Where I_{-111}^m , I_{111}^m and I_{011}^t are the intensities of the highest diffraction peaks of the corresponding respective monoclinic and tetragonal peaks. These expressions were used to calculate the volume fractions of the two polymorphs - further details of which can be found in Chapter 4 Section 4.2.2. The intensities for the tetragonal phase could be substituted for the cubic phase if the volume fraction of cubic to monoclinic phase was to be determined and has been reported by Piosik et al [108]. The expressions however, assumes the tetragonal or monoclinic zirconia phases are evenly distributed in the oxide layer, and that no preferred orientation (texture) exists. Thus, the expression is particularly useful for calculating the volume fraction of zirconium oxide powders [96, 109], but of more limited applicability for layered/graded oxide scales.

As has been established earlier from high temperature corrosion studies reported in the literature, the volume fraction of tetragonal zirconia found in an oxide scale is not constant but rather decreases with increased distance from the metal/oxide interface. Thus, the above expressions do not consider how the phases '*grades*' with oxide thickness. To the best of my knowledge, this caveat has not been reported in the literature, but the expressions have nevertheless been commonly used to calculate volume fractions of the tetragonal and monoclinic phases in zirconium oxide layer [109]. For instance, in XRD, one can determine the tetragonal or monoclinic zirconia volume fraction in a particular sampled volume from within which the X-rays diffract from certain planes in the crystal structure but information on how the volume fraction varies as a function of distance from the metal/oxide interface region to the pre-formed outer oxide layer [71] cannot be extracted. One potential method whereby this formula can be applied more accurately for oxide formed on metal is to use synchrotron X-rays – probing individual grains at different sampling depths within the oxide scale. Another method might involve mechanically removing the oxide, then grinding it to homogenise the mixture and then

carry out X-ray diffraction analysis to obtain fractional quantities of the tetragonal and monoclinic phases formed. The issue here would be to ensure that all the oxide is removed and to ensure that as few impurities as possible are introduced from the mechanical grinding process.

1.8.6 Determination of Pilling-Bedworth Ratio for Zirconia Polymorphs

A dramatic consequence of uncontrolled oxidation of zirconium alloys was demonstrated during the Fukushima Dai-Ichi nuclear accident (Section 1.2). Radiological contamination issues arising from the release of radioactive fission products from damaged fuel rods inside the reactor pressure vessel; the high dose rates from the uranium oxide fuel and the risk in the potential for criticality⁵ are just some of the factors that have prevented the retrieval of the contaminated zirconium alloy fuel rods for analysis and eventual disposal. To the best of knowledge, the temperatures inside the reactor at the time of the explosions have not been reported with any degree of certainty, however it can be inferred taking into consideration that severe cracking of the cladding and rapid oxidation reactions resulting in hydrogen release in this scenario has been reported to be above 900°C [110]. From previous discussions on the oxidation process of zirconium, the oxidation kinetics at these temperatures are likely to have been accelerated in accordance with a linear rate law. The runaway conditions within the reactor core created a high temperature, high pressure environment that would have resulted in a thick oxide having developed on the Zr alloy cladding that was too stressed, eventually leading the oxide scale to crack or undergo spallation.

Given the inaccessibility of obtaining damaged fuel rods for analysis due to high activity from fission products and the likelihood in receiving a lethal radiation dose, it has not yet been confirmed which polymorph(s) of zirconia had developed on the Zr alloy cladding during LOCA. The understanding of this knowledge is crucial when it comes to modelling, controlling and predicting oxidation behaviour of the parent metal and the stress build-up in the oxide scale to assist in the development of a strategy to control, prevent or mitigate accelerated oxide formation. Despite this (and based on previous discussions surrounding oxide formation), it is reasonable to assume that the oxide scale developed on the zircaloy cladding in Fukushima Dai-Ichi would have been comprised predominantly of monoclinic zirconia. This is because the monoclinic zirconia phase is stable from RT up to its transformation temperature of 1170°C as mentioned before. Metastable tetragonal zirconia may however, have also formed in oxide scale due to the high pressures inside the reactor – particularly during LOCA, but the instability of the t-ZrO₂ phase at these temperatures, due to the insufficient compressive stress to stabilise this phase with increased oxide scale thickness (and the 3-5% volume

⁵ Unintended and uncontrolled fission event resulting in high radiation dose.

expansion of the oxide during the post-transition period) this phase would likely transform to the more thermodynamically stable m-ZrO₂ phase.

The Pilling-Bedworth (P-B) ratio is an important aspect in the corrosion of metals as it can be used to determine if the metal will undergo passivation through the generation of a protective oxide film. As mentioned previously, the P-B ratio is defined as the ratio of the volume of the elementary cell of a metal oxide to the volume of the elementary cell of the corresponding metal (from which the oxide is created). If the P-B ratio is less than 1, the oxide film is non-protective for instance the P-B ratio for magnesium is 0.81 [111] which means the oxide (MgO) volume is smaller than that of the parent Mg metal, and so the oxide will crack and thus revealing channels for continued oxidation of the metal substrate. If the P-B ratio is greater than 2, the oxide film delaminates and offers no protection (i.e. iron). If the P-B ratio is greater than 1 but less than 2, the oxide film is passivating and offers protection from further oxidation.

1.8.6.1 P-B Ratio of t-ZrO₂/Zr System

For zirconium oxide, a P-B ratio of 1.56 for is commonly quoted in the literature [20, 61, 83, 101, 112]. This means that during oxidation of zirconium, the consumption of 1 μm of zirconium metal results in the generation of a 1.56 μm-thick oxide or an overall volume increase of oxide of about 56%. However, to the best of knowledge, there are no reports which explicitly state which polymorph of zirconia this is assigned. To find out this information, the general expression for calculating the P-B ratio for an oxide grown on its parent metal can be used and is given by [113]:

$$R_{PB} = \frac{\text{Volume of oxide}}{\text{Volume of metal}} \quad (1.8)$$

$$R_{PB} = \frac{M_{oxide}}{n \cdot \rho_{oxide}} \cdot \frac{\rho_{metal}}{M_{metal}} \quad (1.9)$$

Where M_{oxide} and M_{metal} are the molecular and atomic mass of the oxide and metal in g/mol respectively; ρ_{oxide} and ρ_{metal} are the densities of the oxide and metal in g/cm³ respectively and n is the number of metal atoms per oxide molecule.

The P-B ratio was calculated for the t-ZrO₂ – Zr system using the density provided by Patil et al [91]:

$$R_{PB} = \frac{123.222 \text{ g/mol}}{5.80 \text{ g/cm}^3} \cdot \frac{6.51 \text{ g/cm}^3}{91.224 \text{ g/mol}} \quad (1.10)$$

$$R_{PB} = 1.52$$

The P-B ratio determined is slightly lower than the 1.56 value often quoted in the literature. Another method to calculate the P-B ratio would be calculate the unit cell volume of the tetragonal zirconia structure and divide this by the unit cell volume of the parent zirconium metal. The lattice parameters of tetragonal zirconia are: $a = b = 3.65 \text{ \AA}$ and $c = 5.29 \text{ \AA}$ [91] and for HCP α -Zr metal are: $a = b = 3.23 \text{ \AA}$ and $c = 5.14 \text{ \AA}$ [59]. The expressions used to calculate the unit cell volume for these structures are given in Table 1.3.

$$R_{PB} = \frac{a^2 C}{\frac{\sqrt{3}}{2} a^2 C} = \frac{70.614 \text{ \AA}^3}{46.570 \text{ \AA}^3} = 1.52 \quad (1.11)$$

As can be seen the P-B ratio for tetragonal zirconia is identical whether using expressions involving either molecular weights or lattice parameters of the t-ZrO₂. This is in good agreement with the P-B ratio of 1.50 calculated for t-ZrO₂/Zr using the oxide density obtained from Barker et al [114]. The lower reported figure of 1.50 could be due to the lower temperatures of 1200°C used compared to 1393°C used by Patil et al [91] (used in Equation 1.11) which may have influenced the lattice parameters and densities obtained by these authors. Boysen et al [92] carried out neutron powder diffraction studies of zirconia at 1177°C and reported the density of tetragonal zirconia to be 5.67 g/cm³. Using this value in equation 1.10 resulted in a P-B ratio of 1.61 which is slightly higher than the calculated P-B ratio of 1.52. This could be because higher temperatures used during oxidation tests results in increased kinetic energy gained by the oxygen molecules that causes them to move faster and further apart from each other, occupying a larger volume that results in a decrease in density of the oxide. Although the density of the oxide is dependent on the processing conditions used during oxidation, the expansion of the parent zirconium metal will still be larger compared to the oxide grown owing to the higher coefficient of thermal expansion of Zr and ZrO₂ which is 5.7-7.0 x10⁻⁶ K⁻¹ [115] and 4.75 x10⁻⁶ K⁻¹ [116] respectively, in which case the P-B ratio is expected to reduce with increasing temperature because the Zr metal substrate expands at a faster rate than the oxide.

Another point to consider is that the calculated P-B ratios of 1.52 and 1.60 falls within the experimental error of 5% of the commonly quoted 1.56 figure. The results calculated here indicates that the P-B ratio of 1.56 lies within the range for tetragonal zirconia formation. Based on the available evidence, the P-B ratio of 1.56 commonly quoted in the literature is likely to be an average value calculated from a number of P-B ratios from the t-ZrO₂/Zr system.

1.8.6.2 P-B Ratio of m-ZrO₂/Zr System

The P-B ratio of m-ZrO₂/Zr system was calculated using density parameters obtained from neutron diffraction studies carried out at 27°C by Boysen et al [92] and is shown below:

$$R_{PB} = \frac{123.222 \text{ g/mol}}{0.944 \cdot 5.58 \text{ g/cm}^3} \cdot \frac{6.51 \text{ g/cm}^3}{91.224 \text{ g/mol}} \quad (1.12)$$

$$R_{PB} = 1.66$$

It was found that the P-B ratio calculated for monoclinic-ZrO₂/Zr system was higher compared to tetragonal-ZrO₂/Zr system. In the same study that investigated tetragonal to monoclinic zirconia transformation using neutron powder diffraction but at higher temperatures of 827 °C, Boysen et al [92] reported an m-ZrO₂ density of 5.42 g/cm³. The calculated P-B ratio when used in Equation 1.9 was determined to be 1.63 which is in good agreement with the P-B ratio obtained from Equation 1.12. No literature can be found that reports the P-B ratio of monoclinic zirconia. This is likely to be due to the poor mechanical stability offered by this phase (i.e. severe cracking) and furthermore, most studies that have investigated oxidation behaviour of zirconium alloys have focused predominantly on understanding the behaviour of the t-ZrO₂ phase during oxidation (due to its ability to be stabilised over a wide range of temperature conditions).

The P-B ratio of 1.66 presented in this study for monoclinic zirconia represents a volume expansion of 6% over the P-B ratio of 1.56 quoted for t-ZrO₂ in literature and 9% when compared to the P-B ratio of 1.52 calculated in this study. This is in fairly good agreement with the reported volume expansion of about 5% of the oxide scale seen during the martensitic transformation from tetragonal to monoclinic zirconia commonly stated in literature [60, 65].

1.8.6.3 P-B Ratio of c-ZrO₂/Zr System

The P-B ratio of c-ZrO₂/Zr system was calculated using density parameters from a study by Jaffe et al [117], as shown below:

$$R_{PB} = \frac{123.222 \text{ g/mol}}{6.07 \text{ g/cm}^3} \cdot \frac{6.51 \text{ g/cm}^3}{91.224 \text{ g/mol}} \quad (1.13)$$

$$R_{PB} = 1.45$$

This is in good agreement with the P-B ratio of 1.46 calculated using data obtained from XRD experiments and Rietveld refinement method by Wang et al [118] since the density of the cubic zirconia (6.04 g/cm³) when used in expression 1.13 was very similar. The P-B ratio for cubic zirconia presented in this study is also corroborated using the density of c-ZrO₂ polymorph (from neutron

powder diffraction studies investigating cubic-stabilised zirconia) determined by Martin et al [80] to be 6.16 g/cm³ where the P-B ratio was calculated to be 1.43. But the P-B ratio differs slightly when compared to Katz et al [119] in which the P-B ratio was calculated to be 1.42. This is because the density of the oxide reported by the author was higher at 6.21 g/cm³ and represents a difference of about 2%.

Table 1.4: Summary of P-B ratio calculations of the monoclinic zirconia (m-ZrO₂), tetragonal zirconia (t-ZrO₂), cubic zirconia (c-ZrO₂) and HCP α-Zr.

Crystal Structure	Formula	Density (g/cm ³)	P-B Ratio
m-ZrO ₂	$abc\sin\beta$	5.58	1.66
t-ZrO ₂	a^2C	5.80	1.52-1.60
c-ZrO ₂	a^3	6.07	1.45
HCP α-Zr	$\frac{\sqrt{3}}{2}a^2C$	6.51	---

1.8.7 The Effects of Hydrogen Evolution and Hydrogen Precipitates

Hydrogen absorption plays a crucial role in the overall degradation of Zr alloys used in nuclear reactors. A small fraction of the hydrogen generated as a consequence of metallic oxidation (Equation 1.3) is absorbed into the Zr alloy cladding which then precipitates upon cooling (i.e. during reactor shut-down for maintenance or fuel replacement etc.) as zirconium hydride [120]. The hydrogen produced during reactor operation is generated from 2 main sources:

- (i) Hydrogen produced by radiolysis of water exposed to high energy neutron flux. This is when ionising radiation interacts with water molecules producing radicals⁶ such as H·, OH·.
- (ii) Hydrogen released during oxidation reactions forms hydrogen gas which then migrates from the coolant water into the fuel rod cladding.

As mentioned previously, hydrogen absorption is a prime contributor to the degradation of Zr alloys during reactor service. Typically 15-25% of the hydrogen liberated during oxidation is absorbed into the cladding [121, 122]. This is due to zirconium having a high solubility for hydrogen at elevated temperatures: less than 10 ppm at room temperature [123]; 80 ppm at 300°C; between 50 and 100 ppm at PWR operating temperatures (~320°C) [124] and 200 ppm at 400°C [125]. Once the solubility

⁶ A radical is an atom, molecule or ion that has an unpaired valence electron making them highly reactive. These are generated by redox reactions, ionising radiation and electrolysis.

limit⁷ for hydrogen absorption is exceeded, hydrogen is typically found in solid solution in the α -Zr matrix and as the cladding cools (i.e. during maintenance or periodic shutdown of the reactor), the hydrogen present in the cladding precipitates as zirconium hydride platelets.

The zirconium-hydrogen phase diagram in Figure 1.7 shows that three main hydride phases exist below a temperature of 550°C which are δ -, ϵ - and γ -hydrides. The stable δ -phase is a fluorite structure containing a Face-Centred Cubic arrangement of zirconium atoms with hydrogen occupying the 8-tetrahedrally-coordinated random sites and corresponds to the $ZrH_{1.66}$ composition with lattice parameters $a = b = c = 4.78 \text{ \AA}$ [126]. The δ -hydride phase is the predominant hydride phase to precipitate in reactor-grade zirconium alloys and the measured concentration has been reported to be about 1250 parts per million by weight (wt. ppm) [127]. The stable ϵ -hydride has a Face-Centred Tetragonal (FCT) arrangement of zirconium atoms with hydrogen atoms filling with the tetrahedrally-coordinated sites corresponding to those of the FCC (δ -phase) which results in a stoichiometric ZrH_2 structure and has lattice parameters elongated in the $\langle a \rangle$ direction where $a = b = 4.97 \text{ \AA}$ and $c = 4.52 \text{ \AA}$ [126]. The concentration of metastable γ -hydride measured in zirconium has been reported to be about 500 wt. ppm [128]. The γ -hydride is a metastable phase which also has a FCT structure whereby the arrangement of zirconium atoms and the occupancy of the hydrogen at the tetrahedrally-coordinated sites leads to a stoichiometric ZrH formation with lattice parameters $a = b = 4.67 \text{ \AA}$ and $c = 4.84 \text{ \AA}$ [129]. The concentration of metastable γ -hydride measured in zirconium has been reported to be about 200 wt. ppm [130]. The key differences between the δ - and γ -hydrides is the degree of hydrogen atom ordering on the tetrahedral sites of each phase. There are four hydrogen atoms randomly occupying each tetrahedral site in δ -hydrides, whereas in γ -hydrides, the hydrogen atoms occupy the tetragonal site on alternating (110) planes [130].

⁷ Solubility limit is the maximum amount of solute that can dissolve in a solvent at a specified temperature and pressure.

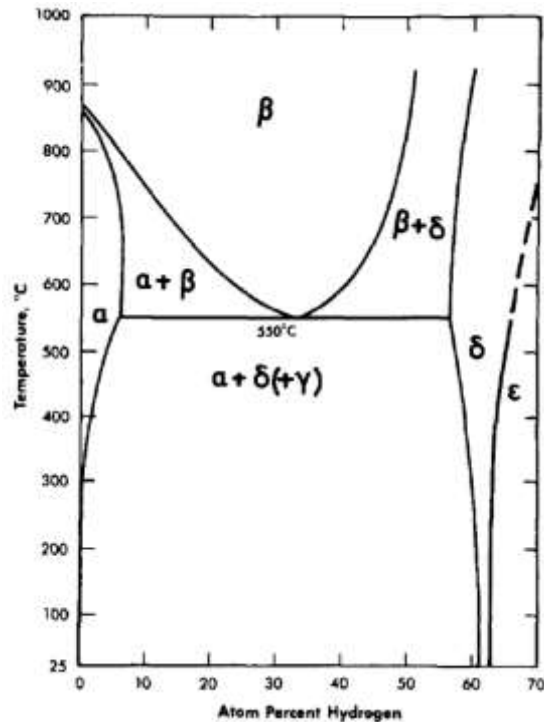


Figure 1.7: The Zr-H phase diagram [131].

The detection of hydride phases using X-ray diffraction has been commonly reported in the literature. One example is where Daum et al [127] used synchrotron XRD at room temperature on stress-relieved Zircaloy-4 samples to investigate the distribution of hydride phases across the cladding following heating at 400°C under a flowing hydrogen (30%) – helium (70%) gas mixture.

Bailey [132] used TEM to analyse hydrides following heat treatment of reactor grade zirconium foil (0.25 mm thickness) at 800 °C under flowing hydrogen which was then quenched to allow hydrides to precipitate at a faster cooling rate. The hydrogen concentration in the hydrided zirconium foil was measured at about 500 ppm. TEM micrographs showed that the hydride precipitates were needle-shaped and were predominant in the (10 $\bar{1}$ 0) basal plane of zirconium. Ells [133] proposed that the hydride precipitates were initially needle-shaped but became platelets with decreasing cooling rate and had agglomerated at grain boundaries. This view is corroborated by Wang et al [134] who used Electron Back-Scatter Diffraction (EBSD) to study δ -hydride formation at α -Zr grain boundaries and Kim et al [135] who used TEM and FIB to study formation of δ -hydrides in Zircaloy-4.

TEM investigations reported by Westlake [136] and Bradbrook [137] revealed that the size of zirconium hydride precipitates is of the order of hundreds of nanometers but the arrangement in bulk zirconium or its alloys appears as long strings of hydrides when analysed using optical microscopy. In a more recent study, Cinbiz et al [51], who investigated hydride orientation following heat treatment

of Zircaloy-4 at 500°C under flowing hydrogen, showed that hydride platelets appear as long strings in excess of 200 μm from optical micrographs.

The orientation of zirconium hydrides is a rate-limiting factor in the high temperature corrosion of zirconium alloys. These precipitates have been reported to form in both circumferential and radial directions [138] within Zr alloy cladding (Figure 1.8) which can occur during shutdown or drying operations of spent nuclear fuel to remove moisture before intermediate storage or transport. This can increase susceptibility to accelerated corrosion. The severity of degradation depends on the location and orientation of these precipitates which tend to be more detrimental in the radial orientation (perpendicular to the cladding) than in the circumferential direction (parallel to the cladding) [51] as the direction of the crack propagation in the former facilitates easier diffusion pathways [19] for the ingress of oxidative species through the oxide scale to the zirconium alloy underneath, resulting in accelerated corrosion of the metal. Furthermore, this may also result in the escape of radioactive Fission Products (FPs) and contamination of the internal components of the reactor pressure vessel. The distribution of hydrides in the form of a rim or layer can eventually lead to cladding embrittlement and reduced fracture toughness which can cause mechanical degradation of the cladding and fuel rod failure – limiting the lifetime of the fuel rods in the reactor and hence, increasing the operational costs.

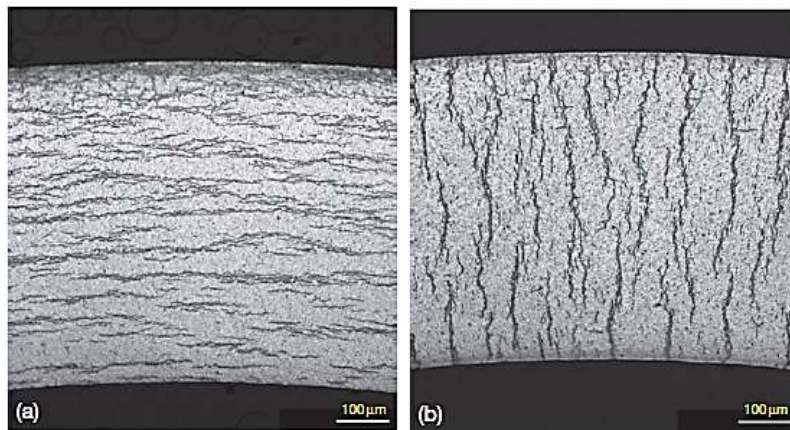


Figure 1.8: Optical micrographs of (a) Circumferential and (b) radial microcracks resulting from hydride orientation [18].

1.8.8 Issues Surrounding Modification of Alloying Elements in Zircalloys

One of the routes explored in attempting to improve oxidation resistance of zirconium alloys was to modify the concentration of alloying elements. Charquet [41] for example showed that increased tin concentrations in Zircaloy-4, from 1.5 wt% to 2 wt% (Figure 1.9) resulted in a weight gain from $0.37 \text{ dm}^{-2}\text{d}^{-1}$ (decimetre squared per day) to $0.58 \text{ dm}^{-2}\text{d}^{-1}$ following autoclave testing at 400°C in a high pressure steam environment (10.3 MPa). In the same study, the author found no tangible difference to oxidation resistance by increasing the chromium concentration to 0.14 wt% in Zircaloy-4 compared to reactor grade Zircaloy-4 which contains about 0.07 wt% chromium.

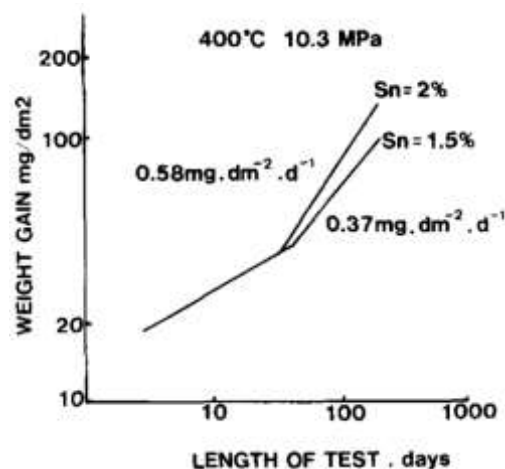


Figure 1.9: Influence of tin content on oxidation resistance of Zircaloy-4 [41].

Cox and Sheikh [139] carried out high temperature corrosion studies on Zircaloy-2 and reported that iron which exists as second phase particles due to its insolubility in zirconium alloys below 400°C (and forms intermetallic precipitates with zirconium, chromium and nickel) migrates out of the precipitates, and forms local agglomerations of pure iron oxide (Fe_2O_3) which was shown using TEM. Following oxidation tests in steam at 400, 500 and 600°C , TEM analysis revealed that the iron was found to have diffused from the zirconium alloy matrix and was found in ZrO_2 layer – the concentrations of which were found to be higher with increased oxidation temperature. The high iron content was found to contribute to increased weight gain (and hence by implication, reduced oxidation resistance). Therefore, any increased iron content in zirconium alloys would tend to cause detrimental effects on oxidation resistance.

The debate surrounding the exact Zr alloy oxidation mechanism in different environments is inconclusive and ongoing, but what the previous discussions clearly demonstrate is that high temperature corrosion of zirconium alloy cladding is an unresolved issue that poses a serious threat to reactor integrity during LOCA conditions, which has not been mitigated by modifying the

concentrations of alloying additions in reactor grade zirconium alloys. Furthermore, any compositional modifications to zirconium alloys may warrant a greater level of regulatory scrutiny prior to implementation in nuclear reactors, since this involves a fundamental modification in a fuel cladding composition, whereas a surface treatment of the extant Zircaloy cladding would typically involve interstitial or substitutional diffusion of elements into only the top few microns of the alloy (and/or a coating of similarly low dimensions).

Given these considerations (and a clear demand for a future role of nuclear energy as previously mentioned in Section 1.3), there has been a surge in research activity to improve cladding materials. One promising route that has been identified is the development of accident tolerant coatings/surface-treated layers. During the Fukushima nuclear accident (Section 1.2), the hydrogen explosions in reactor units 1-3 occurred between 25- and 68-hours following loss of electrical power. Therefore, surface treated layers/coatings on the cladding resulting in a longer period of time to enable a safe resolution to LOCA (in the reactor core) to be determined, would be invaluable. Surface treatments are of particular interest as they have been shown to exhibit excellent oxidation and corrosion protection at elevated temperatures; resistance to mechanical damage; good radiation tolerance and can be fabricated to include elements that allow variability in thermal expansion coefficients, thermal conductivity and suitable neutronic properties which are important considerations in the water-side thermal cycling operation of reactors.

Surface-treated layers/coatings are used to protect metals from corrosion and other environmental attack, thereby improving the longevity of the material to be protected. Surface engineering techniques by which coatings or surface modification treatments are applied are extensively used throughout industry. They are used in the semiconductor sector to build electronic materials [140, 141], and in the aerospace industry, thermal barrier coatings are used to protect surfaces against high operating conditions and corrosive/aggressive environments [142, 143].

Coatings deposited on substrates with low elastic moduli are known to be severely limited by the substrate's poor load bearing-capacity [144] mainly due to the creation of a stepped transition in material properties (i.e. both elastic modulus and hardness). However, thermochemical diffusion treatments can create a more gradual transition in properties from the bulk to the surface, making them especially applicable to (typically) soft and compliant zirconium alloys but, to the best of knowledge, its effect on oxidation resistance has not been systematically investigated in literature. A potential solution may lie in providing load-support using a diffusion treatment before a coating is deposited.

The next section presents an overview of the theory behind the Triode Plasma Nitriding (TPN) thermochemical diffusion treatment and provides supporting evidence for the successful fabrication of plasma-nitrided layers that have resulted in significant and demonstrable improvements in surface properties such as adhesion strength, hardness and wear.

1.9 Plasma Nitriding

There have been rapid advances in the fabrication of coatings using PVD techniques and in recent years have gained widespread industrial acceptance as a method to enhance adhesion, wettability, wear resistance, corrosion resistance and decorative appeal. Coatings fabricated by these techniques and their variants serve to improve service life and quality for engineering tooling and cutting parts. Titanium nitride (TiN) coatings for example are widely exploited in various high speed cutting tools, with 2-10 μm thickness has been found to significantly increase tool life [145]. But their use has also been extended to act as diffusion barriers in contact structures, silicon integrated circuits and solar cells. Furthermore, the use of plasma⁸ in plasma-assisted PVD (PAPVD) allows for improved properties of the coating including improved wear resistance [146], toughness [147], hardness [148] and corrosion resistance [149]. It has been reported that PAPVD-based techniques are one of the most cost effective ways [150] in producing thin films with the ability to combine a number of diffusion and coating treatments. However, PVD techniques produce coatings that would typically exhibit lower chemical bond strength between the coating and the substrate matrix than a surface diffusion-treated layer produced by thermochemical techniques, which would imply adhesion strength of the PVD coating would likely be a limiting factor to coating performance.

1.9.1 Surface Treatments

The majority of surface treatments carried out on Ti and Zr rely on their strong affinity to interstitial elements (i.e. O, C and N) which act as strengthening agents. The inclusion of these interstitial elements increases the c/a ratio of the HCP metallic lattice, reducing the number of active slip systems and enabling the material to become harder.

Nitriding has been a widely used technique for the improvement of the tribological performance of Ti and Zr alloys [151]. Introducing nitrogen into the material enhances wear resistance by forming hard

⁸ Plasma is an electrically conductive gas of ions. Plasma consists of free electrons and atoms that have had some of their orbital electrons removed and is generated (i) at high temperatures or (ii) by applying a bias voltage between the anode and cathode.

nitride precipitates and by pinning dislocations when in solid solution [152] (which is when the crystal structure of the solvent remains unchanged by the addition of solutes and when the mixture remains in a single homogenous phase). The use of gas nitriding has been used previously but is limited by the slow diffusion of nitrogen into the substrate, and typically requires higher temperatures (ie. 1050°C) [153]. Plasma nitriding (PN) is considered a promising technique for introducing interstitial nitrogen into substrates.

The next section covers some of the basic understanding of plasma-assisted surface engineering methods which is crucial to understanding plasma nitriding.

1.9.2 Enhanced Plasma Diffusion Processes: Nitriding

Early plasma nitriding typically required high pressures ranging 0.1-1.0 kPa [154] preventing integration of PVD coating treatments which used different pressures. A gas in a quasineutral state (the charge neutrality of a plasma overall but at smaller scales, the positive and negative charges that make up the plasma give rise to charged regions and electric fields) with a low degree of ionisation⁹ (~0.01%), is maintained by the presence of energetic electrons which create a cascading self-ionisation process due to free electrons¹⁰ being accelerated off the surface towards the anode. The electrons encounter gas molecules/atoms and transfer their energy via inelastic collisions. Some molecules break apart and release valence electrons, which impart energy to nearby molecules, further increasing ionisation which interact with the substrate surface [155].

As the voltage is increased between the anode (chamber) and cathode (substrate), gas molecules begin to ionise which decreases the resistance of the flow of current. Secondary electrons are then emitted, and plasma ignition occurs when sufficient particles have become ionised which requires less voltage to sustain itself [156]. At a certain point on increasing voltage, the abnormal glow region is achieved which is used for plasma-assisted deposition techniques. However, going above a critical value results in the collapse of the plasma and form arcs [157]. Plasma potential distribution is one of the parameters that allows the plasma to induce chemical reactions and determines the energy of the species inside the plasma and the energy with which the species will reach the surface to be treated. This is dependent on the potential difference between the plasma and the substrate surface [158], which typically occurs in the plasma sheath region (which is the volume near a surface, and its

⁹ Ionisation is the process where an atom/molecule acquires a negative or positive charge by gaining or losing electrons. The electrically charged atom/molecule is called an ion and is generated by (i) collisions with other atoms and (ii) interaction with EM radiation.

¹⁰ Free electrons are unbound or loosely bound electrons that are free to move when an external force is applied.

thickness is defined by the mean distance travelled by a secondary electron emitted by the cathode before it makes the first ionisation collision). Lower plasma pressures typically result in larger ion mean free path λ_m , (the average distance travelled by a moving particle between successive collisions which changes its direction or energy or other properties) relative to the sheath thickness, L , which allow ions to reach the electrode with an acceleration potential similar to the voltage drop across the sheath. However, if the gas number density (pressure) increases, this will result in a higher number of collisions across the sheath due to the smaller ion mean free path, with little available energy from the sheath voltage.

Previous work by Davis and Vanderslice [159] used the cathode sheath thickness, L , and the mean free path for charge exchange collisions λ (later developed further by Rickards [160]) to describe the distribution of energies for neutrals and ions energy arriving at the surface of the cathode under glow discharge conditions¹¹.

The following equation defines the number of ions per energy interval:

$$\frac{dN}{dE} = \frac{N_0}{m} \frac{L}{\lambda_m} (1 - E)^{\left(\frac{1}{m}\right)-1} \exp \left[-\frac{L}{\lambda_m} + \frac{L}{\lambda_m} (1 - E)^{\frac{1}{m}} \right] \quad (1.14)$$

where E is the fractional ion energy normalised to the cathode voltage; N_0 is the number of ions entering the cathode sheath; and m is the constant representing the potential drop with respect to the cathode potential ($\sim 4/3$), that takes into account the repulsion between particles of like charge [156]. Equation 1.14 shows that as L/λ_m increases, there are an increased number of collisions and the mean ion energy decreases. The energetic neutral distribution is comparable to the ion energy distribution. Thus, to increase the mean energy of the ions arriving at the cathode (substrate), it is important that L/λ_m should be low, with a ratio of around 1. This is severely restricted in d.c. diode plasma systems because both the gas pressure and cathode voltage need to be reduced in order to lower the number of collisions inside the sheath to reduce the L/λ_m value. This is counterproductive, since reducing the number of atomic/ionic species in the plasma reduces the secondary electron emission sustaining the plasma - since the supply of electrons is dependent on the rate of ionic bombardment of the cathode [156]. Furthermore, the secondary electron yield is known to decrease when the target surface is exposed to reactive gases (i.e. nitrogen and oxygen). Thus, as the surface of the target changes, the ejected electrons would reduce in number which would quench the plasma.

¹¹ This is where the plasma is luminous because electrons gain sufficient energy by excitation collisions which generate photons.

It is therefore crucial to provide an external/auxiliary source of energetic electrons to sustain and enhance the plasma.

1.9.3 The Issues with Diode Plasmas

Diode plasmas used for surface engineering processes have a low degree of ionisation due to the plasma being sustained solely by the secondary electron emission from the cathode. In addition, the high collision cross-section of ions with neutral species depletes the energy of the former in the cathode sheath¹², thereby unable to sustain the plasma. Thus, only 10% of the energy generated by the substrate negative bias voltage is delivered by ions and 90% is provided by energetic neutral species [161]. Plasma enhancement has the ability to influence the mean energy of bombarding species as well as the type of ionic species arriving at the cathode surface. This is typically done by (i) increasing the number of ionising electrons, or (ii) making electron trajectories much longer, and using electrons more efficiently as the probability for an ionising collision is increased [162]. These factors are crucial for plasma-assisted physical vapour deposition (PAPVD) techniques which bombard the substrate with energetic ions. In a d.c. argon diode discharge setup, L/λ is typically in the range 10-15, but this can be much lower (<2) when applied in a triode discharge setup.

1.9.4 The Case for Triode Discharge Systems

Triode systems used to intensify plasmas and PAPVD systems involve the injection of low energy electrons between the vapour source and the negatively biased substrate, typically using a heated negatively biased tungsten filament for this purpose. The auxiliary electron source constitutes the third electrode in the system and hence termed 'triode' configuration. By introducing a hot electron-emitting filament the substrate voltage can be significantly lowered to a few hundred volts (<500 V for diffusion processing and <100 V for PAPVD) [156]. This is because the electron emission current density can be used to control the discharge power without adjusting the pressure (as is the case in diode systems), since the supply of electrons is not dependent on the rate of ionic bombardment of the cathode substrate surface. A typical setup for a triode plasma system is shown in Figure 1.10.

¹² The probability of collisions of energetic ions with gas atoms is high due to thicker cathode sheath regions and so the energy of the ions would be depleted before it reaches the cathode substrate – quenching the plasma.

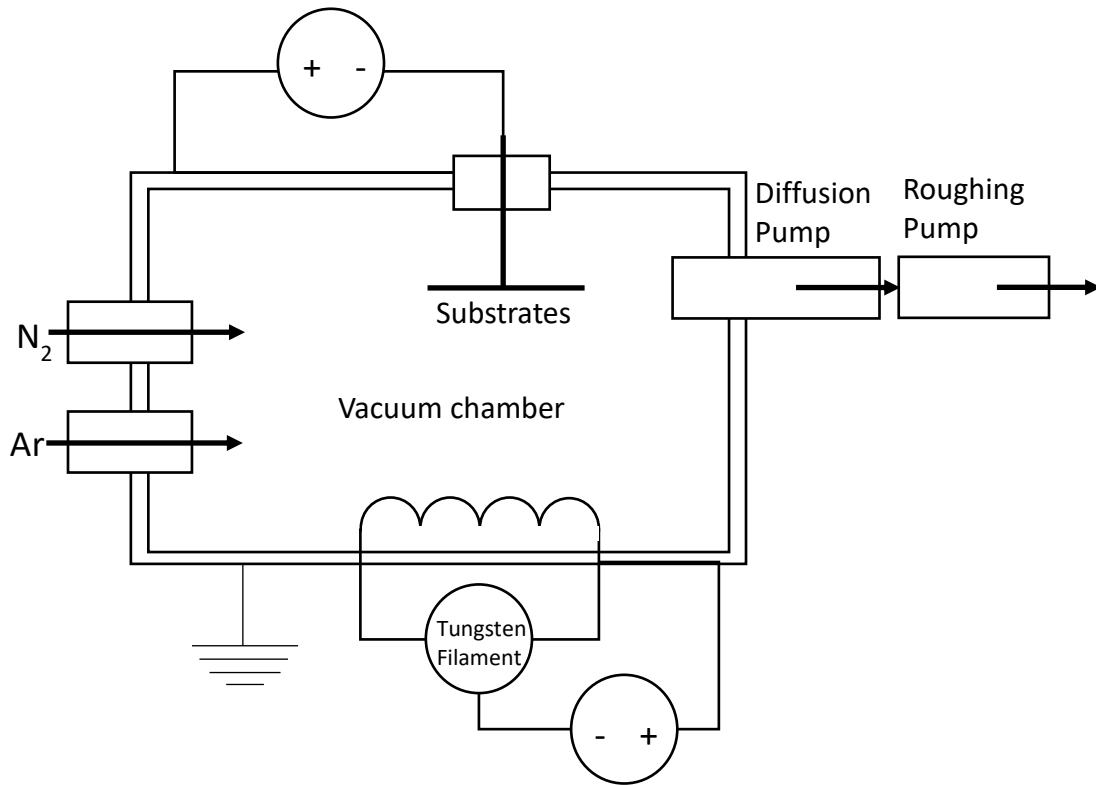


Figure 1.10 : Schematic diagram of a triode discharge system.

The reduction of L/λ_m at low pressures results in an increase in the total ion energy (i.e. higher fraction of ions with maximum energy) thus, a greater proportion of the total energy can be transported to the cathode substrate by ionic species as shown in Figure 1.11. Conversely, when L/λ_m is high (i.e. ~ 10), there is a lower fraction of ions with maximum energy and hence, a lower proportion of energetic ions transported to the cathode.

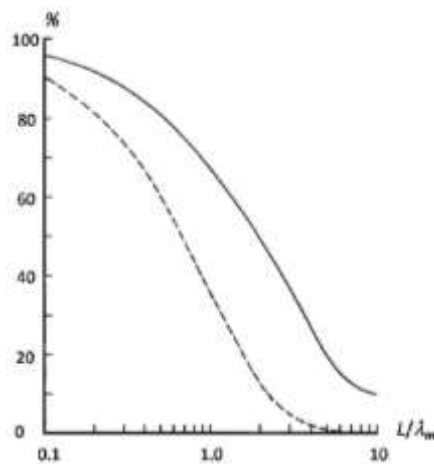


Figure 1.11: Changes in L/λ_m ratio show the fraction of the total energy transported by ionic species (-) is greater than the energy fraction of ions arriving at the cathode (---) [161].

In previous work carried out by Fancey and Matthews [161], they showed that a triode discharge configuration could increase the ionisation efficiency by at least two orders of magnitude relative to diode systems. In triode conditions (where $L/\lambda_m < 1$), the number of species (dose) measured at the cathode would be far less due to fewer neutrals arriving, but the total energy would be increased.

The relation between L , λ_m and cathode voltage V_c provide an estimate of the average ion energy E_i^a :

$$E_i^a = V_c \left[2 \left(\frac{\lambda_m}{L} \right) - 2 \left(\frac{\lambda_m}{L} \right)^2 + 2 \left(\frac{\lambda_m}{L} \right)^2 e^{-\frac{L}{\lambda_m}} \right] \quad (1.15)$$

Equation 1.15 essentially suggests that increased potentials lead to increased ion energies since the mean ion energy is proportional to the voltage applied to the cathode surface. However, the Child-Langmuir relationship which shows the effect of V_c on L , reveals that as the cathode voltage increases so does the sheath thickness, L . So for L/λ_m around 10, the average ion energy is around 10% of V_c , whereas for L/λ_m less than 1, this can be up to 90% of V_c [163].

It has been shown [164] that an increased ion concentration creates a high local effective diffusion coefficient, thus increasing nitrogen penetration into the substrate. It was suggested that the diffusion of ion-vacancy pairs is responsible for the dependence of nitrogen diffusion case depth (in plasma nitriding treatments) on current density, thus explaining why plasma intensified processes result in high Penetration Depths of ions beneath the substrate surface. Furthermore, it is plausible to assume that a higher fraction of bombarding ionised gas species will have sufficient energy to be directly sub-planted into the metallic substrate lattice, increasing rates of bulk diffusion.

Tibbetts [165] showed that cathode sheath ion/neutral collisions increase the dissociation of N_2 gas molecules resulting in an increased flux of atomic nitrogen at the cathode surface and concluded that atomic neutrals were primarily responsible for the nitriding process. The effect of plasma on nitriding was further expounded upon by Fouquet et al [166] who reported that the plasma enhances the nitriding process by increasing the nitrogen concentration but has no effect on the diffusion coefficient which remains temperature controlled. But these experiments were carried out using low ionised plasmas at high pressures with average ion energies at tens of eV, which only provide a higher concentration of reactive species adsorbed at the surface and this can result in no discernible difference in diffusion path. However, it has been demonstrated by Meletis [167] that a minimum particle energy of ~ 200 eV is required for vacancy generation in TiN. It is also plausible to assume that similar energies are required for the formation of ZrN (using Zr as substrates) using plasma-assisted techniques. However, it has also been reported that a minimum energy of 150 eV is required for nitrogen ions to become trapped inside a metal lattice [168]. This is important as it suggests that a few hundred volts at the cathode are sufficient for successful TPN treatment.

At low pressure the reduction of L/λ_m under intensified plasma conditions increases the concentration of ions that have energetic values closer to V_c , of which a higher proportion of these exceed the energetic threshold for sub-plantation, making the nitriding process more effective. But for non-intensified plasma conditions, a high adsorbed solute concentration reduces the activation energy for chemical reactions, resulting in the formation of compound layers typically seen in diffusion treatments. But this is not known to have lasting effects below the compound layer, allowing the diffusion process to be controlled as a function of temperature.

1.9.5 Triode Plasma Nitriding

Plasma intensification makes it possible to perform nitriding at pressures below 1 Pa, whereas previously this was typically carried out at high pressures, ranging from 0.1 to 1 kPa [162]. These low pressures allow the required purity and energy of both ionised vapour and reactive gases to be achieved, resulting in a diffusion-treated barrier comprising of a thick nitrogen diffusion zone and thinner dense nitride compound layer at lower temperatures compared to diode systems. Thornton for example [169] reported that high pressures at low temperatures causes grain boundaries to open up forming a less dense structure, resulting in reduced adatom mobility.

A benefit of triode processes is that it increases bombardment of ions at the surface resulting in higher heat input and improves diffusion kinetics. It has been demonstrated [170] that ion dose influences nitrogen penetration, while surface compound layer formation is promoted by the impingement of energetic neutrals. Hence, increasing the ionisation efficiency results in deeper nitrogen penetration into the material surface and a thinner surface nitride compound layer. The authors were also able to show that increased diffusion of nitrogen by at least five orders of magnitude compared to conventional diode plasma nitriding. In the triode discharge case, this allows successful TPN treatments to be carried out at lower temperatures and shorter durations.

In a diode configuration N^+ (atomic ions) are thought to be the dominant incident ions since the large cathode sheath thickness and the high gas number density influence the occurrence of at least one dissociative collision of a nitrogen N_2^+ molecular ion traversing the cathode sheath. Most of the kinetic energy to the cathode surface is carried by the nitrogen molecular neutrals. But a triode discharge configuration allows the cathode sheath thickness to be considerably reduced due to the high current densities and low cathode bias voltages achievable according to the Child-Langmuir equation. Under low pressure conditions, this results in a near-collisionless sheath. Once the L/λ_m ratio is reduced to less than 1, the likelihood of collisions is significantly reduced and the predominant ionic species becomes N_2^+ ions which carry most of the energy [156].

The availability of nitrogen atomic species is an important benefit to the diffusion into the substrate. When considering that the energy required for nitrogen dissociation at a metal surface is ~ 9.8 eV [171], and under triode conditions, most of the species arriving at the cathode surface have energies close to the applied bias, then the availability of atomic species is also significantly increased.

The d.c. triode configuration also allows the system to operate at significantly lower pressures (< 1 Pa) where L/λ is reduced. The reason for this is that for diode setup at 500 V, there are considerably more energetic neutral species compared to the ionic species present at the vicinity of the workpiece, resulting in discharge nitriding not being fully optimised. Leyland [156] points out that when $L/\lambda \geq 10$, as in the diode setup, only 10% of the total energy is transported by ions but rises to 75% when $L/\lambda = 1$. In terms of the useful ionic species surrounding the workpiece, when compared to the diode setup, the triode performs better below 1000 V and is significantly superior below 500 V and displays effective nitriding at 200 V where the diode plasma becomes ineffective.

1.9.6 The Role of Argon Gas in Triode Systems

Inert gases are typically used during plasma surface treatments. Argon (Ar) is favoured because of its low cost and has proved beneficial for plasma processing. It has been reported [172] that active Ar species (ions and energetic neutrals) are responsible for transferring more than 60% of the energy to the cathode for diode treatments that result in thick cathode sheaths. The beneficial influence of Ar is due lower ionisation cross-section (for electron impact) compared to nitrogen [173]. Furthermore, Ar is a contributory factor to the dissociation of nitrogen by reducing the thermalisation of electrons. Since the injection of Ar reduces the presence of N_2 molecules, the probability of inelastic collisions with electrons is also reduced. Thus, a reduction in electron quenching results in a higher mean electron energy sufficient for effective electron impact ionisation of nitrogen atoms [174]. Furthermore, it has been suggested [175] that Ar ions do not directly contribute to the ionisation of nitrogen atoms but electron-impact ionisation is the primary mechanism for argon-nitrogen discharges. The process is optimised by increasing the Ar concentration until it leads to a deficiency in the available nitrogen at the substrate surface, which results in thinner compound layers. This may lead to increased diffusion zone thickness due to lower impedance to nitrogen diffusion into the substrate lattice. For instance, it has been reported [176] that Ar in plasma nitriding processes can lead to a decrease in lattice parameters of nitrided Ti and such a decrease in cell volume could reduce the nitrogen solubility into the Ti lattice.

1.9.7 The Use of Triode Plasma Nitriding in Diffusion Treatments

Triode systems have been successfully used to improve tribological properties of Ti alloys. This could by extension be used for diffusion treatments of other transition metals such as Zr for instance. The diffusion of N through Zr creates a morphology comprising of several layers, shown schematically in Figure 1.12. It can be seen from the HCP α -Zr base metal the formation of a diffusion zone consisting of nitrogen in interstitial solid solution with Zr (α (N)-Zr) followed by the formation of a compound layer predominantly consisting of Face-Centred Cubic (FCC) ZrN with nitrogen being in interstitial solid solution with α -Zr. In addition to the layered system described, it is plausible to expect Zr_3N_4 precipitates [177] within the ZrN compound layer, although information relating to the crystallographic structure this occurs in is unclear but has been suggested to be in the cubic phase [178]. The Zr-N binary phase diagram in Figure 1.13 shows that α -Zr can dissolve large amounts of nitrogen which strengthens the diffusion zone by impeding dislocation motion.

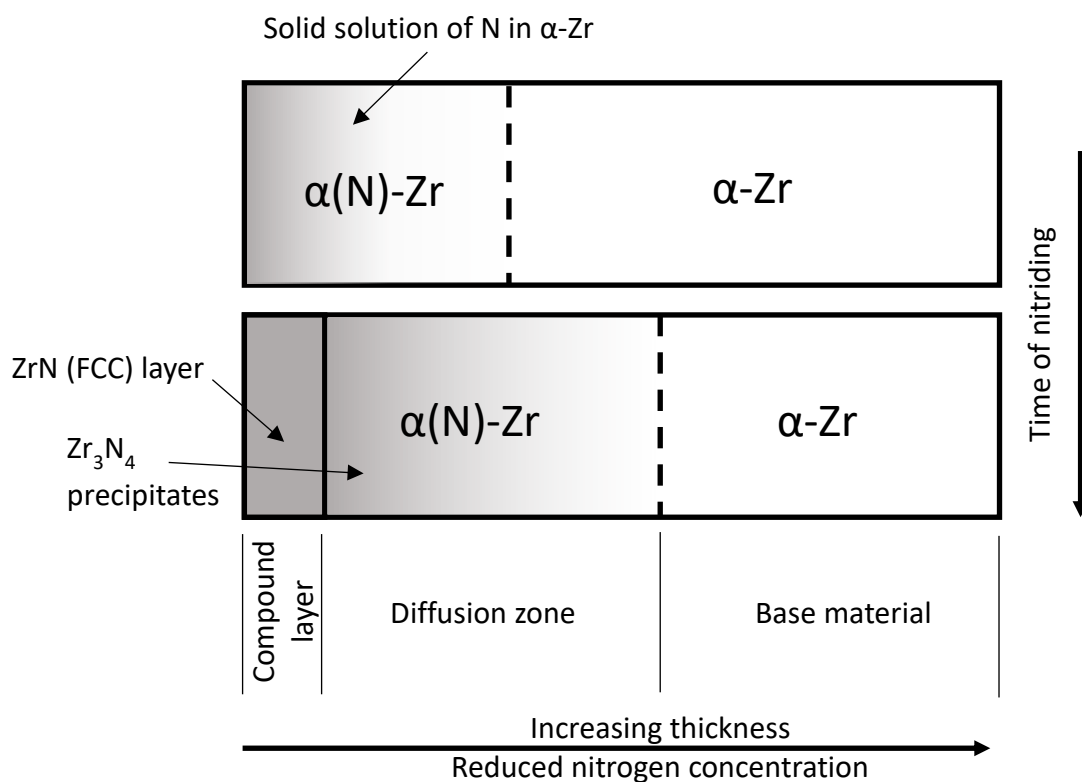


Figure 1.12: Schematic representation of kinetics of formation and growth of nitride surface layers of zirconium (adapted from [179]).

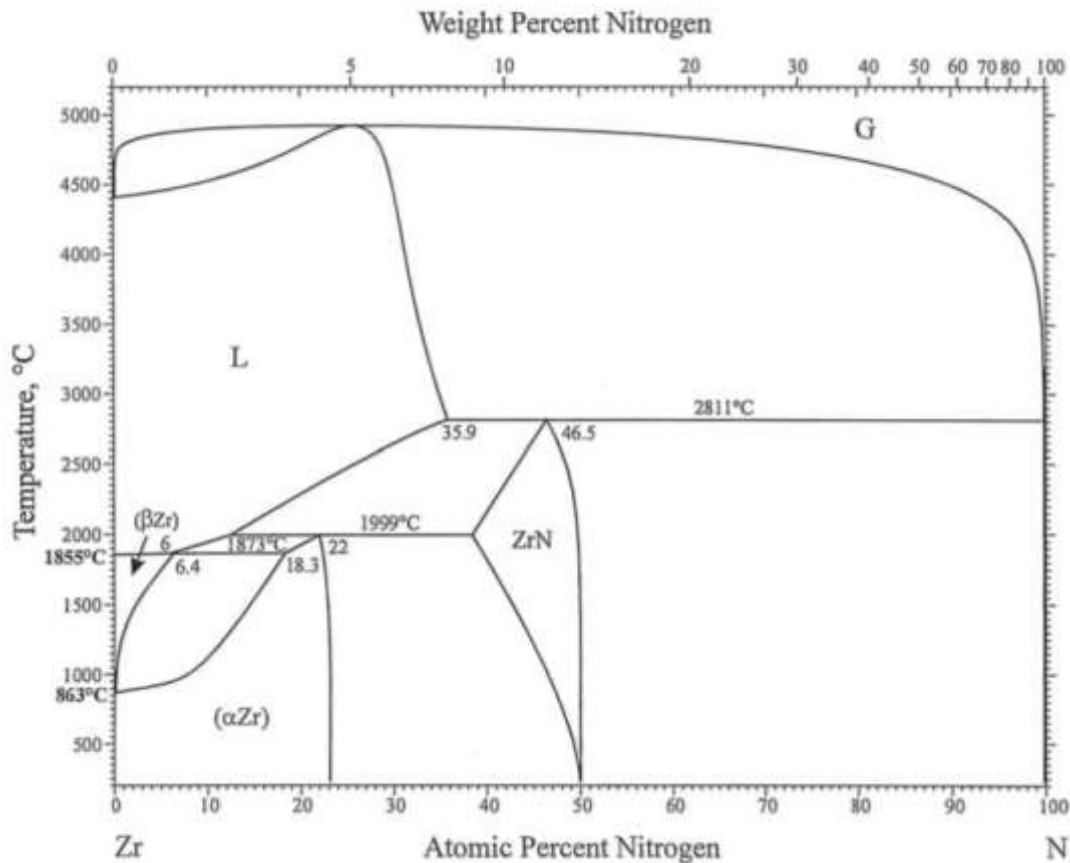


Figure 1.13: Zirconium-Nitrogen binary phase diagram.

Muraleedharan and Meletis [180] reported a thick TiN nitride compound layer formed from plasma nitriding of Ti-6Al-4V alloy with in a three-fold increase in compound layer thickness (from 2 to 6 μm after a 9 hour treatment) at temperatures as low as 480°C compared to conventional ion nitriding (900 °C) of titanium but also showed a reduction in the hardened case depth of the compound layer by up to 20%. They concluded that this was due to the thick compound layer limiting the rate of nitrogen penetration to the underlying substrate in the enhanced plasma process. Kashaev et al [181] showed that lower partial pressures of nitrogen in a triode discharge revealed no compound layer but did have thicker diffusion zones, which suggests that there should be a balanced increase in nitrogen partial pressure to obtain thicker diffusion zone followed by a compound layer. Thus, it is important to control compound layer formation to promote the hardened case depth, which can be carried out by reducing processing times and/or reducing the process substrate negative bias [182]. In particular, nitriding can have negative effects on mechanical strength and fatigue properties of Ti-6Al-4V which deteriorate with increasing treatment duration [183].

For complex shapes, achieving a uniform coverage entailed using high pressures (>1000 Pa). But it has been shown that a cathode sheath thickness lower than 2.5 mm provides excellent uniformity at low pressure (1 Pa) [184] which is available for triode plasma systems. Increasing the voltage tends to

increase the cathode sheath thickness which in turn reduces the hole and recess penetration. Cathode negative bias voltages as low as 200 V have been suggested for complex shapes [185].

Cassar et al [182] demonstrated that TPN treatment significantly improves the wear resistance of Ti-6Al-4V alloy. Samples were polished and sputter-cleaned prior to diffusion treatment carried out at 700°C for 4 hr in a mixture of 70%:30% partial pressure of nitrogen and argon respectively, at a gas pressure of 0.4 Pa. The nitrided samples were then coated with either TiN or CrAlN using PAPVD at temperatures ranging from 400 to 450°C. Wear tests were performed using a low frequency reciprocating-sliding tribometer by applying a Normal Force of 4.0 ± 0.1 N. It was found that using a combination of increasing treatment times during low voltage (LV)-TPN and short treatment times during high voltage (HV)-TPN resulted in a deep diffusion zone and a thicker TiN compound layer (whilst minimising surface roughening) providing better wear resistance than using LV-TPN or HV-TPN separately during the ball-on-plate reciprocating sliding test. This provided a more effective load support compared to either LV-TPN or HV-TPN treated samples and is more effective at absorbing contributions from the substrate thereby having a slightly reduced wear rate. Similar results would be expected for nitride compound layer and nitrogen diffusion zone formation on zirconium and its alloys. This finding is significant as it points to the importance of having a mechanically robust nitrogen diffusion layer to achieve low wear rate. In addition to this, another important outcome is that it serves as a potential avenue that may merit further investigation in the context of this work, due to the high coolant flow pressure inside the reactor core in between fuel elements which may instigate hydrothermal wear of surface-treated layers should this be implemented.

1.10 Motivation Behind the Use of Zirconium Nitride (ZrN) Coatings

ZrN is a hard ceramic material that has been predominantly produced by PVD techniques and is commonly used to coat medical devices, automotive and aerospace components due to its excellent chemical and physical properties, that are similar to those of TiN. It is a refractory compound with high thermal stability [186], high hardness (up to 30 GPa using nanoindentation) [187], low electrical resistivity ($13.6 \mu\Omega\text{cm}$ at RT) [188], good corrosion resistance [189] and decorative potential [190], giving a shiny metallic golden appearance. ZrN-based coatings are relatively recent and have been less studied compared to TiN-based coatings. Their potential as abrasion-resistant coatings on cutting tools, drill bits and wear parts was shown to be promising [191]. ZrN is also being considered for use in advanced nuclear power plants as inert matrix fuel [192] to burn plutonium or long-lived actinides in accelerator driven systems or fast reactors due to its high thermal conductivity ($45\text{-}50 \text{ W(mK)}^{-1}$) [193], low neutron capture cross-section and chemical compatibility with existing nuclear fuel cycle

technologies. Potential applications as a protective coating for radioactive waste storage vessels have also been suggested [194]. Thus, the above mentioned advantageous mechanical and tribological properties makes them attractive as protective surface-treated layers/coatings in harsh environments.

ZrN with mixed metallic, ionic and covalent bonding characteristics has NaCl-type crystal structure each zirconium atom is co-ordinated with six nitrogen atoms where the d-spacing for Zr-N interatomic distance is 2.31 Å and N-N interatomic distance is 3.27 Å. This closely resembles TiN, but has a larger lattice parameter (ZrN, $a = 4.58$ Å and TiN, $a = 4.24$ Å). The Zr-N phase diagram presented earlier in Figure 1.13 shows that zirconium has a high affinity for nitrogen and can form ZrN with N content as low as 23 at% below 863°C, the transus temperature for α -Zr to β -Zr.

Numerous physical vapour deposition methods have been used to deposit ZrN films including: Radio Frequency (RF) and Direct Current (DC) sputtering; Ion plating; DC magnetron sputtering; cathodic arc evaporation [194]; pulsed laser deposition; dual ion beam sputtering, however, despite the numerous successes of TPN diffusion treatments on Ti alloys, resulting in enhanced tribological properties, this treatment has not been reported on Zr (or its alloys) before.

1.11 Current Coating Trends in Nuclear Applications

PVD coatings are currently being used in nuclear reactors. Magnetron sputter deposition, in particular, is the predominant technique used to deposit zirconium diboride (ZrB_2) coatings ranging from 30 μm to 50 μm thickness on uranium dioxide (UO_2) fuel pellets. These are termed Integrated Fuel Burnable Absorber (IFBA) pellets and they absorb excess neutrons during the initial start of the reactor thereby providing a means of controlling reactivity. This is important to ensure that the reactor is in a critical state whereby exactly one neutron goes on to bombard a U-235 atom in a controlled reaction. Sputter deposition has been identified as being fraught with issues surrounding practicality to economic considerations. Some of which include:

1. It is expensive to operate – the sputtering technique consumes almost 50% of the ZrB_2 target before it must be replaced which presents material wastage issues.
2. It is expensive to maintain – a small crew are required to maintain the sputtering equipment, whose duties range from regular cleaning of internal chambers to maintaining pipes and fixtures.
3. It is economically unsustainable to deploy on the new Westinghouse AP1000 reactors. A higher throughput of coated UO_2 pellets in a faster time period is required.

As the limitations of the sputtering technique to achieve commercial objectives are increasingly realised, alternative and improved treatment techniques are required.

Currently thermal spraying is being considered as a potential route. However, early indications point to multi-faceted issues ranging from non-uniform coverage of the substrate to extensive chipping damage and early adhesive failure when subjected to scratch adhesion testing.

1.12 Stabilisation of the Oxide Layer

As discussed in the earlier sections of this chapter, it is apparent that a significant concentration of oxygen at elevated temperatures and under aqueous conditions can detrimentally affect the oxidation resistance and mechanical properties of zirconium alloys, particularly monoclinic zirconia. One of the contributing factors is the significant lattice parameter mismatch between HCP α -Zr ($a = 3.23 \text{ \AA}$, $b = 3.23 \text{ \AA}$, $c = 5.15 \text{ \AA}$) [195] and monoclinic zirconia ($a = 5.15 \text{ \AA}$, $b = 5.21 \text{ \AA}$ and $c = 5.32 \text{ \AA}$) [56]. As the m-ZrO₂ grows, compressive stress develops in the oxide but is insufficient to stabilise this phase due to the large lattice mismatch. Furthermore, the lack of sufficient compressive stress in the oxide layer would reduce its load-bearing capacity and ability to resist mechanical damage (due to the oxide's susceptibility to delaminate from the substrate under mechanical loading). Compressive stress in the oxide layer are important as this can help stabilise a particular phase of an oxide which can be sustained over a large range of temperatures. Stabilisation of the tetragonal or cubic polymorphs of zirconium oxide is one such example. Compressive stresses are able to stabilise the tetragonal phase because the lattice parameters of t-ZrO₂ ($a = b = 3.65 \text{ \AA}$, $c = 5.29 \text{ \AA}$) [91] and HCP α -Zr ($a = b = 3.23 \text{ \AA}$, $c = 5.15 \text{ \AA}$) are similar. Therefore, significant lattice mismatch between the tetragonal oxide phase and zirconium metal as the oxide grows is minimised (compared to monoclinic zirconia).

As mentioned earlier compressive stress in the oxide scale can also arise from the large volume expansion (3-5%) of ZrO₂ during the oxidation process. A wide body of literature has investigated zirconium oxide layers (in relation to the corrosion of zirconium alloys) which typically comprise a mixture of mostly m-ZrO₂ with 8-15% t-ZrO₂. Furthermore, for P-B ratios greater than one, a high compressive stress will develop in the oxide scale. A value of 1.56 for instance signifies large growth stresses in the oxide scale on Zr-alloys, despite the similar lattice parameters of HCP α -Zr and t-ZrO₂. As deduced from P-B ratio calculations in section 1.8.6 earlier, the P-B ratio of 1.56 quoted in the literature is likely to refer to the tetragonal ZrO₂/Zr system.

A common method to stabilise the tetragonal or cubic zirconia phase is to alloy the oxide using a second metallic constituent. Yttrium is added in the form of Yttrium oxide (Y₂O₃) (about 8 mol%) and is used to stabilise the tetragonal or cubic phase of zirconium oxide for the ceramic topcoat for

Thermal Barrier Coatings (TBC) widely employed on crucial components that are exposed to prolonged or high heat loads such as in jet engines and gas turbines in the aerospace industry [196]. The phase-stabilising yttrium atoms randomly occupy the zirconium metal sites via substitutional diffusion, and charge balance is achieved by a number of vacancies on the oxygen sites [197]. The low thermal conductivity properties ($2.3 \text{ W}\cdot\text{m}^{-1}\text{K}^{-1}$ at 1000°C [198]) offered by Yttria-Stabilised Zirconia (YSZ) coatings allow for higher operating temperatures whilst limiting the thermal exposure of structural components, thus facilitating components to operate at temperatures close to, or exceeding their melting points. They are designed to reduce oxidation and thermal fatigue - extending the service life of the component thereby increasing overall thermal efficiency. YSZ also has a relatively high thermal expansion co-efficient ($11 \times 10^{-6} \text{ }^\circ\text{C}^{-1}$) for a refractory ceramic oxide, which helps alleviate thermal stresses that arise due to the thermal expansion mismatch between the top-coat and the underlying metal substrate. These coatings are typically produced by thermal spray or more commonly by Electron Beam-Physical Vapour Deposition (EB-PVD) method with thicknesses ranging from 100 to 500 μm [199]. TBCs have been continuously developed over the last 50 years and now comprise a 4 layer system [200]:

- 1) Metal substrate – this is typically a nickel- or cobalt-based superalloy and provides thermo-mechanical loading of the TBC system.
- 2) Metallic bond-coat consisting of NiCrAlY or NiCoCrAlY alloy of 75-150 μm thickness and typically deposited by plasma spray or EB-PVD methods. This protects the substrate from oxidation or high temperature corrosion and provides the adhesion of the TBC to the substrate.
- 3) Thermally grown oxide (TGO) – high operating temperatures of gas turbine engines ($700\text{-}1100^\circ\text{C}$) result in the in-situ oxidation of the bond-coat at the top-coat interface with a thickness up to 10 μm [201]. The porosity of the ceramic top-coat allows a diffusion pathway for oxygen from the surrounding environment to the bond-coat. Thus, a controlled growth of the bond-coat is ‘engineered’ to ensure that an Al_2O_3 -rich TGO forms, to act as a diffusion barrier to retard further inward diffusion of oxygen.
- 4) Yttria-stabilised zirconia (YSZ) ceramic top-coat ($\text{ZrO}_2\text{-}8\text{mol}\%\text{Y}_2\text{O}_3$) – provides thermal insulation due to its low thermal conductivity. Along with internal cooling, this can result in a surface-to-substrate temperature drop of up to $\sim 300^\circ\text{C}$.

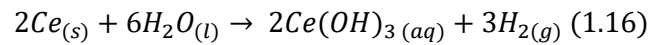
However, the use of YSZ coatings on zirconium alloy fuel rod cladding may bring issues. The low thermal conductivity properties offered by YSZ coatings that are considered advantageous for use in aerospace applications could potentially be detrimental for achieving high thermal efficiencies during

nuclear reactor operation. Application of YSZ coatings (typically several hundred microns thick on aerospace components) on the exterior cladding of fuel rods, may lead to inefficient/reduced heat transfer from nuclear fission reactions (generated from UO_2 fuel pellets) to the coolant, hence reducing efficiency (i.e. heat generation from nuclear fission reactions to the production of electricity). The thermal conductivity offered by YSZ could be increased if the TBC coating thickness was of the order of tens of microns rather than hundreds of microns. It would be prudent to investigate how thermal conductivity changes with thickness under reactor operating conditions and in LOCA scenarios (i.e. temperatures in excess of 700°C), this which could be an avenue for further work (see Chapter 6). Furthermore, the introduction of yttria stabilised zirconia to stabilise tetragonal zirconia can also lead to porosity in the coating which play an important role in lowering thermal conductivity but also can be detrimental to the longevity of the coating as it provides a pathway for oxygen ingress which may lead to further oxidation of the substrate. This may need consideration during coating design.

Potential candidates for stabilising t- or c- ZrO_2 that have been suggested include: cerium (Ce), scandium (Sc), titanium (Ti) and magnesium (Mg) [202]. Scandium has been used in reinforced alloys (i.e. Al-Sc alloys) due to its high strength-to-weight ratio; good corrosion resistance; high melting point of 1541°C and a density as low as aluminium (2.99 gcm^{-3}) which has made it an important element in the production of military equipment [203], but it is uneconomical for two main reasons (i) Sc has a relatively high cross-section for neutron absorption (27.5 barns) compared to zirconium (0.184 barns) [39] compromising neutron economy as many neutrons would be absorbed compared to the fission reactions that it would generate; (ii) Sc is one of the most expensive elements due to its scarcity (fluctuating in the range of \$7000-\$15000 per kilogram [204]). Using scandium to fabricate coatings on tens of thousands of fuel rods in a nuclear reactor would be likely to significantly increase the reactor operator's production costs, but a detailed feasibility study would need to be carried out to investigate this. Scandium-stabilised zirconia (ScZrO_2) has been reported by Lukich et al [205], where the cubic phase is stabilised in fairly narrow temperature range of $700\text{-}800^\circ\text{C}$; however, below this temperature range, the cubic phase is unstable and a phase transition to the lower symmetry rhombohedral phase occurs, resulting in a decrease in thermal conductivity [206] which, although potentially of benefit in TBC applications, is a major drawback for achieving a stabilised tetragonal/cubic zirconia phase over a wide range of temperatures in a fuel clad application.

Cerium is also another alloying element considered to stabilise the tetragonal or cubic phase of zirconia. It has a hexagonal close-packed crystal structure with lattice parameters $a = b = 3.16 \text{ \AA}$, $c = 5.20 \text{ \AA}$ [207] that is similar to zirconium (and therefore tetragonal zirconia [57]) such that the lattice mismatch would allow compressive stress to form to stabilise the tetragonal oxide phase, yet is not so significant as to result in a structural breakdown as is the case with monoclinic zirconia. The low

neutron absorption cross-section of 0.63 barns [39] is slightly higher than zirconium and during oxidation in air, the formation of Ce_2O_3 is thermodynamically favourable. However, Ce reacts readily with water to produce hydrogen as shown in Equation 1.16 [208]:



The concerns surrounding hydrogen evolution (Equation 1.16) may have low/negligible implications in the build-up to a LOCA scenario when considering inclusion of Ce (via substitutional diffusion in a PVD coating comprising of Ce and Zr) would be in low concentrations. However, this is worthy of further investigation and is mentioned in Chapter 6.

The use of Mg as an alloying element to partially stabilise ZrO_2 in a tetragonal or cubic form may provide a potentially more viable solution to enable fuel cladding to last longer during LOCA conditions. Magnesium and Mg-alloys are non-magnetic and have relatively high thermal conductivities (160 W/(m.K)) [209] and is widely distributed in the Earth's crust as mineral deposits and in solution in seawater. Magnesium has a low density of 1.74 gcm^{-3} , which is 35% lower than that of aluminium (Al) (2.7 g/cm^3), and Mg alloys weigh $\sim 25\%$ less than Al at the same stiffness [210]. The high strength-to-weight ratio and low cost [211] makes them attractive for applications that require light-weight materials such as load-bearing structures in aerospace, automotive and microelectronic industries. Thus, they are considered promising alternatives to aluminium alloys for the manufacture of automotive components and have ideal properties for use as biodegradable implants [212]. Magnesium has a hexagonal close-packed crystal structure with lattice parameters $a = b = 3.20 \text{ \AA}$ and $c = 5.20 \text{ \AA}$ [213] which is similar to that of zirconium. Magnesium is also used as a reducing agent in the extraction of titanium, zirconium and uranium from their natural ores [214]. As a reactive metal, Mg can also be used in sacrificial anodes. This is because Mg has a low negative standard electrode potential (-2.37 V) [215]. Mg also has similar atomic radius (150 pm) to Zr (155 pm) [216]. This is particularly useful since this would allow Mg to occupy Zr sites in a PVD coating via substitution and avoid significant lattice distortion [217]. It has been suggested that substitutional solid solutions form if the difference in the radii of metal atoms that replace each other is less than 15% [5]. This favourable size factor allows a diverse range of solute elements including zirconium, yttrium, cerium, aluminium, zinc and thorium [218] in which Mg could be added via substitutional diffusion.

Historically, the use of Mg is well known in the nuclear industry as it was used in the cladding material of Mg-Al cans [25] of Magnox reactors due to its high thermal conductivity and low cross-section for neutron absorption (0.063 barns) [39]. These reactors were designed, constructed and commissioned in the UK in the 1950's and 1960's. Its namesake refers to the magnesium-based cladding (cans), nominally containing 0.80 wt% aluminium together with 50 ppm beryllium and used to house the

natural uranium (U-238) fuel rods [25]. These alloys were chosen because they underwent negligible corrosion during operation (250-450°C) in dry CO₂. Since magnesium-based materials have been successfully used in commercial nuclear reactors, this provides a strong basis to develop magnesium-containing coatings for fuel cladding in current nuclear reactors.

MgO-ZrO₂ oxide systems have been extensively studied before. Sniezek et al [217] produced MgO-ZrO₂ ceramics, the constituents of which were homogeneously mixed and pelletised before using conventional sintering and arc melting methods at 1400-1700°C to investigate the influence of these techniques on its structural properties. The XRD patterns showed dominant peak reflections attributed to the cubic phase, strongly indicating a phase transformation to cubic at 1400°C. However, the scope of the study was limited because it did not attempt to determine whether the cubic zirconia phase could be produced at lower sintering temperatures. A significant factor overlooked by this study is that the inclusion of Mg into ZrO₂ actually lowers the temperature required for cubic zirconia stabilisation to (no more than) 1400°C from 2370°C. This raises an interesting avenue of research to identify the lowest sintering temperature to allow c-ZrO₂ to form and could be taken a step further to investigate the sintering temperature range in which t-ZrO₂ forms, which could be well below the zirconia tetragonal-to-cubic transformation temperature of 2370°C.

MgO-ZrO₂ ceramics have also been studied previously for their potential use as inert matrix fuels (IMFs). This is a nuclear fuel system that replaces the fertile natural uranium (U238) component with a fertile-free matrix to eliminate the production of plutonium-239 (resulting from U238 decay) in the fuel system. Medvedev et al [219] showed that MgO-ZrO₂ ceramics containing at least 30 wt% MgO can form cubic-zirconia by solid solution substitution of Zr with Mg whilst having a higher thermal conductivity of ~16 W/(m.K) compared to uranium dioxide (UO₂) fuel (~7 W/(m.K)).

However, the use of Mg alloys are not fully exploited as much as their aluminium counterparts because of the issues related to corrosion which is particularly poor when exposed to chloride ions or aqueous environments, their susceptibility to wear [215] and low creep resistance; their low capacity for strengthening and poor ductility which have limited their use. Furthermore, the PBR of Mg/MgO is less than 1.0, so the oxide layer on Mg is not protective, since it cracks under tension. Research efforts have led to the development of improved corrosion-resistant Mg alloys with higher ductility [220]. Orlov et al [221] investigated the corrosion resistance of ZK60 Mg alloy (Mg-6Zn-0.5Zr in wt%) to determine whether grain size and chemical composition is a factor in controlling corrosion resistance. Corrosion tests were performed in a sodium chloride (NaCl) electrolyte. The author reported improvements in corrosion resistance of Mg alloys (compared to pure Mg) were linked to a reduction in average grain size (grain refinement) and redistribution of MgZn₂ and Zr₂Zn₃ intermetallic

precipitates at grain boundaries within the Mg alloy microstructure, giving rise to enhanced strength without adversely affecting ductility. The increase in corrosion resistance was attributed to the Hall-Petch type effect whereby grain boundaries act as insurmountable barriers to dislocation motion and hinders the onset of plasticity. Thus, smaller grains result in more grain boundaries that create opposition to dislocation motion and would require greater energy to overcome the diffusion barrier for dislocation movement and this in turn increases the yield strength of the material.

In another study, Zhang et al [222] reported improvements in corrosion resistance of Al-Zn-Mg alloy with Zr content up to 0.2 wt%. The alloy was produced by casting, hot rolling, cold rolling and finally annealed at 400°C for 2 hr. TEM investigations revealed that the addition of Zr to the alloy resulted in precipitates (tens of nm in size) that were uniformly distributed in the alloy matrix. Tensile tests revealed the Mg alloy containing Zr precipitates resulted in a higher yield strength and tensile strength of 24% and 9% compared to Zr-free alloy using. This was attributed to precipitation strengthening mechanisms that impede dislocation motion (i.e. precipitates within a lattice of a material creates physical blockades through which dislocations cannot pass thereby strengthening the material since a greater energy or stress is required to allow dislocation movement to occur to result in plastic deformation.

The ongoing corrosion issues surrounding magnesium, together with the widely differing melting temperature between Mg (650°C) and Zr (1850°C) [216], and the presumed inability to form intermetallic phases due to low solubility of magnesium in zirconium [111] have largely meant that coatings developed avoided the use of magnesium and instead most of the research conducted in this area has focused on using different elements to increase the corrosion resistance of magnesium alloys.

The Mg-Zr binary phase diagram is presented in Figure 1.14 [223] to establish the extent to which Mg and Zr might be soluble in each other. The phase diagram shows that zirconium solubility in magnesium is ~0.5 at% at 653.5°C. The Mg-Zr PVD coatings were produced using magnetron sputtering (Nordiko) PVD rig whereby the substrate temperature was about 225°C [224]. It can be seen from the phase diagram that Mg solubility in Zr is even lower at 0.01 at%. Although some studies have shown that zirconium solubility in magnesium alloys is ~0.5 wt% [223, 225], to the best of my knowledge, there is no available literature on the investigation and study of magnesium solubility in zirconium (and vice versa) or its alloys. Thus, the maximum concentration of magnesium that could be added to zirconium to remain in substitutional solid solution before phase separation occurs is not known. Traditionally, it has been difficult to alloy Zr with Mg, due to their widely differing melting temperatures, however, no such restriction exists with PVD coating methods, where the elements can

be sputtered directly from solid to gaseous form (and vice versa when condensed from ionised vapour onto a metallic solid substrate).

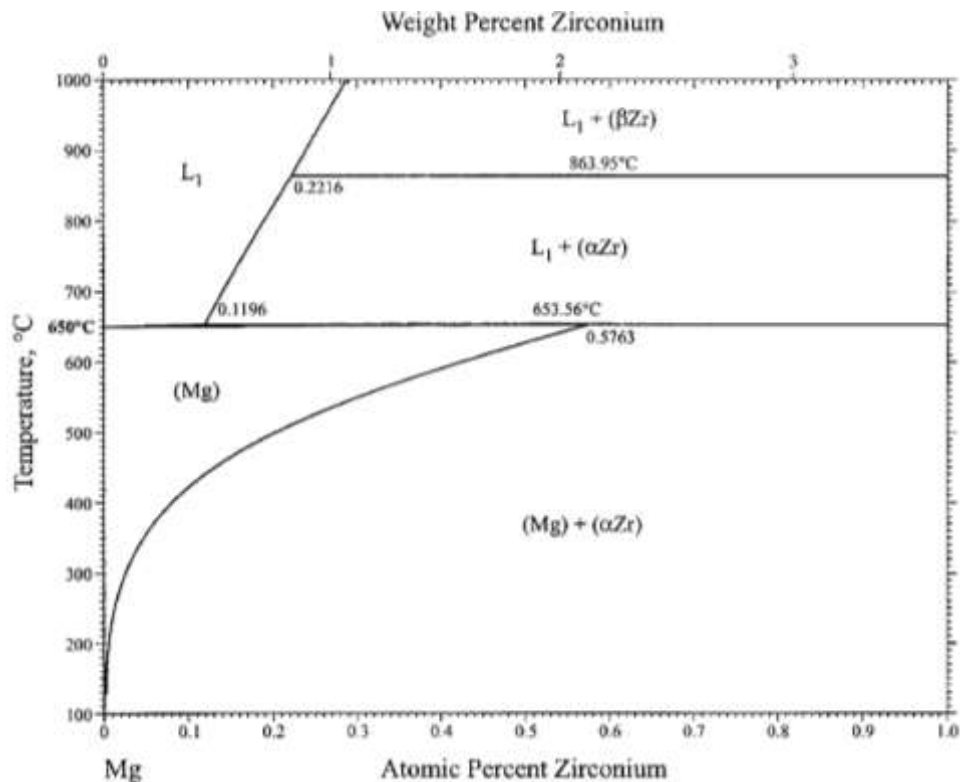


Figure 1.14: Magnesium-rich region of the Mg-Zr phase diagram [223].

1.13 Hume-Rothery Rules for Substitutional Solid Solution

The Hume-Rothery rules [226] are a set of criteria that describe the conditions under which an element (solute) could dissolve in a metal (solvent), forming a solid solution¹³. Solute atoms that have radii much smaller than the solvent atoms (i.e. $r_{\text{solute}} \ll r_{\text{solvent}}$) form interstitial solid solution¹⁴ with the solvent. Solute atoms that have radii that are comparable to that of the solvent atoms (i.e. $r_{\text{solute}} \approx r_{\text{solvent}}$) form substitutional solid solution with the solvent. For an element to be in substitutional solid solution¹⁵ with another element, there are several features of the solute and solvent atoms that determine the degree to which the former dissolves in the latter. These include:

¹³ Solid solution is where an alloying element in a material forms a single homogenous phase. The crystal structure remains unchanged by the addition of solutes.

¹⁴ Interstitial solid solution is where solute atoms occupy sites in the crystal structure where there's not usually an atom.

¹⁵ Substitutional solid solution is where solute atoms replaces the solvent atoms from its regular lattice site.

1. Crystal structure – for appreciable solid solubility, the crystal structures for metals of both atoms must be the same. In the case of magnesium and zirconium, both are hexagonal close-packed crystal structures.
2. Atomic size factor – the difference in atomic size should be less than 15% for complete solid solubility. If the atomic size is greater than 15%, it is less likely that the solute and solvent atoms would be in solid solution with each other. The ionic radius¹⁶ of Mg and Zr is 1.50 Å (150 pm) and 1.55 Å (155 pm) [216] respectively. The difference in the atomic size is therefore:

$$r_{Mg} = 1.50 \text{ \AA} \quad r_{Zr} = 1.55 \text{ \AA}$$

$$\Delta r = 0.05 \text{ \AA}$$

$$\text{Atomic size difference (\%)} = \frac{\Delta r}{r_{Zr}} \cdot 100 \quad (1.17)$$

$$= \frac{0.05 \text{ \AA}}{1.55 \text{ \AA}} \cdot 100\%$$

$$= 3.2\%$$

Where r_{Mg} is the ionic radius of Mg, r_{Zr} is the ionic radius of Zr and Δr is the difference in the ionic radius between Mg and Zr.

The difference in atomic size between Mg and Zr was calculated to be 3.2% which meets the second criterion.

3. Electronegativity¹⁷ factor – the more electropositive one element is compared to the electronegativity of the other element, the greater the likelihood that the elements will form an intermetallic compound instead of being in substitutional solid solution. Thus, the electronegativities of the elements (to be deposited) should be similar. Mg and Zr have similar electronegativity values of 1.31 and 1.33 [227] respectively.
4. Valency¹⁸ factor – if other factors are equal, a metal will have a stronger tendency to dissolve another metal of a higher valency than one of a lower valency. The solute and solvent atoms should typically have the same valence in order to achieve maximum solubility. The

¹⁶ Ionic radius is the radius of an atom's ion in ionic crystals. This is measured from bond lengths between molecules taking into account that atoms will be electrically charged.

¹⁷ Electronegativity describes the tendency of an atom to attract a shared pair of electrons towards itself. If atoms bonded together have the same electronegativity, the electrons will be equally shared. If the electrons of a bond are more attracted to one of the atoms (because it is more electronegative), the electrons will be unequally shared. If the difference in electronegativity is large enough, the electrons will not be shared at all.

¹⁸ The valency of an element is related to how many electrons are in the outer shell.

differences in the valency of Mg and Zr which is 2 and 4 respectively [216] could result in a tendency towards the formation of compounds rather than solid solutions. As a transition metal element, with partially filled d-orbitals, Zr is also multi-valent (e.g. in ZrN). Nevertheless, since Zr has a higher valency than Mg, one might argue that Mg should dissolve Zr more readily than vice versa. However, the implications of the differences between these two elements on solubility have not been commented on in the literature.

1.14 Structure Zone Model for Coating Growth

One of the objectives mentioned in Section 1.1 was to design a magnesium-containing zirconium PVD coating system to investigate whether the inclusion of Mg might stabilise the tetragonal or cubic phase of zirconium oxide (during hydrothermal oxidation) that is intended to delay oxidation and hence enhance the oxidation resistance of zirconium in aqueous conditions. This was achieved by sputter co-depositing Mg and Zr using an unbalanced magnetron sputtering PVD rig (see Chapter 2, Section 2.5 for details). It is useful to characterise the morphological evolution and growth behaviour of these coatings using Structure Zone Models (SZM) which have been used to classify the morphology of coatings deposited by PVD techniques.

The initial model proposed by Movchan and Demchishin [228] described the morphology of Ti, Ni, W, ZrO₂, Al₂O₃ and Fe coatings (with thicknesses ranging 0.3 to 2 mm) deposited by electron beam evaporation. The authors concluded that the coatings could be represented by three structural zones (Figure 1.15) each with its own characteristic structure and physical properties as a function of homologous temperature T/T_m , where T is the substrate temperature and T_m is the melting temperature of the deposited material, both in Kelvin.

In Zone 1, the coating microstructure and texture are controlled by the shadowing effects (arising from geometric interactions between the roughness of the growing surface and the angular directions of the arriving atoms). The adatom mobility is low leading to continued nucleation of grains. The resulting coating texture is an open-voided tapered fibrous structure with domed tops, which results from the low angle oblique incidence of the thermalized particles and the limited diffusion of adatoms on the substrate surface. The former is the result of the collision between the sputtered and discharge gas atoms during the sputtering of atoms from the target surface to the substrate and the latter is due to the low substrate temperature. There is also a high density of lattice imperfections and pores at grain boundaries. Zone 1 structure is observed when the homologous temperature $T/T_m < 0.3$ at discharge pressures < 0.5 Pa.

Thornton [169] further extended the Movchan-Demchishin (3-zones) model by recognising a transition zone between Zones 1 and 2 -referred to as Zone T. Zone T is essentially the limiting form of the Zone 1 structure at zero T/T_m on infinitely smooth substrates. Zone T structure is comprised of wider columns and flat surfaces. This is due to the further promotion of the thermally enhanced surface diffusion owing to an increase in the substrate temperature due to energetic atom bombardment. The promoted diffusion fills the void space between columns and the bombardment makes the column surface flat. However, the surface and bulk diffusion mechanisms are still limited because of the relatively low substrate temperature, resulting in an amorphous crystal structure. Zone T structures can be observed at $0.2 < T/T_m < 0.3$ at gas pressures < 0.5 Pa [229].

At the higher temperatures of Zone 2, surface diffusion is the dominant process leading to the formation of wider columnar grains with defined grain boundaries resulting in higher crystallinity. The grain size increases with T/T_m which may extend throughout the coating thickness. The surface ends of the grains lead to a faceted appearance due to different surface ad-atom mobilities along the surfaces of grains with different crystallographic orientation. In Zone 2, the coating properties are comparable to those of the bulk material mainly because of the tight spacings between columns. Zone 2 structure is observed at $0.3 < T/T_m < 0.5$ at gas pressures < 0.5 Pa [230].

At even higher temperatures of Zone 3, bulk diffusion and recrystallisation are the dominant processes for the formation of coating texture and internal structure. The spaces between the columns are narrower still and the internal thermal crystallisation of the columns occurs, leading to the formation of large equiaxed grains defined by grooved grain boundaries. Zone 3 structure is observed at $0.6 < T/T_m < 1$ at gas pressures < 0.5 Pa [230].

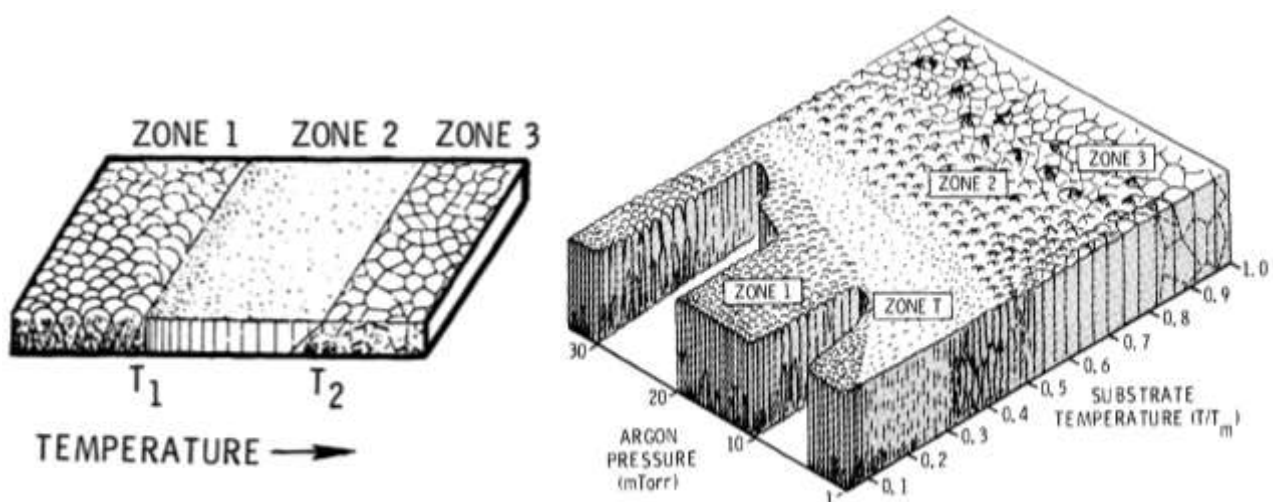


Figure 1.15: Structural zone models for coating growth: (a) Model proposed by Movchan and Demchishin [228] and (b) Model proposed by Thornton [169] for metallic coatings deposited by magnetron sputtering.

The homologous temperature T_h is given in the following expression [231]:

$$T_h = T/T_m \quad (1.18)$$

where T is the substrate temperature and T_m is the melting temperature of the deposited material, both in Kelvin. Using expression 1.18 to determine T_{h1} for *Mg coating* on Zr substrate, gives:

$$T_{h1} = \frac{498.15 \text{ K}}{923.15 \text{ K}}$$

$$T_{h1} = 0.54$$

Using expression 1.18 to determine T_{h2} for *Zr coating* on Zr substrate, gives:

$$T_{h2} = \frac{498.15 \text{ K}}{2128.15 \text{ K}}$$

$$T_{h2} = 0.23$$

The homologous temperature for Mg coating on Zr substrate (T_{h1}) was calculated to be 0.54. According to Thornton's Structure Zone Model, this lies within the range of Zone 2 and the structure formation of the coating is expected to be columnar with the surface expected to exhibit a faceted appearance. The same calculation was applied to Zr coating on Zr substrate and this yielded a homologous temperature (T_{h2}) of 0.23. This lies within the range of Zone 1 of the Structure Zone Model whereby narrow columns are expected with the surfaces expected to exhibit smooth domed appearance. It should be remembered however, that Mg and Zr were co-deposited to form a Mg-Zr PVD coating and therefore the actual values would be slightly different.

For sputtering systems, Thornton's argon gas pressure axis does have an influence on the energy of our depositing species (and thus the surface ad-atom mobility, re-sputtering effects and other phenomena that influence film structure, morphology and surface topography). Other authors have therefore further modified Thornton's model to take account of this, a significant example of this (in the context of the work performed in this thesis) being that of Messier et al [232] who proposed a revised structure zone diagram, with zones 1, T, 2 and 3, where the pressure axis is replaced by an ion energy axis. This took account the relative effects of bombardment and thermal effects as well as the evolutionary growth development of low mobility structures. Anders [233] extended the structure zone diagram to include parameters such as generalised temperature " T^* " which takes into account the potential energy of particles arriving on the surface; normalised energy, " E^* " which describes the displacement and heating effects caused by the kinetic energy of bombarding particles and " t^* " which is the net film thickness that allows the qualitative illustration of film structure.

The critical review of literature has revealed a number of noteworthy points:

- The exact mechanism of zirconium oxidation kinetics is still unresolved despite the litany of studies that have investigated this issue extensively. This information could be used to influence the design and development of surface-treated layer/coatings that act to target early oxide formation before accelerated oxidation kinetics that follow a linear rate law.
- Monoclinic zirconia has a higher propensity to exhibit a greater concentration of defects (i.e. crack propagation) within the oxide compared to tetragonal/cubic zirconia during oxidation. It has been suggested that this was due to the large lattice mismatch between the a , b and c lattice parameters of the monoclinic zirconia (during oxidation and subsequent oxide volume expansion of 3-5%) and the hexagonal close-packed structure of zirconium.
- To the best of my knowledge, the derivation of the Pilling-Bedworth ratio of zirconium oxide polymorphs has not been reported before. Most of the literature investigated simply quote a P-B ratio of 1.56 without specifying which oxide polymorph this was referring to. The associated oxide volume expansion of 3-5% is another figure that is commonly quoted in the literature without substantiating how this was derived. This study has shown that the P-B ratio of 1.56 quoted in literature is attributable to the tetragonal-ZrO₂/Zr system and appears to be an average of several different experiments that have reported on oxide development at different processing conditions. Furthermore, the oxide volume expansion calculated in this study was found to be consistent with the tetragonal to monoclinic zirconia transformation of ~5 vol% quoted in the literature.
- The formation of a hardened diffusion layer and a diffusion zone on a bulk metal surface using TPN diffusion treatments have been successfully used to show enhanced wear resistance properties on titanium but have not reported to show how this influences other properties such as corrosion resistance on zirconium. This treatment technique induces a change in the chemical composition of the existing surface via the interstitial diffusion of nitrogen in the Zr lattice and this provides a higher load-bearing capacity than separate coatings on a bulk surface.
- The production of coatings using additional alloying elements to stabilise a phase in an oxide layer is widely used for high temperature application such as jet engines, gas turbines and core components in the aerospace industry, however, to the best of my knowledge, despite the favourable properties of magnesium as an element, the addition of Mg in small quantities in zirconium to stabilise the tetragonal or cubic phase during oxidation for use in the nuclear industry has not been studied before.

Based on these findings from a critical assessment of the available literature, a summary of the experimental objectives are to:

- Design, develop and test surface-treated nitride layers (comprising of a nitride compound layer and a nitrogen diffusion zone) via TPN diffusion treatment to test the hypothesis that this treatment technique could be used to improve the oxidation resistance properties of zirconium and mitigate the evolution of hydrogen as a result of oxidation reactions.
- Design, develop and test magnesium-containing zirconium PVD coatings using magnetron sputter deposition and study if either of these elements are in solid solution with each other or form separate phases.
- Carry out hydrothermal oxidation tests on sputter co-deposited Zr-Mg coatings (with increasing Mg concentration in the coating) to investigate if tetragonal or cubic zirconia could be stabilised and determine oxidation resistance of the coated surface compared to uncoated zirconium.

Chapter 2 – Experimental Methodology

2.1 Micro-preparation of Samples

Bulk zirconium sheet of 1.0 mm thickness (Advent-RM, 97% purity and temper annealed) was used as the substrate for the TPN diffusion treatment and sputter deposition. The material was cut into substrates of dimensions 20.0 mm x 20.0 mm using a Buehler precision saw with oil lubricant to minimise the effects of mechanical deformation (i.e. twinning). The Zr substrates were mounted in conductive bakelite, then ground using silicon carbide (SiC) paper of decreasing grit size (Table 2.1) and polished using Buehler Automet® with MetaDi Diamond Suspension to reveal the microstructure.

Since this work investigates oxidation resistance of TPN-treated and sputter-deposited zirconium in aqueous environments, it is important to use a water-free solution during polishing stages to avoid potential oxide growth, and ensure the surface is as clean as possible prior to TPN diffusion treatment. An oil-based solution was thus used which has a high synthetic polycrystalline diamond concentration.

An automatic grinding and polishing regime was adopted for this work. The advantage to using this technique as opposed to manual grinding (by hand) is that it minimises bevelling effects. The Zr substrates were ground using silicon carbide (SiC) abrasive papers down to 1200 mesh size ($15.3 \pm 0.5 \mu\text{m}$). The substrates were then polished down to $3 \mu\text{m}$ on Trident cloth, followed by Colloidal silica (Silco - $0.05 \mu\text{m}$) before being ultrasonically cleaned in acetone, rinsed with isopropanol (IPA) to remove remnants of silco on the Zr substrates and dried.

Table 2.1: Procedure for grinding and polishing of bulk Zr metal.

Pad	Solution	Platen speed (rpm)	Rotation	Duration (min)
P800	Water	270	Comp	2
P1200	Water	270	Comp	2
Ultrapad	9 μm (diamond in oil)	200	Contra	3
Ultrapad	6 μm (diamond in oil)	170	Comp	3
Trident	3 μm (diamond in oil)	150	Contra	3
ChemoMet	1 μm (diamond in oil)	150	Comp	5
ChemoMet	Silco	130	Contra	7

2.2 Optical Light Microscopy Imaging

Optical (visible light) microscopy uses reflected light (from the sample) and an array of lenses to magnify images of samples being observed. The objective lens magnifies the image and is observed through the eyepiece. The condenser lens focuses the light from the light source (illuminator) onto a sample (on a small area). The sample is mounted on a movable stage and a combination of coarse and fine focus adjustments can be used to resolve the images with objective lens ranging x5, x10, x20, x50 and x100 magnification where applicable. In this study, a Nikon Eclipse LV 150 optical microscope was used to investigate the surface morphology and the microstructure of bulk HCP α -zirconium metal and TPN diffusion-treated surfaces. The advantages of this technique include: minimal sample preparation, relatively quick and easy to use and low cost. The disadvantage is that the depth of focus decreases with increasing magnification and the resolving capabilities are limited by the wavelengths of visible light (400-700 nm [234]).

2.3 Ion Beam Polishing

Etching of the pure untreated zirconium substrate and cross-section of the plasma-nitrided zirconium samples were performed using ion beam milling (Gatan PECS II) to remove further defects following mechanical polishing using argon ions to achieve a mirror-like finish on the sample, thus revealing a true representation of the sample itself. The advantage of this technique is that the variable angle milling can be adjusted to selectively enhance surface features such as grains. The samples were securely screwed in place in the sample holder and the etching was conducted with an energy of 5 keV at an angle of 4° for a duration of 1 hr. Once the process was finished, the samples were collected from the machine. Analysis of the grains of transition metals (such as Zr and Ti) can be challenging when using optical microscopy following mechanical polishing. Such sample surfaces have traditionally been etched using hydrofluoric (HF) acid or other fluorine-containing solutions as a pickling agent which serve as primary oxide removers. However, HF is a highly corrosive etchant that is difficult/dangerous to handle, and ion beam milling was found to be a suitable alternative to reveal grain structure of these metals.

2.4 Triode Plasma Nitriding Diffusion Treatment

Zirconium substrates were diffusion-treated by Triode Plasma Nitriding in a modified Tecvac IP70L commercial PVD coating unit (Figure 2.1) [235], using a low pressure d.c. triode configuration. The zirconium substrates were sectioned, ground and polished according to the micropreparation regime described in Section 2.1. These substrates were ultrasonically cleaned with acetone, then isopropanol

and finally dried under warm flow of air. Holes were drilled at one the corner of each substrate which were then suspended by a wire inside the chamber.

The modified Tecvac machine is a derivative of the electron-beam physical vapour deposition (EB-PVD) process adapted for high temperature ($\geq 500^{\circ}\text{C}$) plasma-diffusion treatment. The chamber is grounded and served as the anode for the discharge whilst the Zr substrates and holding fixtures formed the cathode. Plasma enhancement was provided by an electron-emitting heated tungsten filament positioned near the base of the chamber. Once the substrates were mounted and the chamber door was closed, the pressure inside the chamber was reduced of 2.0×10^{-5} mbar to remove residual gas (i.e. oxygen). Additional radiant heating was provided by the heating elements (mounted inside near the chamber walls). The zirconium substrates were negatively biased with 600 V to aid sputter cleaning (of the substrates) using argon gas which was introduced inside the chamber at a flow rate of 140 ml/min and this was carried out for 20 minutes. Following sputter cleaning, the argon gas flow rate was reduced to 80 ml/min and the substrates were negatively biased with 200 V. The tungsten filament (located at the base of the chamber) was resistively-heated by passing alternating current through it, which resulted in Ar plasma being intensified (due to energetic electron emission from the filament) which heated the samples to the desired process temperature of 700°C . The process gas (nitrogen) was injected into the chamber at a low pressure of 4.0×10^{-3} mbar (0.4 Pa).

The triode-enhanced plasma-diffusion treatments were carried out for 1.5, 2, 3 and 4 hours in a mixture of 70% partial pressure of nitrogen and 30% partial pressure of argon at a treatment temperature of 700°C where the samples were held to maximise interstitial diffusion rates whilst not driving the Zr microstructure through the $\alpha \rightarrow \beta$ transition which occurs at $810\text{-}865^{\circ}\text{C}$ [236], or causing grain growth that could diminish the core strength of the Zr substrate. This is further aided by additional radiative heating elements which surround the inside of the chamber walls. The temperature is slightly lower with increased height from the bottom of the chamber because the electron impact ionisation tails off exponentially with distance from the tungsten filament, thus the plasma intensity diminishes with height in the chamber. A thermocouple positioned near the samples provides a means to continuously monitor the substrate temperature during treatment process whereby the relevant parameters to reach the desired operating temperature can be adjusted and controlled accordingly. Following the desired TPN treatment duration, the power supplies, gas supplies and radiant heating were switched off and the chamber was left to cool to a temperature less than 150°C . The chamber was then vented and the TPN-treated samples were collected.

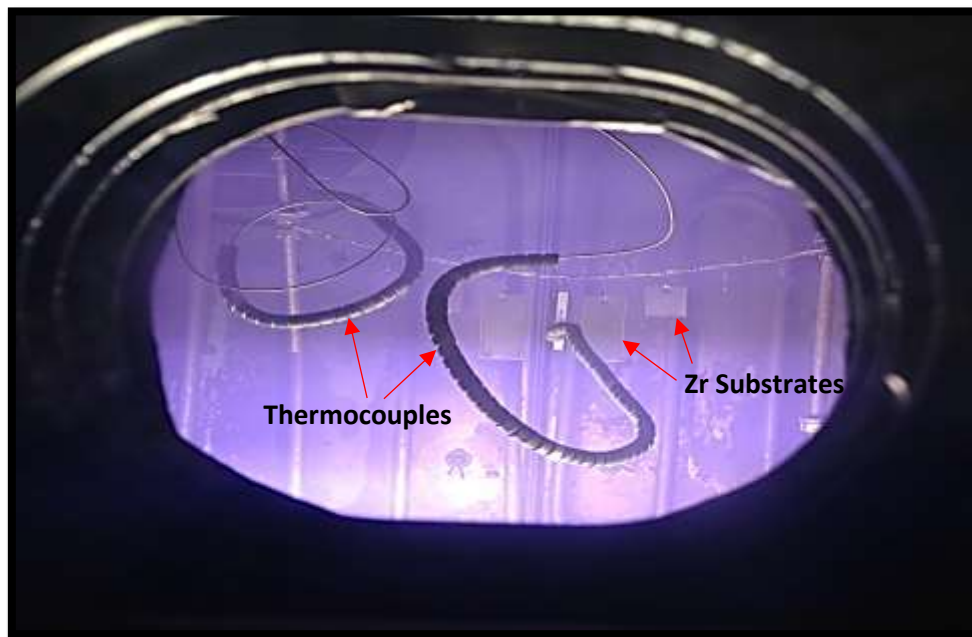


Figure 2.1: Internal view of the chamber showing Zr substrates, and the attached thermocouples in an aura of plasma (purple) during TPN process.

2.5 Sputter Deposition

Sputter deposition is a PVD process which involves a target (cathode) that is bombarded by energetic ions (usually argon ions) generated in a glow discharge plasma that is situated in front of the target. The bombardment of these energetic ions against the target results in the ejection (i.e. sputtering) of target atoms which may then deposit onto the substrates as a coating [237]. During the bombardment process, secondary electrons from the target are emitted which play an important role in maintaining the plasma. Magnetrons (situated behind the target) make use of magnetic fields that act to constrain the secondary electron motion to the vicinity of the target. The magnets are arranged such that one pole is positioned at the central axis of the target and the second pole is formed by a ring of magnets around the outer edge of the target. This increases the probability of ionising electron-atom collisions occurring and hence increases the ionisation efficiency – resulting in a dense plasma (at the target region) which in turn, leads to an increase in ion bombardment of the target, giving higher sputtering rates and therefore, higher deposition rates at the substrates [238]. The increased ionisation efficiency achieved through the use of magnetrons allows the discharge plasma to be maintained at (i) lower operating pressures (10^{-3} mbar compared to 10^{-2} mbar) and (ii) lower operating voltages (-500 V compared to -2 kV) than without using magnetrons. Sputter deposition is a commonly used technique as it results in high purity, dense and stoichiometric coatings that are critical to its functionality [239].

In this study (see Chapter 5), magnesium-containing zirconium coatings were produced using an unbalanced magnetron sputtering (Nordiko) PVD rig. In an unbalanced configuration (Figure 2.2), the outer ring of magnets is strengthened relative to the central pole. This means that not all the field lines are closed between the central and outer poles of the magnetron, but some are 'open' allowing secondary electrons to follow these field lines. The plasma in this case is no longer confined to the target region (as would be the case in a 'balanced' magnetron configuration) and is allowed to flow out towards the substrate. Thus, high ion currents ($>5 \text{ mA/cm}^2$) can be drawn from the plasma without the need to apply excessively high bias voltages to the substrate.

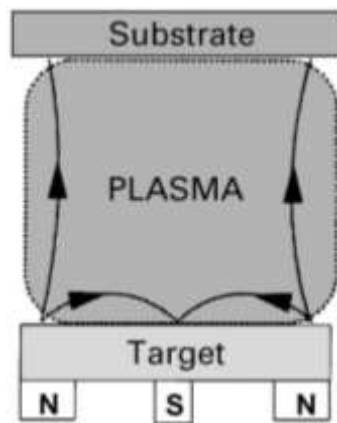


Figure 2.2: Schematic of an unbalanced magnetron configuration.

The configuration of the deposition chamber, target segments and substrates are shown schematically in Figure 2.3. Two Zr target segments (127 mm x 100 mm x 6 mm) at the middle and bottom and one Mg target segment (127 mm x 100 mm x 6 mm) at the top were used (with a total target area of 381 x 100 mm). Polished AISI 316 stainless steel substrates (20 mm x 10 mm x 2 mm) were positioned in parallel with polished Zr substrates (20 mm x 10 mm x 1 mm) and fixed onto the sample holder which was placed 15 cm from the Mg and Zr targets. The stainless-steel substrates served as references to reliably determine Zr and Mg concentrations coating (during GAXRD and EDX spectroscopic analysis) thereby minimising contribution from the underlying Zr substrate. All substrates were ultrasonically cleaned using acetone and then isopropanol for 15 minutes and dried under pressurised flow of warm air. The Zr and Mg target segments were gently cleaned using isopropanol prior to each coating run remove impurities such as oxygen contamination. The coating chamber was evacuated to approximately 2×10^{-5} bar (2×10^{-3} Pa) base pressure.

Prior to deposition, the substrates were sputter cleaned using argon ions at an argon pressure of 3.3×10^{-2} mbar (3.3 Pa) and a flow rate of 54 sccm and substrate negative bias voltage of 500 V for 30 min. Then the argon pressure was adjusted to 4.8×10^{-3} mbar (0.48 Pa) at an argon flow rate of 12.5 sccm for the following target sputter cleaning process which was carried out for 15 minutes. A rotatable

shutter was placed in between the substrate holder and the target cleaning process to inhibit possible contamination (from the targets to the substrates). Following the sputter target cleaning process, the argon flow rate of 12.5 sccm and working pressure of 4.8×10^{-3} mbar (0.48 Pa) were maintained and the substrates were negatively biased to 150 V with a DC-pulse frequency of 250 kHz, whilst the power to the targets were initially 600 W and then increased to 700 W (at a pulse frequency of 80 kHz). Magnesium and zirconium were sputter co-deposited for a duration of 3 hours to obtain full coating coverage of the substrates. Following deposition, the power supply to target and argon inlet supply were shut down and the chamber vented. Approximately 1 hour was awaited before the coated samples were collected from the chamber.

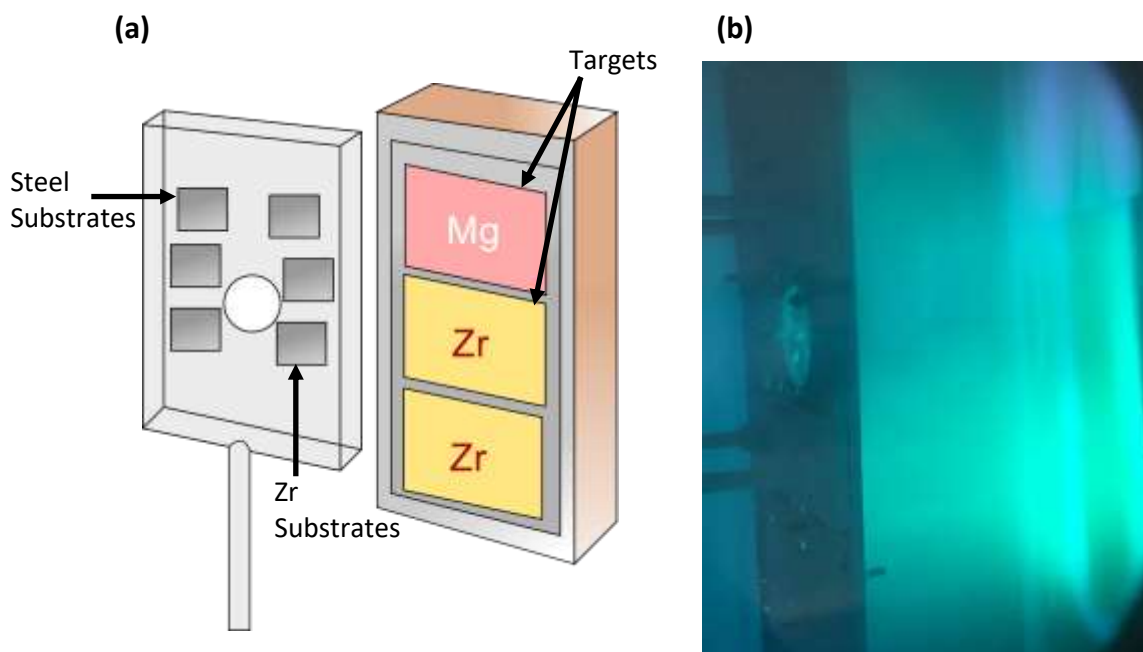


Figure 2.3: (a) Schematic drawing target-substrate arrangement in deposition chamber and (b) plasma glow during operation.

One of the effects on the targets during sputter deposition was the formation of 'racetrack' erosion on both Zr and Mg targets. This occurs as the electric field (E) and the magnetic field (B) are applied perpendicular relative to one another, and the E field intensity decreases with increased distance from the surface. The magnets are typically placed underneath the cathode surface, which allows the magnetic field to traverse radially. This configuration allows the $E \cdot B$ drift to form a circular path over the target surface and this is due to the circular magnetic field of the magnetron focussing the charged plasma species close to the surface of the sputter target resulting in 'racetrack' erosion. However, due to the higher sputter yield of Mg (1.7) relative to Zr (0.7) for a given applied power, the Mg target segment (see Figure 2.4a) was seen to have undergone greater erosion compared to the Zr target segments (See Figure 2.4b) with visual evidence of grain growth due to plasma bombardment heating

in the former. Furthermore, the single array configuration of the targets unavoidably resulted in cross-sputtering of Mg onto Zr, illustrated by the black oxide 'patches' which were subsequently cleaned prior to each run to optimise deposition. Overall, the main disadvantage of this technique is that the target is eventually consumed during the process before having to be replaced, which is dependent on the target power applied, density of the targets, sputter yield and the number of sputter-deposition runs undertaken, to name a few.

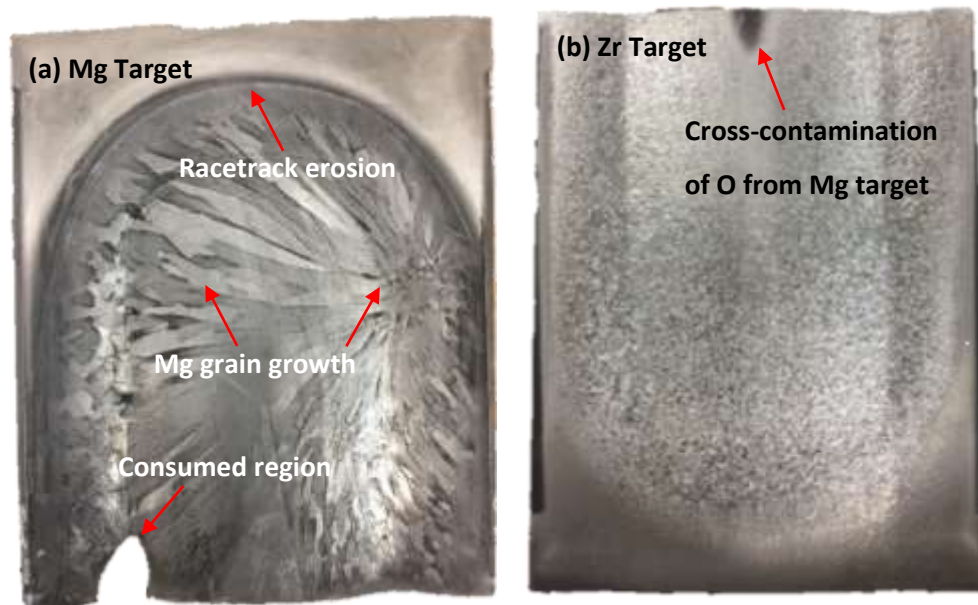


Figure 2.4: (a) Mg target exhibited high material consumption when power was set to 850 W compared to (b) Zr target. Both targets exhibited 'racetrack' effects during sputter deposition but Mg target segment displayed greater erosion due to having a higher sputtering yield relative to the Zr target segment.

2.6 Fundamental Concepts in X-ray Diffraction (XRD)

The short-wave electromagnetic nature of X-rays makes them capable of interacting with materials at the atomic scale. X-rays have short wavelengths approximately equal to the interatomic distance in crystals (1 to 2 Å) and the regularly spaced atoms act as scattering slits for X-rays resulting in a diffraction pattern. When an X-ray beam interacts with an atom, the electrons around the atom oscillate with the same frequency as the incident beam. In most directions destructive interference will occur, where waves are out of phase. In a crystalline material, few directions will have constructive interference which would be the case if the effective path difference of the interference waves being reflected by different planes of a crystal is equal to an integer number of wavelengths, or equal to $2d\sin\theta$, where d is the interplanar distance and θ (2θ) is the incident (and reflected) wave angle (Figure

2.5). This is known as Bragg's law (Equation 2.1) which relates the spacing of the lattice planes to the angular position of diffraction lines, when using monochromated X-rays:

$$2d\sin\theta = n\lambda \quad (2.1)$$

Where n is an integer and λ is the wavelength of the incident beam. X-ray diffraction is based on the detection of the diffracted X-rays once this criteria for Bragg's law is satisfied.

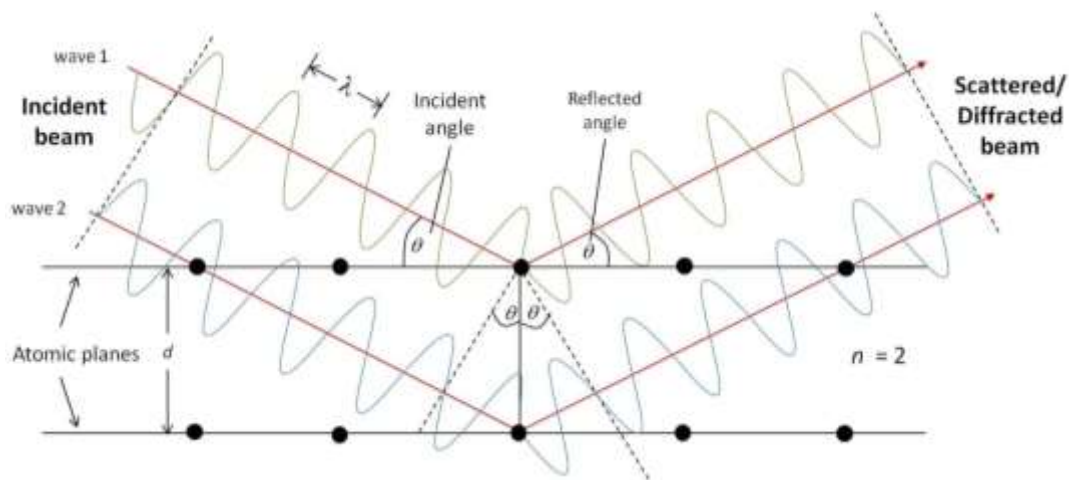


Figure 2.5: Schematic of diffraction of X-rays by a crystal lattice (adapted from Pecharky et al [240]).

2.6.1 Diffractometer Geometry

X-ray diffraction studies are carried out in a diffractometer, where X-rays are produced when high energy charged particles (i.e. electrons), are accelerated through several tens of kV and collide with solid matter. The high energy electrons are produced by heating a tungsten filament cathode in a vacuum sealed X-ray tube which generates the X-rays ($K\alpha$ radiation). The intensity (counts per second) of the diffracted beam is measured by the X-ray detector. The diffractometer also has a monochromator and slits which define and collimate the incident and diffracted X-ray beams. The X-ray source, X-ray detector and sample holder rotate independently, and the advantage of this arrangement is the capability to use various measuring methods. These are held in place by a goniometer which moves at small angular steps (i.e. 0.01°) and stops at each position for a few seconds whilst the diffracted X-rays are counted (from the sample that is mounted at its centre). This is repeated until the user-defined 2θ range is completed. A pattern of the discrete measurements is

produced showing intensity versus 2θ . The diffraction data is compared to a database of patterns known as powder diffraction file (PDF) in order to determine the phase of the material formed.

The beam of high energy electrons is accelerated to strike a target, often copper (Cu). The incident electrons with sufficient energy ionise some of the atoms, releasing Cu 1s (K shell) electrons. An electron in one of the outer orbitals (2p or 3p) occupies the vacant 1s level and the energy released in the transition is manifested in the form of X-rays. The transition energies have fixed values and so display certain characteristic results in terms of X-ray wavelength. For Cu, the 2p \rightarrow 1s transition (called $K\alpha$), yields an X-ray wavelength of 1.54051Å and the 3p \rightarrow 1s transition (called $K\beta$), 1.3922Å. The $K\alpha$ transition is more frequent and more intense than $K\beta$ and so it is used most often in diffraction experiments. $K\alpha$ in fact, has 2 wavelengths $K\alpha_1$ and $K\alpha_2$ corresponding to 1.54051Å and 1.54433Å respectively.

The scattered (diffracted) X-rays (from the sample) exit through a beryllium window to the receiving end of the detector and are converted to electrical signals that are displayed onto a screen as an X-ray diffraction pattern. It is called a pattern and not a spectrum because a spectrum implies energy change (see Raman spectroscopy section 2.7) whereas XRD is the scattering of X-rays measured as the intensity as a function of diffraction angle 2θ . Though Cu is commonly used, other metals such as molybdenum, chromium, cobalt (amongst others) which have different $K\alpha$ values relative to Cu can also be used [241]. The $K\alpha$ and $K\beta$ are represented by defined monochromatic peaks, caused by the electronic transitions within the atoms. This is an inefficient process in that only a small fraction of the incident electron beam is converted into X-rays upon interaction with the target material. Most of the energy is converted to heat and so the anode to which the Cu is fixed must be continuously cooled to avoid it melting. Often, a single crystal monochromator can be used to obtain monochromatic X-rays (e.g. Cu- $K\alpha_1$).

2.6.2 Glancing Angle X-ray Diffraction

Glancing angle (or grazing incidence) XRD is an important development of classical XRD - especially its increasing use in the evaluation of thin layers and coatings produced in surface engineering of materials. It is difficult to accurately determine the phases formed in films and coatings using the conventional (symmetrical, θ - 2θ) Bragg-Brentano configuration, since this tends to produce low diffracted intensities from the treated surface and higher intensity peaks from the substrate, due to the high Penetration Depth of X-rays in materials (that increases with the angle of incidence), which can generally exceed the thickness of the treated surface/coating. It is more convenient to use the X-ray diffraction technique at glancing angle (Seeman-Bohlin configuration) to minimise contribution (of phase detection) from the substrate. In this geometry, shown in Figure 2.6, the X-ray incident theta-

angle is fixed to a small value, and only the angle between the incident beam and the diffracted beam (2θ) is varied, moving just the detector arm. Thus, the incident beam is focused in (and the diffracted signals predominantly arise from) a limited depth from the surface, reinforcing its diffraction pattern from the treated surface/coating, while the signal from the substrate is reduced due to the small angle of incidence and reduces the penetration of X-rays into the surface (to typically only a few microns), compared to the standard θ - 2θ diffraction (typically several tens of microns). Under these conditions, the depth of analysis does not depend on 2θ , but is controlled by the angle of incidence. However, care must be taken with data interpretation – since a fixed angle of incidence may cause only a limited number of lattice planes to be sampled. This is particularly important for coatings analysis, where a strong preferred texture (i.e. crystallographic orientation) often occur. During the collection of the diffraction pattern, only the position of the detector is changed and the incident angle and beam path length are kept constant. At low incidence angles, the X-rays penetrate only the treated layer/deposited coating of a sample.

GAXRD studies for this work were performed with a X'Pert³ Diffractometer (Philips Panalytical, the Netherlands) (Figure 2.6) using monochromated Cu K α_1 radiation ($\lambda=1.54056 \text{ \AA}$) operated in a Seeman-Bohlin geometry to investigate the phase structure of the diffusion-treated TPN samples, sputter-deposited coatings and the hydrothermally oxidised samples. The tube acceleration voltage and current used were 40 kV and 30 mA respectively. The scans were acquired with data collected over a 2θ range of 25° to 80° with a step size of 0.02° , and at incident angles of 2° , 4° and 6° . Bulk untreated materials such as polished Zr substrates were scanned using Bragg-Brentano θ - 2θ geometry. The crystalline phases present were determined by peak fitting the resultant pattern using PDF4+ software, i.e. comparing the angular positions of peaks to those reported in PDFs from the International Centre for Diffraction Data (ICDD) [242] which were used for the identification of phases. The Penetration Depth of the X-rays at a given incident angle into the nitride layer was calculated using the Beer-Lambert law in AbsorbDX software, to indirectly infer thickness of the TPN-treated layer and oxide scales.

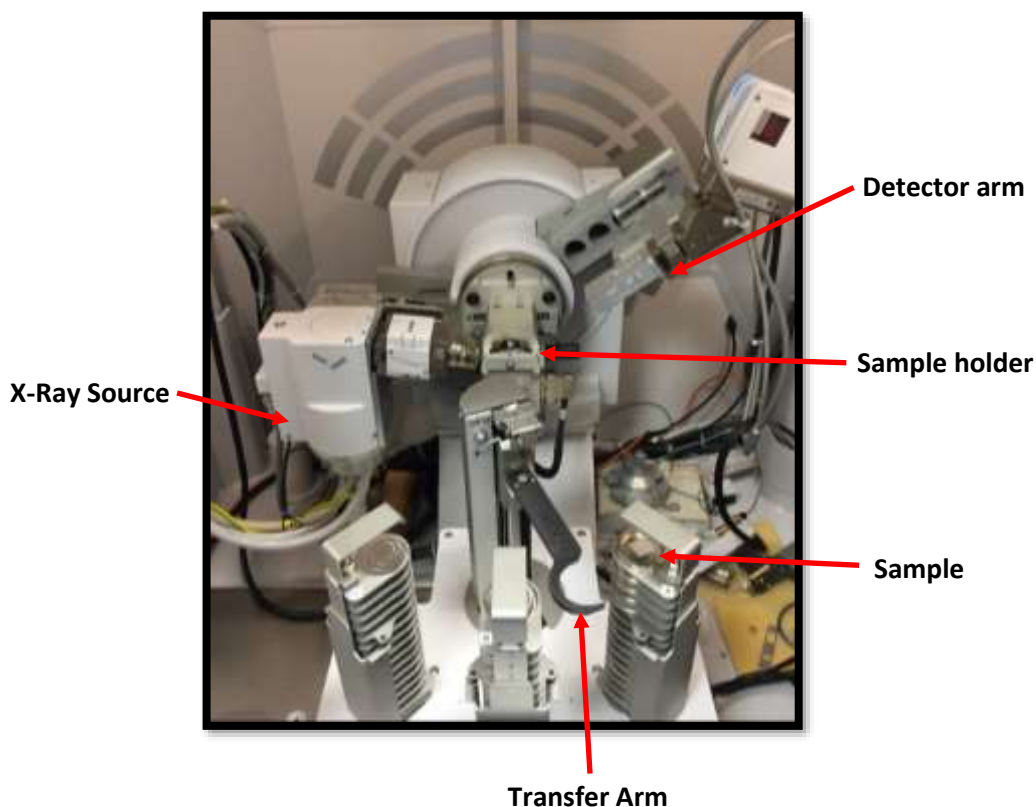


Figure 2.6: Philips Panalytical X'Pert3 (Netherlands) was used to carry out GAXRD experiments at the XRD facility, The University of Sheffield.

2.7 Vibrational Modes using Raman Spectroscopy

Raman spectroscopy is a technique based on the analysis of light inelastically scattered from a sample surface, produced by vibrational interaction of the light with inter-atomic bonds of a material. It occurs when a photon excites a sample molecule in a certain vibrational state to a higher virtual state which then drops down to a lower energy level which is at a slightly higher point than the initial energy level. This shift in wavenumber or frequency is known as the Raman shift.

When an incident monochromatic light interacts with an electron in a sample, the electron absorbs the energy from the incident photon and it rises to a virtual energy state¹⁹. The energy transferred E , is given by the following formula:

$$E = h\nu_i \quad (2.2)$$

Where h is Planck's constant ($6.63 \times 10^{-34} \text{ Js}^{-1}$) and ν_i is the frequency of the incident photon. The electron falls back to a lower energy state by losing energy. If the energy lost equals the energy of the incident photon (i.e. $h\nu_i = h\nu_s$, where ν_s is the frequency of the scattered photon), the electron falls

¹⁹ The virtual state is the energy of the laser.

back to its initial energy level and emits a photon (Figure 2.7(a)). Since the energy lost is equivalent to the energy of the incident photon, the released photon has the same frequency as the incident photon (i.e. $\nu_i = \nu_s$). This is known as Rayleigh scattering and is an example of elastic scattering. Majority of the light that interacts with a sample occurs via this mechanism. However, when electrons lose energy from the virtual state, they can also fall back to a different energy level. In this case, the energy lost by the electron is different to the energy absorbed from the incident photon (i.e. $h\nu_s \neq h\nu_i$). Thus, the photon emitted by the electron has energy that is different to the incident photon which is possible since the emitted and incident photons have different frequencies. This gives rise to Raman scattering (Figure 2.7(b)) and less than 1% of the total scattered intensity occurs via this mechanism.

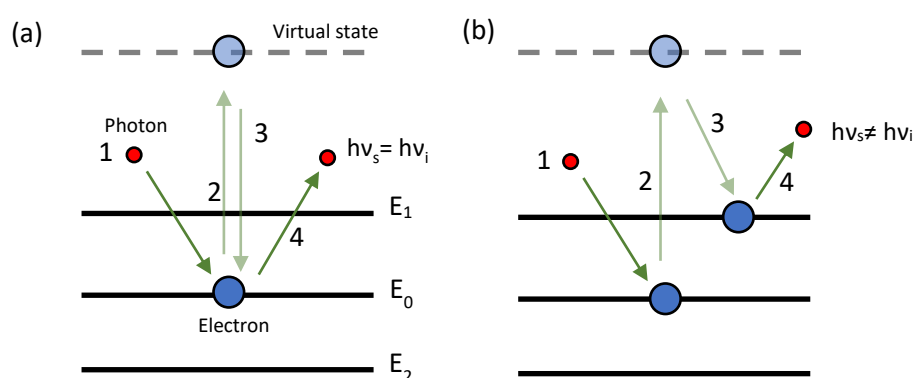


Figure 2.7: Schematic of the energy level diagram showing (a) Rayleigh scattering and (b) Raman scattering.

Light from the area under analysis is passed through a set of lenses and a monochromator (analyser), and a plot of the intensity of the scattered light versus the frequency shift results in a Raman spectrum of the sample.

The Raman frequency shift (cm^{-1}) is calculated using the following equation:

$$\bar{\nu} = \frac{1}{\lambda_{inc}} - \frac{1}{\lambda_{scat}} \quad (2.3)$$

Where λ_{inc} and λ_{scat} are the incident and scattered wavelengths respectively. Raman active bands of the diffusion-treated TPN samples and hydrothermal autoclaved samples were determined (from which phases were deduced by comparison with the literature) using a Renishaw inVia Raman microscope with 514 nm laser. Spectral analyses were performed using the Renishaw WiRE software, supplied with the spectrometer. The frequency shift acquisition was taken from 0 to 1000 cm^{-1} with the spectrum adjusted to minimise the effects of cosmic background radiation. The Raman active bands shown as peaks relate to the energies for the detection of molecular interatomic bond

vibrations within a sample i.e. the frequency shifts are characteristic of certain interatomic bonds (that can be inferred to be those between particular, often different elements).

2.8 Determination of Surface Roughness

Optical profilometry uses wave properties of a light to compare the optical path difference between the substrate surface and the reference surface. Inside an optical profiler, a light beam is split – reflecting half the beam from the substrate which is passed through the focal plane of the objective and the other half of the split beam is reflected from the reference mirror (Figure 2.8). When the distance from the beam splitter to the reference mirror is the same distance as the beam splitter is from the substrate and the split beams are recombined, constructive and destructive interference occurs in the combined beam wherever the length of the light beams vary. This generates light and dark bands known as interference fringes. Since the reference mirror is of known flatness, the optical path differences are due to the height variances of the substrate. The interference beam is focused into a digital camera whereby the lighter fringes result from constructive interference darker fringes result from destructive interference. In an interference image, each transition from light to dark represents one-half of a wavelength of difference between the reference path and the substrate path. If the wavelength is known, it's possible to calculate the height differences across a surface from which a 3D coloured map of the surface could be obtained.

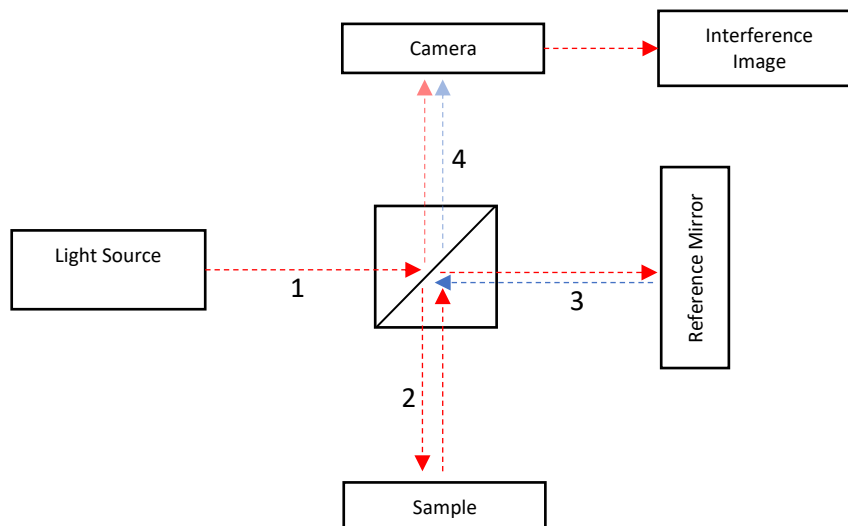


Figure 2.8: Schematic of the process for generating an interference image using optical profilometry. In this study, a Veeco-Dektak 150 scanning stylus optical profilometer was used to map the surface topology and to compare surface roughness of the pure Zr substrates, TPN-treated samples and hydrothermally oxidised samples. Surface roughness information would be useful to investigate the effect of increasing TPN treatment time on pure zirconium substrates and how the surface roughness

varies following hydrothermal oxidation in a high pressure/temperature environment. The microscope consists of a module which provides green and white illumination, a scanner assembly and a measurement objective. Five measurements each at random positions were recorded to calculate an average surface roughness R_a value. High-definition 3D surface maps were obtained from many scans (>200), which were analysed using Vision 3D analysis software. The parameters used for calculating surface roughness included back-scan: 25 μm ; length: 50 μm ; Threshold: 5% with a 10x magnification on the objective lens.

2.9 Determining Surface Morphology and Elemental Composition using Scanning Electron Microscopy (SEM) and Energy Dispersive X-ray Spectroscopy (EDX)

Scanning electron microscope (SEM) is a type of electron microscope that produces images of a sample by scanning the surface with a focused beam of electrons. It is used to study the morphology of specimens and can achieve a resolution better than 1 nm. The following is a brief description of the operation of an SEM. The instrument comprises of an electron gun consisting of a thermionic cathode (typically a tungsten filament²⁰) which is heated by an electric current and emits electrons in the column chamber that is under high vacuum ($\sim 5.0 \times 10^{-5}$ Pa). Beneath the electron gun is an anode which is connected to the positive pole of a high voltage source and attracts the negatively charged electrons. The electric field between the anode and cathode accelerates these primary electrons downwards (typically with an acceleration voltage ranging from 1 to 50 kV). This forms a broad diverging electron beam. An electromagnetic condenser lens and objective lens finely focuses the electron beam on the specimen surface and scanning coils (located above the objective lens) are used to adjust the position/direction of the electron beam onto the sample.

As the incident primary electrons strike the surface, electrons of the specimen surface atoms are released, known as secondary electrons (SE). These are low energy electrons (<50 eV) that are ejected from the conduction or valence bands of the sample via inelastic scattering interactions with the beam electrons. Thus, SEs originate from the top few nanometers from the sample surface and are detected by an SE detector. The basic principle of the SEM is however, primarily to detect the secondary electrons to build up a high-resolution image of the sample surface. To increase the number of secondary electrons detected, a positively biased grid is placed in front of the detector which attracts the secondary electrons and is detected by the SE detector which generates a magnified image of the sample.

²⁰ Tungsten is used as it has a high melting point allowing it to be electrically heated for electron emission and because of its low cost.

Primary electrons can also be scattered from the sample and are known as backscattered electrons (BSE) which are higher energy electrons. Secondary electron detectors are inefficient at detecting BSEs because (i) few electrons are emitted in the angle at which the detector is subtended and (ii) the positively biased grid has little ability to attract the higher energy BSEs. Thus, dedicated BSE detectors are positioned above the sample. Since heavier elements (high atomic number) backscatter electrons more strongly than lighter elements (low atomic number), they appear brighter in the image.

The raster scan directs the beam onto a part of the sample and the number of electrons is recorded in the SE detector, the signal is amplified and is displayed as a dot in the top corner of a display monitor. The electron beam adjusts slightly to the next point and stops again, and the measurement is repeated. Primary electrons arriving at low incidence angles will release many SEs compared to normal incidence angles. The bright and dark regions represent the topography of the surface that the electrons are scanning. This is continued until an image appears on the monitor.

X-rays are also emitted when an electron beam removes an inner shell electron from the sample (resulting in an unstable state), causing a higher energy electron on the outer shell to fill the inner shell. This releases energy in the form of X-rays that is characteristic to each element²¹. The energy and intensity of the X-rays is measured by an X-ray detector, from which the elements present in the sample can be determined with appropriate calibration standards of known composition.



Figure 2.9: Philips SEM XL30 was used to analyse the surface morphology.

²¹ It is characteristic because each element has a unique set of energy levels – and so the transition from higher to lower energy levels produces X-rays with frequencies that are characteristic to each element.

In this study, scanning electron microscopy (SEM) (Philips XL30 (Figure 2.9)) (field emission gun) was used to carry out morphological and elemental composition analysis of the diffusion-treated TPN Zr layers, sputter-deposited Zr-Mg coatings and the hydrothermally oxidised samples. An accelerating voltage of 15-20 kV with samples positioned at a working distance of 15 mm was used and SEM micrographs were generated in secondary electron (SE) and backscattered electron (BSE) mode. An Energy-dispersive X-ray (EDX) detector was used in conjunction with INCA software for qualitative and quantitative analysis with samples positioned at a working distance of 7 mm.

2.10 Nanoindentation

Indentation techniques such as Rockwell, Vickers, Brinell and Knoop are used to determine the hardness of mostly bulk materials. However, the increasing use of treated layers/coatings necessitates the use of lower indentation loads. This is because it becomes increasingly difficult to make accurate indentation measurements of mechanical properties without introducing contributions from the underlying substrate. Low load instrumented indentation methods allow accurate measurement of hardness as well as other material properties such as elastic modulus, something the conventional microhardness tests (i.e. Vickers) cannot do, as hardness (from Vickers technique) is determined by measurement of dimensions/depth of the indentation imprint on the material and compared against reference values for the material being analysed.

Nanoindentation evolved from the Vickers hardness test and in recent years has become one of the most widely used techniques to analyse the mechanical properties and elastic modulus of films, coatings and surface-treated layers. The geometry of the tip is typically a three-sided diamond pyramid (Berkovich geometry) which is pressed into the material being analysed resulting in elastic and plastic deformation. It is held at optimum force which induces creep of the material under the tip which is finally unloaded leading to partial elastic recovery of the material. A force (mN) – displacement (nm) curve is generated from the collected data and the area under the loading and unloading regions of the curve provides information relating to the elastic and plastic deformation of the material being tested.

The disadvantage of the technique is that, despite the use of low loads that generate low maximum displacements, contributions from the substrate is still a possibility - especially if the coating/treated surface is thin ($\leq 1 \mu\text{m}$). This is because elastic and plastic zones are induced below the tip, which are much deeper than the maximum indentation depth. In order to ensure there is as minimum influence from the substrate when measuring the hardness and elastic modulus of the treated surface/coating,

the size of the contact impression is kept small relative to the film thickness, done to achieve a high degree of spatial resolution. Usually, this is less than 10% of the film thickness.

The Oliver and Pharr [243] method has been widely used to measure the nanoindentation hardness and elastic modulus of materials and are calculated from the recorded load-displacement curve. This technique allows the determination of these parameters from indentation load and displacement measurements to be made without the need for direct optical imaging, as in the case of conventional microindentation hardness tests. During unloading of the tip, only elastic displacements are recovered, and so the elastic constants of the sample can be calculated using the unloading part of the curve (Figure 2.10), which can be approximated by the following relation:

$$P = \alpha(h - h_f)^m \quad (2.4)$$

Where P is the indentation load, α and m are constants, h is the displacement and h_f is the final (plastic) displacement after unloading.

The depth between the indenter and the specimen, h_c , is determined from the load-displacement data using:

$$h_c = h_{max} - h_s = h_{max} - \varepsilon \frac{P_{max}}{S(h_{max})} \quad (2.5)$$

Where h_{max} is the maximum displacement at the point of unloading, h_s is the sink-in depth, P_{max} is the maximum indentation load, ε is a constant related to the indenter geometry and $S(h_{max})$ is the slope of the unloading curve.

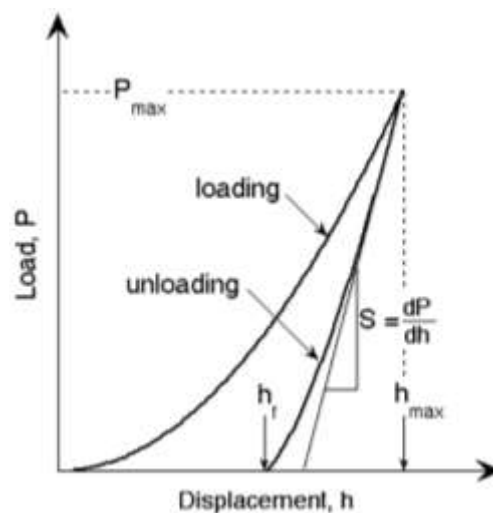


Figure 2.10: An indentation load-displacement curve showing regions that are used to determine hardness [244].

The sample hardness, H_s , is determined from the following relation:

$$H_s = \frac{P(h_{max})}{A(h_{max})} \quad (2.6)$$

Where $A(h_{max})$ is the contact area at maximum indenter penetration which is determined by calibrating the shape function from indents on a standard material such as fused silica.

Measurement of the unloading stiffness is calculated from:

$$S(h_{max}) = \frac{dP}{dh} h_{max} = \sqrt{\frac{4A(h_{max})}{\pi}} E^* \quad (2.7)$$

The elastic modulus of the sample is then determined from the reduced elastic modulus of the sample and indenter tip, E^* :

$$\frac{1}{E^*} = \frac{(1-\nu_1^2)}{E_1} + \frac{(1-\nu_2^2)}{E_2} \quad (2.8)$$

Where E_1 and ν_1 , and E_2 and ν_2 are the Young's modulus and Poisson's ratio of the indenter and the sample, respectively. For the diamond indenter tip $\nu_1 = 0.07$ and $E_1 = 1,140 \text{ GPa}$ [244]. Often the issue with coatings and surface treatments is that ν_2 is difficult to determine precisely.

Surface nanoindentation measurements were performed using a Hysitron Inc. Triboscope™ equipped with a Berkovich triangular-pyramidal diamond indenter with an approximate tip radius of curvature of 150 nm. Approximately nine indentations were carried out on the surface of the TPN diffusion-treated samples, hydrothermally oxidised TPN-treated Zr samples and sputter co-deposited samples in a 3x3 grid array with a 10 μm spacing between each indent at a load of 4 mN. The hardness vs. contact depth profiles were plotted for these samples.

2.11 Scratch Adhesion Testing

Adhesion is an important factor in coating/surface-treated layer performance for many applications. Scratch testing is commonly used to measure adhesion of PVD ceramic coatings. A hemispherical diamond stylus of radius 200 μm (Rockwell C geometry) is drawn across the surface of the coated substrate/treated surface at a constant speed, over a defined range of linearly-increasing Normal Force (F_N - applied force by indenter perpendicular to the treated surface) applied over a defined distance. The damage along the scratch track is recorded as a function of the applied force where Acoustic Emission (AE) from the treated layer/coating-substrate system is also monitored. This is the release of elastic energy during crack growth and the magnitude of the AE signal depends on the size of the cracks produced (Table 2.2). Increasing the applied force results in a progressive increase in surface damage, until a critical load (L_c) is reached (Table 2.3) - identified as a failure mode from

Tangential Force curves (F_T). A combination of frictional stresses, elastic-plastic indentation stresses and internal residual stresses lead to coating failure.

Table 2.2: Parameters used in scratch adhesion profiles.

Parameter	Symbol	Description
Tangential Force	F_T (N)	The force that opposes the relative motion between a moving stylus and the surface that is being scratched by the stylus.
Normal Force	F_N (N)	The force exerted by the stylus onto the workpiece.
Penetration Depth	P_d (μm)	The penetration of the stylus into the coating.
Acoustic Emission	AE	Elastic waves produced as a result of damage events from the stylus penetrating into the sample.

The force of the stylus drawn across the surface is known as the tangential or frictional force (F_T). As F_N is progressively increased, the stress generated in the coating results in through-thickness cracking (such as tensile or conformal cracking [245]). Chipping damage also occurs on the sides of the scratch track which can be identified from optical micrographs. The appearance of these defects denotes the critical load at which cohesive failure occurs (known as L_{C1}). The load at which this failure mode occurs is gained from the F_N value which can be inferred from the F_T profile. A sudden increase in the F_T gradient denotes adhesive failure (L_{C2}) which is the penetration of the coating by the indenter where the substrate is first exposed. As before, the value of L_{C2} is obtained by recording the point at which L_{C2} occurs on the F_T profile and determining where this occurs on the F_N profile. The final failure mode is complete spallation (L_{C3}). This is the spallation of the coating or the treated layer from the substrate which is seen as an erratic pattern and a further change in the gradient of the F_T scratch profile. The surface topography following the L_{C3} failure mode is seen as a brighter image from optical micrographs compared to that of the coated/surface treated layer at L_{C2} – indicating exposure of the underlying substrate in the scratch track.

Table 2.3: Description of failure events, observations and corresponding critical loads [246].

Critical Load	Failure Description	Observation
L_{C1}	Cohesive failure within the layer.	Onset of cracking and chipping damage at the scratch track.
L_{C2}	'Adhesive' failure/disbondment of the layer.	Penetration into substrate.
L_{C3}	Ploughing of indenter into the substrate.	Complete coating/layer spallation with only substrate visible along scratch track.

An Anton Parr commercial scratch tester (Springfields Fuels Ltd, Westinghouse Electric Co.) (Figure 2.11) was used to assess the adhesion strength of the diffusion treated TPN-Zr layer; sputter deposited

Zr-Mg coatings and oxide scales formed following hydrothermal oxidation tests, performed according to ASTM C-1624-05 [247]. This test identifies the adhesion strength and mechanical failure modes of ceramic coatings on metal substrates at ambient temperature but is often adapted to other conditions. The load ranged from (i) 0 to 30 N for the TPN diffusion-treated layers; (ii) 0 to 35 N for the hydrothermally oxidised samples and (iii) 0 to 40 N for the sputter-deposited Zr-Mg coatings, at a rate of 10 mm/min for a scratch distance of 10 mm. The substrate surface and diamond tip were cleaned with isopropanol before each scratch to remove possible contamination. The topology of each scratch track was assessed using a built-in optical microscope although both SEM and 3D surface profilometry techniques can also be used separately. Critical loads: L_{c1} , L_{c2} and L_{c3} were determined from an average of 3 scratches carried out on each treated sample, and their values were based on the observation and description of the damage events described in BS EN 1071-3:2005 [248].

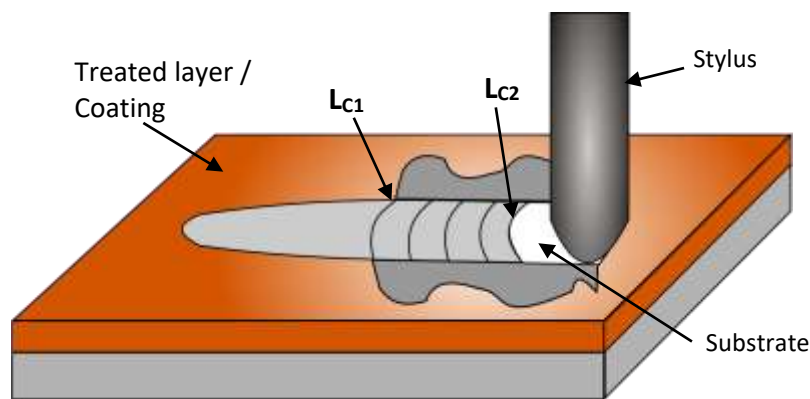


Figure 2.11: Schematic of failure modes from scratch adhesion measurements.

2.12 Hydrothermal Oxidation Testing

Hydrothermal oxidation tests were performed in a stainless steel autoclave containing deionised water (Figure 2.12) to investigate oxidation behaviour of the treated samples. The diffusion-treated TPN samples (that had undergone longer treatment times (i.e. 2, 3 and 4 hr)) and the sputter-deposited samples were hydrothermally oxidised (separately) by placing the samples in an autoclave containing deionised water at room temperature (RT) (at atmospheric pressure) which was increased to 360°C (at a rate of 5°C per min) and held for 3 days (and extended to 7 days for the magnesium-containing zirconium sputter PVD coatings) according to ASTM G2 [75] under high pressure water (18.7 MPa) conditions. Once finished, the samples were then cooled at a rate of 5°C per min and removed from the autoclave. For the TPN-treated Zr samples, these were weighed before and after hydrothermal oxidation tests and the difference was divided by the total area of each sample to determine the oxide weight gain in milligrams per decimetre squared (mg/dm^2).

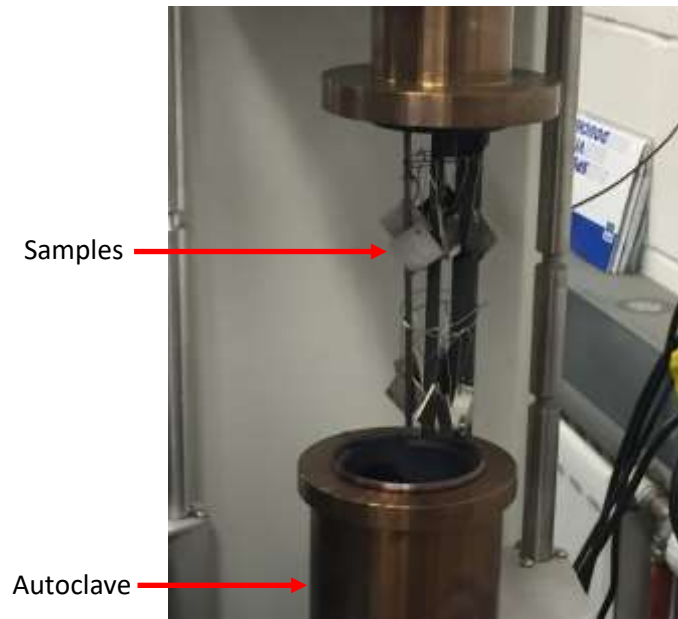


Figure 2.12: Hydrothermal oxidation test rig showing magnetron sputter-deposited coatings which was performed at 360°C for 3 and 7 days.

Chapter 3 – Triode Plasma Nitriding Diffusion Treatments

3.1 Plasma-nitriding of Zr: Trial Runs

The temperature (and other key parameters such as pressure and concentration) required for successful and effective TPN diffusion treatment and triode plasma oxidation (TPO) treatments has been extensively studied by Leyland, Matthews and co-workers [182, 185, 235, 249, 250]. These studies have in recent years concentrated primarily on Ti and Ti-alloys for aerospace and potential biocompatibility applications. However, despite their microstructural similarities no literature has been found that explores such treatments of Zr-based substrate materials to improve the surface properties.

The objective of this part of the study was to determine the optimum temperatures and duration for which successful nitriding would take place on Zr substrates. Leyland et al [185] previously demonstrated that it is possible to produce effective dc discharge plasma nitriding at a workpiece negative bias as low as 200V under low pressure (<1 Pa) thermionic triode conditions, compared to conventional diode configurations at high pressure (>100 Pa), where it is difficult to achieve effective results below 500 V, due to high L/λ values and results in low energies/intensities of energetic gas/plasma species arriving at the workpiece. Explanation for this disparity lies in the different ion and neutral energy distributions in both systems and was discussed in Chapter 1 Section 1.9.5. Furthermore, plasma nitriding has been shown to improve surface microhardness and load-bearing capacity of Ti-6Al-4V substrates at temperatures in the 400-700°C range [251]. This knowledge provided an effective start-point for this investigation.

Untreated pure Zr substrates (dimensions 20 mm x 20 mm x 1 mm) were hot-mounted in bakelite and ground using SiC papers down to P1200 grit size and polished down to 1 μm polycrystalline diamond suspension with final polishing by colloidal silica. An automatic regime with single pins was used to stabilise the bakelite-mounted Zr substrates during the grinding and polishing process. It was found however, that this did not remove some of the 'deeper' scratches that had formed at the edge of the substrates as a result of grinding, though this was not an issue for samples mounted in cross-section due to having a smaller surface area compared to Zr substrates. Thus, manual grinding was employed to remove the remaining defects.

Fig 3.1(a) shows an SEM micrograph of pure Zr in the untreated (as-received) condition. The substrate surface can be seen to be coarse - owing to the processing technique adopted to manufacture the Zr

metal (work hardened and temper-annealed) and was found to contain contamination across the surface.

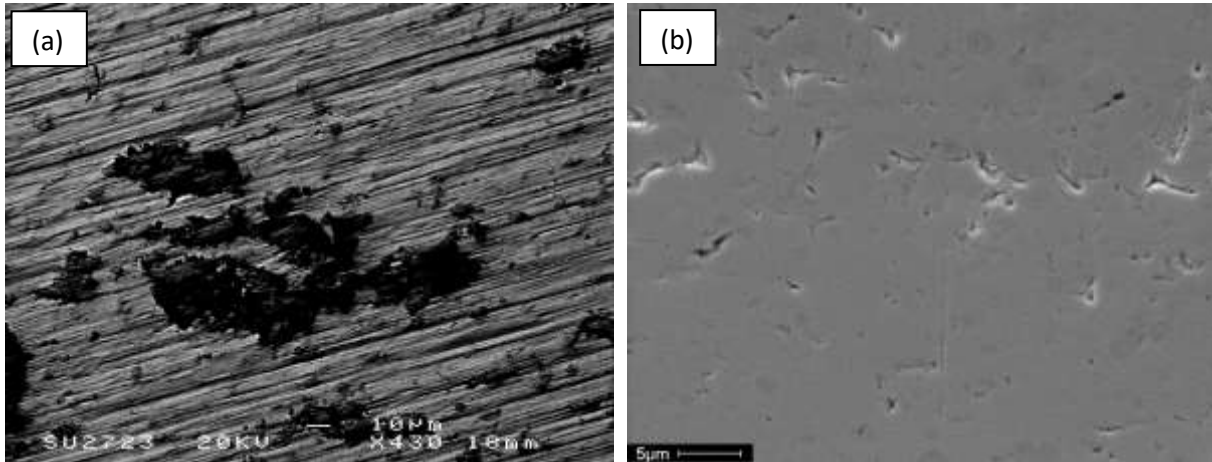


Figure 3.1: Secondary electron image of (a) as-received HCP α -Zr surface showing impurities and (b) HCP α -Zr after 9 μm diamond polish is used which shows some scratches.

The SEM image in Figure 3.1(b) shows a largely smooth Zr surface, though some defects remained from the 9 μm stage, which were removed after subsequent polishing technique down to 0.05 μm with colloidal silica (outlined in Chapter 2, Section 2.1). It should be noted that obtaining a perfectly defect-free surface was not the primary objective, however, having a polished mirror surface as far as reasonably practicable is desirable as this minimises contamination or unwanted impurities; reduces surface roughness and thus optimises adhesion properties between the treated layer and the substrate [252].

The zirconium metal was etched using a Hydrofluoric acid (HF)-based solution which comprised of HF – (5 vol.%), Nitric acid (HNO_3) – (35 vol.%) and H_2O – (60 vol.%) [253] for 10 seconds to enhance the α -phase grain contrast of the metal. However, the HCP α -Zr microstructure was seen to have been only partially etched. The fact that the α -Zr phase is particularly resistant to chemical attacks resulted in the individual α -Zr grains not being clearly demarked by the HF-based etchant as shown in the optical micrograph in Figure 3.2. Another technique used to observe the α -Zr grains was ion polishing and this was used to etch the metal after the mechanical polishing stage (see Chapter 2, Section 2.3 for details). The HCP α -Zr microstructure could be clearly observed using optical microscopic image analysis presented in Figure 3.3(a). The average grain size was determined to be $\sim 12 \mu\text{m}$ using the ASTM-E112 standard method [254].

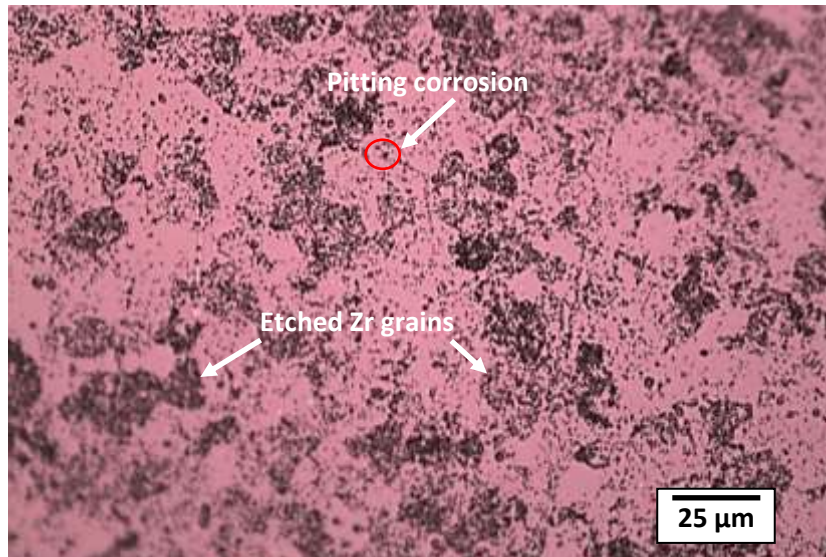


Figure 3.2: Demarked grain boundaries of Zr grains shows the Zr surface has high resistance to chemical attack after being etched in a HF-based etchant.

The polished zirconium substrates were then cleaned in acetone and isopropanol then dried under warm flowing air before TPN diffusion treatment using the following conditions (See Chapter 2, Section 2.4 for details):

Table 3.1: Conditions used during plasma nitriding.

Parameter	Output
Temperature (°C)	700°C
Duration (h)	1.5, 2, 3 & 4
Pressure (Pa)	0.5
Substrate bias (V)	-200
Partial pressure mixture (%)	70:30 (Nitrogen:Argon)

Following TPN diffusion treatment at 700°C for 1.5 hours, optical image analysis of the TPN-treated surface in Figure 3.3(b) revealed that the grain size remained virtually unchanged compared to the untreated HCP α -Zr shown in Fig. 3.3(a). Grain size comparisons of the untreated pure zirconium substrate and the TPN diffusion-treated sample does not appear to show evidence of grain growth under the above-mentioned treatment conditions. Furthermore, the morphology of the nitrided surface in Figure 3.3(b) shows the grains are more pronounced and protruded relative to HCP α -Zr

grains seen in Figure 3.3(a), but this is likely due to the effects of the argon sputter cleaning process used prior to diffusion treatment resulting in the preferential etching of grains. The limited resolution and magnification of the optical microscope further highlighted the difficulty in observing the microstructure of the nitrided surface using optical microscopy alone and so a higher magnification for imaging using SEM was required.

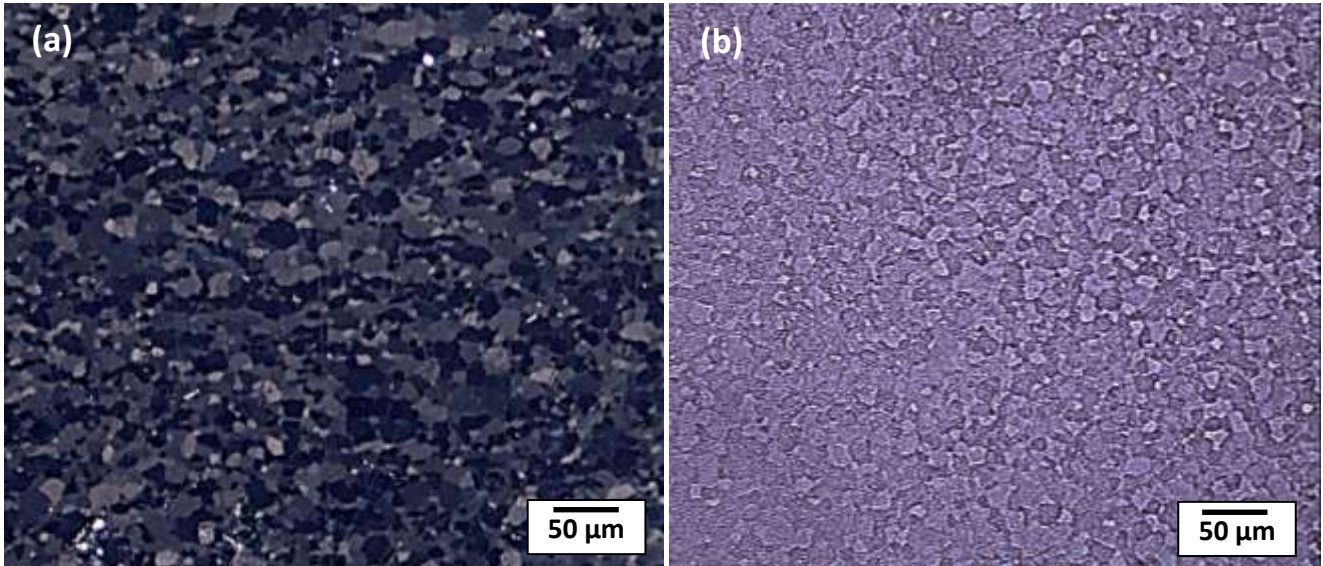


Figure 3.3: Optical micrographs of (a) bulk HCP α -Zr (ion polished) and (b) TPN diffusion-treated Zr surface which show no observable grain growth of α -Zr.

For SEM analysis, the diffusion-treated TPN-Zr sample was mounted in conductive bakelite resin then carbon coated to allow the dissipation of charge build-up due to the insulating nature of the TPN-treated layer. The SEM micrograph in Figure 3.4 shows the zirconium surface following TPN treatment after 1.5 hours whereby the TPN-treated Zr grains could be seen due plasma etching effects on the grains [255].

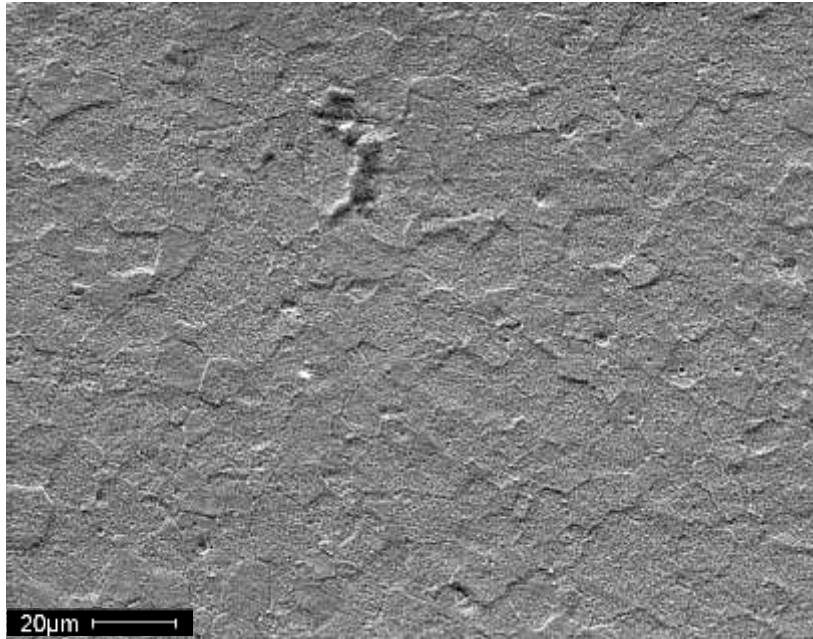


Figure 3.4: SEM micrograph of the TPN-treated Zr surface morphology in SE mode.

Energy Dispersive X-ray (EDX) spectroscopy was used to evaluate the elemental composition of the TPN-treated surface, and the spectrum presented in Figure 3.5 revealed the presence of nitrogen at the surface which was determined to be 20 at% and zirconium and oxygen comprised 75 at% and 5 at% respectively. Visual inspection of the substrates showed a golden appearance after diffusion treatment which indicated that a treatment duration of 1.5 hr was sufficient for effective interstitial nitrogen diffusion into the HCP α -Zr lattice.

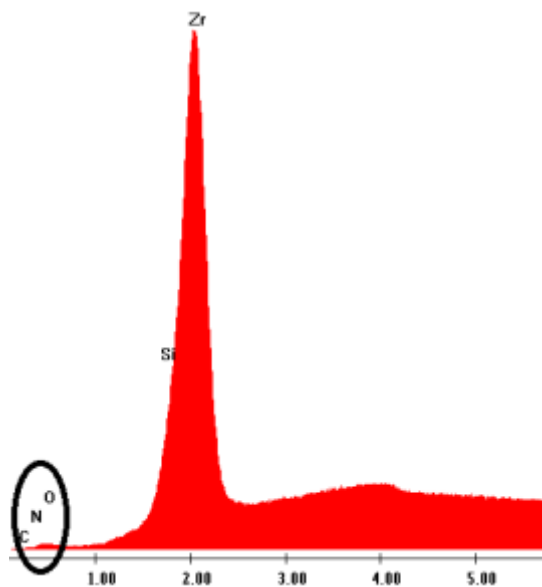


Figure 3.5: Elemental composition obtained from EDX analysis, shows the presence of Zr and N.

An estimate of the thickness of the nitride compound layer was inferred from EDX line scans. Figure 3.6 shows the Zr composition gradually decreasing towards the edge of the sample as it proceeds towards the bakelite mount, which is shown by the abrupt increase in the detection of carbon. The presence of nitrogen is shown as a small but noticeable profile which is plotted individually (inset graph) as the large contributions from Zr skewed much of the contribution from nitrogen. The distance between the two most prominent peaks is indicative of the nitride compound layer, the thickness of which was estimated to be significantly less than 1 μm . Cassar et al [256] carried out TPN-diffusion treatment on Ti-6Al-4V under similar conditions and showed that the TPN-treated layer contained of a 250-500 nm compound layer at the surface. However, it should be noted that TEM investigations using focused ion beam (FIB) are required to accurately determine the nitride compound layer thickness due to the limitations of using SEM to observe thicknesses below 1 μm . Unfortunately, this could not be performed due to technical issues surrounding TEM availability but is commented on as a recommendation for future work in Chapter 6.

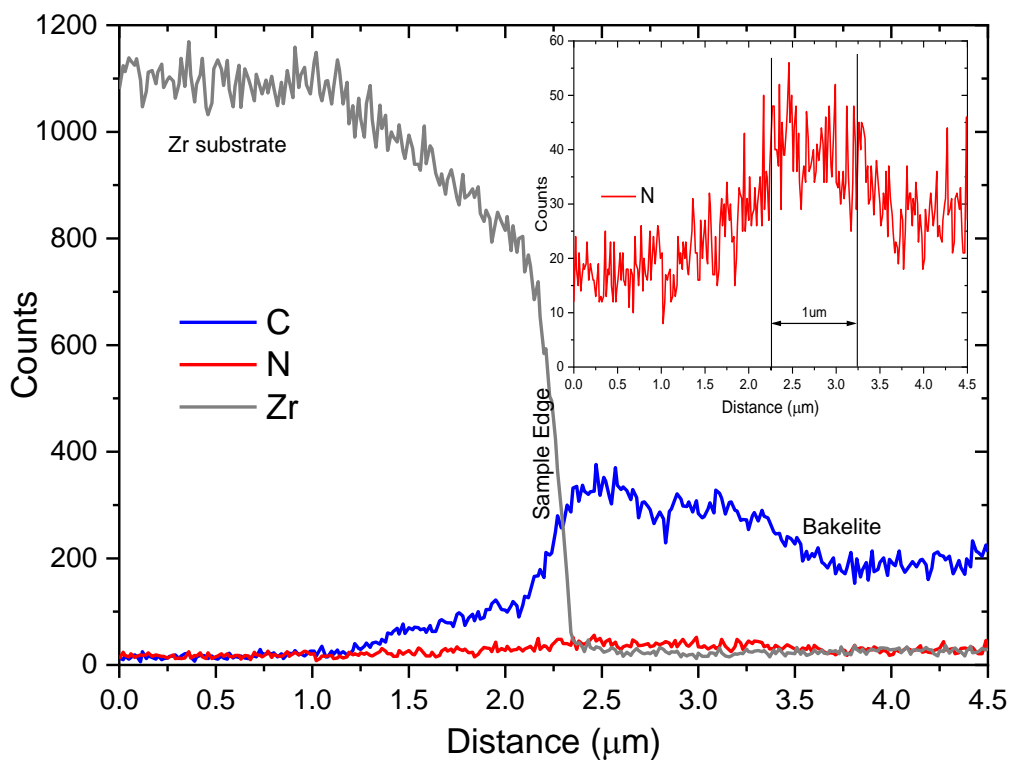


Figure 3.6: SEM cross-section of plasma-nitrided Zr and EDX Line-scan from Zr>ZrN layer>Bakelite.

3.2 Microstructure of TPN-treated Zirconium

The next set of TPN diffusion treatments involved increasing the treatment duration to 2 hr, 3 hr and 4 hr. This was done to enhance the load-bearing capacity of the diffusion-treated layer (via the nitrogen at interstitial sites of the HCP α -Zr lattice) and to investigate the impact this has on mechanical properties of the TPN-treated layers. A low substrate negative bias of 200 V and a high nitrogen partial pressure (nitrogen:argon gas ratio 70:30) were used. This would allow the nitrogen ion species to arrive at the zirconium surface at optimal energy, enabling the diffusion of these species at random interstitial sites of the HCP α -Zr lattice, thus increasing the case depth of the nitrogen diffusion zone when low substrate biases are used. These conditions also minimise the build-up of a compound layer which become saturated with nitrogen at the interstitial sites which can decrease the thickness of the nitrogen diffusion zone due to the lower diffusion co-efficient of the nitride compound layer.

To facilitate comparable analysis of the diffusion-treated layers, parameters such as chamber temperature and substrate bias voltage were kept constant with only treatment time increased. Following nitriding, the substrates displayed a shiny golden appearance as shown in Figure 3.7 (identical to the 1.5 hr treatment), which is indicative of the presence of a ZrN compound layer [257]. The golden colour appeared to be uniform at all the durations tested, clearly showing a thermochemical reaction had occurred, with regions of discoloration along the edges. This observation was also reported by Yetim et al [258] who showed the plasma-nitrided samples were golden and opaque in appearance which reduced at the edges. This is due to the relatively low substrate negative bias (200 V, low pressure triode/high current treatment) adopted in this work and is known to give small contributions to cathode sheath effects, arising from an increased ion bombardment at the outer edges of the substrate (causing heating effects). This resulted in re-sputtering and net removal of the nitride compound layer (due to the intense bombardment at the outer edges) which led to grains near the edges of the sample to appear more pronounced compared to the rest of the nitrided surface (Figure 3.8) [235, 257].

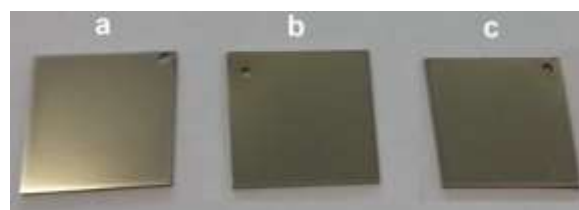


Figure 3.7: TPN-treated Zr samples nitrided for (a) 2 hr; (b) 3 hr and (c) 4 hr respectively, showing a shiny reflective golden appearance.



Figure 3.8: Optical micrograph of the 4 hr TPN-treated Zr showing more pronounced Zr microstructure towards the edge of the TPN-treated surface due to cathode sheath edge effects.

The SEM micrograph (in BSE mode) of the 4 hr TPN-treated surface in Figure 3.9(a) appears to show a grain-like topology which was found to be identical to the 2 hr and 3 hr TPN-treated samples. It is unlikely that these features are grain boundaries since the average size of grain boundaries is about 0.5 nm [259] and such features would be too small to be resolvable in an SEM from a non-etched surface. What is observed are protuberances resulting from the nitriding diffusion treatment. To observe the nitride grains, a higher resolution imaging technique such as focused ion beam (FIB) along with transmission electron microscope (TEM) would be useful. On closer inspection of the BSE image in Figure 3.9(a), TPN treatment appears to subtly show darker regions that highlight the boundaries of the zirconium grains. Given that the average Penetration Depth of backscattered electrons in the sample is about 80 nm, this would indicate that the nitride compound layer is thin – possibly hundreds of nanometers thick – again, TEM investigations would be useful to determine this thickness.

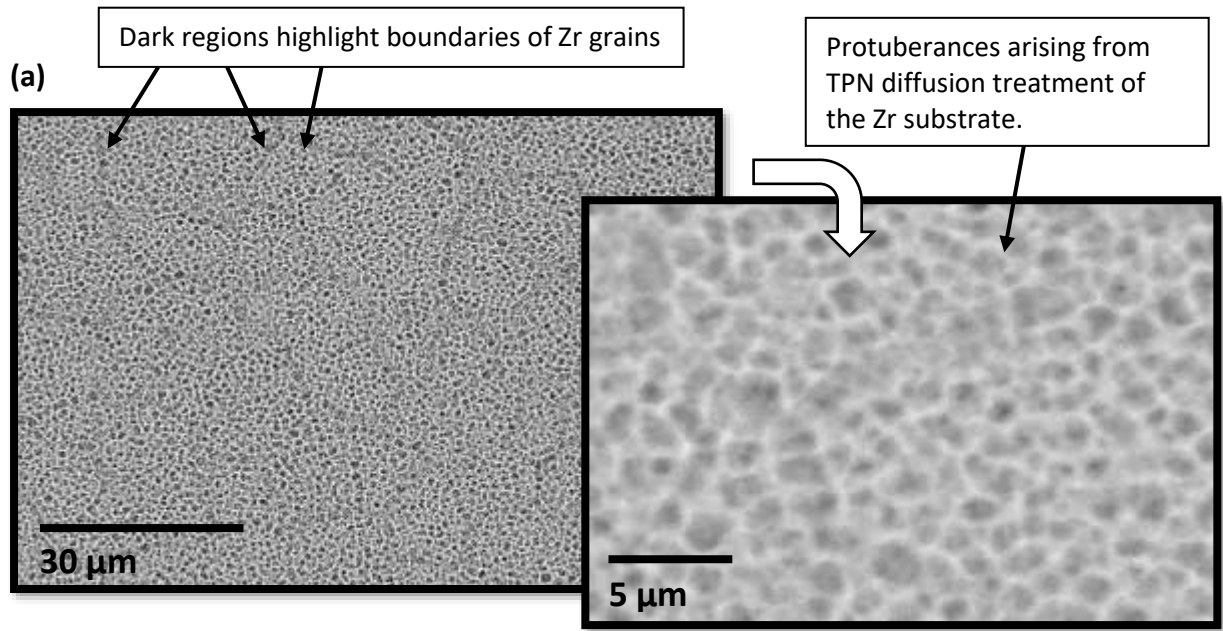


Figure 3.9: (a) SEM micrograph in BSE mode of the 4 hr TPN-treated surface show the 12 μm grain boundary structure of zirconium grains and (b) EDX elemental maps of the TPN-treated surface show the presence of zirconium (highlighted in red) and nitrogen (highlighted in green).

EDX elemental mapping of the 4 hr TPN-treated surface in Figure 3.9(b) predominantly shows the presence of zirconium (highlighted in red) and regions where nitrogen (highlighted in green) were detected. On closer inspection of the EDX map for nitrogen, it can be seen that the nitrogen appears at or near the edges of the Zr grains. Interstitial elements such as nitrogen prefer to migrate towards the grain boundaries because it is less dense than at the grains and does this via a hopping mechanism [260] at interstitial sites of HCP α -Zr lattice.

Table 3.2: Elemental composition obtained from EDX analysis for the 2 hr, 3 hr and 4 hr TPN-treated surface.

Treatment duration	2 hr	3 hr	4 hr
Element	Atomic %	Atomic %	Atomic %
Zr	67.2	65.6	63.4
N	25.8	29.1	32.4
O	5.4	3.2	3.5
Fe	0.9	1.2	0.4
Ni	0.4	0.6	0.2
Cr	0.3	0.3	0.1

Quantitative analysis in Table 3.2 reveals the nitrogen content increases with treatment duration. The highest nitrogen content was for the 4 hr treated sample which was 32.4 at% and 63.4 at% for zirconium. Nitrogen concentration was found to have increased for each treatment duration compared to the ~20 at% (nitrogen content) for the 1.5 hr treated (mentioned previously), demonstrating that longer treatment times resulted in greater nitrogen diffusion concentration in the α -Zr matrix that forms the sub-surface nitrogen diffusion zone and surface nitride compound layer.

The presence of oxygen on the nitrated surface could be due to the high affinity of oxygen for zirconium [83] which increases the likelihood of the formation of zirconia. Furthermore, compositional analysis also showed the presence of small quantities of iron (Fe), nickel (Ni) and chromium (Cr). The presence of Fe was from the cross-sputtering of the steel sample holder used during plasma nitriding, and nickel and chromium was from the 'nichrome' wire used to suspend the samples.

The appearance of the diffusion-treated surfaces was found to be characteristic of plasma-assisted processes, particularly the colour and surface roughness. Atomic force microscopy (AFM) was used to analyse the topography of the nitrated surface and to investigate the effects of increased duration on the microstructure. The effect of increasing the process duration for nitriding of bulk zirconium is presented in Figure 3.10. AFM images of the TPN-treated surface in Figure 3.10(a) shows the growth of nodular protuberances. On closer inspection of the AFM images, these protuberances appear to exhibit a uniform size of about 1 μm in diameter and 250 nm – 300 nm in height which was the case for TPN-treatment durations used. Three-dimensional AFM topographical maps of the treated surface

in Figure 3.10(b) shows that TPN treatment resulted in rough surface particularly for the 3 hr and 4 hr treatment durations. This could be due to the saturation of the interstitial sites in the HCP α -Zr lattice with nitrogen that results in the growth of the nitride compound layer which increases in thickness with increased treatment time and creates a rough topography seen in the AFM images. Cassar et al [261] reported similar observations following Triode Plasma Oxidation of Ti-6Al-4V alloy at 700 °C for 4 hours (in an argon:oxygen gas ratio of 30:70%) that resulted in a 1.8 μm thick titanium oxide compound layer. The author observed protuberances from AFM topographical maps and attributed this to oxide grains.

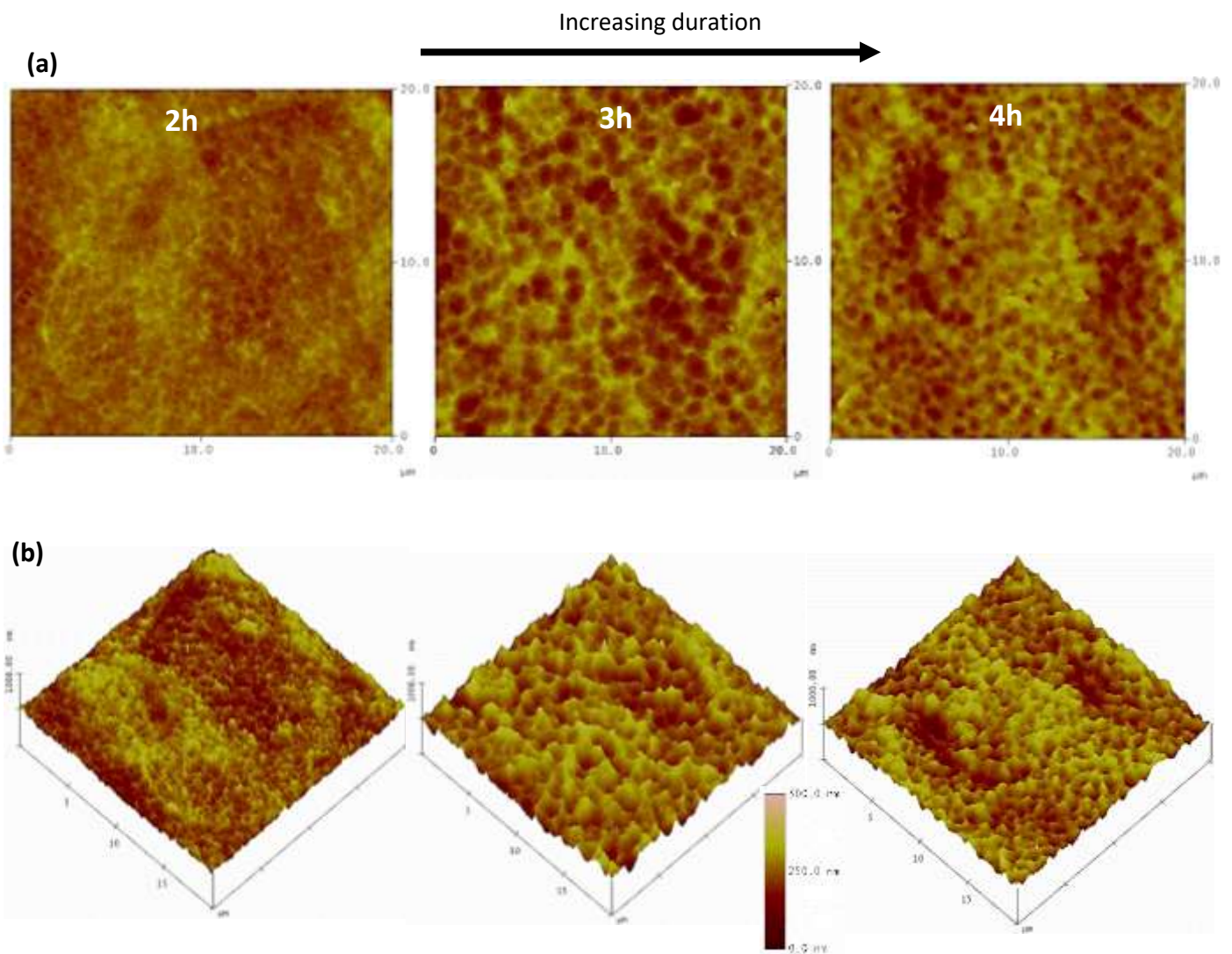


Figure 3.10: Surface topographic maps of the 2 hr, 3 hr and 4 hr TPN-treated Zr samples using (a) AFM imaging of the surface and (b) AFM three-dimensional topographic maps which show protuberances.

As a recommendation for future work which is commented on in Chapter 6, TEM investigation of the TPN-treated surface should be carried out to identify nitrided grains which may help elucidate the provenance of these protuberances and to determine the thickness of the nitride compound layer for the 2 hr, 3 hr and 4 hr TPN-treated samples. Treatment times could be extended beyond the maximum of 4 hr adopted in this study to obtain a thicker compound layer, which could then be investigated for hardness and adhesion properties. It would also be interesting to investigate whether there is an overall benefit with regards to the oxidation behaviour (of the TPN-treated surface) by having a much thicker nitride compound layer or whether this might spall off under aqueous conditions and this is also commented on in Chapter 6 – Recommendations.

3.3 Surface Roughness of the TPN-treated Surface

Literature investigating the effects of TPN treatment time on surface roughness is scarce. Here, an attempt is made to analyse this on TPN-treated Zr samples. Five random locations were chosen on each surface of the 2 hr, 3 hr and 4 hr nitrided samples, and optical profilometry measurements were made to determine the average surface roughness values (R_a). The stage of the optical profiler (on which the sample was mounted) was tilted to allow reflected beams to provide 3D colour maps of the treated surface and the relative heights between each of the surface features.

The mean surface roughness for the 2 hr, 3 hr and 4 hr TPN-treated samples were determined to have R_a values of 0.45, 0.67 and $0.87 \pm 0.2 \mu\text{m}$ respectively, and the results provide evidence that TPN treatment process increases the roughness of the bulk surface which was found to increase with nitriding duration compared to untreated pure zirconium ($0.12 \pm 0.2 \mu\text{m}$). This can be partially attributed both to the sputter-etching process during sputter-cleaning and to the diffusion process the effects of which could be seen between the comparison of untreated pure Zr and the 4h TPN-treated sample in Figure 3.11. Identical profilometry images were obtained for the 2 hr and 3 hr TPN-treated samples. The effect of this is superimposed on the roughening induced by the growing compound layer and nitrided diffusion zone which increases interstitial nitrogen in the bulk lattice sites, allowing the compound layer to grow and limiting further nitrogen inward diffusion into the material bulk. The surface topography after nitriding shows a grain-like structure, similar to previous reports which studied plasma-nitrided Ti alloys surfaces [152, 258, 262].

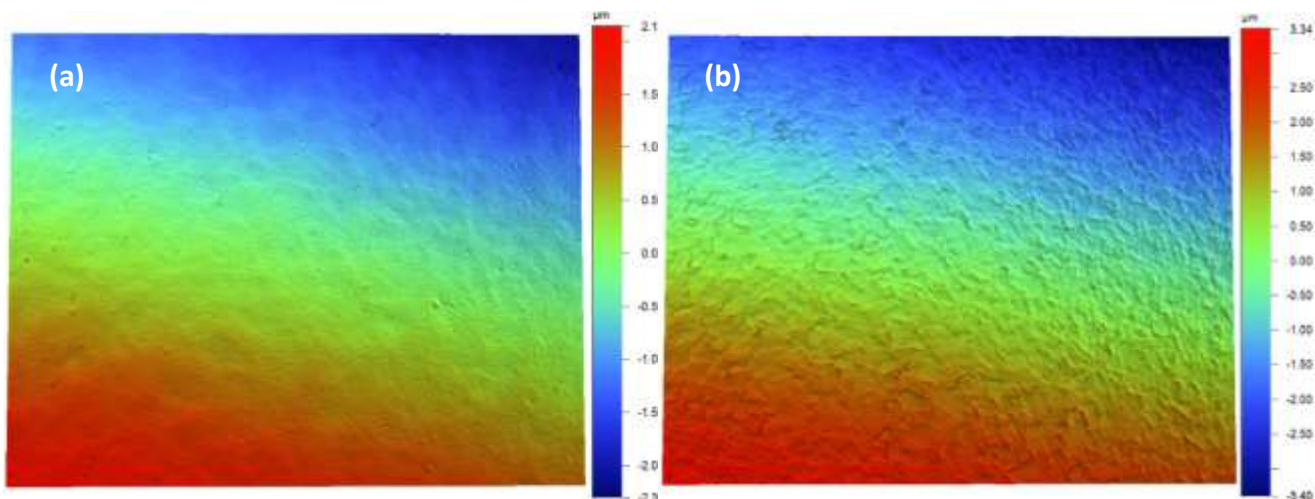


Figure 3.11: Optical profilometry images comparing surface roughness of (a) untreated pure Zr and (b) 4 hr TPN-treated Zr show increased surface roughness after diffusion treatment.

Taken together, the optical micrographs, SEM/EDX analysis and surface roughness profilometry measurements provide strong evidence that the bulk HCP α -Zr has been nitrided at all the treatment durations.

3.4 Determining Nitrided Layer Thickness in Cross-section

In order to determine the thickness of the nitrided layer, the 4 hr diffusion-treated TPN-Zr sample was mounted in cross-section in conductive bakelite resin, ground then polished according to the micropreparation regime detailed in Chapter 2, Section 2.1, and finally cleaned using isopropanol and acetone and dried under warm flow of air before being carbon coated (to dissipate charge build-up of the insulating nitrided layer). Figure 3.12(a) illustrates the region where the nitride compound layer and nitrogen diffusion was expected to form (which was expected to be several microns thick), however, no visible nitride layer was observed in back-scattered electron (BSE) mode or detected using EDX analysis (Figure 3.12(b)). A plausible explanation for why the nitride compound layer was challenging to detect using SEM/EDX spectroscopic analysis could be due to: (i) high surface roughness of the nitride compound layer, (ii) the nitride compound layer being too thin ($<1 \mu\text{m}$) to resolve sufficiently using SEM to obtain high resolution micrographs of the treated layers.

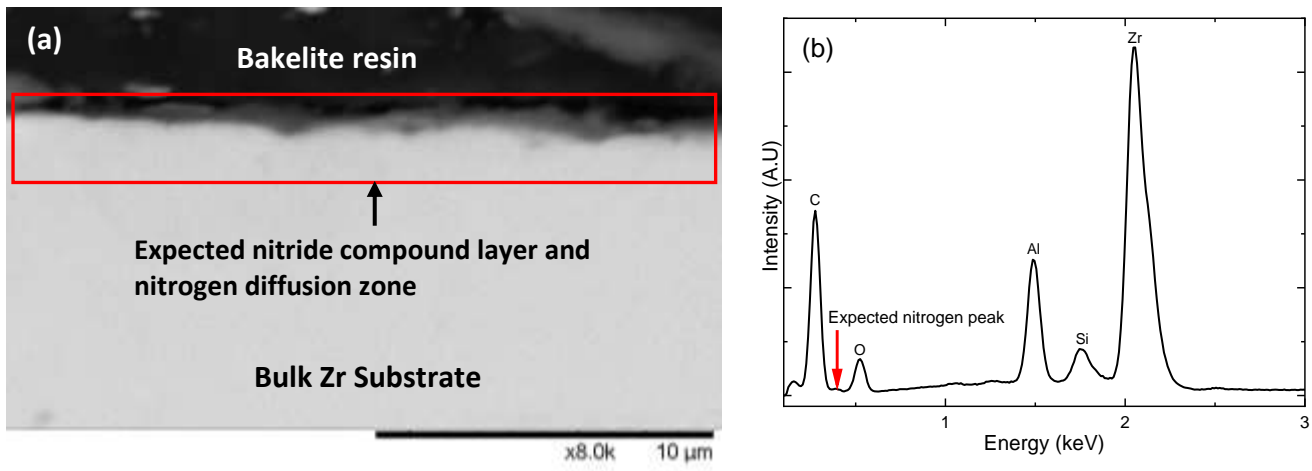


Figure 3.12: (a) SEM micrograph of the cross-section of the 4h nitrided Zr and (b) EDX spectrum showing where nitride layer was expected to be detected.

One route investigated to better observe the TPN diffusion-treated layers was to etch the samples. This was carried out to highlight the nitride layer which appeared to be unobservable after mechanical polishing. An etchant regime comprising of HF (10 ml): HNO₃ (45 ml): H₂O (45 ml) [253], for 1 minute at room temperature was used, however, this was unsuccessful in revealing the diffusion-treated layer or the microstructure of the bulk HCP α -Zr.

Furthermore, with thin layers, rounding at the edges of the sample can limit the observation and detection the nitrided layer. To get around this, a strategy is put forward whereby two diffusion-treated samples should be cross-sectionally mounted face to face, which can then be coated with carbon/gold (to allow charge dissipation during SEM analysis) as shown in the schematic in Figure 3.13. Configuration of the TPN-treated samples in this way would avoid 'edge rounding' effects during the grinding and polishing process and this may help ease the identification of the nitrided layer during SEM analysis.

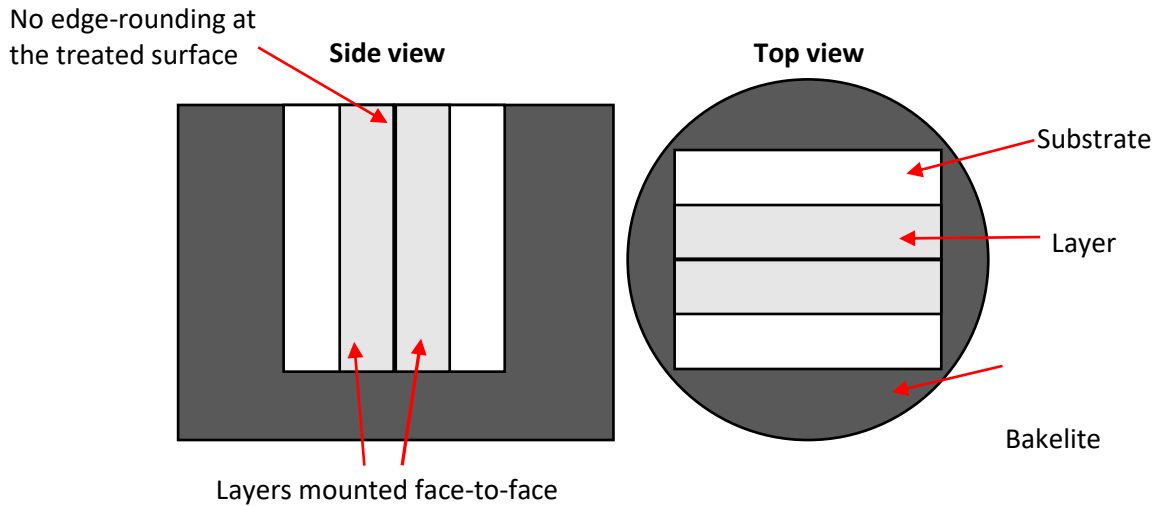


Figure 3.13: Schematic to prevent edge-rounding during grinding and polishing.

3.5 The Use of Ion Polishing to Observe the Nitrogen Diffusion Zone

The use of conventional mechanical polishing technique alone was demonstrated to be insufficient to detect the nitride compound layer or nitrogen diffusion zone when analysed in cross-section using optical microscopic analysis or SEM. A novel approach was developed, whereby an automated argon ion polishing machine (Gatan PECS II) was used to obtain a finer degree of polishing (via etching) of the TPN-treated Zr sample in cross-section after mechanical polishing (see Chapter 2, Section 2.3 for details). To the best of my knowledge, this preparation technique for analysis of diffusion-treated layers has not been reported in the literature. This successful attempt resulted in the observation of the nitrogen diffusion zone using optical microscopic analysis as shown in Figure 3.14.

This technique yielded three important outcomes:

1. The HCP α -Zr microstructure could clearly be observed.
2. The microstructure of the nitride diffusion zone was observed.
3. The thickness of the nitrogen diffusion zone could be measured.

The cross-sectional optical micrograph of the 2 hr, 3 hr and 4 hr TPN-treated samples in Figures 3.14(a), (b) and (c) shows the thickness of the nitrogen diffusion zone was measured to be $23 \pm 1 \mu\text{m}$. In addition, a uniform dark layer of $3 \pm 1 \mu\text{m}$ could be observed just below the nitrogen diffusion zone. This was attributed to 'shadowing' effects arising from the etching regime used during ion polishing resulting in some surface damage. However, the nitride compound layer was not observed from the optical micrograph in Figure 3.14 as the thickness of this layer is significantly less than $1 \mu\text{m}$, which

was also difficult to identify using SEM. Techniques such as Glow Discharge Optical Emission Spectroscopy (GDOES) or TEM analysis could be used to determine the thickness of the compound layer and this is suggested as a recommendation in Chapter 6. GDOES is a spectroscopic method for the quantitative analysis of samples which are used as a cathode in a d.c. plasma. Atoms of the sample are removed by sputtering with argon ions. The sputtered atoms are pass into the plasma by diffusion. Photons are emitted with excited waves that have characteristic wavelengths which are recorded by a spectrometer. A spectrum of the concentration in atomic percent as a function of depth would enable the determination of the thickness of the treated layer.

Observation of the cross-section shows that the nitrogen diffusion zone is of uniform thickness, suggesting a homogenous treatment across the surface area. Small variations in depth across the section may be due to presence of impurities. Interestingly, Leyland et al [156] reported occasional inconsistencies in the depth and quality of the nitrided layer case depth in Triode Plasma Nitriding treatments of stainless steel when no hydrogen was employed (for substrate cleaning) - particularly at low voltages. But in this case, the use of hydrogen for surface cleaning could not be considered due to the extent of interaction of hydrogen with zirconium and the associated formation of zirconium hydride precipitates which may lead to severe embrittlement (as discussed in Chapter 1, Section 1.8.7) [133].

The optical micrographs in (Figure 3.14) clearly demonstrates that ion polishing is a successful complimentary technique (in addition to mechanical polishing) that can be used to obtain a surface finish that would adequately allow the observation of the nitrogen diffusion zone without the need to use HF for etching, and can, by extension could be used for films and coatings. Nevertheless, the differentiation between the nitride compound layer and nitrogen diffusion zone proved to be challenging using ion polishing alone. However, the use of EBSD may provide answers by providing information about crystal orientation and phases in a material. It does this by differentiating grain orientation and/or sizes of the stoichiometric ZrN of the nitride compound layer and the Zr grains of the bulk metal represented as different colours in a colour-coded map, thereby an indirect measurement of the nitride compound layer thickness might be obtained. Scanning Transmission Electron Microscopy (STEM) with Electron Energy Loss Spectroscopy (EELS) is another technique that could be used to infer nitride compound layer thickness. EELS technique uses the energy distribution of electrons that pass through a thin sample to analyse the content of the sample and create images with unique contrast effects. High energy electrons (60 – 300 kV) are used to interrogate the sample. EELS data typically consists of either detailed, energy loss spectral information from the sample (spectroscopy) or images that have contrast created by the energy loss properties of the distribution

of material in the sample which tend to work best for elements with low atomic numbers so this would be ideal for detecting nitrogen of the nitride compound layer.

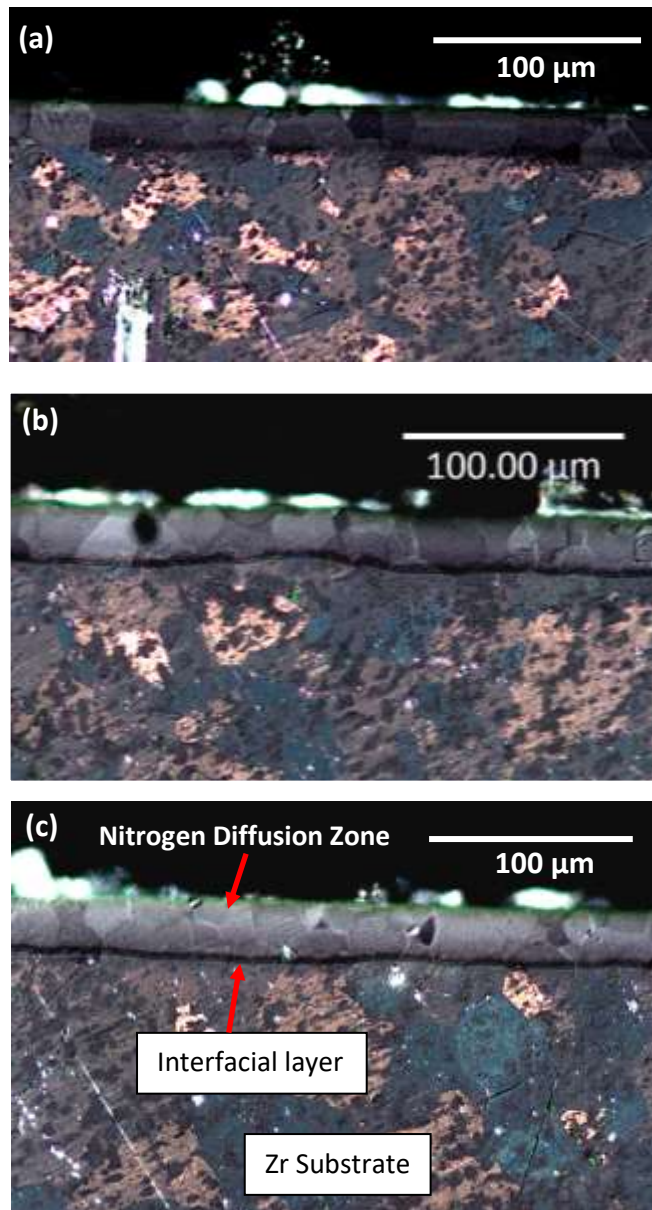


Figure 3.14: Cross-sectional optical micrographs of the (a) 2 hr (b) 3 hr and (c) 4 hr TPN-treated Zr sample shows the nitrogen diffusion zone after ion polishing.

The next section discusses results obtained from GAXRD to determine the crystallographic phase structure of the TPN-treated surface.

3.6 Determining Crystallographic phases Using Glancing-Angle XRD

The TPN-treated zirconium samples were characterised using GAXRD in order to study the phase composition of the diffusion-treated layer formed on the surface of the metal. GAXRD studies were performed using a Philips X'Pert³ (Panalytical) diffractometer and monochromated Cu $K\alpha_1$ X-rays, with data collected over a 2θ range of 25° to 80° with a step size of 0.02° , and incident angles of 2° , 4° and 6° for the TPN-treated samples. Directing the X-ray beam at low incident angles allowed the X-ray Penetration Depth to be reduced and controlled, thereby increasing the signal-to-noise ratio of the diffusion-treated layer relative to the underlying zirconium substrate i.e. focusing on the diffusion-treated region of the material. The tube acceleration voltage and current used were 40 kV and 30 mA, respectively.

GAXRD patterns of the 4 hr TPN-treated surface in Figure 3.15 reveal the presence of two zirconium nitride phases: stable stoichiometric Face-Centred Cubic (FCC) zirconium nitride (ZrN) [263] (PDF no. 01-078-1420) and metastable Zr_3N_4 [178]. The peaks indexed to the ZrN phase was found to be highest at an incident angle of 2° and was found to decrease with increased angle of incidence (i.e. 'deeper' into the TPN-treated layer towards the substrate). The main peak for the ZrN phase was detected at the (111) reflection at a 2θ angle of 34.1° which is the primary peak for ZrN (as ICDD card confirms). Other peaks associated with ZrN included (002) 39.4° , (022) 56.9° , 66.9° (113) and 71.3° (222). For the ZrN phase, a slight peak shift to lower angles of 2θ can be seen for the (111), (002) and (022) planes when compared against the ICDD standard for ZrN [263]. The ZrN phase obtained in this study was found to be in good agreement with literature [129, 263].

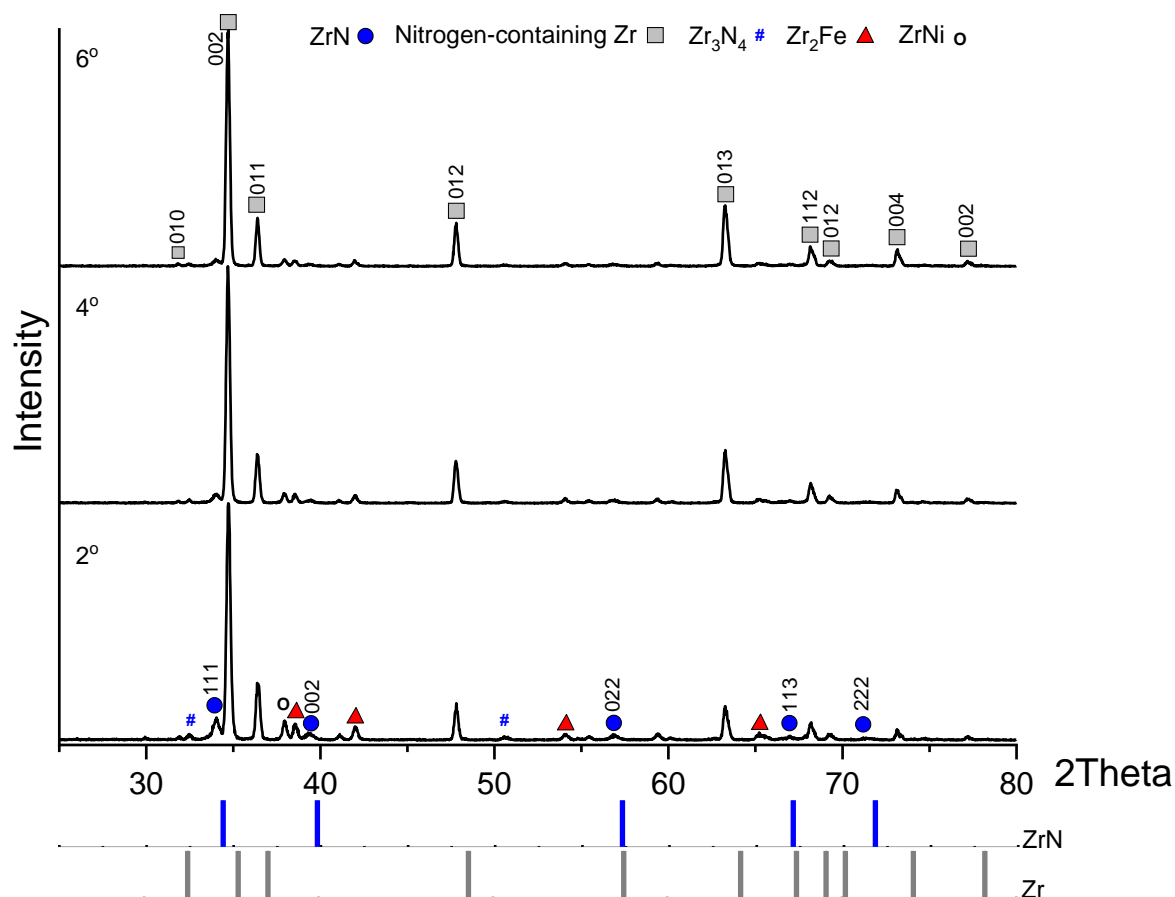


Figure 3.15: GAXRD of the 4 hr plasma-treated Zr at incident angles 2, 4 and 6° showing the presence of ZrN phase [263] (PDF no. 01-078-1420) and nitrogen-containing Zr phase [59].

The Penetration Depth of X-rays for the TPN-treated zirconium surface at a given incident angle is presented in Table 3.3. These values were determined using AbsorbDX phase analysis software where the Penetration Depths are derived using the Beer-Lambert law (*Appendix 1*). Table 3.3 shows that at an incident angle of 2°, the X-ray Penetration Depth at the (111) reflection is 1.09 μm into the specimen. The peak intensities for the ZrN phase are highest at 2° incident angle and can be seen to be negligible at an incident angle of 4°. From the earlier discussion in Chapter 1 Section 1.9.7, a fully stoichiometric ZrN compound is expected to form. For the GAXRD pattern at 2° angle of incidence (i.e. shallow depth into the TPN-treated layer), dominant peaks attributed to the nitrogen-containing Zr phase were detected which suggests the detection of the nitrogen diffusion zone and thus indicating that the thickness of the nitride compound layer is likely to be significantly lower than 1 μm (i.e. than that derived in Table 3.3) – possibly a few hundreds of nanometers thick.

Table 3.3: X-ray Penetration Depths for ZrN at 2, 4 and 6° incident angles.

2Theta	hkl	X-ray Penetration Depth (μm)		
		2°	4°	6°
33.83	111	1.091	3.265	5.385
39.27	200	1.098	3.294	5.390
56.74	220	1.111	3.346	5.407
67.74	311	1.115	3.362	5.423
71.18	222	1.126	3.366	5.431

The nitrogen-containing Zr phase can be seen to feature prominently in the GAXRD pattern. This phase was found to closely resemble HCP α -Zr phase [59] (PDF no. 01-089-3045) in terms of the number of peaks and exhibited similar peak intensities. However, the peaks can be seen to be shifted to lower angles of 2θ indicating the incorporation of nitrogen in solid solution in the zirconium matrix (where nitrogen would be interstitially diffused at random interstitial sites of the Zr lattice), which in turn generated higher interplanar spacing. The peaks for this phase can also be seen to maintain similar intensities with increased angle of incidence which is consistent with the region of the nitrogen diffusion zone shown earlier from the cross-sectional optical micrograph in Figure 3.14. Furthermore, the Zr-N binary phase diagram (Figure 1.13) shows that, in thermodynamic equilibrium, the α -Zr lattice is limited to accepting only appreciable amounts of nitrogen (up to about 24 at%), but the lattice may be forced to accept more nitrogen atoms by plasma processing. Therefore, a supersaturated nitrogen interstitial solution may be formed, which distorts the Zr lattice and thus shifts the nitrogen-containing Zr peaks to lower angles of 2θ as seen from the GAXRD pattern in Figure 3.15.

On closer inspection, the peak shifts of the nitrogen-containing Zr phase appear to be higher than for the ZrN reference phase. For instance, the peak shift of the nitrogen-containing Zr phase in the (002) reflection is about 0.7° relative to the reference Zr phase whereas the peak shift for the ZrN phase for the (111) reflection is about 0.4° (relative to the reference ZrN phase). The higher difference of the peak shifts to lower angles of 2θ for the nitrogen-containing Zr phase suggests greater severe lattice distortion of the nitrogen diffusion zone compared to the ZrN phase of the compound layer. This is because during TPN treatment, at low substrate bias (-200 V), nitrogen ion species arriving at the surface are able to interstitially diffuse at random sites in the HCP α -zirconium lattice, which results in an expansion of the lattice parameters of the Zr sites. However, with increased treatment time, the interstitial sites become saturated and a stoichiometric Face-Centred Cubic ZrN compound layer is formed which limits further nitrogen diffusion due to a lower diffusion coefficient of nitrogen in ZrN compared with nitrogen in pure zirconium and allowing the ZrN compound layer to increase in thickness with treatment time. On the balance of evidence, the detection of a nitrogen-containing zirconium phase and the slight shift to lower angles of 2θ of the peaks indexed to the ZrN phase

indicates that the nitride compound layer is thin - likely to be hundreds of nanometers in thickness. The severity of the lattice distortion can be determined using TEM analysis and this is commented on in Chapter 6 - Recommendations.

To the best of my knowledge, TPN diffusion treatment of zirconium has never been reported in the literature. However, TPN treatment of titanium has quite extensively been investigated. Titanium has similar structural properties to zirconium, for instance they are both group IV transition metals; the α - β transition is around 882°C [264]. One key difference however, is that titanium forms rutile (tetragonal), anatase (tetragonal) and brookite (orthorhombic) polymorphs upon oxidation whereas zirconium forms monoclinic, tetragonal and cubic polymorphs. Nonetheless, TPN treatments carried out on titanium would provide good comparisons for nitrogen diffusion zone and compound layer formation. In one study, Cassar et al [256] performed TPN diffusion treatments on Ti-6Al-4V alloy metal at -200 V substrate bias at 700°C for 4h which was the same parameters used in the TPN treatment of zirconium. The author reported a compound layer thickness of around 0.25 μm comprising of Face-Centred Cubic titanium nitride (TiN) phase and a nitrogen diffusion zone (just below the nitride compound layer) using TEM. The GAXRD patterns showed a shift to lower angles of 2θ and this was attributed to an interstitial solid solution of nitrogen having distorted and expanded the Ti lattice. In a different study, Cassar et al [261] used Triode Plasma Oxidation to show that α -Ti peaks shifted to lower angles of 2θ , attributed to the dissolution of interstitial oxygen that resulted in an expansion of the Ti-metal lattice that formed an oxide compound layer and oxygen diffusion zone (oxygen-containing titanium phase).

As mentioned earlier, Zr_3N_4 (Cubic) phase was one of the other minority nitride phases detected, with diffraction peaks at 2θ angles of 32.5° and 50.6° in the (112) and (123) reflections respectively. The intensities of these peaks can be seen to decrease with increasing incident angle and the phase was negligible at an incident angle of 6°, which suggests a thin layer of Zr_3N_4 (maybe less than 500 nm) had formed near the surface of the compound layer. There is little evidence in the literature that report the formation of Zr_3N_4 following TPN treatment, however, it would be interesting to further characterise this using TEM analysis. The formation of Zr_3N_4 using different fabrication routes has been previously reported by Fragiell et al [265], who used reactive magnetron sputtering to deposit ZrN onto AISI 316L-grade stainless steel and progressively increased the nitrogen concentration during deposition. It was reported that as the nitrogen concentration increases, the N/Zr ratio also increases, leading to the metastable Zr_3N_4 phase formation, when the ratio reaches a value of 1.4 [266].

In a different deposition technique, Pichon et al [177] for example used ion beam assisted deposition (IBAD) to sputter deposit Zr onto silicon wafers and amorphous silica in a nitrogen/argon (50:50)

atmosphere. The author found that lower temperatures (500°C) favour the formation of metastable Zr_3N_4 whilst at higher temperatures (700°C) nitrogen can be implanted into the growing Zr film leading to the formation of stable ZrN. This would suggest Zr_3N_4 had formed initially at/near the substrate interface followed by ZrN formation. This appears to be in contradiction to the findings from this work, which show that Zr_3N_4 peak intensities are highest at an incident angle of 2° and decrease when approaching the substrate interface at higher incident angles. This discrepancy could be due to the fact that a different treatment technique and deposition parameters such as temperatures, pressures and durations were adopted in this work for fabrication of the TPN-treated layers which may have influenced its formation at these conditions. The beneficial properties of Zr_3N_4 include high hardness (around 26 GPa [267]) and good chemical and thermal stability, although the effect this has when the overall compound layer and diffusion zone thickness is considered is not well understood, but nonetheless is beyond the scope of this study.

One method that might be used to increase the thickness of the nitride compound layer and nitrogen diffusion zone would be to carry out TPN treatments for a longer duration (i.e. 8 hr) at low substrate negative bias (i.e. 200 V) to achieve a sufficiently 'deep' nitrogen diffusion zone case depth. This should be followed by a higher substrate negative bias (i.e. 600 or 800 V) for a short duration (i.e. 1 hr) to achieve a thick nitride compound layer. This step could introduce greater surface defects due to higher energies of nitrogen ions bombarding the substrate so the short 'burst' durations may need to be adjusted. The study could investigate the optimum hardness and adhesion properties that could be obtained using TPN diffusion treatments and is further commented on in Chapter 6 – Recommendations.

3.7 Determining Vibrational Modes of the Plasma-Nitrided Zr Layer Using Raman Spectroscopy

Raman spectroscopic analysis was performed on the 2 hr, 3 hr and 4 hr TPN-treated Zr samples and the spectra are presented in Figure 3.16. Raman spectroscopy was performed at room temperature using 514 nm wavelength green laser photons with a power of 20 mW and cosmic background inference removed.

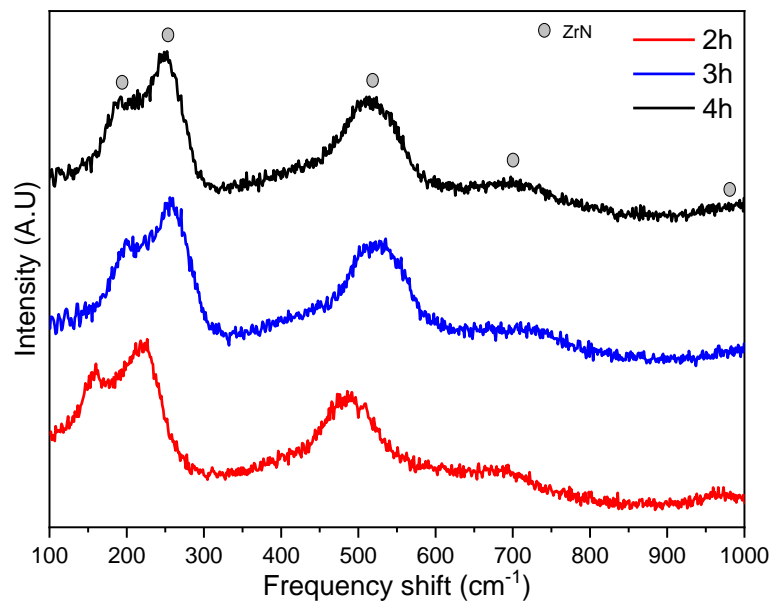


Figure 3.16: Raman spectra of the plasma diffusion treated Zr showing evolution of ZrN bands with treatment time.

The spectra of the TPN-Zr treated for 2, 3 and 4 hr durations can be seen to be dominated by five peaks at 198 cm⁻¹, 248 cm⁻¹, 512 cm⁻¹, 700 cm⁻¹ and 980 cm⁻¹ attributed to ZrN. Given that the average depth of the 514 nm laser into the sample (which is dependent on composition, density etc.) is about 300 nm [268], this is consistent with range for the detection of the ZrN compound layer (with an estimated thickness determined to be less than 1 μm from earlier discussions).

What is interesting from the Raman spectra is the shift to higher frequencies from the 2 hr to 3 hr TPN-treated samples, but little or no shift from the 3 hr to 4 hr durations. The precise reason for this disparity has not been reported in the literature. However, from the AFM images in Figure 3.10, the surface morphology for the 2 hr sample is slightly different when compared to the 3 hr sample, and the GAXRD patterns suggests that the nitride compound layer is hundreds of nanometers in thickness. Since the Penetration Depth of the Raman laser into the sample is about 300 nm [268], the slight shift of the 2 hr TPN-treated sample might indicate the boundary of the ZrN compound layer and the

interstitial nitrogen diffusion zone. This would however, require further investigation to confirm this. The Raman spectra for the 3 hr and 4 hr TPN-treated samples is in excellent agreement with the Raman spectrum reported by Spengler et al [269] (shown in Figure 3.17) in which Raman bands were attributed to ZrN around 198 cm^{-1} , 240 cm^{-1} , 510 cm^{-1} , 720 cm^{-1} and 1000 cm^{-1} . The Raman spectrum in Figure 3.17 can also be seen to show a high degree of peak broadening, whereas in this work, the peaks for the TPN-treated surface exhibited narrower bands. An explanation for this disparity may lie in the difference in the treatment techniques used whereby a compound layer is created chemically using TPN diffusion treatment in this work, whereas a nitride film is deposited using PVD coating technique with different parameters (such as pressure, temperature, duration etc) used in the work of Spengler [269] to fabricate the nitrided layer.

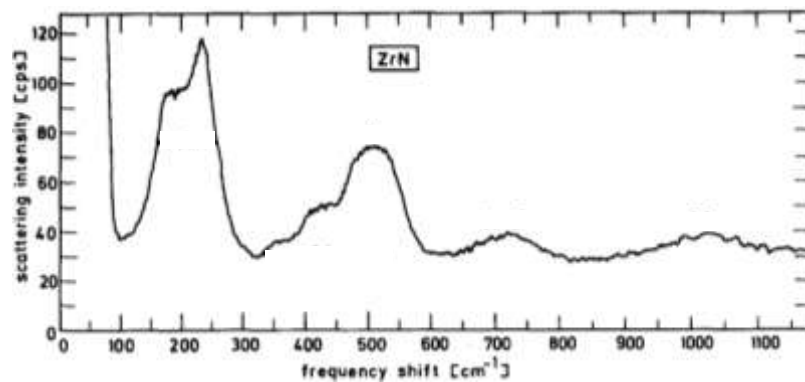


Figure 3.17: Raman scattering of ZrN [269].

In comparison, Chen et al [270], reported that ZrN peaks were dominant at 185 , 230 and 497 cm^{-1} frequency shifts which correlates well with the Raman data for the 3 hr and 4 hr TPN-treated sample carried out in this work. Constable et al [271] reported Raman bands attributed to FCC ZrN in the range 200 - 300 and 500 - 800 cm^{-1} peak positions, which is in good agreement with Raman spectra of the diffusion-treated TPN-Zr samples presented in Figure 3.16. The Raman bands at the peak positions obtained in our work were also in good agreement those reported by Singh et al [272] in which magnetron sputtering was used to fabricate ZrN films onto austenitic stainless steel (D9-grade) at 600°C (Figure 3.18). Although a different fabrication route was adopted, Figure 3.18 shows the Raman bands were identified in the 210 cm^{-1} , 500 cm^{-1} , 700 cm^{-1} and 980 cm^{-1} regions which is consistent with the ZrN peak positions obtained in this work. The author proposed that peak broadening and low intensity of the peaks exhibited in the Raman spectrum of magnetron sputtered ZrN films (Figure 3.18) is indicative of a tendency to amorphization [272] due to structural disordering and defect accumulation, however, to the best of my knowledge, this view is not reported elsewhere in the literature.

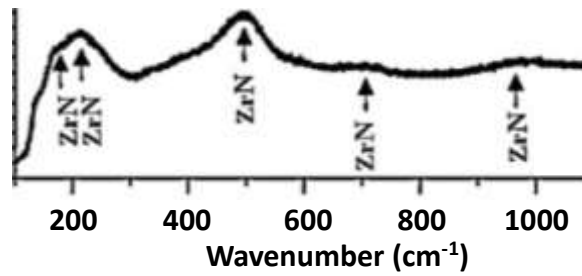


Figure 3.18: Raman Spectrum of ZrN coatings fabricated by magnetron sputtering at 600°C [272].

3.8 Hardness Measurements Using Nanoindentation

Nanoindentation testing was carried out on the untreated pure zirconium and ZIRLO™ (Zr-1%Nb-1%Sn-0.1%Fe) substrates to determine the baseline hardness of the metal substrate, which was then compared against hardness measurements carried out on TPN diffusion-treated samples. It should be noted that the late arrival of ZIRLO™ substrates as a result of commercial sensitivities surrounding the material and extensive downtime of the Tecvac machine (used to carry out the diffusion treatments) due to component failure meant it was not possible to carry out TPN treatments on ZIRLO™ substrates.

3.8.1 Nanoindentation of Bulk Zr and ZIRLO Substrates

HCP α -Zr and ZIRLO™ substrates were ground and polished according to the micropreparation regime detailed in Chapter 2 Section 2.1 prior to nanoindentation testing. A constant load of 4 mN was used and nine indents were made using a 3x3 grid array with a 10 μ m spacing between each indent on the surface of the polished substrates, as shown in the AFM images Figure 3.19(a) HCP α -Zr and (b) ZIRLO™. It was found that at a contact depth of 150 nm, the hardness of the bulk HCP α -Zr and ZIRLO™ substrates was determined to be 4.40 ± 0.20 GPa and 3.50 ± 0.20 GPa respectively.

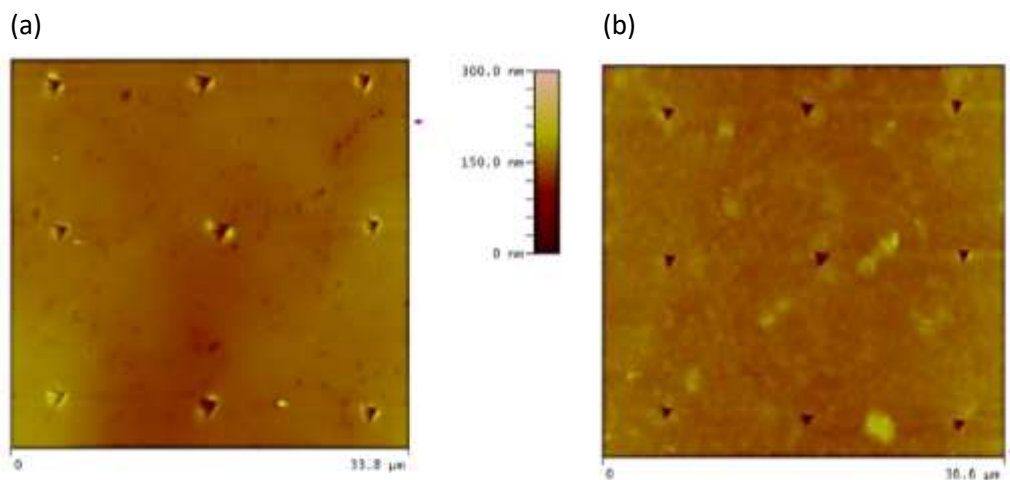


Figure 3.19: AFM image showing indents on (a) Zr and (b) ZIRLO™ substrates used to obtain hardness measurements.

Nanoindentation results revealed the hardness of ZIRLO™ was 25% less than that of the unalloyed pure zirconium. The load vs. displacement graphs in Figure 3.20 illustrate that the plastic (permanent) displacement is similar both the pure Zr and ZIRLO™ at 120-125 nm, however, the displacement at maximum load is clearly higher for the ZIRLO™ substrate (~250 nm) compared to pure Zr (~200 nm) indicating higher ductility. This could arise from two sources: The first is the technique used to manufacture the ZIRLO™ substrates which was cold-rolled and stress-relieved whereby the material is heated and held to a suitable temperature, prior to cooling the metal to a controlled rate, which is slow enough to allow the removal of crystal defects, internal stress and dislocations. This results in the material being ductile. The second is that the pure (unalloyed) zirconium was temper-annealed and work-hardened which had undergone slightly different process heat treatments which is likely to have contributed to the lower displacement at maximum load for the unalloyed pure zirconium compared to the ZIRLO™ substrate.

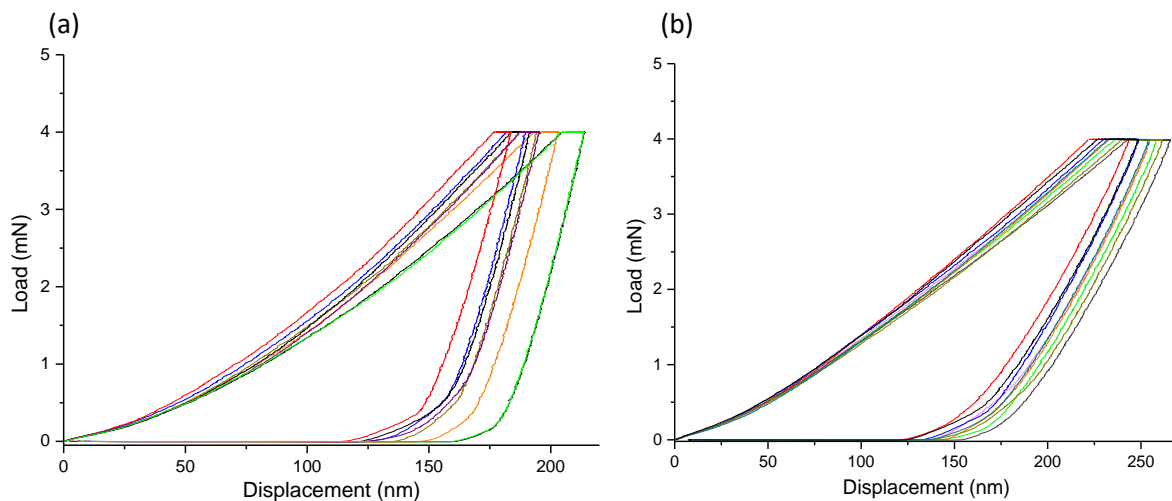


Figure 3.20: Load vs Displacement graphs showing nine indents for: (a) bulk Zr and (b) ZIRLO™.

Kuroda et al [273] carried out nanoindentation tests on pure zirconium (99.9% purity) with loads up to 1.5 mN. The average hardness obtained was 3.8 GPa. In the same study, the author showed that the average hardness obtained for pure zirconium with non-stoichiometric zirconium hydride ($ZrH_{1.518}$) inclusions was slightly lower at 3.5 GPa. Kесе et al [274] carried out nanoindentation tests on Zircaloy-2 (Zr-1.5Sn-0.15Fe-0.1Cr-0.05Ni in wt%) [275] and showed the average hardness of the bulk metal was 3.0 GPa for a higher indentation load of 10 mN than the 4mN load used in this study. Lu et al [276] investigated hardness of Zr using molecular dynamics simulations of nanoindentation, and found that hardness values lie between 3.5-4.5 GPa. This is in good agreement with the results obtained in this study. To the best of my knowledge, nanoindentation hardness studies of ZIRLO™ have been scarcely reported. Rico et al [277] for instance measured the hardness of ZIRLO™ to be 1.9 GPa. The difference was attributed to zirconium hydride (ZrH_2) inclusions in the ZIRLO™ bulk matrix in the author's work

and is known to induce cracks and defects in the lattice via formation of zirconium hydride precipitates, making the structure more brittle resulting in a lower measured hardness than the ZIRLO™ matrix without (ZrH₂) as was the case in this work. Overall, the results for hardness measurements for pure zirconium obtained in this work were found to be in good agreement with those reported in previous studies investigating hardness of pure zirconium.

3.8.2 Nanoindentation of TPN-Treated Zr

Nanoindentation tests were performed with the 2 hr, 3 hr and 4 hr TPN-treated Zr surface. Since the nitride layer comprises of the nitride compound layer (determined previously to be significantly less than 1 μm thickness) and the nitrogen diffusion zone (determined previously to be about 23 μm thickness), the hardness that is measured is likely to be a contribution of both and hence termed - 'composite' hardness. As previously mentioned in Chapter 2 Section 2.10, a load of 4 mN was used and nine indents were made in a 3 x 3 array grid with a 10 μm spacing between each indent. The size of the contact impression was kept small relative to the film thickness, typically less than 10% of the nitride compound layer thickness – to ensure minimal contribution from the HCP α-zirconium substrate.

The graph of the hardness (GPa) as a function of contact dept (nm) is presented in Figure 3.21. It can be seen that at a depth of 100 nm, the hardness of the 4 hr TPN-treated surface was measured to be 12.2 ± 0.5 GPa and the highest hardness value obtained was is about $15.9 \text{ GPa} \pm 0.5 \text{ GPa}$ at a contact depth of 85 nm. This is at least 2.5 times the hardness of the untreated pure Zr and the findings of this study suggests that TPN thermochemical diffusion treatment of pure Zr resulted in a significant improvement of the surface hardness compared to untreated pure Zr. As can be seen from Figure 3.21, linear indents reveal a gradual decrease in hardness with contact depth. The maximum contact depth of the indenter into the treated zirconium sample was ~130 nm which is possibly 20-25% of the expected thickness of the nitride compound layer (and greater than 10% limit [244] for effects from the substrate or in this case nitrogen diffusion zone). Thus, the hardness that is measured is a 'composite' hardness value from the nitride compound layer and the nitrogen diffusion zone - both of which contribute to the overall hardness measured (as mentioned previously).

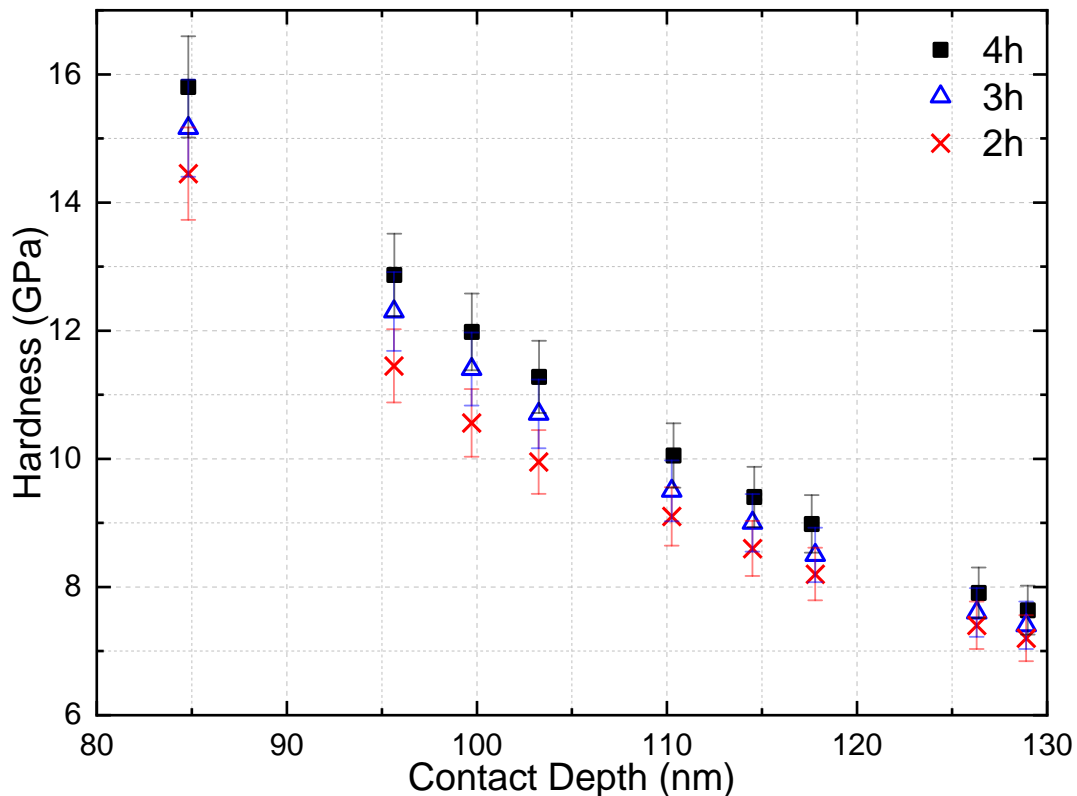


Figure 3.21: Nanoindentation graph of the 2 hr, 3 hr and 4 hr TPN-treated samples show how apparent hardness of the nitride compound layer decreases with contact depth.

The ‘composite’ hardness of the 4 hr TPN diffusion-treated surface can be seen to be slightly higher than the 3 hr sample at similar contact depths. This is because increased treatment time would result in a thicker nitride compound layer [278] (comprising of ZrN phase which has a FCC structure as determined earlier from GAXRD patterns and Raman spectra). The contribution to the overall measured hardness from the compound layer increases (due to increase in thickness with treatment time) and less so from the nitrogen diffusion zone (comprising of nitrogen at random interstitial sites in the Zr lattice) – hence, a higher ‘composite’ hardness was obtained for the 4 hr TPN-treated sample compared to the 3 hr TPN-treated sample. However, as the indenter penetrates further into the diffusion-treated layer, the ‘composite’ hardness values for the TPN-treated samples were found to decrease due to a decreased contribution from the nitride compound layer and an increased contribution to the measured ‘composite’ hardness from the nitrogen diffusion zone. Similarly, the ‘composite’ hardness of the 3 hr TPN diffusion-treated surface was found to be higher than the 2 hr TPN-treated sample. This is an interesting finding as this indicates that treatment times at low substrate biases and high partial pressure of nitrogen (70:30 nitrogen:argon gas mixture) can be tailored to provide the desired nitride compound layer thickness relative to the nitrogen diffusion zone that can influence the overall measured ‘composite’ hardness of the diffusion-treated layer. This is

because longer treatment times result in a greater number of interstitial sites of the zirconium lattice being filled by the nitrogen ion species which forms the nitrogen diffusion zone. The saturated interstitial sites allow the formation of a nitride compound layer comprising of a stoichiometric ZrN phase that increases in thickness with increased treatment time whereby the nitrogen diffusion zone increases the load-bearing capacity of the nitride compound layer resulting in the higher 'composite' hardness values being obtained for the 4 hr TPN diffusion-treated sample. Furthermore, nitrogen interstitially diffused in the HCP α -Zr (resulting the formation of a nitrogen diffusion zone) acts to impede dislocation motion – thereby making the surface-treated region harder. The results from nanoindentation measurements suggests that TPN diffusion treatment of HCP α -Zr bulk metal resulted in a higher 'composite' hardness of the diffusion-treated layer (comprising of the nitride compound layer and nitrogen diffusion zone) compared to untreated bulk zirconium metal and ZIRLO™. Due to technical issues and availability surrounding the nanoindentation equipment, multiple repeats of hardness measurements could not be performed on the same sample, thus, there may be a level of uncertainty in the hardness measurements obtained.

It is difficult to compare the hardness values obtained in this study to the literature because the TPN diffusion treatment technique used produces a nitride compound layer with a thicker nitrogen diffusion zone underneath, whereas PVD techniques produce thick coatings typically with a columnar structure. Pilloud et al [279] deposited a 3.5 μm thick ZrN coating on stainless steel substrates using magnetron sputtering of a zirconium target in an argon-nitrogen mixture and reported a hardness value of 21.8 GPa. Qi et al [187] used magnetron sputtering to deposit 1.1 μm thick ZrN coatings on silicon Si (111) wafer and reported hardness values of 19.7 GPa. Wu et al [280] used DC magnetron sputtering to produce 2.2 μm ZrN coatings and reported an average hardness value of 22.3 GPa. This is rather interesting because as can be seen from this discussion, nanoindentation tests carried out on PVD coatings typically report coating thicknesses of several microns with hardness values ranging 19-23 GPa, whereas TPN diffusion treatment resulted in a thin ZrN nitride compound layer (likely to be hundreds of nanometers) and a thick nitrogen diffusion zone with the maximum hardness value of 15.9 GPa \pm 0.5 GPa. This suggests that the nitrogen diffusion zone plays a role in enhancing the load bearing capacity of the nitride compound layer and contributing to the 'composite' hardness obtained.

Overall, TPN diffusion treatment of zirconium was shown to significantly improve the hardness-depth profile of the treated Zr surface. This was attributed to the formation of a thick nitrogen diffusion zone which provides a high load-bearing capacity to the thin nitride compound layer. An avenue of further research would be to increase the TPN treatment duration (i.e. 4 hr, 8 hr and 12 hr) to obtain a thick nitride compound layer (of a few microns) as well as a thick nitrogen diffusion zone and investigate the changes in the 'composite' hardness profiles. This could also lead to an extension of a further study

that investigates varying substrate bias voltage (increase in ion bombardment energy) and how this affects the nitrogen diffusion case depth and the formation of the nitride compound layer as well as the role played in enhancing the 'composite' hardness of the TPN-treated surface. This is commented on in Chapter 6 – Recommendations.

3.9 Scratch Adhesion of the TPN-treated Zirconium Samples

Scratch adhesion tests on TiN diffusion-treated layers [256, 281] have been previously studied and have been reported to exhibit good adhesion properties. This is an important quality in the aerospace industry as coatings/treated layers on metal components are required to maintain their mechanical integrity when operating in high temperature environments. In nuclear reactors, it is crucial to have good adhesion properties of treated layers on components that can withstand the high-pressure coolant flow between fuel rods during operation and high-temperature oxidation of components during LOCA scenarios. To the best of my knowledge, adhesion properties of TPN diffusion-treated layers on zirconium have scarcely been reported in literature. This section aims to investigate adhesion properties of treated layers as a function of treatment duration.

During scratch adhesion tests, the load applied by the stylus onto the sample (Normal Force - F_N) and the force applied by the stylus parallel to the treated-surface (Tangential Force - F_T) were used to determine the critical load of failure (L_c). Acoustic Emission (AE) signals arising from damage events of the treated layer due to the stylus penetration into the sample (along with the Tangential Force) were used to elucidate cracking behaviour of the scratch track. The Penetration Depth into the TPN-treated surface were obtained from the Anton Parr scratch adhesion tester; these parameters are described in Chapter 2, Section 2.11 - Tables 2.2 and 2.3.

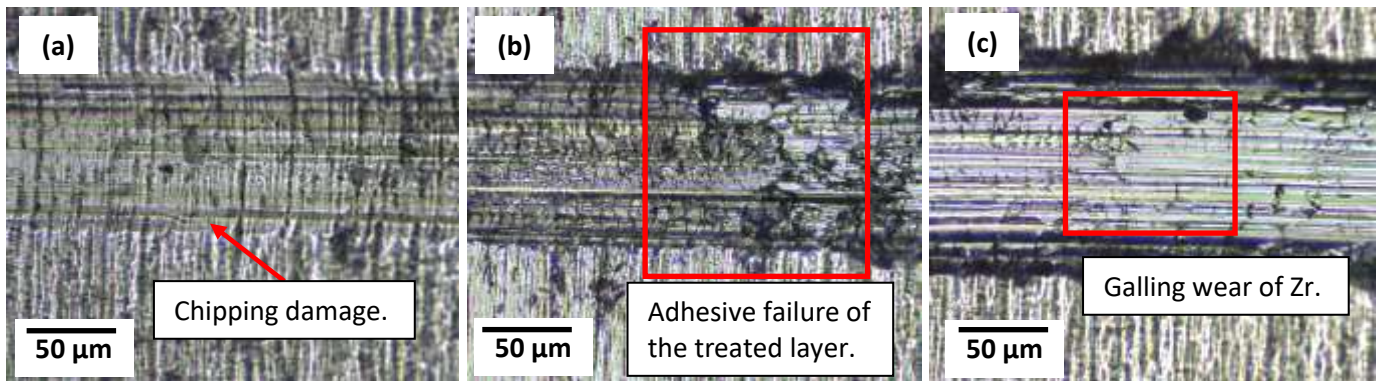
Initially, the scratch adhesion tests were conducted with an applied Normal Force up to 30 N, to determine the optimum normal loading range suitable for identifying failure modes. The increase in Tangential Force measurements and Acoustic Emission (AE) signals indicated increased cracking along the scratch track, leading to layer failure and spallation. However, optical microscopy was also used to qualitatively determine and corroborate the L_c values leading to a more accurate and reliable identification of layer failure.

When progressive force up to 10 N was applied, cohesive failure was identified, however, it was found that the force was too low for noticeable 'adhesive' failure to occur. On the other hand, when a progressive load up to 50 N was applied, critical loads (cohesive, 'adhesive' failure and complete spallation) occurred at low loads in close proximity to each other. This led to an overlap of defects,

cracks and other failure modes making it challenging to suitably distinguish between cohesive or 'adhesive' failures using optical microscopy or SEM. A series of trial and error tests conducted on the plasma-nitrided samples revealed that a progressive load ranging from 0 to 30 N was the appropriate range to identify failure modes. As the load was increased, the layer-substrate system was driven to failure which produced mechanical damage to the nitrided layer through a combination of elastic/plastic indentation stresses, frictional forces and residual internal stresses present in the layer/substrate system to induce failure modes.

3.9.1 Adhesion of the 2 hr TPN-treated Zr Sample

The 2 hr TPN-treated Zr scratch test loading profiles are presented in Figure 3.22. The optical micrograph in Figure 3.22(a) shows chipping damage on the sides of the scratch track indicating cohesive failure. The critical load (L_{c1}) at which cohesive failure occurred was 6.0 N. The scratch profile revealed linearly increasing perturbations in the Tangential Force ($F_T(N)$) as the normal applied force was increased, showing the different stages of behaviour as the tip penetrated the TPN-treated surface. It can be seen from the optical micrograph in Figure. 3.22(b), that as the Normal Force was progressively increased, the frequency of tensile cracks (shown as semi-circular arcs) along the track also increased. The magnitude of the AE signals (Figure 3.22(d)) can also be seen to increase leading up to adhesive failure of the TPN-treated layer which is a release of elastic energy during crack growth. The critical load (L_{c2}) at which adhesive failure of the TPN-treated layer occurred was 11.1 N at a Penetration Depth of $\sim 20 \mu\text{m}$. This is consistent with the thickness of the nitrogen diffusion zone determined earlier in Figure 3.14.



(d)

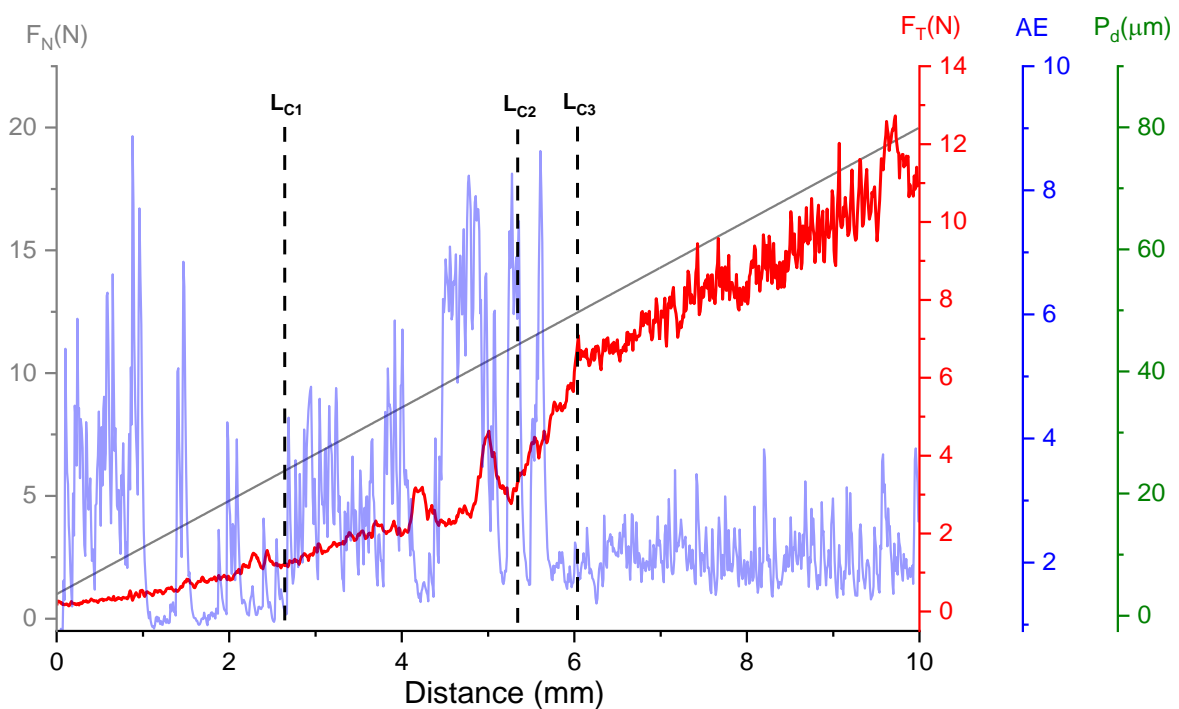


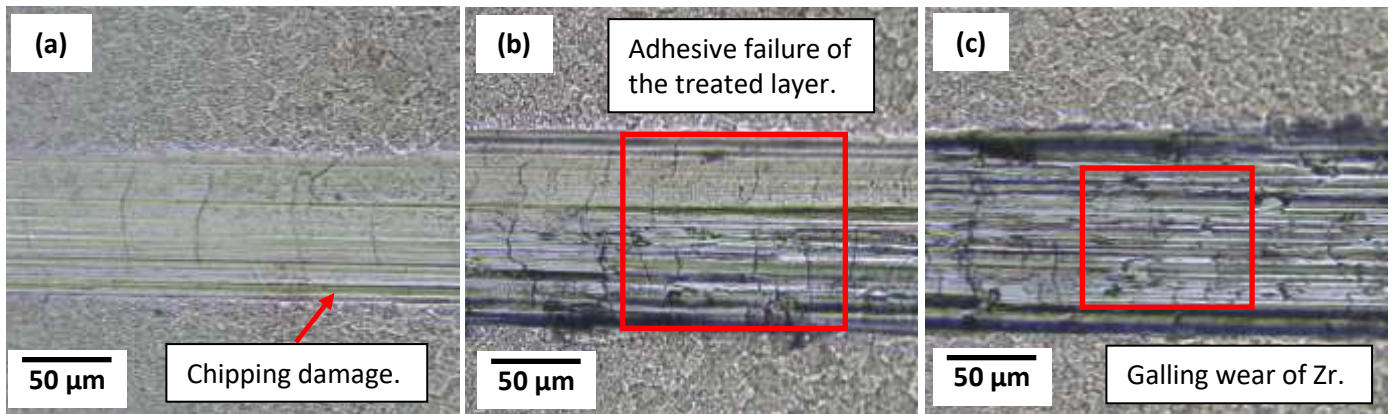
Figure 3.22: Scratch test for the 2 hr TPN-treated Zr show optical micrographs of (a) cohesive failure; (b) adhesive failure (c) complete spallation of the treated layer and (d) loading profiles at the points at which L_{C1} , L_{C2} and L_{C3} failure modes occur, identified using a combination of Tangential Force (F_T), Acoustic Emission (AE) and Penetration Depth (P_d) data.

A sharp increase in gradient of F_T loading profile indicated complete spallation of the nitrogen diffusion zone and continues to be drawn over the zirconium substrate until the end of the scratch run. This can be seen to be represented by an increased erratic pattern of the F_T loading profile (Figure 3.22(d)). The critical load (L_{C3}) at which complete spallation of the TPN-treated layer occurred was 12.5 N. This is further evidenced from the AE profile that decreased significantly when the stylus was drawn along the zirconium substrate. The optical micrograph in Figure 3.22(c) shows cracks and defects on the

exposed HCP α -zirconium metal. This is probably a result of galling wear, which is caused by the friction and adhesion of metal surfaces that are in sliding contact with each other and results in the transfer of material between metallic surfaces [282]. In this case, the zirconium metal is transferred to the diamond stylus followed by tearing of the HCP α -Zr crystal structure.

3.9.2 Adhesion of the 3 hr TPN-treated Zr Sample

The 3 hr TPN-treated Zr scratch test loading profiles are presented in Figure 3.23. Cohesive failure was determined through identification of chipping damage on the sides of the scratch track shown in Figure 3.23(a). The critical load (L_{c1}) at which cohesive failure occurred was 9.5 N. The increase in frictional force along the scratch track results in stress build-up and plastic deformation of the treated layer which is relieved through tensile cracking. As before, propagation of these cracks could be seen to increase in severity (from the optical micrograph in Figure 3.23(b)) leading up to 'adhesive' failure of the treated layer and is corroborated by an increase in magnitude of the AE signals. The critical load (L_{c2}) at which adhesive failure of the TPN-treated layer occurred was 15.0 N at a Penetration Depth of $\sim 22 \mu\text{m}$. This is consistent with the thickness of the nitrogen diffusion zone determined earlier in Figure 3.14. It can be seen that the critical load to failure for the 3 hr TPN-treated sample is higher than the 2 hr sample (Table 3.4). This is likely because of the increased load-bearing capacity of the nitrogen diffusion zone due to higher number of lattice sites of the bulk zirconium metal that are filled by the interstitial nitrogen and a thicker nitride compound layer (compared to the 2 hr TPN-treated sample) with increased treatment duration which act to increase the load-bearing capacity of the treated layer - thereby increasing the critical load to failure.



(d)

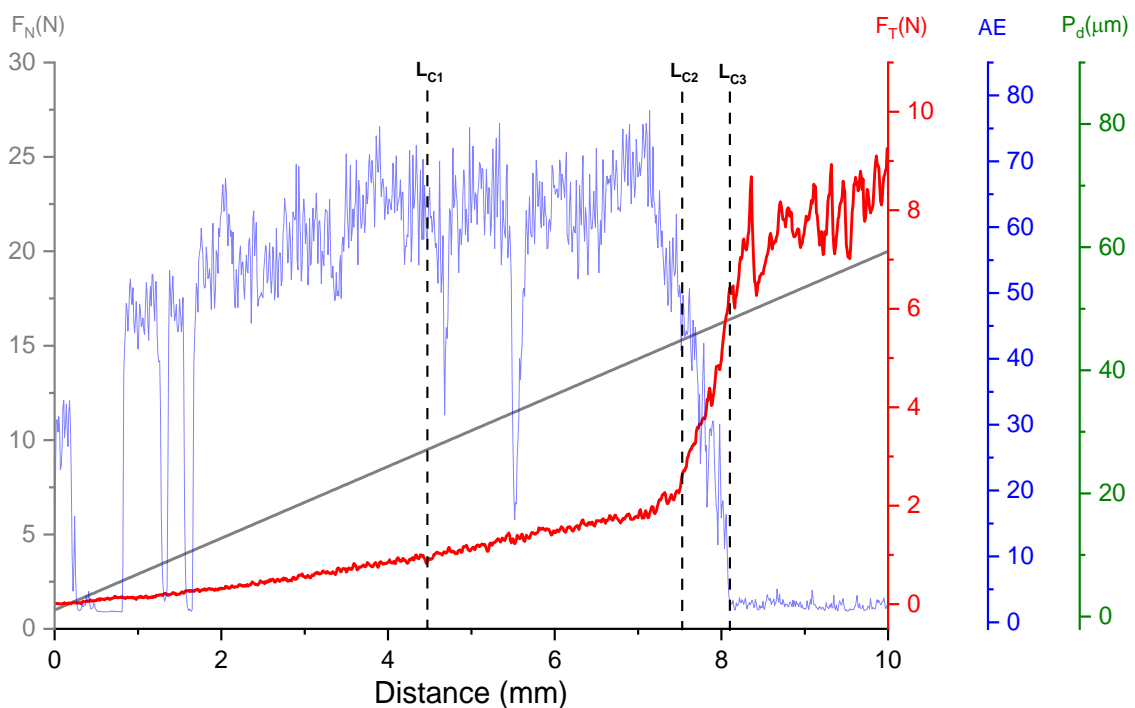


Figure 3.23: Scratch test for the 3 hr TPN-treated Zr show optical micrographs of (a) cohesive failure; (b) adhesive failure (c) complete spallation of the treated layer and (d) loading profiles at the points at which L_{C1} , L_{C2} and L_{C3} failure modes occur, identified using a combination of Tangential Force (F_T), Acoustic Emission (AE) and Penetration Depth (P_d) data.

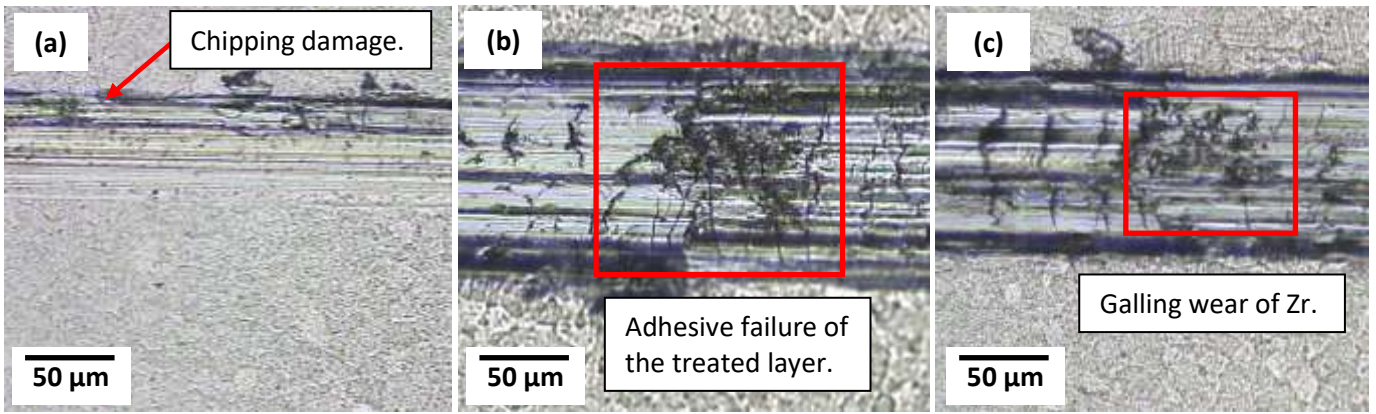
A sharp increase in gradient of F_T loading profile indicated complete spallation of the nitrogen diffusion zone. The critical load (L_{C3}) at which complete spallation of the TPN-treated layer occurred was 17.0 N. This was the region where the bulk zirconium metal had been exposed as can be seen from the optical micrograph in Figure 3.23(c). The AE profile could also be seen to decrease significantly which is consistent with the observation of the AE signal of the 2 hr TPN-treated sample Figure. 3.22(d). As

before, cracks and defects were prominently featured on the exposed HCP α -zirconium metal indicating galling wear.

3.9.3 Adhesion of the 4 hr TPN-treated Zr Sample

The 4 hr TPN-treated Zr scratch test loading profiles are presented in Figure 3.24. Cohesive failure was determined through identification of chipping damage which could be seen as a pile-up of material at the edges of the scratch track shown in Figure. 3.24(a). The critical load (L_{C1}) at which cohesive failure occurred was 8.5 N at a Penetration Depth of about 11 μm (Figure. 3.24(d)) which is similar to the values obtained for the 2 hr and 3 hr TPN-treated samples. Following cohesive failure of the treated layer, tensile cracking along the scratch track was seen to an increase in severity leading up to 'adhesive' failure (Figure 3.24(b)) and this is shown by an increase in magnitude of the AE signal in Figure 3.24(d). The critical load (L_{C2}) at which adhesive failure of the TPN-treated layer occurred was 15.5 N at a Penetration Depth of $\sim 25 \mu\text{m}$. This is consistent with the thickness of the nitrogen diffusion zone determined earlier in Figure 3.14 and in fairly good agreement with the Penetration Depths obtained at L_{C2} determined for the 2 hr and 3 hr diffusion-treated samples. The critical load to failure at L_{C2} was found to be highest for the 4 hr TPN-treated sample. This suggests that increased treatment duration results in an increased resilience to failure of the treated layer. This is likely due to a higher number of lattice sites at the bulk metal filled by interstitial nitrogen and a thicker nitride compound layer (compared to the 2 hr and 3 hr TPN-treated samples) which provides an increased the load-bearing capacity of the treated layer allowing high critical loads to be reached before failure occurs. It would be useful to carry out scratch adhesion tests on samples subjected to longer TPN treatments (i.e. 8 hrs and 12 hrs) which would result in much thicker nitride compound layers and study what affect having a thicker nitride compound layer has on adhesion properties and the achieving a higher critical load to failure of the treated surface.

It is interesting to note the slightly different pattern of the Tangential Force scratch loading profile compared to the previous samples. This could be due to accumulation of crack defects along the scratch track that may influence spallation of some regions of the treated layer compared to the 2 hr and 3 hr samples.



(d)

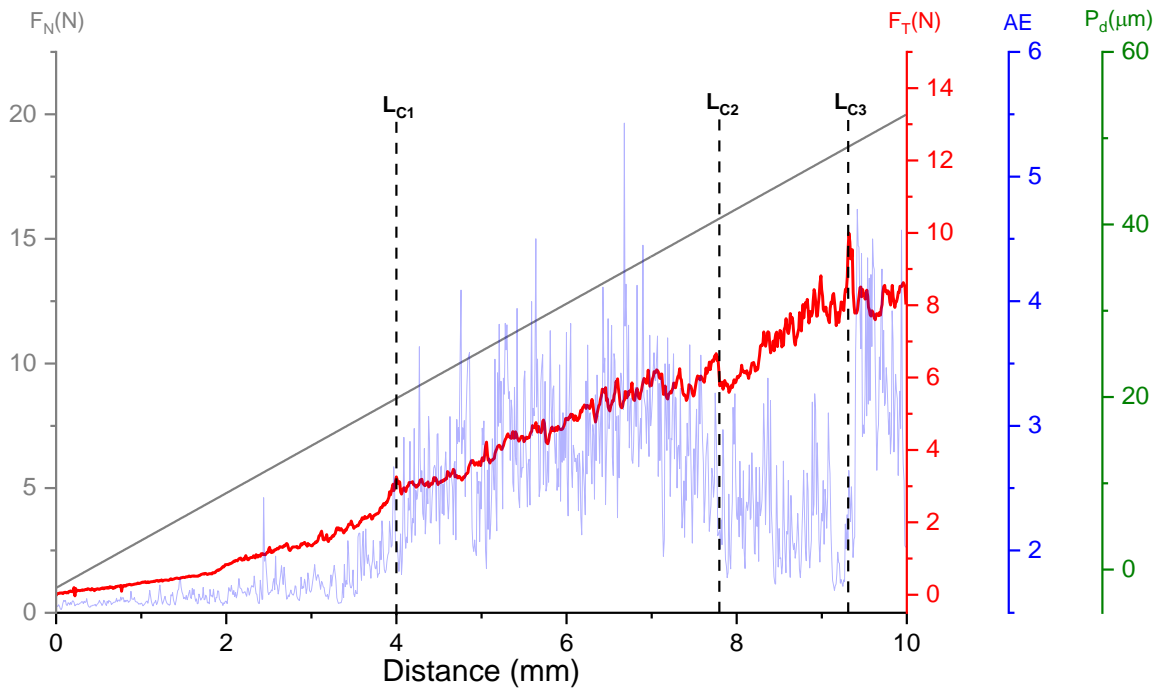


Figure 3.24: Scratch test for the 4 hr TPN-treated Zr show optical micrographs of (a) cohesive failure; (b) adhesive failure (c) complete spallation of the treated layer and (d) loading profiles at the points at which L_{C1} , L_{C2} and L_{C3} failure modes occur, identified using a combination of Tangential Force (F_T), Acoustic Emission (AE) and Penetration Depth (P_d) data.

As the indenter load on the sample was progressively increased, a sharp increase in gradient and erratic fluctuations of the Tangential Force profile indicated complete spallation failure at L_{C3} . The critical load at which this occurred was 17.0 N.

Table 3.4: Summary of the critical load values for the 2 hr, 3 hr and 4 hr TPN diffusion-treated Zr samples.

Sample	L _{C1} (N)	L _{C2} (N)	L _{C3} (N)
2 hr TPN Zr	6.0	11.1	12.5
3 hr TPN Zr	9.5	15.0	17.0
4 hr TPN Zr	8.5	15.5	17.0

It is also interesting to note that the scratch test profiles for any of the treatment durations did not indicate the penetration of the nitride compound layer. This would have been expected to occur at low normal loads during the scratch test since the thickness of the nitride compound layer was determined to be significantly less than 1 μm (as mentioned previously). This is because the Rockwell C tip used (of 250 μm diameter) is too large to detect the point at which the tip penetrates the compound layer, much of which would have delaminated. It has been suggested that the Rockwell C indenter used provides reliable information on adhesion properties for surface-treated layers/coatings with thicknesses greater than 1 μm but becomes challenging below this limit.

3.10 Summary

In summary, the results presented in this chapter make several noteworthy contributions which increase our understanding of the effects of plasma-nitriding of zirconium substrates. Principally the findings show that TPN thermochemical diffusion treatment was successful in the fabrication of a nitride compound layer comprising of stoichiometric Face-Centred Cubic ZrN phase of thickness significantly less than 1 μm (likely to be hundreds of nanometers) and a ~ 23 μm thick nitrogen diffusion zone. From GAXRD patterns, the peak shift to lower angles of 2θ for peaks attributed to a nitrogen-containing metallic-Zr phase when compared to HCP α -Zr peaks, indicated that nitrogen was in interstitial solid solution with the zirconium lattice.

The 'composite' hardness of the treated layer was shown to be significantly improved after TPN treatment (ranging between 10 to 12 GPa) compared to untreated zirconium or ZIRLO™ substrates (4.5 and 3.5 GPa respectively). Increasing treatment time was shown to result in higher 'composite' hardness of the TPN-treated layer. The scratch adhesion profiles demonstrated that increased plasma treatment duration resulted in an increased load-bearing capacity of the treated layer, owing to the use of low substrate bias and high partial pressures of nitrogen. The 4 hr TPN-treated sample showed higher resilience to failure before critical loads were reached compared to the 2 hr and 3 hr TPN-treated samples. This indicates that overall, longer treatment times result in an improved load-bearing capacity of the TPN-treated layer.

Chapter 4 – Hydrothermal Oxidation Tests

4.1 Background

One of the most important aspects of a successful layer or surface treatment intended to be used in the core of nuclear reactors is its stability in water at operating temperatures/pressures. In this regard, an attempt was made to investigate and analyse oxidation behaviour of TPN-treated Zr samples in simulated reactor conditions. Previous studies have focused on thermal oxidation behaviour of zirconium nitride coatings/layers in air [192, 283, 284], but a survey of the literature showed that hydrothermal oxidation studies of TPN surface-treatments have not been reported.

Hydrothermal oxidation tests of the TPN-treated Zr samples were performed (at Westinghouse Pittsburgh, USA) with deionised water in an autoclave at 360°C for 3 days at a pressure of 18.7 MPa to investigate the oxidation behaviour and stability of TPN-treated zirconium samples in pressurised water conditions (simulating reactor environments without neutron irradiation) according to the ASTM G2-06 method [104]. Further details of the experimental parameters can be found in Chapter 2, Section 2.12. The aim of this work was to test the hypothesis that TPN diffusion treatment could be used to improve the oxidation resistance of bulk zirconium metal in aqueous conditions via the formation of a zirconium nitride compound layer and nitrogen diffusion zone on the diffusion-treated surface. In this study, Optical Microscopy, GAXRD and SEM/EDX techniques were used to determine phase formation and post-corrosion composition evaluation. Nanoindentation hardness measurements and scratch adhesion tests were used to analyse hardness and adhesion strength properties respectively, and these results were compared to the TPN-treated Zr samples previously discussed in Chapter 3.

4.2 Hydrothermal Oxidation Testing in Water

The morphology of the hydrothermally oxidised TPN-treated Zr sample diffusion-treated for 4 hr was analysed using SEM in BSE mode and presented in Figure 4.1. The micrograph revealed extensive cracking across the surface and exhibited interconnecting micro-cracks creating a network of diffusion pathways allowing for water and oxygen migration into the oxide scale. Similar cracking behaviour at the surface of the oxide scale was also seen for the 2 hr and 3 hr TPN-treated samples. The presence of microcracks at the surface of the oxide scale was found to be consistent with observations from SEM micrographs of Zircaloy-4 reported by Harlow et al [62] and Preuss et al [102] hydrothermally oxidised at 360°C.

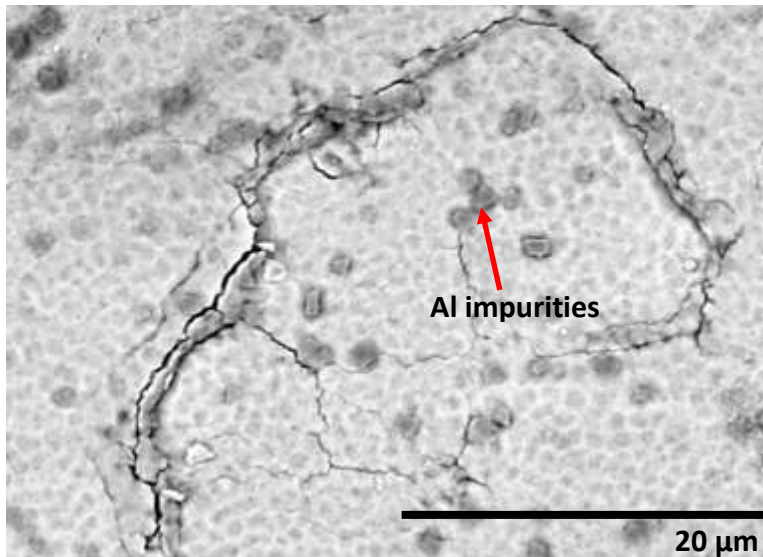


Figure 4.1: SEM micrograph in BSE mode of the hydrothermally oxidised 4h TPN-treated sample showing micro-cracks on the oxide surface formed following hydrothermal tests at 360°C for 3 days. The dark artefacts present on the oxide surface were identified as aluminium- and oxygen-rich regions from EDX analysis (Figure 4.2). This was not detected for the TPN-treated samples from SEM/EDX analysis in Figure 3.9 or from GAXRD patterns presented in Figure 3.15 and is likely to be aluminium (possibly oxide) impurities inside the autoclave due to insufficient cleaning (of the autoclave) prior to hydrothermal oxidation tests.

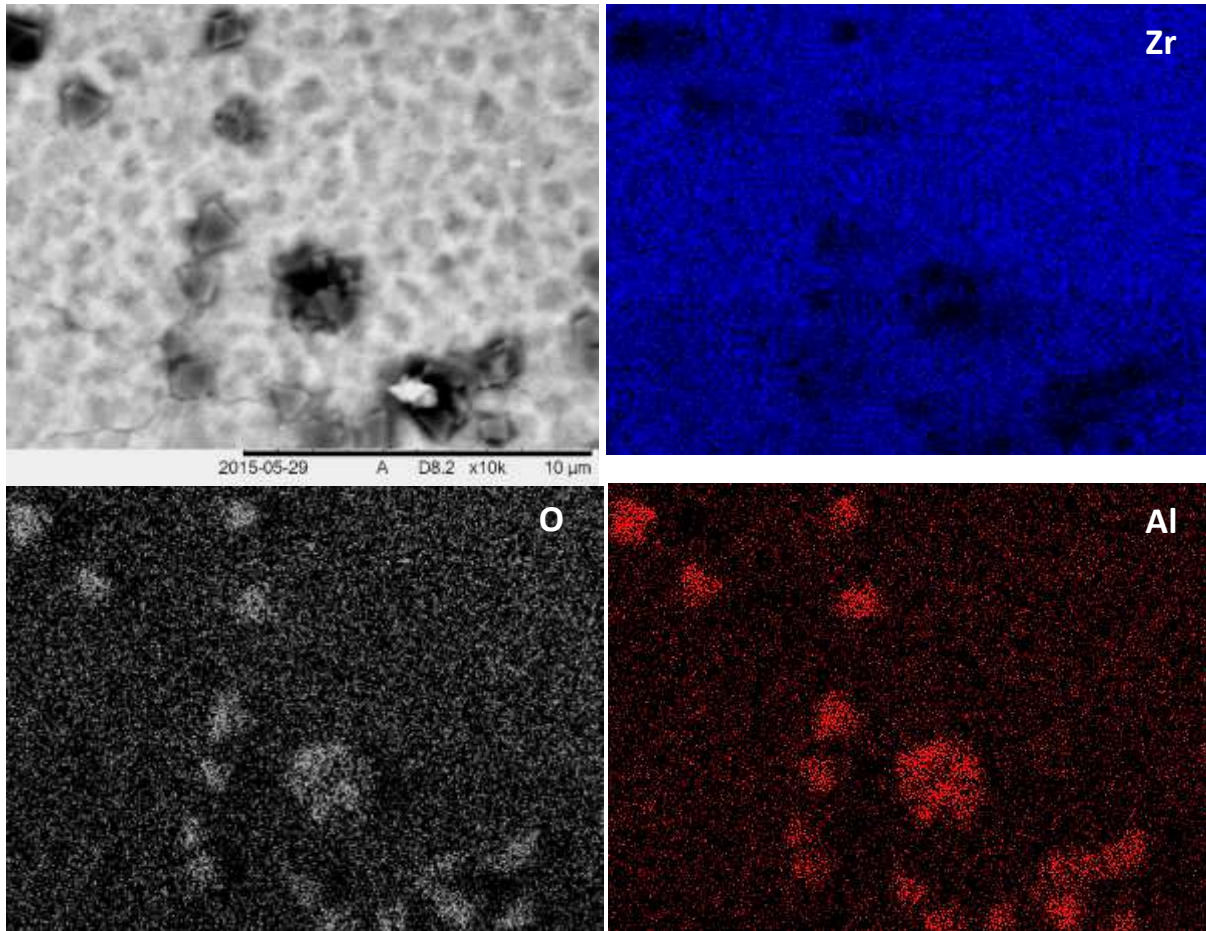


Figure 4.2: SEM micrograph in BSE mode shows aluminium and oxygen contamination (highlighted in bright red and grey from EDX analysis) on the surface of the oxide scale following hydrothermal oxidation at 360°C for 3 days.

The samples were weighed before and after hydrothermal oxidation tests and the difference was divided by the total area of each sample to determine the weight gain in mg/dm². These are presented in Table 4.1.

Table 4.1: Hydrothermally oxidised TPN-treated Zr samples showed slightly lower weight gains compared to pure Zr under the same conditions.

Hydrothermal Corrosion Testing at 360°C for 3 days		
TPN Duration	Reference	Weight Gain (mg/dm ²)
2 hr	A_TPN_2hr	131
3 hr	A_TPN_3hr	129
4 hr	A_TPN_4hr	126
Untreated pure Zr	A_Zr	150

Table 4.1 shows the 2 hr, 3 hr and 4 hr TPN-treated samples hydrothermally oxidised at 360°C for 3 days showed similar weight gains of 131, 129 and 126 mg/dm² respectively. The untreated pure zirconium had a weight gain of 150 mg/dm² which is greater than the oxide weight gain formed on any of the TPN-treated samples. However, the oxide weight gain for the TPN-treated samples are on the similar order of weight gain as the untreated pure Zr. An interesting point to note is that although the TPN treatments show a slight improvement in oxide weight gain with time, the weight gain was found to decrease with increased TPN treatment time. Furthermore, the oxide scale formed on the TPN-treated Zr samples for all treatment durations was measured to be 10 ± 0.5 µm (discussed further in Section 4.2.1). This result is surprising for 2 main reasons. The first is that the oxidation rate for zirconium (as was mentioned in Chapter 1 Section 1.8.2) follows either parabolic or cubic kinetics. Even if a linear rate law for oxidation kinetics was considered, it would be expected that the oxide weight gain should be higher. The second is that the environment causing the conditions for oxide growth would still be present during hydrothermal oxidation (360°C, 18.7 MPa for 3 days) so the oxide scale should be thicker. But as just mentioned, the oxide scale thickness was similar for all TPN treatment durations. The cross-sectional SEM micrograph in Figure 4.3(a) shows the oxide scale to contain cracks and suggests that the oxide scale is brittle and 'flaky', where the oxide is likely to have undergone some material loss (indicating oxide spallation). Therefore, on the balance of evidence, from the comparisons of the weight gains following hydrothermal oxidation of TPN-treated samples and the untreated pure Zr substrates, the actual weight gain and the oxidation rate and thickness is likely to have been higher than measured because of the similar measured oxide scale thicknesses for these samples indicating oxide spallation at these conditions. Although the TPN treatments did not significantly improve the oxidation resistance of zirconium, it did not make it worse either.

To the best of my knowledge, there have been no studies that have reported on hydrothermal oxidation of untreated pure zirconium at these conditions. A litany of studies investigating the oxidation resistance of zirconium alloys exist in the literature because of the wide commercial application as cladding and core components in nuclear reactors. As such, previous studies have primarily focussed on oxidation behaviour of Zr alloys such as Zircaloy-2, Zircaloy-4 and ZIRLO™ in different environments - including steam, low and high temperature water and neutron bombardment (to analyse radiation damage on cladding) [50, 90, 285, 286]. However, the latter introduces the added complexity of swelling and creep effects arising from neutron irradiation, which goes beyond the scope of this study. Following successful trials, neutron irradiation investigations should be carried out to gain an in-depth understanding of how the surface-treated layer will perform under neutron bombardment and this subject is commented on in Chapter 6 - Recommendations.

Analysis of the weight gains obtained in this work reveals important findings when compared to the reported figures in the literature. Hillner et al [47] for example, showed that hydrothermal oxidation tests of Zircaloy-4 specimens at 360°C in deionised water for 250 days resulted in a weight gain of ~130 mg/dm². The author identified that this falls within the pre-transition regime, characterised by the formation of an oxide scale that grows thicker in accordance with a cubic rate law, however, the author failed to mention the crystallographic structure of the oxide scale. Similar weight gains were obtained for the TPN-treated samples investigated in this study but only in 3 days, indicating TPN-treated Zr samples had undergone rapid oxidation at these conditions. Wei et al [88] demonstrated that untreated ZIRLO™ substrates showed a weight gain of only ~15 mg/dm² in 10 days when tested in lithiated water (2 wt.ppm) at 360°C. In a different study, Yueh et al [287] hydrothermally oxidised untreated ZIRLO™ substrates at 360°C (with varying Sn content) and reported low oxide weight gains of 20-30 mg/dm² after 25 days. Kim et al [288] reported that oxidation of Zircaloy-4 and ZIRLO™ substrates at 700°C (steam environment) resulted in oxide weight gain of less than 5 mg/dm² when tested for one hour but a significant increase to 400 mg/dm² was determined when tested at a temperature of 1200°C. From Table 4.1, untreated pure zirconium hydrothermally tested at 360°C showed an oxide gain of about 150 mg/dm² after 3 days. Thus, when comparing oxide weight gains of pure Zr and the Zr alloys reported in the literature, it can be deduced that the pure zirconium substrate performs 10 to 30 times worse. This is because of the corrosion resistance offered by the elements that form intermetallic precipitates such as tin, iron and chromium [289]. As mentioned in Chapter 1 Section 1.7.2, the low solubility of iron, chromium and tin generate intermetallic precipitates within the individual grains to give increased mechanical strength by hindering dislocation movement – but do not segregate to the boundaries. At reactor operating temperatures (300-330°C), the thermodynamic driving force is insufficient to allow these elements to segregate to the grain boundaries in the same way that interstitial elements such as nitrogen, carbon, oxygen and boron can migrate via a hopping mechanism [260] at interstitial sites of α -Zr lattice. For example, chromium (used in stainless steel) is a strong nitride former [290] and will travel a shorter distance towards the grain boundaries compared nitrogen. Both these elements prefer to migrate to the grain boundary because it is less dense than at the grains. For this reason, nitrogen or oxygen tend to produce precipitates with alloying elements that they are most reactive with and have the strongest affinity for, in or near the grain boundaries, which leads to a precipitation hardening effect for the reason described previously.

In zirconium, the alloying elements involved cannot migrate nor segregate to the grain boundaries at these temperatures so they coalesce locally over a few atom lengths to produce a coherent phase that becomes large enough to precipitate out, because of the stress differences between the lattice

parameters of the growing intermetallic precipitate, and the parent HCP α -Zr metal it is growing out of. In zirconium alloys, the main function of the alloying elements is to generate precipitates (as intermetallic phases) within the grains of the HCP α -Zr metal to precipitation strengthen the zirconium metal – but does not lead to segregation at the grain boundaries that could cause chemical composition profiles that would otherwise lead to galvanic effects and intergranular corrosion [291], or create a multi-phased structure (i.e. via Zr polymorphs) that might damage the corrosion properties. The beneficial side-effects of this are two-fold:

1. The intermetallic precipitates improve the mechanical strength of the alloy by hindering dislocation motion. Intermetallic precipitates within the zirconium lattice serve as pinning points creating physical blockades that act to halt dislocation movement, requiring a greater amount of stress to be applied to overcome the barrier. Impeding dislocation movement in this way will hinder the onset of plasticity and hence increase the yield strength and hardness of the material.
2. The alloying elements that form the intermetallic precipitates play an important role in controlling and reducing the oxidation rate [42]. The low oxidation rate offered by intermetallic precipitates results in a pore-free, dense, stressed and elastically constrained oxide scale [292] that is durable during the early stages of oxidation of Zr alloys, and serves to protect the metal. Thus, the intermetallic phases being precipitated within the grains has a negligible deleterious effect on the corrosion of the alloy. This compared to thicker oxide scales (formed with increased oxidation treatment time) that exhibits diminishing compressive stress (with thickness), volume expansion and microcracks in the oxide scale resulting in the oxide scale being non-protective.

It can be deduced therefore, that the precipitation hardening process that improves the corrosion resistance of zirconium alloys described previously is absent for the hydrothermally oxidised pure Zr presented in this study. The net benefit for zirconium alloys during oxidation is that the corrosion chemistry of the oxide is changed whereby the alloying elements are substituted at random Zr sites in the oxide scale that is changing the charge characteristics of the oxide.

Despite the slight improvement in the oxidation performance of the TPN-treated Zr surface in aqueous conditions compared to pure Zr, the results show that TPN treatment did not worsen the oxide weight gain. The beneficial properties deduced in Chapter 3 such as improved surface hardness, good adhesion of the TPN-treated layers and good chemical and neutronic compatibility with Zr-alloy, suggests that it may be more promising to have a TPN-treated layer at the fuel/cladding internal interface, where hydrothermal oxidation is not an issue (as fuel cladding internals comprise of UO_2

fuel pellets and are backfilled with helium gas. This subject would be an avenue of research worthy of further investigation. The next sub-section will analyse the crystallographic structure of the oxide layer to better understand the oxidation process and potential routes that could be taken to increase oxidation resistance.

4.2.1 Cross-sectional SEM Analysis of the Oxide Scale formed on TPN-treated Zr and Untreated Pure Zr Following Hydrothermal Oxidation

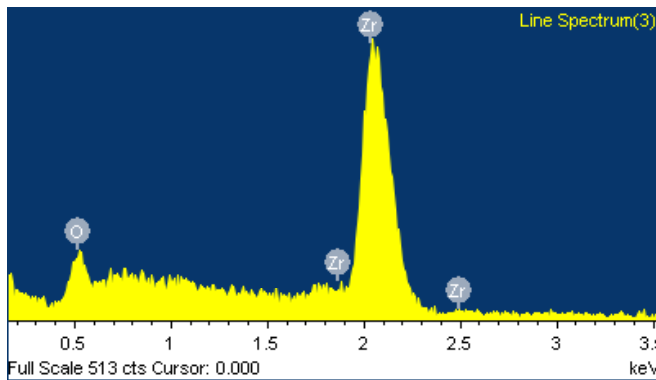
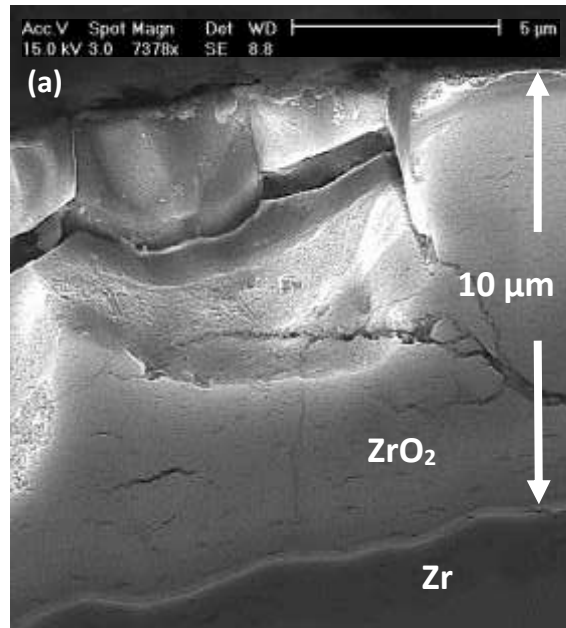
Cross-sectional SEM micrograph of the hydrothermally oxidised (4h) TPN-treated sample is presented in Figure 4.3(a) and revealed the oxide scale thickness to be $10 \pm 0.5 \mu\text{m}$. The thickness was found to be identical for the oxide scales formed following hydrothermal oxidation of samples that were TPN-treated for 2 hr and 3 hr. This demonstrates that the TPN treatment duration did not significantly affect the thickness of the oxide scale developed following hydrothermal oxidation testing. EDX analysis on the oxide scale in Figure 4.3(b) revealed the oxide elemental composition to be 68.4 at% oxygen, 31.6 at% zirconium. The micrograph further revealed that the cracks formed in the oxide scale were perpendicular to the substrate surface and extend much deeper into the oxide layer - as far as the oxide/substrate interface. Interestingly, it was also found that crack formation increased in severity with distance away from the oxide/substrate interface.

The relation of the oxide thickness and its weight gain is typically expressed in the following convenient formula: $1.5 \text{ mg/dm}^2 = 0.1 \mu\text{m}$ [50], which expresses that for every $0.1 \mu\text{m}$ Zr consumed results in a weight gain of about 1.5 mg/dm^2 . Using this simple relation (with the oxide weight gain of 126 mg/dm^2 from the A_TPN_4hr sample) to solve for the oxide thickness y in this work for calculating the weight gain gives:

$$y = \frac{0.1}{1.5} \times 126 \quad (4.1)$$

$$y = 8.4 \mu\text{m}$$

The calculated oxide scale thickness obtained from the expression in 4.1 is slightly lower than the thickness of the oxide scale formed on the TPN-treated Zr (measured from the SEM micrograph in Figure 4.3). It is worth noting that the expression provides an estimation of the thickness and would vary depending on the conditions used during the oxidation test. For instance, this relation was found to be in reasonable agreement when Arima et al [50] tested this under flowing CO_2 for Zircaloy-2, but may show differences under high pressure/temperature aqueous conditions.



Element	Atomic%
O	68.4
Zr	31.6
Total	100.0

Figure 4.3: (a) Cross-sectional SEM micrograph of the oxide scale formed on the hydrothermally oxidised TPN-Zr at 360°C, 3 days (A_TPN_4hr) and (b) EDX data show Zr and O elements present in the oxide scale.

The thickness of the oxide scale following hydrothermal oxidation suggests that the ZrN compound layer (which was determined to be much less than 1 μm in Chapter 3 Section 3.6) had been entirely consumed and that the nitrogen-containing diffusion zone had been partially consumed by about 10 ± 0.5 μm into the TPN-treated layer. The literature investigating how this occurs is scarce. However, a closer look at the binding energies between zirconium, nitrogen and oxygen might offer some insight. The binding energy data for Zr-Zr obtained from X-ray Photoelectron Spectroscopic (XPS) data is 178.9 eV; for Zr-N this is 179.6 eV and for Zr-O this is 182.3 eV [293]. This might suggest that the binding energy of nitrogen to zirconium is similar to zirconium itself, where the binding energy of oxygen to zirconium is higher than both. This would require further research, but it might explain how oxygen can readily replace nitrogen in ZrN and chemically convert it oxide. Unlike the a nitride (or oxide)

compound, neither interstitial nitrogen that forms the nitrogen diffusion zone (or interstitial oxygen) are chemically bound to the zirconium metal itself, but the solubility of oxygen in zirconium is higher than that of nitrogen – and this implies (but does not directly prove) that oxygen uptake in zirconium metal will be faster than that of nitrogen at any given temperature.

The cross-sectional SEM micrograph in SE mode (presented in Figure 4.4) shows crack propagation and spallation near the outer pre-formed oxide scale (furthest away from the oxide/metal interface) – revealing crater-like features. This is an indication that the oxide scale could be brittle and supports the argument that the oxide weight gain and thickness of the oxide scale may have been higher than measured following hydrothermal oxidation at 360°C for 3 days.

The extensive crack defects and porosity present in the oxide scale increases its susceptibility to spalling and delamination and severely limits its overall load-bearing capacity under mechanical strain. Three main factors for this process have been attributed to the spallation process: (i) Lattice mismatch at the metal interface between the zirconia structure and the Zr substrate [294]; (ii) Differences in thermal expansion coefficient between the zirconium metal and the growing oxide [77], which generates compressive stress in the oxide and the tensile stress in the metal and (iii) gradual reduction of compressive stress within the growing oxide scale. This could lead to further migration of oxidative species into the Zr alloy cladding through cracks and pores resulting in an accelerated oxidation rate and reduced oxidation resistance of the Zr alloy.

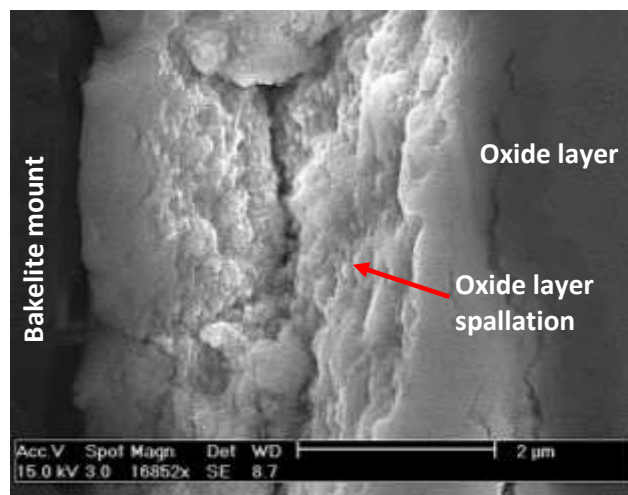


Figure 4.4: Cross-sectional SEM micrograph of (A_TPN_4hr) sample near the pre-formed outer oxide layer showing spallation of the oxide scale near the oxide surface.

The cross-sectional SEM micrograph of the oxide scale formed on the untreated pure zirconium substrate following hydrothermal oxidation is presented in Figure 4.5. The oxide scale thickness was measured to be $12.1 \pm 0.5 \mu\text{m}$ which is greater than the oxide scale formed on the TPN-treated zirconium under the same oxidation conditions. This is in fairly good agreement with the oxide weight gain of $150 \text{ mg}/\text{dm}^2$ determined for the untreated pure Zr in Table 4.1. The micrograph shows evidence of lateral microcracks which increase in severity with distance from the oxide/metal interface region. Oxide spallation near the pre-formed outer oxide scale was also observed. This shows how easily oxide material is lost through spallation which is likely to have occurred during hydrothermal oxidation. This supports the earlier proposition that the oxide weight gain and oxide scale thickness may have been higher than measured due to the spalling of the oxide scale during hydrothermal oxidation.

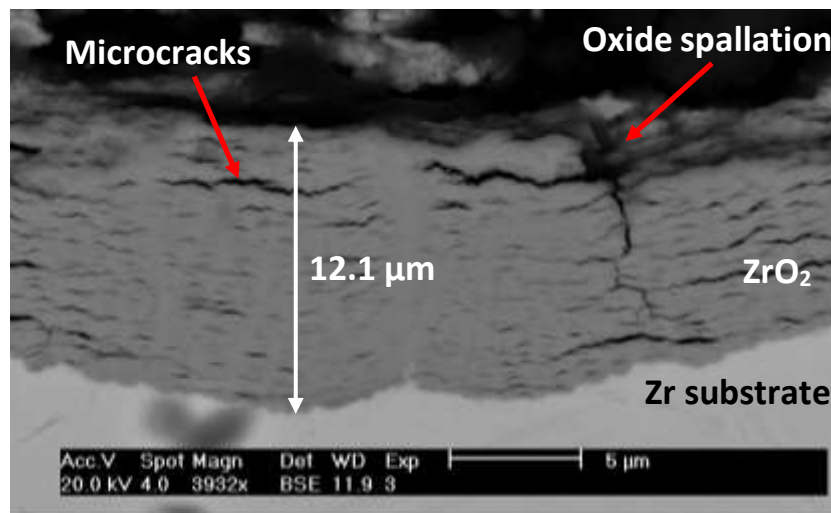


Figure 4.5: Cross-sectional SEM micrograph of the oxide scale formed on the hydrothermally oxidised pure zirconium at 360°C, 3 days.

4.2.2 Phase Analysis of the Hydrothermally Oxidised TPN-Zr

Glancing-Angle X-Ray Diffraction was used for the identification of phases formed on the hydrothermally oxidised 4h TPN-Zr sample (A_TPN_4hr) and is presented in Figure 4.6. This was performed using a Philips X'Pert³ (Panalytical) diffractometer (CuK_α radiation) operated in glancing-angle configuration (Seeman-Bohlin geometry) at incident angles ranging from 1° to 8° with a step size of 0.02 and a time step of 5 seconds in the 25° to 80° range of 2θ.

It is apparent from the GAXRD patterns that monoclinic zirconia (m-ZrO₂) was the predominant phase detected from incident angles ranging between 1 and 8°. Identical GAXRD patterns were also obtained for the hydrothermally oxidised 2 hr and 3 hr TPN-treated samples. The majority of the peaks were indexed to the monoclinic zirconia phase with the highest intensity peak of this phase detected (200) reflection at a 2θ angle of 34.1°. It can be seen from the GAXRD patterns that the peak intensities remain largely unchanged with increased angle of incidence with the exception of the ($\bar{1}11$) peak at 2θ angle of 28.2° which shows a slightly decreasing intensity with lower angles of incidence. The monoclinic zirconia phase was found to be detected at an incident angle of 8° (i.e. deeper into the oxide scale) which corresponds to an X-ray Penetration Depth of about 8.5 μm into the ZrO₂ layer²². The peak positions for the m-ZrO₂ phase can be seen to be in good agreement when compared with Kudoh et al [56] (Figure 4.6) and are consistent with findings reported by Smith et al [295] and Hill et al [296]. Tetragonal zirconia was also identified in the (011) reflection at 2θ angle of 30.4°. This phase was detected at an incident angle of 8° and decreased with lower incident angles. This indicates that the tetragonal zirconia phase is present in higher concentrations closer to the metal/oxide interface region. At an incident angle of 5° (i.e. further away from the metal/oxide interface region), the peak intensity of the tetragonal phase is negligible. The GAXRD pattern in Figure 4.6 also shows a slight shift to lower angles of 2θ indicating an increase in lattice parameters due to interstitial diffusion of oxygen in the bulk metal. In addition, the oxide scale growth is further accelerated due to the rapid diffusion paths for oxygen through the oxide scale (e.g. column boundaries, grain boundaries) as well as oxygen ingress through the network of microcracks formed in the growing oxide scale shown in Figures 4.3 and 4.4.

²² X-ray Penetration Depth was calculated using AbsorbDX tool associated with PDF4+ phase analysis software.

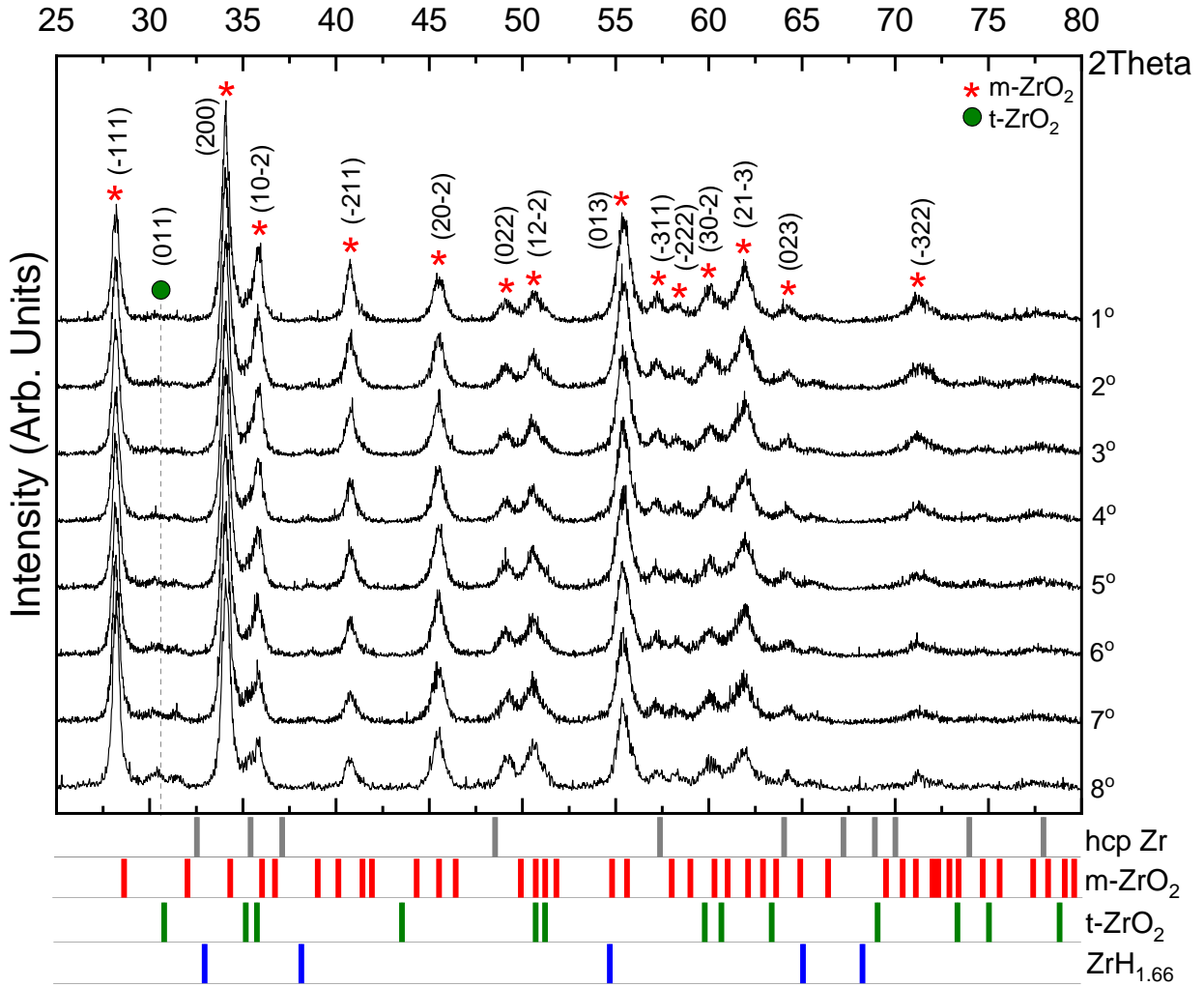


Figure 4.6: GAXRD patterns of the 4 hr TPN-Zr sample following hydrothermal oxidation test at 360°C 3 days show majority of the peaks are identified with the formation monoclinic zirconia. The phases formed and peak positions were compared with HCP α -Zr [59], m-ZrO₂ [56], t-ZrO₂ [57] and ZrH_{1.66} [126].

The volume fraction of the monoclinic and tetragonal zirconia polymorphs in the oxide layers was calculated using the Garvie-Nicholson formulae [106] in equations 1.6 and 1.7 (refer back to Chapter 1, Section 1.8.5 for details) which is shown below. This was carried out using the intensity values from the GAXRD pattern obtained at an incident angle of 8° because this was the intensity of the tetragonal zirconia peak was recorded to be highest at this incident angle. The volume fraction of monoclinic zirconia in the oxide is:

$$X_m = \left[\frac{I_{002}^m(281) + I_{-111}^m(308)}{I_{002}^m(281) + I_{-111}^m(308) + I_{011}^t(31)} \right] \cdot 100 \quad (4.2)$$

$$X_m = \sim 95\%$$

The volume fraction of tetragonal zirconia in the oxide is:

$$X_t = \left[\frac{I_{011}^t(31)}{I_{002}^m(281) + I_{-111}^m(308) + I_{011}^t(31)} \right] \cdot 100 \quad (4.3)$$

$$X_t = \sim 5\%$$

The volume fraction measurements of tetragonal zirconia for zirconium oxide scale comprising of a monoclinic/tetragonal-zirconia mixture near the zirconium alloy metal/oxide interface region have been widely reported in the literature. Lin et al [78] reported tetragonal zirconia content of about 8 vol% at the metal/oxide interface following hydrothermal oxidation at 350°C in water and found that the volume fraction decreased with oxide thickness. Yilmazbayhan et al [63] measured the tetragonal zirconia volume fraction to be 14 vol%, and decreasing to 7 vol% with increased distance away from the substrate interface. Polatidis et al [70] reported similar findings of 10-15 vol% tetragonal zirconia near the interface region. Petigny et al [77] used in-situ XRD to measure the tetragonal volume fraction of Zircaloy-4 and reported values of 10-15 vol% near the metal/oxide interface region, decreasing to about 5 vol% in the oxide scale located more than 3 μm away from the interface region.

As can be seen, the volume fraction of tetragonal zirconia (Equation 4.3) is slightly lower than the values reported in the literature. One reason for this could be because the maximum operating incident angle on the diffractometer is 8°. The X-ray Penetration Depth at this angle corresponds to an oxide thickness of about 8.5 μm. When comparing the measured oxide scale thickness of ~10 ± 0.5 μm to the GAXRD pattern presented in Figure 4.6, the SEM micrograph (Figure 4.3(a)) confirms that the oxide scale thickness is greater than that determined from attenuation depth of X-rays at an incident angle of 8° (which was 8.5 μm). This means that the metal/oxide interface is not detected when the highest incident angle of 8° is used where the X-ray Penetration Depth is also greatest. If the interface region was detected, then a few of the peaks of the GAXRD pattern obtained may have shown α-Zr peaks indicating the detection of the bulk zirconium metal. It is apparent therefore, that the oxide scale detected at 8° incident angle (from the GAXRD patterns in Figure 4.6) is a few microns away from the interface region. Furthermore, if 8-16 vol% t-ZrO₂ content - widely reported in the literature is to be believed, this would indicate that the volume fraction of 5 vol% for t-ZrO₂ is not at the oxide/metal interface but rather some distance away from the interface region.

The average crystallite size was calculated using the Scherrer Formula [297]:

$$D = \frac{K\lambda}{\beta \cos \theta} \quad (4.4)$$

Where,

D = crystallite size (nm)

K = 0.9 (Dimensionless shape factor, Scherrer constant)

λ = 0.15406 nm (wavelength of X-ray source)

β = FWHM (in radians)

θ = peak position (in radians)

Peak fitting of the diffraction pattern (of the 8° incident angle) was performed to determine the zirconia crystallite size. The fitting was performed manually using Origin software package and the background ‘noise’ was removed using a built-in linear model. The required parameters used to calculate the average crystallite size are shown in Equation 4.4 and the results are shown in Table 4.2:

Table 4.2: Average zirconia crystallite size calculated using the Scherrer equation.

Peak Position (2Theta)	FWHM	Crystallite Size D (nm)
28.19	0.17	46.43
30.27	0.18	44.27
34.08	0.17	47.08
35.79	0.20	39.96
40.75	0.18	45.66
45.51	0.18	46.69
49.11	0.19	45.02
50.65	0.21	42.79
55.44	0.20	44.56
57.17	0.19	45.53
58.37	0.20	44.11
60.11	0.22	40.78
61.90	0.21	42.26
64.17	0.20	45.12
71.29	0.21	45.07
Average Crystallite Size (nm)		44.36

The average of the m- and t-ZrO₂ phases at an incident angle of 8° was calculated to be ~44 nm. This falls within the expected crystallite grain size range of 40-60 nm reported by Yilmazbayhan et al [63] from X-ray synchrotron radiation results of hydrothermally oxidised Zircaloy-4 at 360°C. In a different

study, Garner et al [76] carried out TEM and EBSD analysis on hydrothermally oxidised Zircaloy-4 samples and reported crystallite grain size ranging 10-50 nm. This is also in fairly good agreement with the calculation presented in this work.

It is worth noting that peaks for the FCC ZrN compound layer - identified in Figure 3.15 following TPN diffusion treatment were not detected from the GAXRD pattern in Figure 4.6. The primary peak positions for the ZrN phase would have been expected in the (111) reflection at 2θ angle of 34.1° or (200) reflection at 2θ angle of 39.3° . Furthermore, peaks attributed to the nitrogen-containing Zr phase which would have been identified as Zr peak shifts to lower angles of 2θ , were also not identified from the GAXRD pattern. This suggests that the ZrN compound layer and part of the nitrogen diffusion zone had been consumed by the oxide scale.

The GAXRD pattern in Figure 4.6 shows none of the peaks match the peak positions for the detection of the zirconium hydride phase. As previously mentioned in Section 1.8.7, once the solubility limit for hydrogen absorption is exceeded, hydrogen is typically found in solid solution in the α -Zr matrix and as the cladding cools (i.e. during maintenance or periodic shutdown of the reactor), the hydrogen present in the bulk metal precipitates as zirconium hydride [48]. However, the oxide scale thickness formed following hydrothermal oxidation was $10\ \mu\text{m}$ (Figure 4.3(a)) and from the GAXRD pattern in Figure 4.6, at 8° angle of incidence, the X-ray Penetration Depth into the oxide scale is $8.5\ \mu\text{m}$ which is $1.5\ \mu\text{m}$ away from the interface region. Therefore, the presence of zirconium hydride precipitates cannot be discounted since the X-ray Penetration Depth is too low for the detection of zirconium hydride which would be present in the bulk metal and by extension it cannot be concluded at this stage whether the nitride compound layer and nitrogen diffusion zone (developed using TPN diffusion treatment of bulk HCP α -Zr substrate) was successful in impeding the diffusion of hydrogen or the formation of zirconium hydride precipitates upon cooling.

In the literature, Moya et al [75] reported zirconium hydride (ZrH_2) phase (from XRD peaks) beneath the monoclinic oxide scale after hydrothermal oxidation tests of Zircaloy-4 at 360°C for 5 days. A dominant peak attributed to ZrH_2 was exhibited at 2θ angle of $\sim 33^\circ$. As a recommendation for future work, it would be worth configuring the diffractometer to allow GAXRD to be performed at higher incident angles to analyse the interface region (particularly the outer bulk metal surface) where zirconium hydride is expected to form. Neutron diffraction is another technique that could be used to detect the presence of zirconium hydride in the bulk metal [298]. This investigation would be useful since neutrons have a comparatively higher Penetration Depth into the sample to X-rays and the contribution to the diffracted intensity of atoms with low Z atomic number is strong even in the presence of higher Z (atomic number) elements which would be ideal for the detection of zirconium

hydride. Furthermore, as an extension to this study, it would be worth carrying out hydrothermal oxidation treatments for longer period of time (i.e. 50 days) to investigate if hydrothermal treatment time increases the probability of hydride formation in bulk zirconium which has been reported for zirconium alloys in the literature [96, 299]. Despite the onset of oxidation of the TPN-treated samples, this is an encouraging result to emerge from the data, since bulk the zirconium does not show obvious signs of cladding embrittlement (largely due to the distribution and orientations of ZrH₂ precipitates in the Zr alloy cladding) which is considered to be a major problem in the nuclear industry.

On the balance of evidence presented in this study, a benefit of the ZrN compound layer is that it increases the overall 'composite' hardness of the TPN-treated layer (Chapter 3, Section 3.8.2). But once the ZrN compound layer is entirely consumed by the oxide scale, the benefit of having a nitrogen-containing diffusion zone is that the nitrogen in the interstitial sites of the zirconium lattice suppresses oxygen migration into the diffusion zone - thereby delaying oxidation compared to pure zirconium.

As mentioned previously, the oxide scale thickness of $10 \pm 0.5 \mu\text{m}$ shows that the nitrogen diffusion zone was partially consumed by about $10 \mu\text{m}$ with $\sim 13 \mu\text{m}$ of the diffusion zone remaining (since the thickness of this layer was determined to be about $23 \pm 1 \mu\text{m}$ - see Figure 3.14). Since the weight gain and the thickness of the oxide scale formed on the TPN-treated surface is lower compared to pure zirconium. This shows that there is evidence of sustained resistance to oxygen ingress by the nitrogen diffusion zone compared to untreated pure zirconium. But it is not known to what extent the sustained resistance to oxygen ingress would be. This would require further investigation and is commented on in Chapter 6 – Recommendations.

On the balance of the evidence presented, the results suggest that the first few oxide layers formed generate a high level of stress because of the Pilling-Bedworth ratio effect. The oxide grows by inward diffusion of oxygen so that in forming a new layer of oxide, the metal-oxide interface is elastically constrained. Tensile stress is generated in the HCP α -Zr metal substrate as a reaction to the compressive stress created by the P-B ratio of the tetragonal zirconia to the substrate. Thus, tensile stress in the substrate may have a tendency to expand the metal lattice structure and enhance the inward diffusion of oxygen through the oxide scale and into the metal.

The compressive stress in the oxide therefore, is highest at the Zr-ZrO₂ interface and decreases with distance from the oxide/metal interface [102] and diminishes to the point where the (metastable) tetragonal zirconia phase is no longer elastically constrained and therefore reverts back to monoclinic zirconia phase. As new t-ZrO₂ forms at the interface and the pre-formed t-ZrO₂ moves further away from the interface, the compressive stress in the oxide continues to diminish and is associated with a volume expansion of about 3-5 vol% [64, 108] of the oxide. This is likely the main cause of the network

of cracks observed in the oxide scale (from SEM micrograph in Figures 4.3(a) and 4.5) as it continues to grow from the metal during oxidation. This provides an explanation for why cracks appear less frequently near the metal-oxide interface and more cracks observed near the outer oxide scale providing pathways for the compressive stress to be relieved. The volume expansion would cause any existing cracks within the oxide scale to grow or multiply and creates additional compressive stress that would lead to the oxide scale to spall. A similar compressive stress gradient is present in the oxide scale formed on the TPN-treated layer due to similar oxide growth mechanism. Qi et al [300] analysed the oxidation behaviour of magnetron sputtered ZrN films on Si wafers using high temperature X-ray diffraction (HT-XRD) and concluded that the volume expansion of the oxide was responsible for the compressive stress - originating from the P-B ratio effect, giving rise to the martensitic transformation from the tetragonal phase to the monoclinic phase (whereby t-ZrO₂ is no longer constrained due to diminishing compressive stresses that are insufficiently stabilise the t-ZrO₂ phase). This results in the presence of defects such as cracks that are interconnected across the porous oxide scale that allow further migration of oxidative species into the bulk Zr metal through cracks and pores resulting in an accelerated oxidation rate and reduced oxidation resistance of zirconium.

In zirconia-toughened alumina, (metastable) t-ZrO₂ (~20 wt%) [301] is induced into the alumina matrix which is hot-pressed to compact the structure at high temperature and is then cooled. There is a propensity for t-ZrO₂ to transform back to m-ZrO₂ but is prevented from doing so because the tetragonal zirconia is constrained by the alumina. As the cracks propagate through the alumina, it reaches a tetragonal zirconia particle that is constrained by compressive stress which can be relieved as the oxide continues to grow – allowing the t-ZrO₂ to transform to m-ZrO₂. This expands the aluminium matrix and causes cracks in the oxide scale because of its inability to accommodate the volume expansion. The stress associated with the expansion due to the phase transformation acts in opposition to the stress that promotes the crack propagation [302]. As the crack approaches a critical size where the material could fail, it reaches a tetragonal zirconia particle that allows the constrained stress of the matrix to be relieved and transforms the crack into several smaller cracks – each of which require energy to grow into a critical size again. This counterintuitive mechanism of inducing more cracks makes the material tougher, because the energy associated with crack propagation is dissipated both in the tetragonal to monoclinic transformation and in overcoming the compressive stress due to volume expansion [303]. The physical mechanism described is analogous to the growing oxide in this study. The cracks present in the oxide prior to reaching a critical size approach tetragonal zirconia that is no longer elastically constrained and transforms to monoclinic zirconia allowing compressive stress to be relieved through the generation of new smaller cracks. But in this case, this makes the oxide

more 'friable' at the surface and so the severity of the cracks is greater at the pre-formed outer oxide scale.

4.2.3 Raman Spectroscopy of the Hydrothermally Oxidised Sample

Although some qualitative studies and research have been carried out on zirconia using Raman spectroscopy [90, 304], information about the zirconia polymorphs formed on TPN-treated zirconium after hydrothermal oxidation is rather scarce. In this work, Raman measurements were collected using a Renishaw inVia Raman microscope with 514 nm laser and the frequency shift acquisition was taken from 0 to 1000 cm^{-1} with the spectrum adjusted to minimise the effects of cosmic background radiation. This was carried for the A_TPN_4hr sample (hydrothermally oxidised 4 hr TPN-treated) at 360°C for 3 days and compared against the 4 hr TPN-treated sample (discussed previously) and the Raman spectra are presented in Figure 4.7.

The Raman spectrum of the TPN-treated Zr sample hydrothermally oxidised at 360°C for 3 days exhibited multiple Raman bands which ranged from 100 to 700 cm^{-1} , all of which are attributable to m-ZrO₂ (confirming that the oxide scale was detected). This was found to be in good agreement with Kurpaska et al [305], who showed Raman bands corresponding to m-ZrO₂ in similar peak positions to those of the results presented in this study. It is interesting to note that the Raman spectrum for the A_TPN_4hr sample exhibited no peaks that could be attributed to t-ZrO₂ phase. The average depth of the 514 nm laser into the sample (which is dependent on composition, density etc.) is about 300 nm [268] which is close to the surface of the oxide scale. This is consistent with the findings from the GAXRD patterns presented in Figure 4.6 which show no t-ZrO₂ peaks were detected at an incident angle of 1° – near the preformed outer oxide layer. Taken together, the results confirm earlier findings that tetragonal zirconia concentration is highest at the metal/oxide interface and decreases with increased distance from the interface region as t-ZrO₂ phase is no longer elastically constrained and therefore reverts to the thermodynamically favourable monoclinic zirconia. Thus, it is unsurprising that t-ZrO₂ is not found near the oxide scale surface. Furthermore, the Raman spectrum for the (4 hr) TPN-treated sample (Figure 4.7(a)) can be seen to be dominated by two strong peaks at 238 cm^{-1} and 498 cm^{-1} attributable to ZrN which is within the range for the detection of the nitride compound layer - determined to be significantly less than 1 μm (Figure. 3.15). However, the A_TPN_4hr sample did not exhibit any ZrN peaks and given that the Raman sampling depth is about a few hundred nanometers [268] (as mentioned earlier), this suggests that the ZrN compound layer was consumed at these conditions.

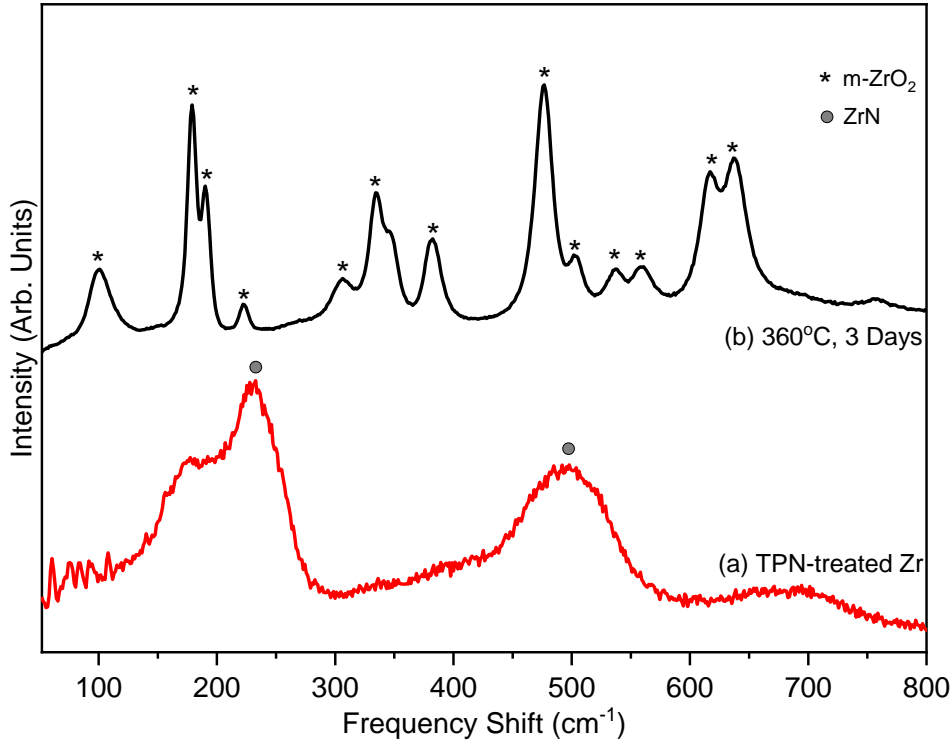


Figure 4.7: Raman spectra showing comparisons of (a) TPN-treated Zr; (b) A_TPN_4hr sample.

4.2.4 Surface Roughness Measurements of the Hydrothermally Oxidised Samples

The average surface roughness (R_a) of the TPN-treated Zr samples hydrothermally oxidised at 360°C for 3 days were determined from optical profilometry measurements from five locations chosen on the surface. The results in Figure 4.8 indicate that there is a significant increase in the surface roughness (more than 2x) of the oxide scale following hydrothermal treatment of the A_TPN_2hr, A_TPN_3hr and A_TPN_4hr samples with R_a measured to be $2.14 \pm 0.05 \mu\text{m}$, $2.25 \pm 0.05 \mu\text{m}$ and $1.93 \pm 0.05 \mu\text{m}$ compared to the TPN-treated Zr of $0.45 \pm 0.05 \mu\text{m}$, $0.67 \pm 0.05 \mu\text{m}$ and $0.87 \pm 0.05 \mu\text{m}$, respectively. The differences in the R_a values obtained for the hydrothermally oxidised TPN-treated samples could be due to the presence of defects i.e. cracks and pores that were identified earlier from SEM micrographs of the cross-section and of the surface of the oxide scale. Another likely source might be from the effects of oxide spallation mentioned earlier that resulted in a rough and uneven surface topology that might account for the higher surface compared to TPN-treated Zr.

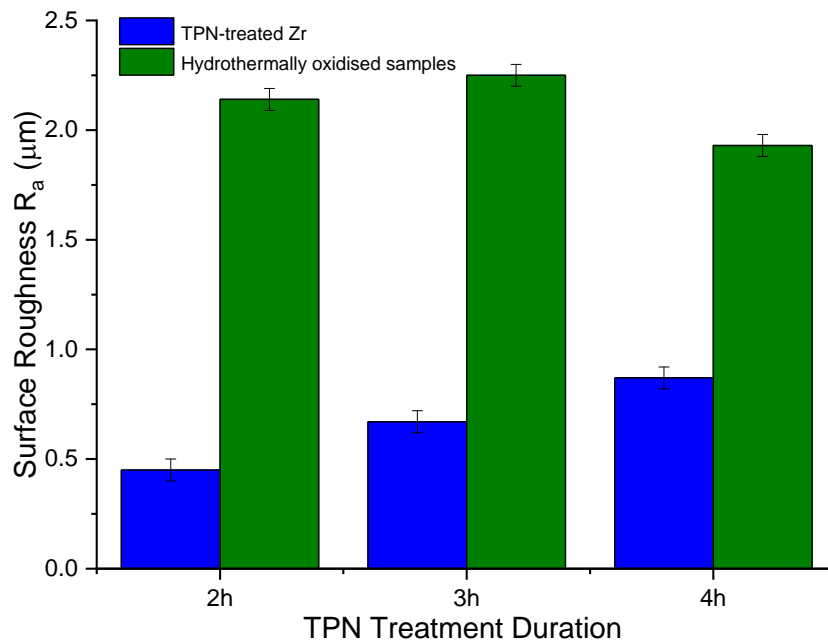


Figure 4.8: Surface roughness (R_a) of the hydrothermally oxidised TPN-treated samples was measured to be much higher (more than 2x) compared to TPN-treated samples.

4.3 Nanoindentation Hardness Measurements of Oxide Scales following Hydrothermal Oxidation of Plasma Nitrided Diffusion-Treated Layers

Nanoindentation measurements were performed to determine the hardness of the oxide scale formed on the hydrothermally oxidised TPN-Zr samples diffusion-treated for 2, 3 and 4 hours. A load of 4 mN (as for the TPN-treated samples) was applied and nine indents were made in a 3x3 array grid. The size of the contact impression was kept small relative to the film thickness, typically less than 10% of the oxide scale thickness in order to ensure there was minimum influence from the substrate when the hardness and elastic modulus of the oxide scale was measured.

4.3.1 Hardness Measurements of Hydrothermally Oxidised Samples

The hardness vs. depth profile in Figure 4.9 shows that at a contact depth close to 200 nm, the hardness of the oxide scale formed on the A_TPN_2hr, A_TPN_3hr and A_TPN_4hr samples were determined to be 3.1 ± 0.2 GPa, 3.3 ± 0.2 GPa and 3.5 ± 0.2 GPa respectively. This shows that the oxide scales for the different diffusion treatments exhibited similar hardness values following hydrothermal oxidation test at 360°C for 3 days. It has been established earlier in Figure 4.3(a) that the thickness of the oxide scale formed on each of these samples was measured to be 10 ± 0.5 µm which could explain why similar hardness values were obtained. The slight variation of the hardness values for the oxide

scales might be due to the variation in the number of crack defects or severity of oxide spallation particularly near the pre-formed outer oxide scales as was observed from the cross-sectional SEM micrograph in Figures 4.3(a) and 4.4. In addition, the hardness values are much lower than the TPN-treated Zr samples (~12 GPa) and lower than the untreated pure Zr which exhibited a hardness value of 4.40 ± 0.12 GPa (Figure 3.20). This is not surprising due to the porous structure of the monoclinic oxide scale which is considered to be brittle [75]. Due to technical issues and availability surrounding the nanoindentation equipment, multiple repeats of hardness measurements could not be performed on the same sample, thus, there may be a level of uncertainty in the hardness measurements obtained.

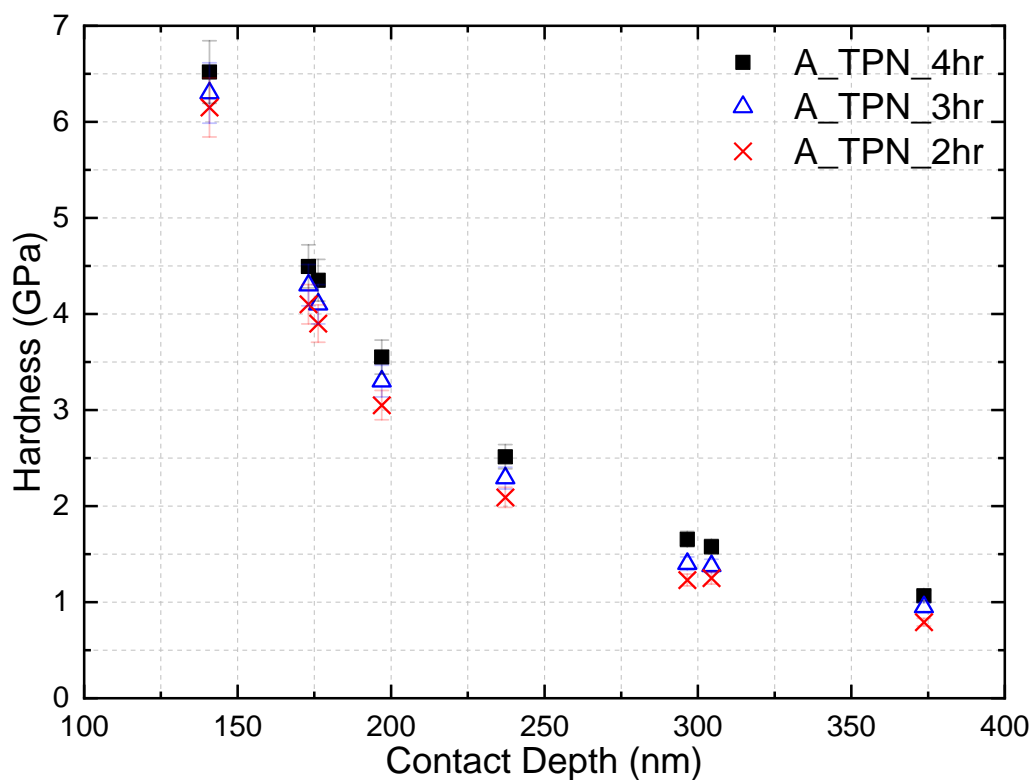


Figure 4.9: Hardness (GPa) vs. contact depth (nm) plot shows the hardness of the oxide scale formed on each of the TPN-treated samples decreases with contact depth.

Literature investigations revealed that nanoindentation hardness of zirconium oxide was scarce. Cheng et al [306] demonstrated that the ZrO_2 films produced by plasma electrolytic oxidation (PEO) on Zircaloy-4 resulted in oxide layer thicknesses of $\sim 25 \mu m$ and measured hardness values ranging from 2 to 6 GPa. Varying levels of defects such as cracks and porosity (due to the different PEO treatment parameters applied) were proposed as a likely explanation for the hardness disparity between the oxidised samples. The range of values however, is in good agreement with the hardness values obtained in this study for oxide scales formed on untreated bulk Zr [307] as well as oxide scales formed on TPN-treated Zr samples. Furthermore, the possibility of substrate contribution to hardness

measurements of the oxide scale is considered low due to the small contact depth of the indenter into the oxide scale of $\sim 300\text{-}400$ nm compared to the oxide thickness (measured to be $\sim 10 \pm 0.5$ μm).

One route to confirm how brittle and loosely adhered the oxide scale is, would be to use AFM or optical profilometry to generate 3D topographical images to analyse the indents. An indication that the oxide scale would be brittle is if the oxide layer had spalled at or around the region of the oxide where indent impressions have been made. In this work, this could not be identified due to the high surface roughness of the oxide scale which made it difficult to image by AFM. Notwithstanding, scratch adhesion tests were also performed to highlight this point, and these are presented and discussed in the following section.

4.4 Scratch Adhesion of Oxide scales following Hydrothermal Oxidation of Plasma Nitrided Diffusion-Treated Layers

In this study, scratch adhesion tests were performed on the oxide scales formed on the TPN-treated Zr samples following hydrothermal oxidation at 360°C for 3 days. A higher load of up to 35 N was required to penetrate the thick oxide scale ($\sim 10 \pm 0.5$ μm) compared load applied on the TPN-treated Zr samples. The results and findings from the scratch adhesion tests hydrothermally oxidised TPN-Zr samples are discussed in this section. Details of the failure mode descriptions are discussed in Chapter 2, Section 2.11. For simplicity, the diffusion-treated TPN-Zr samples hydrothermally oxidised are referred to the designations provided in Table 4.1.

4.4.1 Scratch 'Adhesion' Testing of Hydrothermally Oxidised 2h TPN-treated Zr Samples (A_TPN_2hr)

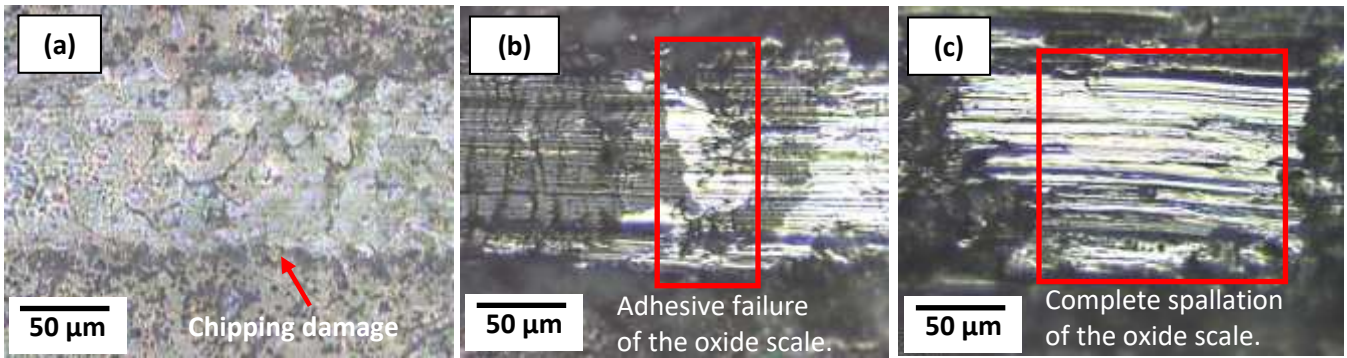
The scratch test loading profiles of the A_TPN_2hr sample are presented in Figure 4.10. The optical micrograph in Figure 4.10(a) shows irregular half-crested cracks and chipping damage, identified as dark spalled regions at the sides of the scratch track which indicate cohesive failure of the oxide scale. The chipping damage of the oxide scale can be seen to be more extensive than the chipping damage of the TPN-treated layers diffusion-treated Zr 2hr as shown in Figure. 3.22(a). The critical load (L_{c1}) at which cohesive failure of the oxide scale occurred was determined to be 11.5 N. Tensile cracking could also be observed on the scratch track following the failure mode at L_{c1} which occurs due to the stress generated in the oxide as a result of the force of the stylus being drawn across the surface. Such defects detected at low loads are an indication that the oxide scale is very brittle. This is in good agreement with earlier observations of the surface and cross-sectional morphology from SEM

micrographs (in Figure 4.3(a) and Figure 4.4 respectively) which show extensive interconnecting microcracks in the oxide scale. As mentioned previously, this would tend to make the oxide porous to oxidative species (and thus lead to spallation failure at low loads).

It can be seen from the optical micrograph in Figure. 4.10(b), that as the Normal Force was progressively increased, the frequency of tensile cracks along the track also increased. The magnitude of the AE signals (Figure 4.10(d)) can also be seen to increase leading up to adhesive failure of the oxide which is a release of elastic energy during crack growth. The critical load (L_{C2}) at which adhesive failure of the oxide occurred was 16.4 N. This is the penetration of the oxide scale by the indenter whereby the TPN-treated Zr is first exposed (Figure 4.10(b)) at a Penetration Depth (P_d) of 12.5 μm which would be within the region of the nitrogen diffusion zone. The Penetration Depth value determined from the scratch adhesion profiles is in fairly good agreement to the thickness of the oxide scale of $10 \pm 0.5 \mu\text{m}$ presented in Figure 4.3(a).

A noteworthy observation from optical micrograph in Fig. 4.10(b) is that oxide material could be seen on the scratch track after the TPN-treated Zr sample was first exposed. A possible explanation for this could be that the oxide had spalled as a result of ploughing and built up at the leading edge of the indenter and was eventually 'flattened' underneath the indenter as the scratch test progressed. This is evidenced from the optical micrograph (Figure. 4.10(b)) which shows that residual 'ploughed' oxide appears to have been re-deposited and flattened several microns along the scratch trail after L_{C2} failure mode had been reached. Thus, it is important to verify microscopic imaging with scratch loading profiles to ensure correct interpretation of results can be deduced.

A steep increase in gradient of the Tangential Force F_T curve indicated that complete spallation (L_{C3}) of the oxide occurred at a load of 18.3 N (Figure. 4.10(d)). This is shown in the optical micrograph in Figure. 4.10(c) that revealed only the TPN-treated Zr surface following spallation of the oxide scale. The Penetration Depth of $\sim 35 \mu\text{m}$ at which L_{C3} occurs exceeds the region of the nitrogen diffusion zone case depth and is therefore, likely to be the exposed HCP α -Zr.



(d)

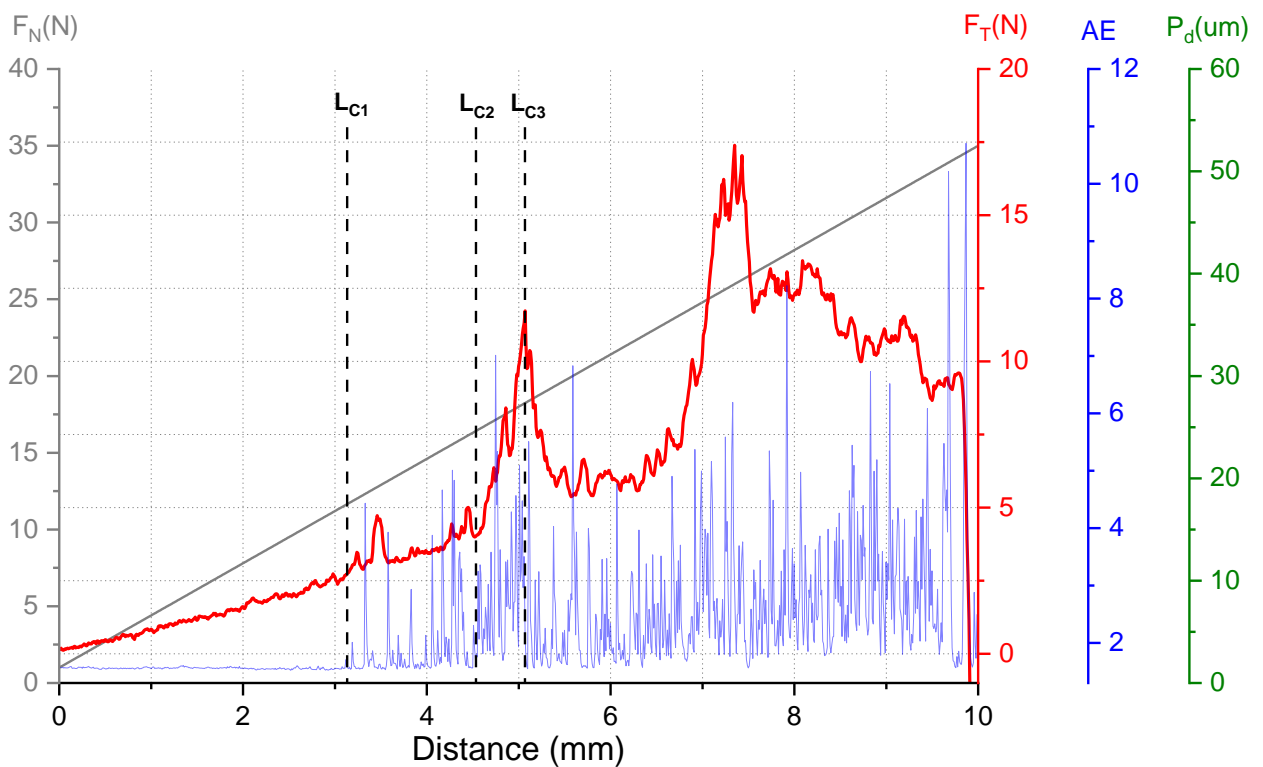


Figure 4.10: Scratch test for the A_TPN_2hr show optical micrographs of (a) cohesive failure; (b) adhesive failure (c) complete spallation of the oxide scale and (d) loading profiles at the points at which L_{C1} , L_{C2} and L_{C3} failure modes occur, identified using a combination of Tangential Force (F_T), Acoustic Emission (AE) and Penetration Depth (P_d) data.

It is interesting to note that the F_T signal decreases after failure at L_{C3} followed by a slanting erratic pattern before a second much larger peak is observed (at a distance of 7.5 mm from the start of the scratch track). This could be due to the failure of the HCP α -Zr metal as shown in the micrograph in Figure 4.11 in which a large crack (perpendicular to scratch track) was exhibited on the Zr metal that extended the entire width of the scratch track. This is probably a result of galling wear. Galling is caused by friction and adhesion of metal surfaces that are in sliding contact with each other and results

in the transfer of material between metallic surfaces [282]. In this case, the zirconium metal is transferred to the diamond stylus followed by tearing of the HCP α -Zr crystal structure.

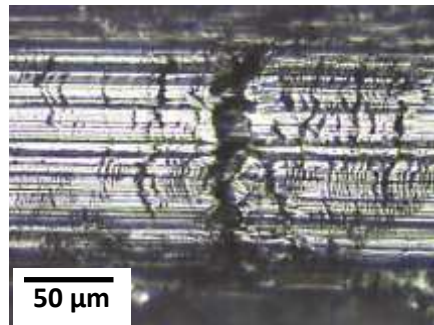


Figure 4.11: Optical micrograph of failure of the HCP α -Zr substrate showing a large crack (galling wear) resulting from the indenter load applied.

4.4.2 Scratch 'Adhesion' Profiles of Hydrothermally Oxidised 3h TPN-treated Zr Samples (A_TPN_3hr)

The scratch test loading profiles of the A_TPN_3hr sample and associated optical micrographs are presented in Figure 4.12. As before, chipping damage was identified (optical micrograph in Figure 4.12(a)) as dark spalled regions at the sides of the scratch track which indicate cohesive failure of the oxide scale. The critical load (L_{C1}) at which cohesive failure of the oxide scale occurred was determined to be 12.4 N which is in fairly good agreement with the A_TPN_2hr sample. Analysis of the optical micrograph in Figure 4.12(b) showed that the scratch track exhibited tensile cracking which was more predominant and occurred at a higher frequency compared to the A_TPN_2hr sample. This is consistent with the increase in AE signals (Figure. 4.12(d)) following cohesive failure which indicates increased cracking behaviour – probably from tensile cracking observed on the scratch track. As the Normal Force was progressively increased, the magnitude of AE signals could also be seen to increase leading up to adhesive failure of the oxide. The critical load (L_{C2}) at which this occurred was 17.5 N at a Penetration Depth of 11.5 μm . This is consistent with the oxide scale thickness determined earlier (Figure 4.3(a)) in and falls within the region of the nitrogen diffusion zone.

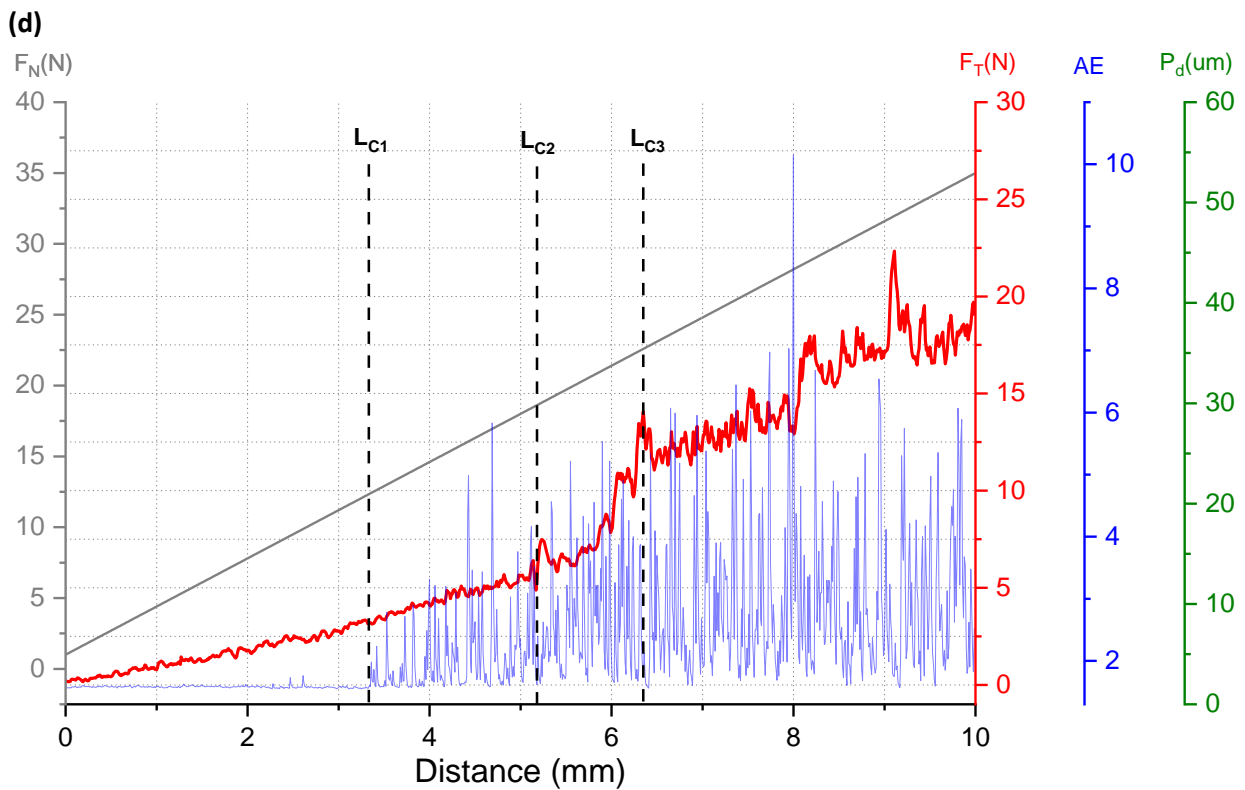
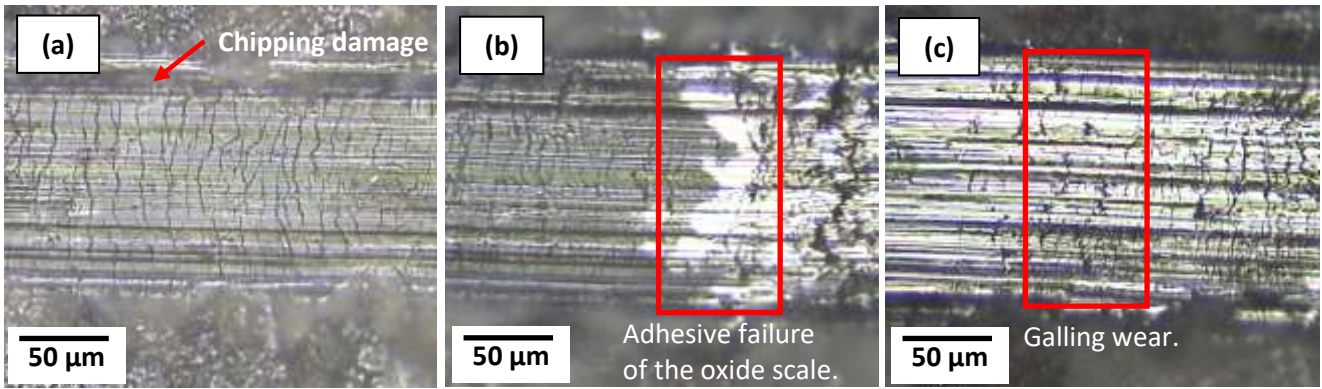


Figure 4.12: Scratch test for the A_TPN_3hr show optical micrographs of (a) cohesive failure; (b) adhesive failure (c) complete spallation of the oxide scale and (d) loading profiles at the points at which L_{C1} , L_{C2} and L_{C3} failure modes occur, identified using a combination of Tangential Force (F_T), Acoustic Emission (AE) and Penetration Depth (P_d) data.

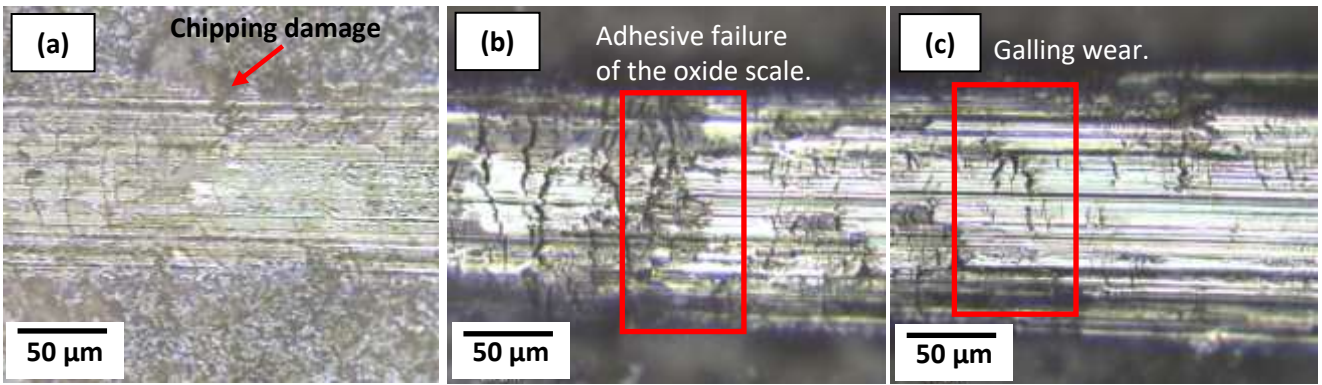
The differences in the values obtained for Normal Force and Penetration Depths for the A_TPN_2hr and A_TPN_3hr samples could be due to the slightly different load-bearing capacity of the oxide scale due to variations in crack propagation that would follow along the path of least resistance [308], and the volume of oxide spallation that takes place as the indenter is drawn across the oxide. For instance, some regions of the oxide may have undergone a slightly higher severity of oxide spallation due to pre-existing defects such as microcracks that may have propagated in directions that would be more

susceptible to oxide spallation during scratch testing, or regions of oxide that had already spalled following hydrothermal oxidation at 360°C for 3 days. This may explain why oxide scales for the A_TPN_2hr and A_TPN_3hr samples exhibited different crack behaviour and frequency (as identified from optical micrographs) under the same load which is reflected in the Tangential Force curves (F_T) obtained for the A_TPN_2hr and A_TPN_3hr samples. As the Normal Force is further increased (for the A_TPN_3hr sample), the critical load at which complete spallation at L_{C3} occurred was determined to be 22.5 N at a Penetration Depth of 27 μm . This could possibly be the HCP α -Zr substrate, since this is beyond the region of the nitrogen diffusion zone (thickness of $\sim 23 \mu\text{m}$ from Figure 3.14) and the optical micrograph in Figure 4.12(c) shows galling wear which as mentioned earlier typically occurs as a result of friction between the Zr metal in sliding contact with the stylus resulting in material transfer from the former to the latter.

4.4.3 Scratch Adhesion Profiles of Hydrothermally Oxidised 4h TPN-treated Zr Samples (A_TPN_4hr)

The scratch test loading profiles of the A_TPN_4hr sample and associated optical micrographs are presented in Figure 4.13. The graph shows that cohesive failure occurred at a critical load (L_{C1}) of 14.0 N which was observed (from optical micrograph in Figure. 4.13(a)), identified as the onset of chipping damage on the sides of the scratch track and the presence of tensile cracks leading up to L_{C1} . As the load was progressively increased, the frequency of tensile cracks along the scratch track also increased, which is consistent with observations of the A_TPN_2hr and A_TPN_3hr samples, and this was shown by an increase in AE signals (Figure. 4.13(d) indicating increased cracking behaviour).

Crack propagation increases through the oxide scale as the stylus is drawn across the surface (with increasing normal force) leading to more severe tensile cracks (Figure. 4.13(b)) and spallation of the oxide scale. The critical load (L_{C2}) at which adhesive failure occurred was determined to be 27.0 N at a Penetration Depth of $\sim 15 \mu\text{m}$. The extensive damage and ploughing of the oxide as well as microcracks along the scratch track observed from optical micrographs is indicative that the oxide scales are brittle and porous. It is interesting to note that the oxide scale in Figure. 4.13(b) at the sides of the scratch appears blurred. This is likely due to the oxide in this region had spalled from the extensive chipping damage resulting in oxide 'craters' which makes it difficult to resolve using optical microscopy due to the differences in the depth of field.



(d)

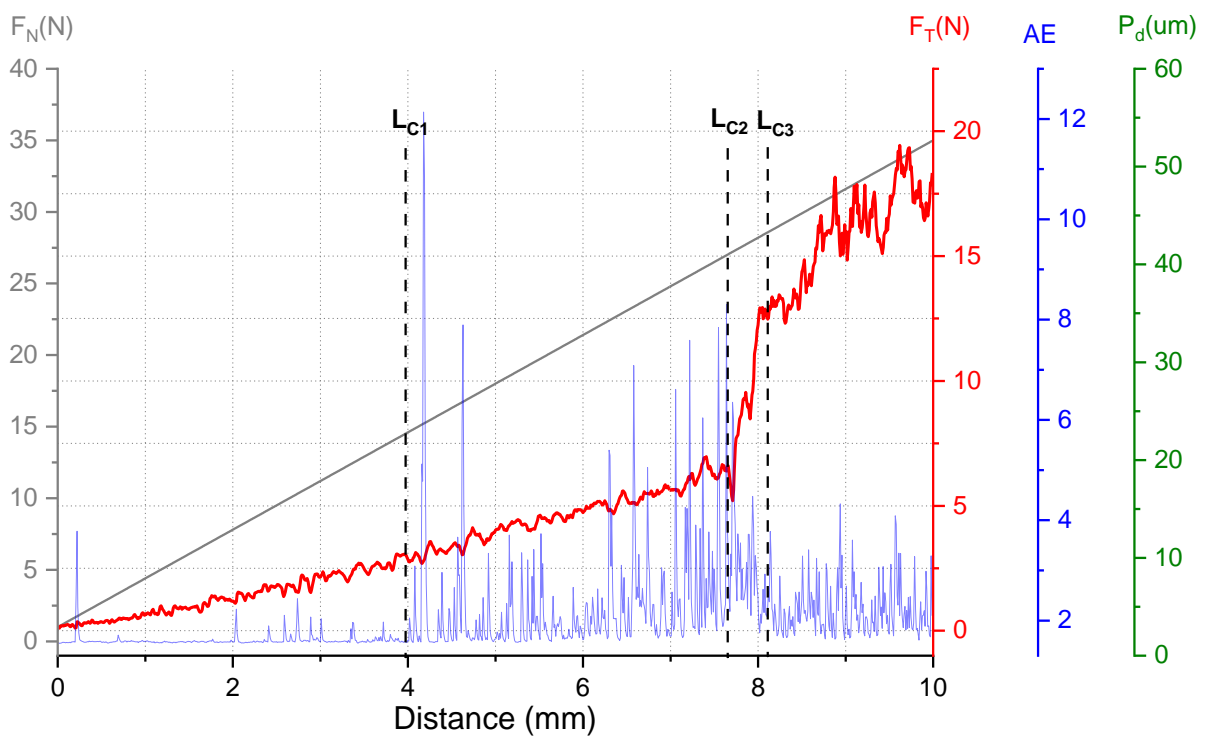


Figure 4.13: Scratch test for the A_TPN_4hr show optical micrographs of (a) cohesive failure; (b) adhesive failure (c) complete spallation of the oxide scale and (d) loading profiles at the points at which L_{c1} , L_{c2} and L_{c3} failure modes occur, identified using a combination of Tangential Force (F_T), Acoustic Emission (AE) and Penetration Depth (P_d) data.

Table 4.3: Summary of the critical load values for the hydrothermally oxidised 2 hr, 3 hr and 4 hr TPN diffusion-treated Zr samples.

Sample	L_{c1} (N)	L_{c2} (N)	L_{c3} (N)
A_TPN_2hr	11.5	16.4	18.3
A_TPN_3hr	12.4	17.5	22.5
A_TPN_4hr	14.0	27.0	28.0

The critical load (L_{C3}) at which complete spallation of the oxide scale occurred was determined to be 28.0 N at a Penetration Depth of about 35 μm , before the HCP α -Zr substrate was completely exposed (Figure 4.13(c)). For all three failure modes, the A_TPN_4hr oxide scale was seen to exhibit a higher load-bearing capacity before failure compared to the A_TPN_2hr and A_TPN_3hr samples (Table 4.3), despite the TPN-treated Zr samples being subjected to the same hydrothermal test conditions - forming similar oxide thicknesses of about $10 \pm 0.5 \mu\text{m}$ (Figure 4.3(a)). The Tangential Force curves (F_T) resulted in slightly different patterns for all three treatment times. A plausible explanation for these findings as alluded to earlier is that, as the load is progressively increased, the brittle oxide scale promotes a build-up of material at the leading edge of the indenter resulting in spallation, and the spalled oxide at the front of the indenter is pressed beneath the tip giving an inaccurate impression that it is the adhered oxide layer, thus increasing the critical load to failure. This can occur at different regions along the scratch track depending on the volume of spalled material that is pulled beneath the Rockwell diamond scratch tip.

4.5 Summary

On the balance of evidence presented in this study, it was found that the hydrothermal oxidation (at 360°C, 18.7 MPa for 3 days) of TPN-treated zirconium slightly improved the oxidation resistance compared to untreated pure zirconium. Since the oxide scale formed on the TPN-treated samples was measured (from cross-sectional SEM micrograph in Figure. 4.3(a)) to be $10 \pm 0.5 \mu\text{m}$ and exhibited similar weight gain for all TPN-treated samples, it is likely that the thickness of the oxide scale and oxidation rate of the TPN-treated samples and the untreated pure Zr may have been higher than measured. The SEM micrographs also show the oxide scale to contain microcracks, which increase in severity with distance away from the oxide/metal interface. Taken together, this indicates that the oxide scale is likely to have undergone material loss due to spallation during hydrothermal oxidation. Although the TPN treatments did not significantly improve the oxidation resistance of zirconium when compared to untreated zirconium, it did not make it worse either.

The hydrothermal oxidation of pure zirconium was found to offer poor oxidation resistance when compared to the oxidation performance of Zr alloys under similar conditions reported in the literature. This is because the elements that form intermetallic precipitates such as tin, iron and chromium in zirconium alloys play an important role in controlling and reducing the oxidation rate [42]. The low oxidation rate offered by intermetallic precipitates results in a pore-free, dense, stressed and elastically constrained oxide scale [292] that is durable during the early stages of oxidation of Zr alloys, and serves to protect the metal. However, this precipitation hardening mechanism which is absent in

pure zirconium results in thicker oxide scales that exhibits diminishing compressive stress (with thickness); volume expansion (of the oxide scale) and microcracking in the oxide scale which is non-protective.

The GAXRD patterns and Raman spectroscopic results (of the hydrothermally oxidised TPN-treated Zr samples) presented in this work showed that the highest volume fraction of the tetragonal phase is at the oxide/metal interface region. It has been widely reported in the literature that compressive stress is highest at this region and is responsible for the partial stability of this phase. As the oxidation process continues and the oxide scale grows thicker, the (metastable) tetragonal zirconia is no longer elastically constrained and is destabilised due to the diminishing compressive stress with distance away from the interface. The breakdown of the t-ZrO₂ allows the transformation to the m-ZrO₂ with an associated volume expansion of the oxide scale which was shown to be porous and brittle [87].

During hydrothermal oxidation, the ZrN compound layer is entirely consumed and as the oxide grows into the nitrogen-containing diffusion zone, the interstitial nitrogen is replaced by the oxygen from the dissociation of water. Oxygen interstitially diffuses at vacancy sites and causes the lattice of the bulk substrate to expand [192] which was deduced from XRD peaks showing a peak shift to lower angles of 2θ for the m-ZrO₂ phase. The evidence presented suggests that the nitrogen diffusion zone provides a sustained resistance to oxygen ingress whereby the nitrogen in the interstitial sites suppresses oxygen migration into the diffusion zone as quickly as it otherwise might. This is a promising finding that allows surface treatment strategies to be developed for improved oxidation resistance. Scratch adhesion loading profiles and associated micrographs of the oxide scale formed on TPN-treated Zr samples revealed extensive chipping damage and tensile cracking along the scratch track indicating that the oxide layer is brittle which supports the findings from SEM micrographs of the surface and cross-section of the oxide scale.

On the balance of evidence presented in this study, it can be deduced that the monoclinic polymorph of the zirconia does not offer suitable oxidation resistance, necessary for the stabilisation of the oxide layers formed in high pressure autoclave conditions and hence, unsuitable for reactor environments. One method to potentially increase the stability of the oxide would be to allow the oxide to form in the 'natural' oxidation process during high temperature conditions and incorporate a third element to stabilise the tetragonal or cubic zirconia phase over a wide range of temperatures as the oxide grows - thereby increasing oxidation resistance.

Chapter 5 – Sputter-deposited Zirconium-Magnesium Coatings

5.1 Fabrication of Zr-Mg Coatings using Magnetron Sputtering

Zr-Mg PVD coatings were produced using an unbalanced magnetron sputter PVD rig. The aim of this study was to determine to what extent magnesium and zirconium would be soluble in each other, in a Zr-Mg alloy coating. Details of the experimental setup are described in Chapter 2, Section 2.5. Magnesium and zirconium targets were used for sputtering because it was important to try to obtain a Zr-Mg alloy coating to promote the required coating oxidation behaviour. Following the discussion with regards to the benefit of stabilising the tetragonal zirconia phase over a wide temperature range (Chapter 1, Section 1.12); the Hume-Rothery rules for substitutional solid solution for Mg and Zr (Chapter 1, Section 1.13) and the growth of columnar structures following magnetron sputtering (Chapter 1, Section 1.14), the objective of this part of the study was to investigate whether adding magnesium (via substitutional diffusion) would be in solid solution with zirconium and whether this might induce a magnesium-stabilised tetragonal zirconia phase during oxidation.

5.1.1 Targets with Applied 600W Power

The first iteration of sputter deposition experiments was carried out with 600 W power supplied to both Zr and Mg targets. The stainless steel substrates (dimensions: 2 cm x 2 cm) were negatively biased with 150 V at a fixed working distance of 15 cm between targets and substrate holder (to which the substrates were mounted). The substrates were mounted at the top, middle and bottom of the substrate holder – see schematic in Chapter 2, Section 2.5, Figure 2.3 and the substrates were sputter co-deposited with magnesium and zirconium for a duration of 2 hours. Camera images of the coated substrates are presented in Figure 5.1. The region around the drilled holes (1.5 mm diameter) at the corner of each coated substrate exhibited discoloured lines which is where the fixtures were placed that held the substrate to the sample holder during sputter deposition. All the substrates showed they were partially coated, irrespective of their location on the substrate holder. Visual inspection of the coated sample in Figure 5.1(a) (that was located near the bottom of the substrate holder during sputter deposition) appears to show a ‘graded’ deposition. The associated SEM micrograph of the morphology appears to show grain-like features that are likely to be columns with a diameter of the order of about 1 μm . EDX analysis of one area of the graded region revealed a zirconium-rich elemental composition comprising of Zr, Mg and O in approximate concentrations of 88.2 at%, 7.8 at% and 4.0 at% respectively. Figure 5.1(b) (which was fixed near the middle of the substrate holder during sputter deposition) showed about half of the substrate was coated. Figure 5.1(c) (which was fixed near the

top of the substrate holder during sputter deposition) showed majority of the substrate was coated. The associated SEM micrograph (for Figure. 5.1(c)) of the morphology appears to show grain-like features that are likely to be columns with a diameter of the order of about 1 μm which is similar to that of the Zr-rich graded-composition sample (Figure 5.1(a)). The EDX analysis for Figure 5.1(c) revealed a magnesium-rich elemental composition of the coating comprising of Mg, Zr and O in approximate concentrations of 89.5 at%, 8.6 at% and 1.9 at% for Mg, Zr and O respectively. The grains appear to be more well-defined for the coating with high Mg content (Figure 5.1(c)) compared to the coating with high Zr content (Figure 5.1(a)). A possible explanation for why the substrates were not fully coated might be due to re-sputtering effects whereby high substrate bias results in higher energy ions bombarding the target which leads to higher energy atoms being sputtered. This could lead to the re-sputtering of coated regions leading to coating non-uniformity that can be seen in the camera images.

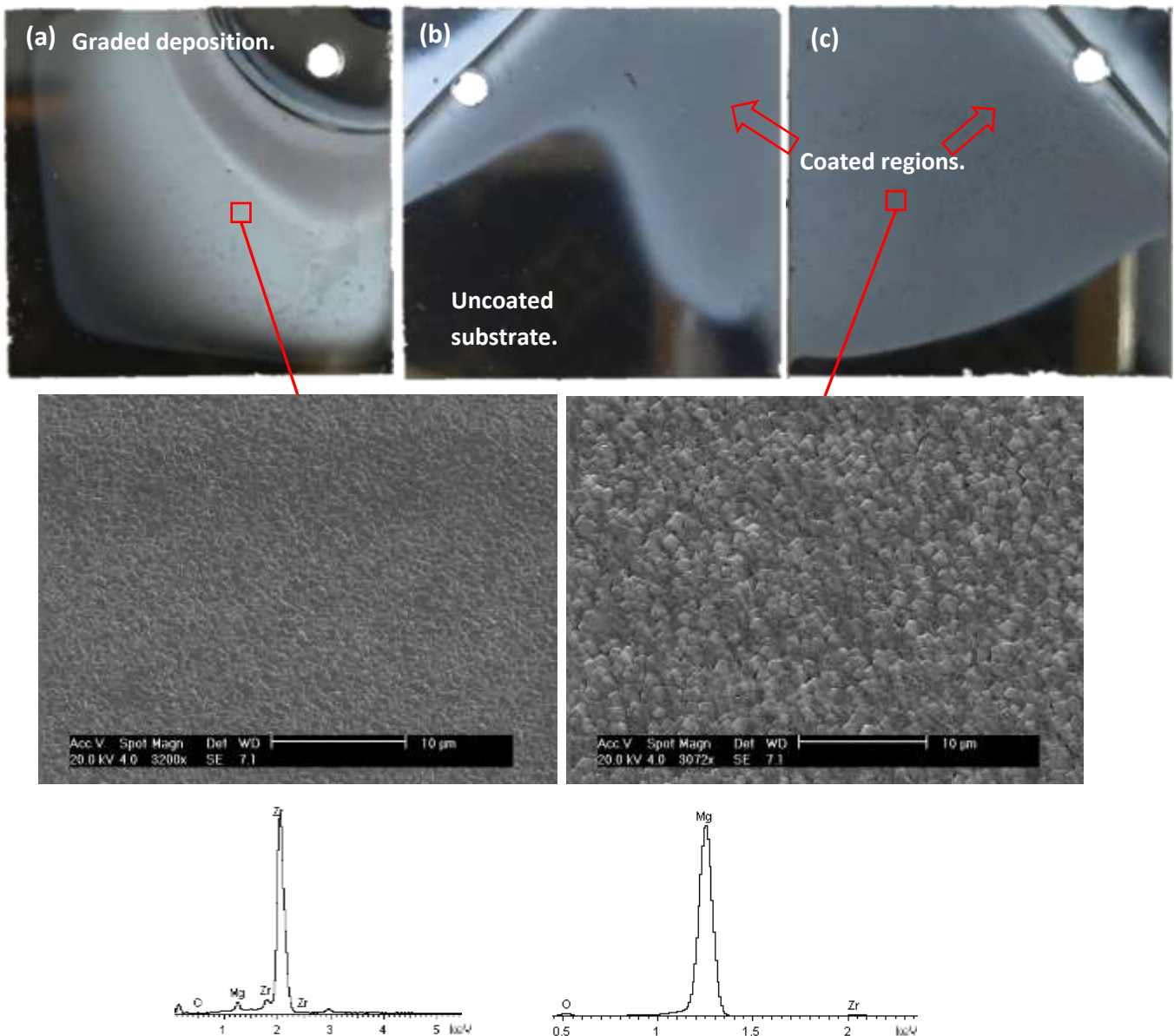


Figure 5.1: Camera images of sputter co-deposited Zr-Mg coatings on stainless steel substrates (2cm x 2cm) carried out at 600 W at target-substrate distance of 15 cm and negative substrate bias voltage of 150 V which show (a): graded deposition; (b) mostly coated and (c) partial coating of the substrates. SEM micrographs shows the morphology and EDX spectra shows Zr-rich and Mg-rich regions in Figure 5.1(a) and (c) respectively.

One possible method to obtain full coating coverage might be to increase the applied substrate negative bias which could likely result in an increase in the bombardment intensity of coating atoms (from the target) onto the substrate. But a higher potential difference would result in a similar flux of zirconium and magnesium atoms arriving at the substrate with a higher kinetic energy. This may have the negative effect of increasing the re-sputtering of the coating at the sample edges, leading to poor

thickness uniformity – as was previously observed from the images in Figure 5.1(a), (b) and (c). Thus, the substrate negative bias was kept constant at 150 V for the following sputter deposition run.

In the next sputter deposition run, both zirconium and stainless steel substrates (dimensions: 2 cm x 2 cm) were used and positioned on the sample holder in the same configuration mentioned previously (i.e. zirconium and stainless steel substrates (one of each) near the top, middle and bottom of the substrate holder). Sputter cleaning of the substrate was carried out for 10 minutes. The substrate negative bias was kept constant at 150 V but the power supplied to both the Zr and Mg target segments was increased to 700 W and the coating deposition was carried out for a duration of 2 hours. Following deposition, a cooling period of 5 minutes was awaited before the chamber door was opened. The camera image of the sputter co-deposited Zr-Mg coating on Zr substrate is presented in Figure 5.2. It was apparent that some regions of the coating had undergone severe spallation after the samples were taken out of the deposition chamber. Visual observation of some regions of the coating (Figure 5.2) could be seen to have ruptured - leading to the rapid debonding, flaking and the eventual delamination of the coating revealing the polished substrate underneath. One reason for this might be due to the high levels of compressive growth stress in the coating that may be amplified by differential thermal contraction upon cooling. The curvature of the partially spalled coating flakes is also indicative of high levels of stress in the coating. However, there is also the suggestion of insufficient sputter cleaning prior to coating deposition - and/or cross contamination of remaining oxygen-rich material re-sputtered from the target surfaces in the early stages of the coating run (shown in Figure 2.3) - creating a thin, brittle interlayer (between the substrate and the co-deposited coating). This could result in poor coating/substrate interfacial adhesion leading to rupture, spallation and delamination of the coating from the substrate.



Figure 5.2: Camera image showing spallation of the Zr-Mg coating on zirconium substrate when the sample was taken out of the deposition chamber following 5 min cooling time.

Further sputter deposition runs were carried out with an applied power to the target of 700 W, substrate bias of -150 V and a target-substrate distance of 15 cm. Both the zirconium and stainless steel substrates (dimensions: 2 cm x 2 cm) were positioned on the sample holder in the configuration shown in the schematic in Figure 5.3 below. Sputter cleaning of the substrates was increased to 25 minutes and the coating duration was increased to 3 hours with the cooling time extended to 1 hour, prior to being taken out of the deposition chamber. The approximate magnesium concentration for each of the samples were determined from EDX analysis of the coated surface and is also shown in the schematic relative to the position on the sample holder. Time limitations meant that only 2 samples could be analysed. These were the coatings containing: (i) 25 at% magnesium, 70 at% Zr and 5 at% oxygen – referred to as Zr-rich coatings and (ii) 53 at% magnesium, 35 at% Zr and 12 at% oxygen – referred to as Mg-rich coatings (the positions of these samples on the substrate holder is shown in the schematic in Figure 5.3). The camera images of the two of the Zr-rich and Mg-rich sputter co-deposited samples are presented in Figure 5.4.

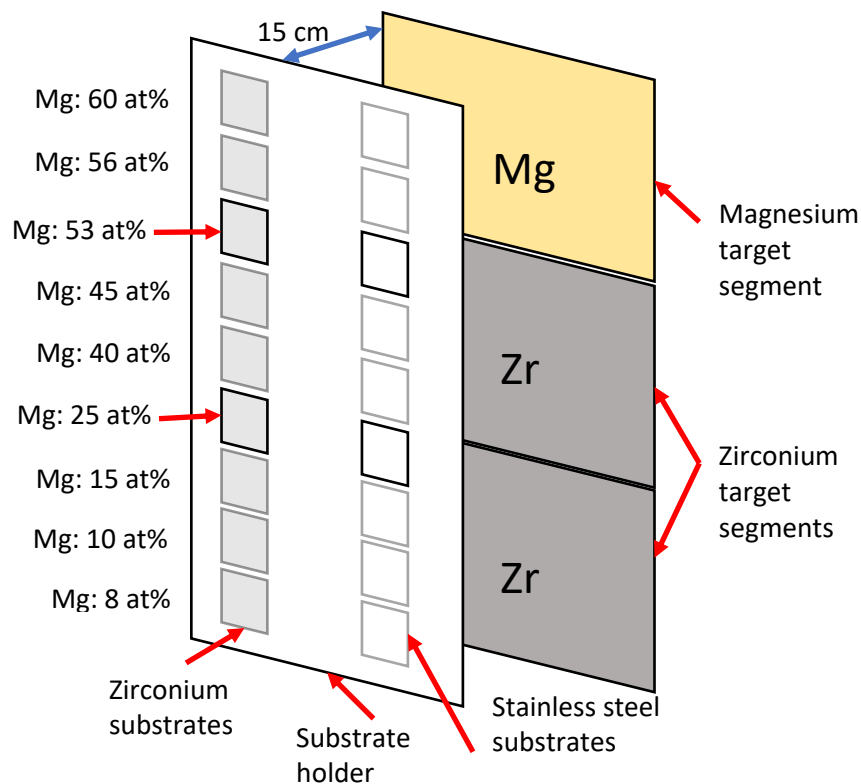


Figure 5.3: Schematic of the configuration of substrates on the substrate holder during sputter deposition at 700 W target power, 3 hours coating duration and one hour cooling time, along with approximate EDX elemental compositions. The Zr-rich (Mg: 25 at%) and Mg-rich (Mg: 53 at%) samples were taken forward for SEM analysis.

Table 5.1: EDX elemental composition of the sputter co-deposited Zr-Mg samples. The Zr-rich (Mg: 25 at%) and Mg-rich (Mg: 53 at%) samples highlighted in grey were taken forward for detailed characterisation.

Mg Concentration (at%)	Zr Concentration (at%)	Oxygen Concentration (at%)
8	88	4
10	87	3
15	79	6
25	70	5
35	58	7
45	47	8
53	35	12
56	34	10
60	26	14

The Zr-rich sample in Figure 5.4(a) was located near the bottom half of the sample holder (opposite the zirconium target segments) and the Mg-rich sample in Figure 5.4(b) was located near the top half of the sample holder (opposite the magnesium target segment). The dark-grey regions at one of the corners of each sample is where the fixtures were placed that held the substrate to the sample holder during sputter deposition as mentioned previously. The sputter deposition run was successful in that a full coating coverage of the sample was achieved compared to previous deposition runs (see Figures 5.1 and 5.2). What is also apparent is the distinct colour differences of the coatings following sputter deposition. The coated substrate in Figure 5.4(a) exhibited a dark-grey colour whilst Figure 5.4(b) exhibited a light-grey/whitish complexion. Visual inspection of the coated substrates revealed that there were no obvious signs of coating spallation, surface debris or foreign artefacts on the coated surface.

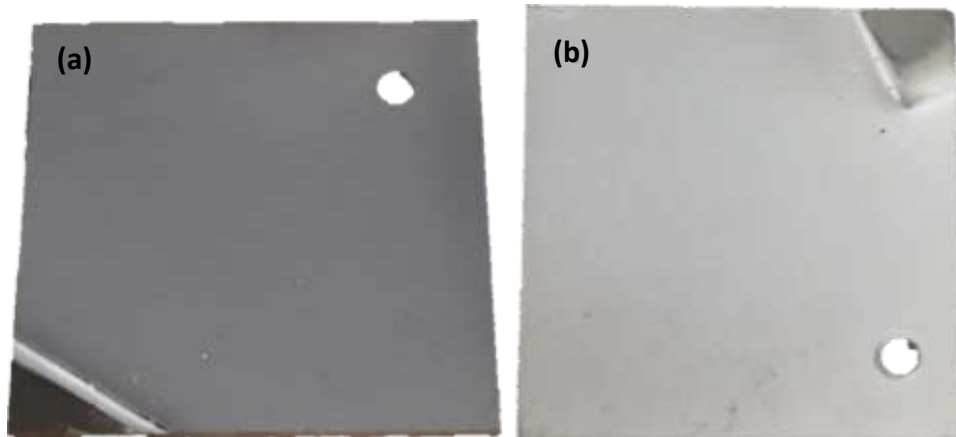


Figure 5.4: Camera images of the sputter co-deposited Zr-Mg coatings on Zr substrates that were located on (a) lower half and (b) top half of the substrate holder (shown in the schematic configuration in Figure 5.3). The differences in the surface colour is likely to be due to the differences in Mg and Zr concentrations in the coating.

5.1.2 SEM/EDX Spectroscopy Analysis of Zr-Mg Coatings

SEM analysis of the Zr-rich sample was carried out and presented in Figure 5.5. The SEM micrograph of the surface in Figure 5.5(a) shows irregularly-shaped grain-like features giving a faceted appearance. According to the Structure Zone Model described earlier in Chapter 1, Section 1.14, Figure 1.15, the faceted morphology is consistent with Zone 2. This is indicative of the columnar structure of the coating, which evolves as a result mostly of the line-of-sight deposition (shadowing effects). In Zone 2, surface diffusion is the dominant process during film growth leading to the formation of wider columns and well defined grain boundaries compared to Zone 1 or Zone T. Interestingly, the diameter of the columnar grains ranged from a few microns to about 15 μm which suggests competitive grain growth during film formation. Messier et al [232] proposed a revised structure zone model whereby the microstructure and nanostructure of germanium coatings (with T_h reported to be ~ 0.5) were investigated using TEM. The author reported column diameters of thick coatings (10 to 30 μm) to be of the order of hundreds of nanometers. Given that the T_h for Mg-containing coating on Zr substrate was calculated to be 0.54 (Chapter 1, Section 1.14), it is likely that the actual column diameters are hundreds of nanometers in width. As a point for future work, it would be useful to perform cross-sectional TEM analysis to determine the columnar diameter of the coating. EDX analysis of the coated surface carried out previously and shown in Figure 5.5(b) confirmed a zirconium-rich coating which comprised approximately 70 at% - zirconium, 25 at% - magnesium and 5 at% - oxygen (summarised in Table 5.1). The high zirconium content detected in the coating in Figure

5.5(b) could be explained by considering the position of the substrates on the substrate holder. In this case, the substrates were positioned near the bottom half of the substrate holder (opposite the two Zr target segments). During the deposition run, a higher concentration of sputtered zirconium atoms were deposited on the substrates resulting in a Zr-rich coating, compared to sputtered magnesium atoms (where the Mg target segment is located above the Zr target segments (see Figure 5.3 for schematic configuration of setup)). The low oxygen content detected in the coating (from EDX spectroscopy) may have initially formed on the magnesium or zirconium target segments (and cross-contaminated some regions of the zirconium target segments) from residual oxygen in the chamber during the sputter deposition run. The oxygen may well have sputtered off the target segments, together with the zirconium and magnesium atoms, which were then incorporated in the coating and may form an oxide if there is sufficient quantities of oxygen in the coating.

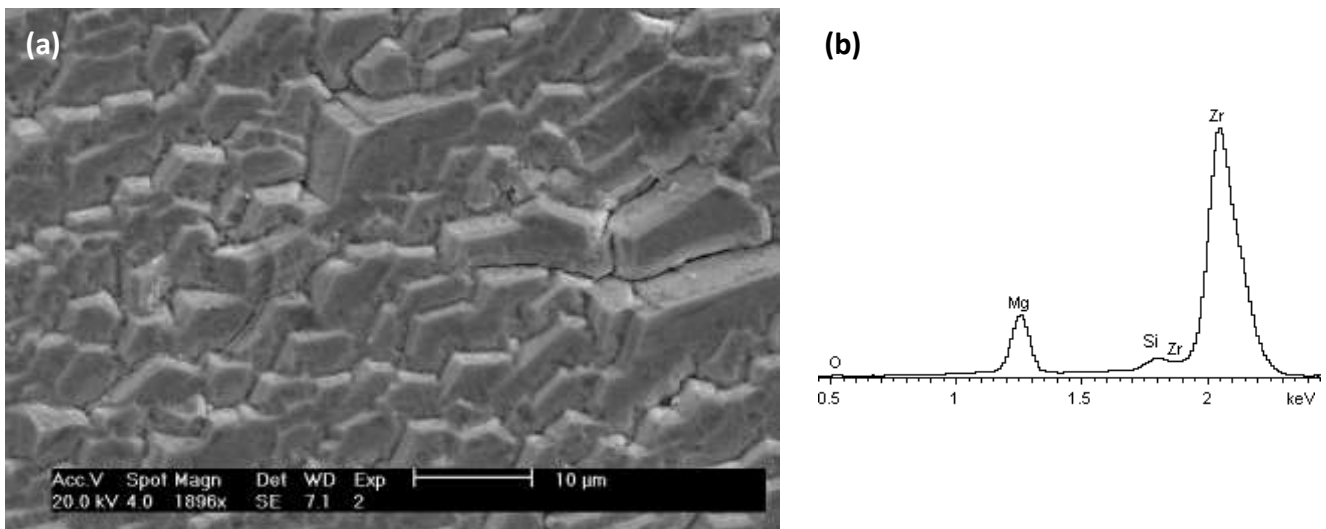


Figure 5.5: (a) SEM surface morphology of the Zr-rich sample shows column sizes ranged from 2 μm to about 15 μm in diameter and (b) EDX spectrum of the coated surface revealed a zirconium-rich coating (Mg content 25 at%).

SEM analysis of the Mg-rich sample was carried out and presented in Figure 5.6. EDX analysis of the coated surface carried out previously and shown in Figure 5.6(b) confirmed the coating was magnesium-rich comprising approximately: 53 at% - magnesium, 35 at% - zirconium and 12 at% - oxygen (summarised in Table 5.1). The SEM micrograph of the surface morphology in Figure 5.6(a) shows a faceted microstructure similar in appearance to that of the Zr-rich coating. Again, according to the Structure Zone Model described earlier in Chapter 1, Section 1.14, Figure 1.15, the faceted morphology and the well-defined grain boundaries are consistent with Zone 2 whereby surface diffusion effects dominate film formation. The morphology is also indicative of a columnar structure

whereby the column widths could be seen ranging from 2 μm to about 12 μm in diameter. This is likely because of competitive grain growth. Another factor that is likely to affect the smaller diameter coating columns observed for the Mg-rich coating is the higher T_h value for Mg (0.54) compared to Zr (0.23) (calculated in Chapter 1, Section 1.14) which suggests a higher surface diffusivity of Mg adatoms during film growth. The columnar structure appears to be more pronounced and protruded compared to the Zr-rich coating which could arise from shadowing effects [169]. As mentioned previously, the actual column diameters may well be hundreds of nanometers, but this would require further investigation at higher magnification using SEM or possibly TEM analysis.

On closer inspection of the SEM micrograph in Figure 5.6(a), it can be seen that the surface morphology Mg-rich coating appears to be more porous (between columns) than that of the Zr-rich coating in Figure 5.5(a). This might be because of a combination of high nucleation and growth rates that will tend to promote an open columnar structure (with inter-columnar voids) – and the presence of more inter-columnar (porous) volume in the Mg-rich coating (due to its higher number of smaller diameter columns) is likely a natural consequence of the (comparatively) higher nucleation rate for the Mg-rich coating. Luthier and Levy [309] reported performed SEM and TEM analysis to investigate the microstructure and nanostructure of magnetron sputtered TiAlON coatings. The author showed that the microcolumns (column diameter greater than 1 μm) were separated by voided regions of about 0.1 μm . This was attributed to the low adatom mobility ($T_h < 0.5$) of the sputtered atoms on the substrate surface that produced intercolumnar porosity.

The high magnesium content detected in the coating from the EDX spectrum in Figure 5.6(b) could be explained by considering the sputtering yield²³ of both magnesium and zirconium. The sputtering yield for magnesium is 1.4 whereas for zirconium this is 0.7. This means that an energetic argon ion arriving and bombarding the magnesium target will result in more Mg atoms being sputtered (roughly double) compared to Zr atoms (from the Zr target segments) at a given argon ion energy. Hence, a greater concentration of sputtered magnesium atoms were sputtered onto the zirconium and steel substrates that are positioned near the top of the sample holder (opposite the Mg target segment) compared to the substrate positioned near the bottom of the sample holder (opposite the two Zr target segments) where a greater concentration of sputtered Zr atoms were deposited onto the substrates resulting in a Zr-rich coating seen in Figure 5.5. The EDX spectrum in Figure 5.6(b) also shows the oxygen content detected in the Mg-rich coating (Mg: 53 at%) was higher (12 at%) compared to the oxygen content of 5 at% detected for the Zr-rich (Mg: 25 at%) coating for similar reasons described previously whereby

²³ Sputtering yield refers to the number of atoms ejected from a target with respect to momentum transfer per argon ion bombarding the target.

oxygen contamination from the target segments (arising from residual gases in the chamber) may have been sputtered onto the substrate and incorporated into the growing coating during deposition.

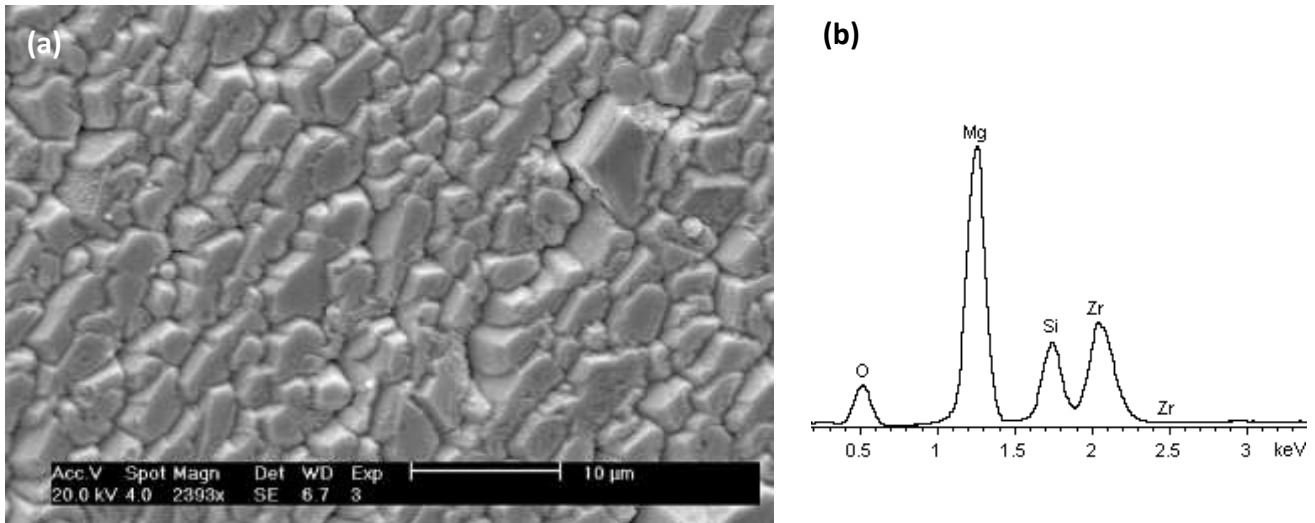


Figure 5.6: (a) SEM surface morphology shows column sizes ranged from 2 μm to about 12 μm in diameter and (b) EDX spectrum of the coated surface revealed a magnesium-rich coating (Mg content 53 at%).

Cross-sectional SEM analysis of the Zr-rich (Mg: 25 at%) and Mg-rich (Mg: 53 at%) samples was performed to determine the thickness of the coatings following sputter co-deposition and the micrographs are presented in Figure 5.7. This was carried out in back-scattered electron (BSE) mode because the features in the coating and the contrast between the coating and the substrate could be easily distinguished. The thickness was measured from five locations along the coating and the average was taken. Figure 5.7(a) shows that the average thickness of the Zr-rich coating (Mg: 25 at%) was measured to be $25.2 \pm 0.5 \mu\text{m}$. The coating thickness was found to be uniform and appeared to be dense along the length of the coating. Figure 5.7(b) shows that the average thickness of the Mg-rich coating (Mg: 53 at%) was measured to be $26.5 \pm 0.5 \mu\text{m}$ which is not too dissimilar to the thickness of the Zr-rich coating and was also found to be uniform and dense along the length of the coating (parallel to the substrate).

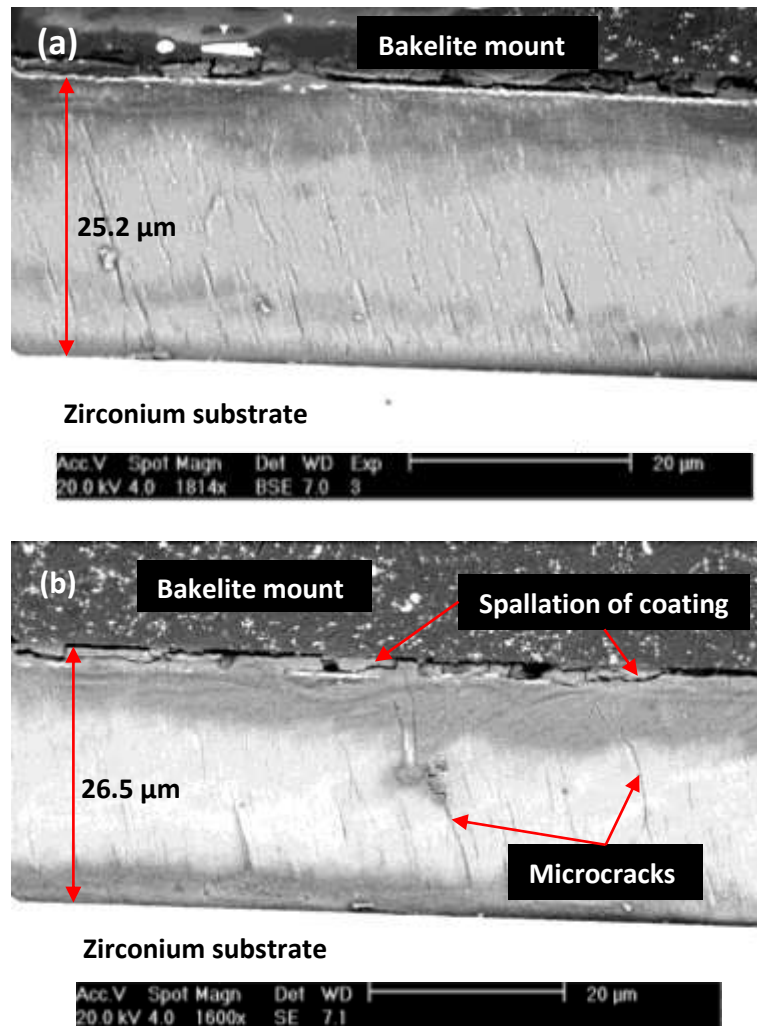


Figure 5.7: Cross-sectional SEM micrographs of the coatings in BSE mode of (a) Zr-rich (25 at%) and (b) Mg-rich (53 at%) samples revealed coating thicknesses of 25.2 μm and 26.5 μm respectively.

The surface of the Mg-rich coating (Mg: 53 at%) (coating/bakelite interface region) in Figure 5.7(b) can be seen to show evidence of coating spallation whereas this was seen to a lesser extent for the Zr-rich coating (Mg: 25 at%). Evidence of microcracks could also be seen to extend from the substrate/coating interface to the outer surface region where spallation of the coating was observed. Furthermore, the SEM micrograph shown in Figure 5.8 of one of the regions of the Mg-rich coating surface exhibited microcracks, and crack propagation could be seen to extend tens of microns mainly along the edges of the columns (where they appear to have coalesced) but also across columns. However, microcracks on the Zr-rich coating surface was not seen. This may be because the inclusion of magnesium at high concentrations such as in the Mg-rich coating could result in the coating being highly stressed. The difference in the co-efficient of thermal expansion (CTE) of the zirconium ($5.7-7.0 \times 10^{-6} \text{ K}^{-1}$) and magnesium ($25-26 \times 10^{-6} \text{ K}^{-1}$) elements that form part of the coating [310] could also mean that at a sufficiently high magnesium concentration (such as the Mg-rich sample), the coating suffers tensile

cracking on cooling (due to the CTE mismatch) which is manifested as microcracks in the coating which can lead to coating spallation.

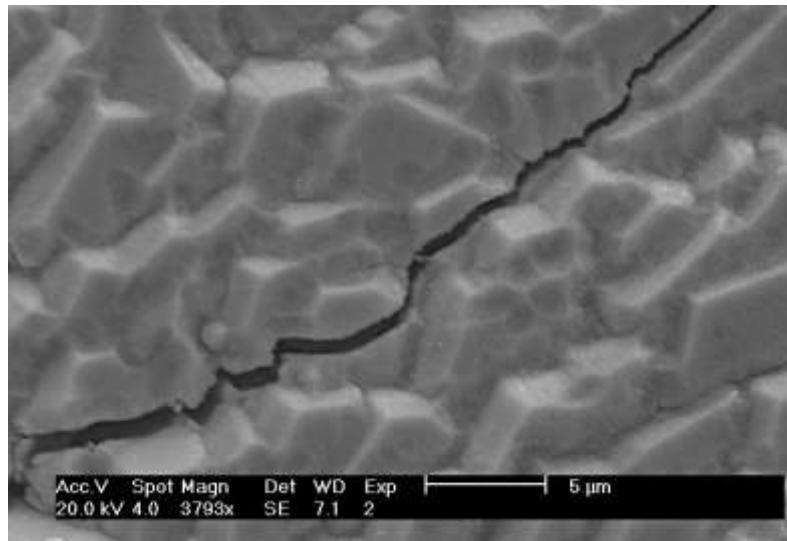


Figure 5.8: SEM micrograph of the magnesium-rich coating (Mg content 53 at%) show microcracks on the surface.

5.1.3 Glancing-Angle XRD Analysis of the Sputter Co-deposited Coatings

The GAXRD patterns of the sputter co-deposited Zr-Mg coatings on stainless steel substrates with magnesium concentrations that ranged from 8 at% to 60 at% (summarised in Table 5.1) are presented in Figure 5.9. GAXRD experiments were performed on sputter co-deposited coatings on stainless-steel substrates (rather than pure zirconium substrates) to avoid the potentially confounding influence of zirconium lattice reflections (from the underlying Zr substrate) on the diffraction patterns obtained. This was performed using a Philips X'Pert³ (Panalytical) diffractometer (CuK_α radiation) operated in glancing-angle configuration (Seeman-Bohlin geometry) at an incident angle of 4° with a step size of 0.02 and a time step of 5 seconds in the 25° to 80° range of 2θ.

For the Zr-Mg coating containing 8 at% Mg content, a broad raised profile was observed over a 2θ range of 30-35°, followed by a broad peak at a 2θ angle of 35.4°. The GAXRD trace also shows a shift to lower angles of 2θ indicating an expansion of lattice parameters [311] and shows that the broad peak could be attributable either to Zr or Mg due to the close proximity of the peaks in the (011) reflection for both. This is likely due to a combination of Mg and Zr being in substitutional solid solution with each other and the development of compressive stress in the coating. On closer inspection of the Mg: 8 at% GAXRD trace in Figure 5.9, the MgO phase at a 2θ angle of 37.0° appears to be in close

proximity to the Zr and Mg phases (in the (011) reflection). The primary lattice peak for MgO is in the (002) reflection at a 2θ angle of 43.3° as shown in Figure 5.11. However, the MgO peak at a 2θ angle of 37.0° which is in the (111) reflection has a much smaller peak intensity and therefore can be discounted as a candidate phase.

Another phase which was analysed as a candidate phase which might be attributable to the broad peak was zirconium oxide. This was a consideration because of (a) possibility of residual oxygen inside the chamber during deposition and (b) the process temperature inside the vacuum chamber is about 225°C [224] at the substrate holder which may create the conditions for oxide formation, if sufficient quantity of oxygen is present. As was established in Chapter 1, Section 1.8.1, the most likely polymorph of zirconia to form under the process temperatures used during deposition was the monoclinic zirconia phase which is stable from room temperature up to 1170°C . But no other m-ZrO₂ peaks were identified that could be attributable to the peaks of the GAXRD trace of the Mg: 8 at% coated sample. Thus, it is unlikely that the 2θ peak position of $\sim 36.5^\circ$ could be attributable to m-ZrO₂.

Lawal et al [224] produced aluminium-based (Al-Ni-Ti-Si-B) coatings using magnetron sputter deposition on stainless steel substrates at low pressure (0.3 Pa) and presented GAXRD patterns that showed a raised broad peak in the $35^\circ < 2\theta < 55^\circ$ range. The author reported difficulty in indexing the broad XRD peak which could be populated by many of the reflections attributable to the metallic phases of the aluminium-based coating. The broad peak which initially may have been thought of as the formation of an amorphous structure was concluded to be an ultrafine nanocrystalline Al₃Ni intermetallic phase following TEM analysis.

To the best of my knowledge, literature investigating intermetallic phase formation resulting from the mixing of Zr and Mg is scarce. One of the beneficial effects of zirconium inclusion in magnesium alloys is that it acts as a grain refiner [223]. The addition of small amounts of zirconium (0.4-0.8 wt%) to Mg-based alloys such as Mg-Zr-RE²⁴ have been reported to reduce the as-cast grain size of the Mg alloy by at least two orders of magnitude compared to without Zr addition [312] - producing a near equiaxed and more uniform microstructure and thereby improving the mechanical properties of the alloy. It does this by bonding with the Rare Earth element to form intermetallic precipitates. Reducing the grain size decreases the amount of possible 'pile up' of dislocations at the grain boundaries – thus a higher stress is necessary to move dislocations across grain boundaries resulting in a higher yield strength of the alloy. The intermetallic precipitates formed create stress fields within the alloys and creates a physical blockade through which dislocations cannot pass. Therefore, dislocations require greater energy or greater stress to be applied to overcome the energetic barrier for diffusion across

²⁴ RE is a Rare Earth element.

the boundary. This precipitation strengthening mechanism increases the overall yield strength of the alloy. In this study, combining Zr and Mg might lead them to want to form an intermetallic phase possibly in the form of $ZrMg_2$ precipitates [223]. But the low sputter deposition temperature of (225°C) prevents this from happening and there do not seem to be any peaks in the GAXRD data that would clearly indicate that an intermetallic phase had formed. The formation of an intermetallic phase cannot be completely discounted as the precipitates may either be very small or sparsely distributed in the coating. However, if intermetallic compounds were trying to form (but unable to do so), this might lead to stresses in the coating that would change the HCP lattice parameters and result in the shift to lower angles of 2θ seen in the GAXRD patterns. TEM and XPS techniques could be used to provide more evidence and is noted as a recommendation for future work. Due to technical issues surrounding the TEM machine resulting in significant downtime, TEM analysis could not be carried out for the Zr-Mg coatings produced in this study but would be useful to further investigate the potential reasons for why a broad raised profile was seen for the Mg 8 at% sample in this case.

It can be seen from the Mg: 8 at% GAXRD pattern that the close proximity of the Mg and Zr peaks in the (010), (011), (012) and (112) reflections mean that either of these phases could serve as potential candidates attributable to these peaks as they are almost indistinguishable and this makes it challenging to conclusively determine whether the peak is Mg or Zr – particularly as the peaks are broad. The main peak in the (011) reflection can be seen to be shifted to lower angles of 2θ by about 2.1° , and a shift to lower angles of 2θ was identified for the (110) and (112) peaks indicating an increase in lattice parameters.

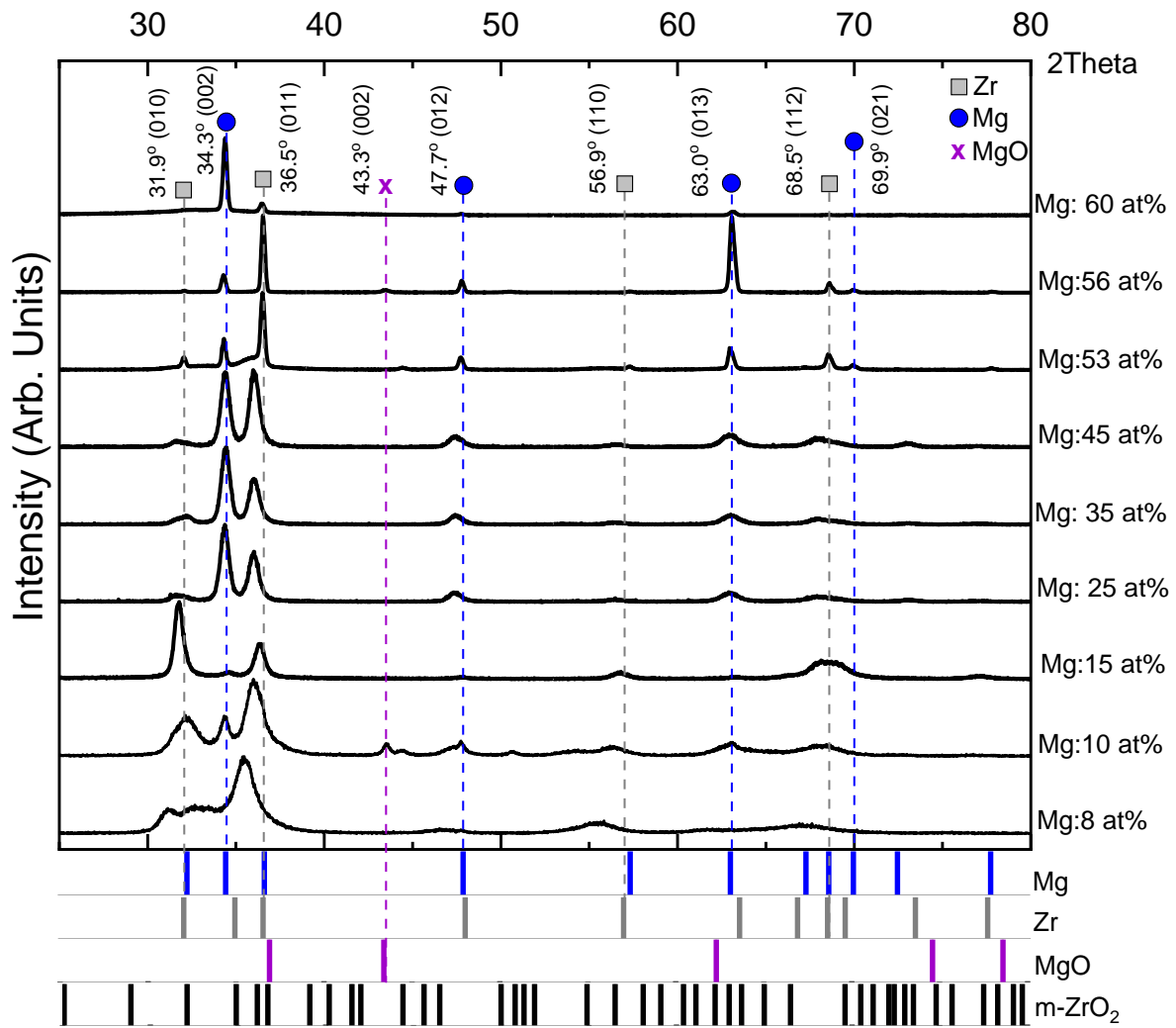


Figure 5.9: GAXRD pattern of the sputter-deposited Zr-Mg coating on stainless-steel substrates. The patterns are compared to peak positions found in literature: Mg [213], Zr [195], MgO [313] and m-ZrO₂ [56].

The GAXRD pattern for the Mg: 10 at% sample also exhibited broad peaks, majority of which were attributable to either the Mg or Zr phases. The peaks did not exhibit a raised broad profile and could be seen to be sharper and more defined compared to the Mg 8 at% sample, whereby some of the peaks could be indexed to the Mg phase in the (002) and (013) reflections. The Zr (011) reflection could again be seen to shift to lower angles of 2θ but to a lesser extent (by $0.5^\circ 2\theta$) compared to the Mg: 8 at% sample. As before, the broad peaks obtained for the Mg: 10 at% GAXRD pattern were difficult to definitively index to Mg and Zr phase - especially in the (011), (012) and (112) reflections due to the close proximity of these peak positions for the Mg and Zr phases on the 2θ scale. However, if there were separate Zr and Mg phases, there would be evidence of 'peak-splitting' which would indicate phase separation. For instance, in the (002) or (013) reflections - seen more clearly in Figure 5.10, there is a noticeable difference in the 2θ angle between Mg and Zr, so if there was phase

separation, there would have been two peaks – one indexed to Zr and the other to the Mg phase. However, the GAXRD pattern for the Mg: 10 at% sample did not show any evidence of ‘peak-splitting’ that would indicate phase separation.

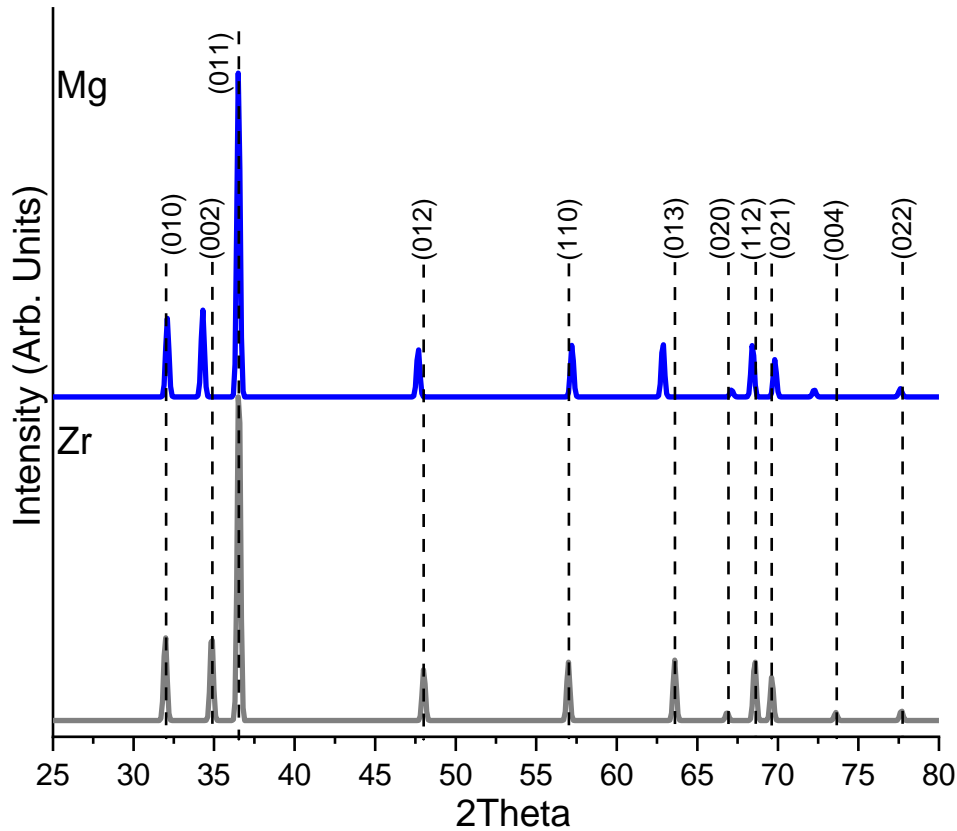


Figure 5.10: XRD reference patterns of Zr [195] and Mg [213] Phases show slight differences in the peak positions for some of the peaks such as the (002) and (013). If there was evidence of peak-splitting (in Figure 5.9), separate peaks would have been exhibited which might have been indexed to Zr or Mg phases indicating phase separation. However, this was not seen from the GAXRD patterns in Figure 5.9.

Thus, it is not clear using the GAXRD patterns alone to determine which phase these broad peaks are attributed to, which could indicate solid solution of Mg and Zr with each other. However, one potential route to help identify reflections that may be either be Mg or Zr phases (or a solid solution of both) would be to conduct electron microscopic analysis i.e. EBSD, or FIB with TEM. This would enable the determination of lattice parameters which could then be compared to lattice parameters of Mg or Zr reported in the literature.

Interestingly, MgO peak was identified at a 2θ angle of 43.3° in the (002) reflection for the Mg: 10 at% sample. As mentioned previously during SEM/EDX analysis of the Mg: 25 at% sample, low oxygen content was detected in the Zr-Mg coatings (but MgO or m-ZrO₂ peaks were not detected for this

GAXRD pattern – possibly because of the low oxygen content of 5 at% in the coating). Following sputtering, a black loosely-adherent powder (which could be magnesium oxide) formed on the Mg target segment with a surface coverage of about 20% and was also observed on the Zr targets. But it is unlikely that MgO (which is a compound) would be re-sputtered onto the zirconium or stainless steel substrates since sputter deposition is an atomistic process. It is possible however, that residual oxygen in the deposition chamber may have initially formed on the magnesium and zirconium target segments during the sputter deposition run which may well have sputtered off the target segments, together with the zirconium and magnesium atoms, which were then incorporated in the coating and from the GAXRD pattern of the Mg: 10 at% sample, the peak at a 2θ angle of 43.3° in the (002) reflection suggests MgO may have formed. For the Mg: 56 at% sample, where oxygen content of 10 at% was detected from EDX analysis, a small peak in the (002) reflection indexed to MgO could be seen. It is likely that the peak at 2θ angle of 43.3° is the MgO phase because this is the primary MgO reflection (that has the highest peak intensity) in the reference MgO pattern [313] which is presented in Figure 5.11.

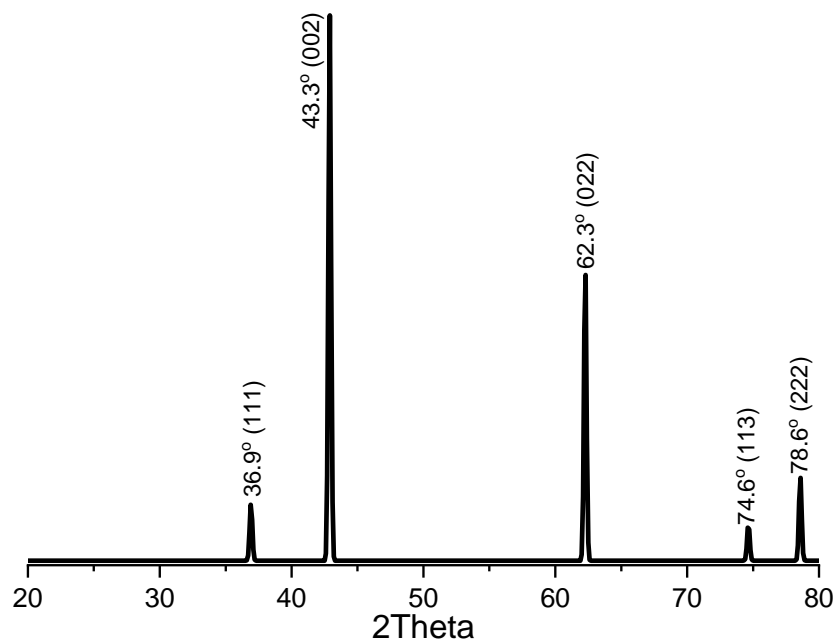


Figure 5.11: MgO peak reflections.

The Mg: 15 at.% GAXRD pattern shows that the peak intensity in the (002) reflection at a 2θ angle of 34.3° to be almost negligible in this pattern whereas the peak intensity is high or forms the dominant peak in other GAXRD patterns at the same reflection. The GAXRD trace for the Mg: 15 at% sample shows similar broad peaks to that of the GAXRD traces of the Mg: 8 at% and Mg: 10 at% samples, whereby the (010), (011), (110) and (112) reflections could be attributable to either the Zr or Mg phase. The (010) reflection at a 2θ angle of 31.9° shows this peak to have the highest intensity for the

Mg: 15 at% pattern, but at higher Mg concentrations (see Figure 5.9), this peak appears to be of low intensity or negligible. The limited available literature on sputter co-deposition of Mg-containing coatings do not provide a clear answer for this disparity. It would be worth repeating this set of experiments several times to confirm this finding. Unfortunately, technical issues and breakdown of the Nordiko PVD rig meant that the coating deposition runs could not be repeated at the time. The peaks were seen to be broad and shifted to lower angles of 2θ (similar to the previous GAXRD traces) which would indicate an increase in lattice parameters high levels of compressive stress in the coatings. As before, no evidence of 'peak-splitting' was identified where Zr and Mg peaks may be distinguishable such as at the (002), (110), (013) or (021) reflections which would otherwise indicate phase separation.

The GAXRD pattern for the Mg: 25 at% sample exhibited slightly narrower peaks compared to the previous Mg: 8 at.%, Mg: 10 at% and 15 at% GAXRD patterns. The peaks show a shift to lower angles of 2θ and the peaks in the (002), (011), (012) and (112) reflections can be seen to be broad enough to accommodate both the Zr and Mg peaks (similar to the previous GAXRD traces) due to the close proximity of the Zr and Mg phases to the peaks seen in the GAXRD pattern. The GAXRD pattern shows that magnesium inclusion at 25 at% shows no evidence of unmixing into separate phases. The GAXRD pattern for the Mg: 35 at% sample shows a very similar pattern to the Mg: 25 at% trace in terms of peak positions and the same shift to lower angles of 2θ could be seen especially for the (011) and (012) reflections. Interestingly, the GAXRD pattern for the Mg: 45 at% sample shows an increase in the intensity of the peak in the (011) reflection which appears to exhibit identical intensity to the (002) reflection at a 2θ angle of 34.3° – possibly due to the increase in magnesium content in the coating. Again, the peaks were seen to be broad could accommodate both the Zr and Mg phases in the (010), (011), (012), (013) and (112) reflections – supporting the view that magnesium and zirconium could be in substitutional solid solution with each other.

These findings are interesting because magnesium and zirconium do not typically co-exist (i.e. as an alloy) as the GAXRD data for the magnesium-containing zirconium coatings appears to suggest. A possible explanation for this might be derived when considering the Hume-Rothery rules for substitutional solid solution (see Chapter 1, Section 1.13 for details). Both magnesium and zirconium adopt a HCP crystal structure and have similar outer electron orbital configurations and therefore inherently quite compatible. The electronegativity of both Mg and Zr are 1.31 and 1.33 [227] respectively which means electrons will be more equally shared. Both magnesium and zirconium also have fairly similar atomic sizes – 150 picometers and 155 picometers [314] respectively, and partly as a consequence of this, their HCP crystal lattice parameters are also quite similar (as XRD ICDD cards confirm), thus, they are 'dimensionally' compatible having a favourable atomic size factor of 3.2%

which is within the 15% limit for solid solubility. It is recognised however, that since the atomic size of Mg and Zr are very similar, the shift to lower angles of 2θ (seen from the GAXRD patterns) is likely due to a combination of Mg and Zr being in substitutional solid solution with each other and the development of compressive stress in the coating due to increased Mg inclusion in the Zr-Mg coating. However, magnesium is in Group II with a valency of 2 and zirconium is a transition metal in Group IV with a valency of 4. As the differences between the solute and solvent atoms become more unequal, solid solutions become more restricted and there is a greater tendency to form intermetallic compounds. Therefore, zirconium has an unfavourable valence for solid solution in magnesium. Another argument would be consider that the ionic radii of both Mg and Zr (150 pm and 155 pm respectively) relate to the Mg-Mg and Zr-Zr bonding of the pure elemental metals. Thus, mixing two elements of different valency may result in changes to the effective inter-atomic spacing (i.e. a shift to lower angles of 2θ suggests larger lattice parameters) possibly resulting in lower bond strength between Mg-Zr compared to Zr-Zr or Mg-Mg. It is not fully understood why this might be the case without conducting TEM investigations and XPS binding energy measurements. Since Zr is a transition metal (with partially-filled d-orbitals) and Mg is alkaline-earth metal, transition metals can adjust their d-orbital electron fill - and take up different valency in compounds (ie. Zr is not necessarily always 4+, whereas Mg is usually 2+). Therefore, if there are any adjustments are required, it could be due to the inclusion of Zr and the differences in the valency between these two elements might contribute to the build-up of compressive stress in the coating, but this would require further research. One method to measure compressive stress would be use the $\text{Sin}^2(\psi)$ method. This is performed by measuring the diffraction angle 2θ with different tilting angles ψ and generating a graph of 2θ as a function of $\text{Sin}^2(\psi)$ to determine the compressive stress [300].

There is also the indication that magnesium and zirconium are possibly in solid solution with each other. In one example of (FCC) copper (Cu) and nickel (Ni) (as two elements with complete solid solution compatibility with each other across the entire composition range), their melting points (T_m) are different. Both Cu and Ni have are identical in atomic size (35 pm) [314]. Nickel has a much higher T_m of 1455°C compared to the T_m for copper of 1085°C [216]. Both Ni and Cu can therefore, co-exist in the liquid state since the boiling point (T_B) of Cu is 2562°C which is much higher than the T_m of Ni. The key difference in the case of Mg and Zr is that the T_B of Mg is 1090°C which is far below the T_m of Zr (1855°C [216]), so they cannot co-exist in the liquid state – and cannot therefore, be cast as an alloy. However, since sputter PVD permits direct conversion from solid, to (ionised) gas, to solid (avoiding the liquid state), it is possible to co-deposit atomistically, the two elements in solid solution with each other, whereby they might be expected to co-exist in the solid state. Furthermore, taking the example of Zr and Ti (transition metals in the same periodic table group, with similar electron configurations),

they are both HCP metals, with complete solid state solubility with each other [315] and (again) their melting points are different (1668 °C for titanium compared to 1855 °C [216]), but the difference is close enough for them to co-exist in the liquid state as well. However, their atom sizes are surprisingly different (Zr is about 11% bigger than Ti (155 pm compared to 140 pm respectively [216])), yet they are still structurally compatible. Thus, even if Mg and Zr were quite different in atom size, it probably would not have a big effect on their inherent solubility in each other, since their electronic structures are in any case compatible.

In contrast to the previous GAXRD patterns, the GAXRD pattern for the Mg: 53 at% sample exhibited much narrower peaks. This enabled a few of the peaks to be indexed to either the Zr or Mg phase such as the peaks in the (002), (013) and (021) reflections, since the Zr and Mg peaks at these 2θ positions could be distinguished more easily. The highest peak intensity could be attributable to the Zr phase at a 2θ angle of 36.5° in the (011) reflection. The GAXRD pattern for the Mg: 56 at% sample showed similar pattern to the Mg: 53 at% sample with a noticeable increase in the (013) peak which could be attributable to the Mg phase. The increase in peak intensity of the (013) reflection suggests an increased number of grains oriented in this reflection which suggests an increased magnesium concentration in the coating.

The GAXRD pattern of the Mg 60 at% content is interesting in that there are three main peaks that were identified from the pattern with the dominant peak being in the (002) reflection at a 2θ angle of 34.3° which is attributable to the Mg phase. Similar to the Mg: 53 at% and Mg: 56 at% samples, the peak in the (002) reflection can be seen to be narrow indicating larger crystallite size compared to the Zr-rich coatings. The two other (much smaller) peaks – one which is attributable to the Zr phase in the direction of the (011) plane, and the other was attributable to the Mg phase in the direction of the (013) plane. It is interesting to note that the peaks in the direction of the (011) and (013) planes were much smaller for the Mg: 60 at% sample than for the Mg: 53 at% and Mg: 56 at% samples. The exact reason for this is not yet known and to the best of my knowledge, this has not been reported in the literature. Unfortunately, due to technical issues surrounding the Nordiko PVD rig, this set of coating deposition runs could not be repeated but it would be worth however, carrying out multiple repeats and then determine if similar GAXRD patterns are obtained.

The average crystallite size (of magnesium and zirconium of the coating) was calculated for each of the GAXRD patterns using Scherrer's equation (as was previously demonstrated in Chapter 4, Section 4.2.2). Peak fitting of the diffraction patterns was performed manually using Origin software package and the background 'noise' was removed using a built-in linear model. The required parameters used

to calculate the average crystallite size are shown in Equation 4.4 and the results are presented in Table 5.2.

Table 5.2: Average crystallite size determined from GAXRD patterns using Scherrer's equation.

Mg Concentration (at%)	Crystallite Size D (nm)
8	8.2
10	8.3
15	9.5
25	9.8
35	10.4
45	10.7
53	28.9
56	29.3
60	30.1

The GAXRD patterns in Figure 5.9 show that as the magnesium content in the Zr-Mg coating was increased, the peak intensities exhibited narrower peak widths. For the GAXRD patterns showing 8 at% to 45 at% magnesium concentration range, the average crystallite size increased from 8.2 nm to 10.7 nm. However, for 53 at% to 60 at% magnesium concentration range, the peaks are noticeably narrower; and the average crystallite size increased from 28.9 nm to 30.1 nm. This is most likely occurring due to the much higher surface diffusivity of Mg compared to Zr resulting in competitive grain growth of smaller diameter columns (of hundreds of nanometers) during coating growth.

5.1.4 Nanoindentation Hardness of Zr-Mg Coatings

Nanoindentation measurements were performed on the Zr-rich (Mg: 25 at%) and Mg-rich (Mg: 53 at%) sputter co-deposited samples using a Hysitron Inc. Triboscope™ equipped with a Berkovich triangular-pyramidal diamond indenter. A number of indents were carried out on the surface of the coated samples at a load of 4 mN with a 10 μm spacing between each indent. The hardness vs contact depth profiles of the Zr-rich and Mg-rich coatings are presented in Figure 5.12.

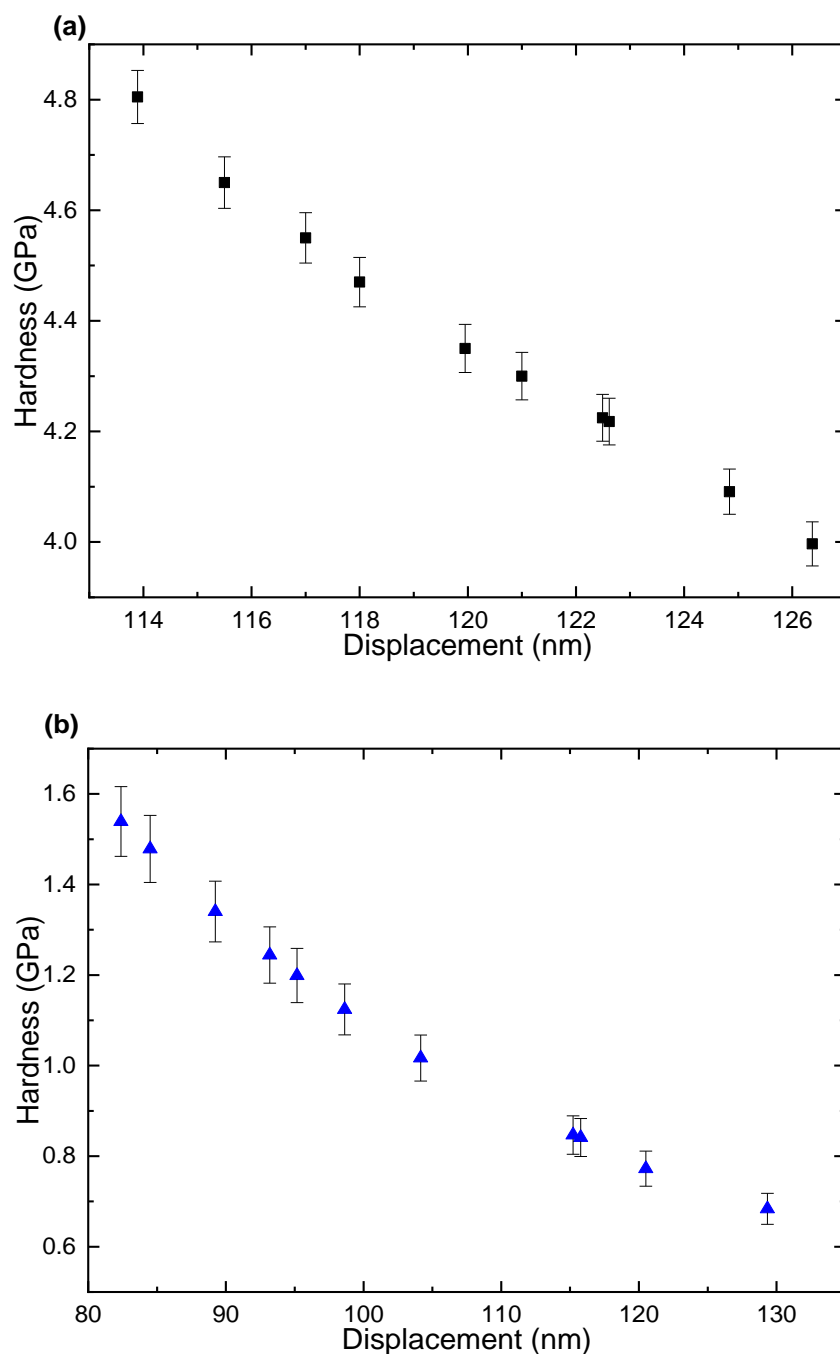


Figure 5.12: Hardness vs displacement graphs of (a) Zr-rich and (b) Mg-rich sputter-deposited coatings.

It can be seen from Figure. 5.12(a) that at a contact depth of 120 nm, the hardness value for the Zr-rich coating is approximately 4.32 ± 0.10 GPa. This is slightly lower than the hardness obtained for pure untreated zirconium substrate of 4.40 ± 0.12 GPa determined in Chapter 3, Section 3.8.1. At the same contact depth of 120 nm, the hardness of the Mg-rich coating in Figure. 5.12(b) was determined to be significantly lower than the Zr-rich coating at 0.81 ± 0.09 GPa. This suggests that the inclusion of magnesium in the sputter co-deposited coatings influences the hardness properties of the Zr-Mg coating and shows that the hardness of the Zr-Mg coating system decreased with increased magnesium content. Furthermore, the SEM image of the surface of the Mg-rich coating in Figure 5.6(a) appears to show inter-columnar voids and the presence of more inter-columnar (porous) volume in the Mg-rich coating (due to higher number of smaller diameter columns compared to the Zr-rich coating (as mentioned previously) may also contribute to the lower hardness of the Mg-rich coating. Furthermore, magnesium is generally considered to be a 'soft' metal compared to zirconium. Although nanoindentation hardness values for magnesium was not found in the literature, the Brinell hardness of magnesium is about 260 MPa which is much lower than 650 MPa for zirconium [216]. It would be worth determining the hardness of magnesium metal using nanoindentation so that comparison with pure zirconium could be made. Due to technical issues and availability surrounding the nanoindentation equipment, multiple repeats of hardness measurements could not be performed on these samples, but would be useful to carry out including on other sputter-deposited samples to corroborate this finding.

5.1.5 Scratch Adhesion Tests of Zr-Mg Coatings

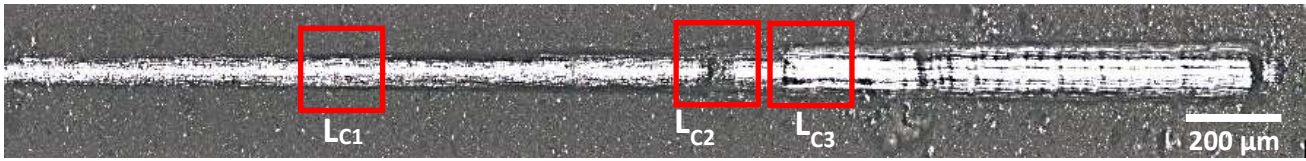
Scratch adhesion tests was performed to measure the adhesion of the Zr-rich (Mg: 25 at%) and Mg-rich (Mg: 53 at%) sputter co-deposited coatings (on zirconium substrates). A normal load of 40 N was used and the sample was traversed at a speed of 10 mm/min for a distance of 10 mm. Three scratch adhesion tests were carried out for each sample and the Tangential Force profiles were compared to ensure that similar scratch behaviour was observed. The scratch profiles presented in this section are from the third scratch test for each sample. The sample surface and diamond tip of the stylus were cleaned with isopropanol prior to each scratch to minimise cross-contamination. As previously mentioned in Chapter 2, section 2.11, optical microscopic analysis, Acoustic Emission (AE), Tangential Force (F_T) and Normal Force (F_N) measurements were used to determine critical loads to failure (L_{C1} , L_{C2} and L_{C3}) of the coatings.

The scratch test profile for the Zr-rich (Mg: 25 at%) coating is presented in Figure 5.13. The onset of chipping damage was identified on the edges of the scratch track from the optical micrograph in Figure

5.13(a) which indicated cohesive failure of the coating. This was corroborated from the F_T profile in Figure 5.13(b) that showed an increased gradient and an enhanced erratic pattern. The critical load (L_{C1}) at which cohesive failure of the Zr-rich coating occurred was determined to be 16.5 N. An encouraging result from the optical micrograph (Figure 5.13(a)) is that material damage at the edges of the scratch track did not appear to be extensive with increased applied Normal Force (F_N). Furthermore, defects such as tensile cracking (which typically occur following the onset of chipping damage) was not observed from the optical micrographs. The higher hardness of the Zr-rich coating (compared to the Mg-rich coating determined in Figure 5.12(a)) and the appearance of a dense uniform coating from the cross-sectional SEM micrograph in Figure 5.7(a) (whereby the microcracks in the coating were not as extensive as the Mg-rich coating) also supports this proposition.

The scratch profile shows a sharp increase in the gradient of the Tangential Force curve (F_T) as the normal applied load was progressively increased. The critical load (L_{C2}) at which adhesive failure of the Zr-rich coating occurred was determined to be 33 N and was identified where the indenter had penetrated the coating which could be seen from the optical micrograph in Figure 5.13(a). This corresponds with the Penetration Depth of $\sim 27 \mu\text{m}$ which is consistent with the thickness of the Zr-rich coating ($25.2 \mu\text{m}$) determined from cross-sectional SEM analysis in Figure 5.7(a). The high loads required to penetrate the coating is a indication of increased resistance to cracking defects and a high load-bearing capacity of the coating. Exposure of the underlying zirconium substrate could be seen from the optical micrograph in Figure 5.13(a) which indicated complete spallation of the coating from the substrate underneath. The critical load (L_{C3}) at which this failure occurred was determined to be 35 N.

(a)



(b)

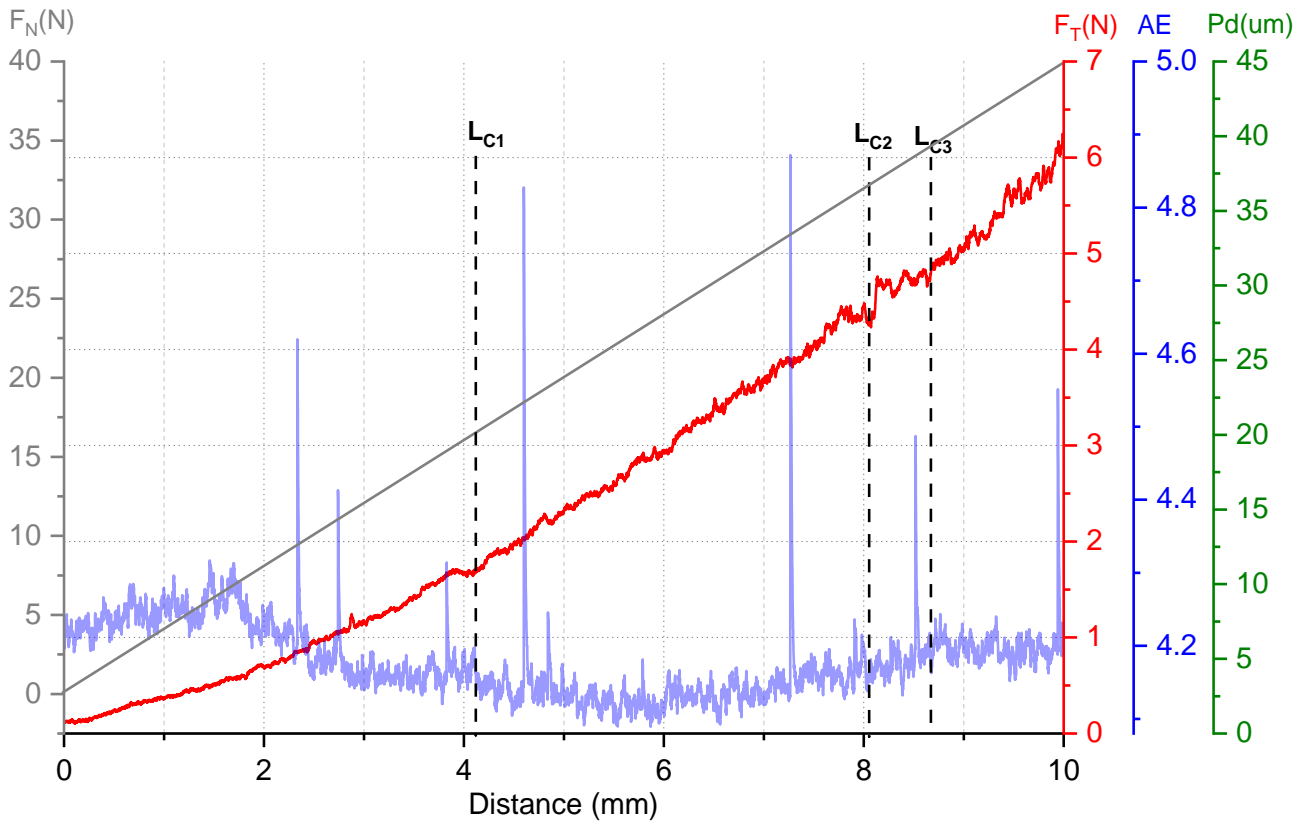


Figure 5.13: Scratch adhesion test of the Zr-rich (Mg: 25 at%) coating showing (a) optical micrograph of scratch track and (b) scratch adhesion profiles and the critical loads (L_c) to failure.

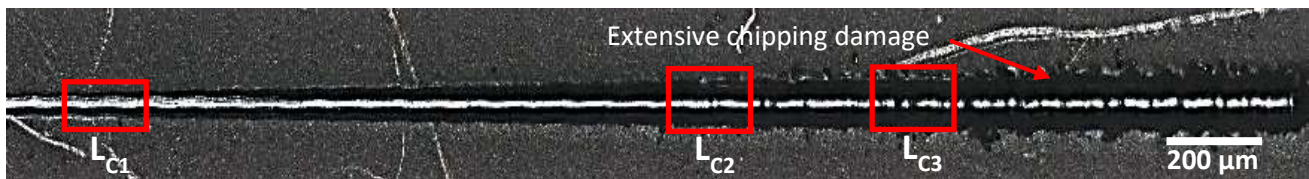
The scratch test profile for the Mg-rich (Mg: 53 at%) coating is presented in Figure 5.14. The optical micrograph in Figure 5.14(a) shows the early occurrence of severe chipping damage demarcated by dark regions at both edges of the scratch track which was found to increase in severity as the load was increased. It can also be seen that chipping damage was found to more extensive for the Mg-rich coating (compared to the Zr-rich coating) whereas the chipping damage for the Zr-rich coating can be seen to be constrained closer to the scratch track. This suggests that the Mg-rich coating could be more brittle than the Zr-rich coating. Figure 5.14(b) shows that chipping damage of the coating occurred about three millimetres from the beginning of the scratch track and an increase in the AE

signals indicating cracking of the coating. However, observation of the cracking could not be resolved at higher magnification using optical microscopy due to the high roughness of the coating.

The critical load (L_{C1}) at which cohesive failure of the coating occurred was 12 N which is much lower than the L_{C1} value of 16.5 N determined for the Zr-rich (Mg: 25 at%) coating. As the load was progressively increased, the Tangential Force curve (F_T) exhibited an increased gradient and erratic perturbations until adhesive failure was reached at a critical load (L_{C2}) of 23 N. This is much lower than the 33 N critical load for adhesive failure of the Zr-rich coating which indicates a lower load-bearing capacity for the Mg-rich coating. The Penetration Depth at which adhesive failure occurred was about $\sim 28 \mu\text{m}$ which is consistent with the thickness of the Mg-rich coating of ($26.5 \mu\text{m}$) determined from cross-sectional SEM analysis in Figure 5.7(b). The scratch adhesion profiles show that increased magnesium content and higher oxygen contamination of the coating lead to a lower load-bearing capacity of the Mg-rich coating (compared to the Zr-rich coating) and this is consistent with the low hardness of the coating determined in Figure 5.12(b). Furthermore, the higher concentration of microcracks in the Mg-rich coating (seen in Figure 5.7(b)) would facilitate crack propagation as the indenter is penetrated with a progressively increasing load resulting in a lower load-bearing capacity of the coating.

As the normal applied load (F_N) was progressively increased further, the Tangential Force curve can be seen to show an enhanced erratic profile. It was difficult to identify whether the critical load (L_{C3}) had been reached using the optical micrograph in Figure 5.14(a) alone due to the high roughness of the Mg-rich coating mentioned earlier. Based on the evidence presented in the previous scratch adhesion profiles presented in Chapter 3, Section 3.9 and Chapter 4, Section 4.4, it is reasonable to assume that this is galling wear of the underlying zirconium substrate. This indicates complete spallation of the coating from the substrate and the critical load (L_{C3}) for this failure was determined to be ~ 27 N.

(a)



(b)

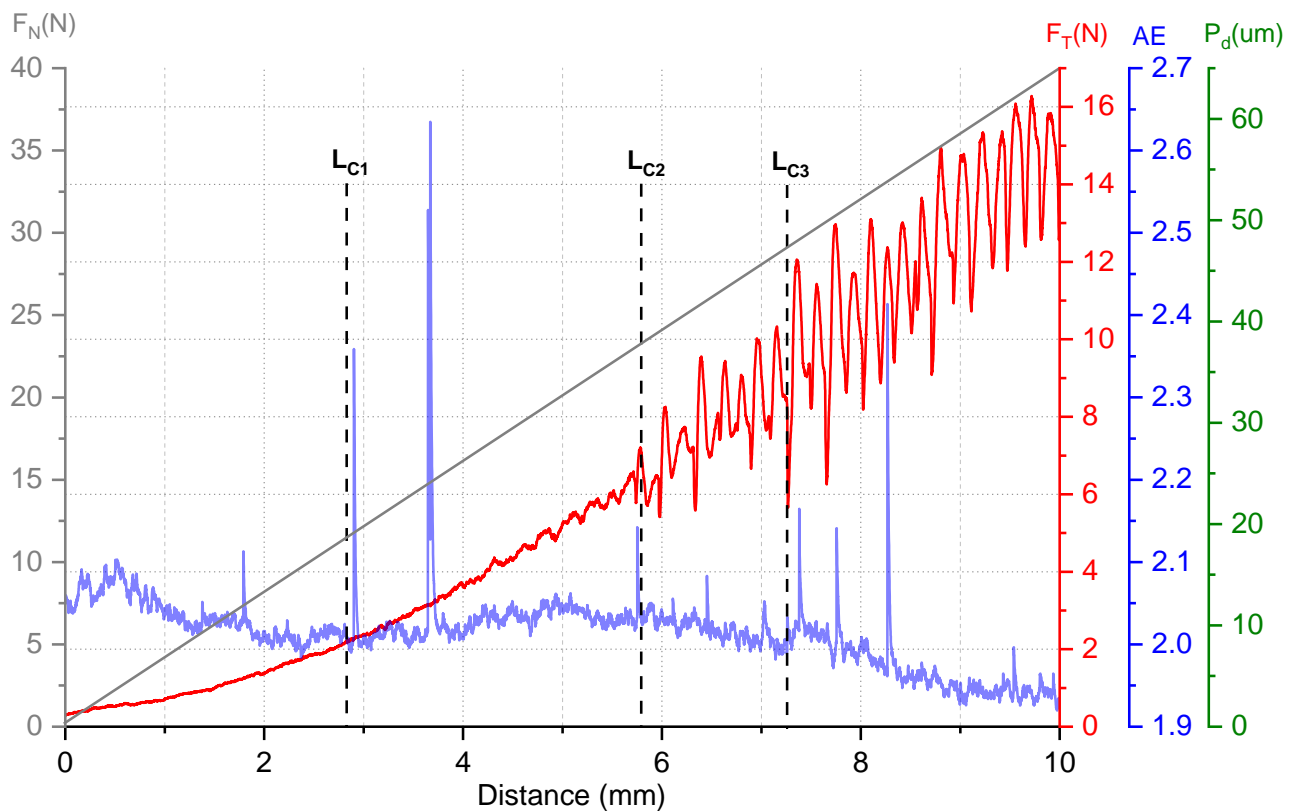


Figure 5.14: Scratch adhesion test of the Mg-rich (Mg: 53 at%) coating showing (a) optical micrograph of scratch track and (b) scratch adhesion profiles and the critical loads (L_c) to failure.

Overall, the scratch adhesion profiles of the Zr-rich (25 at%) coatings demonstrate higher load-bearing capacity and improved failure characteristics compared to Mg-rich (53 at%) coatings. These findings suggest that Zr-rich coatings show higher critical loads to failure and offer higher resistance to defects generated along the scratch track without significant spallation of the material from the underlying zirconium substrate compared to Mg-rich coating.

5.2 Hydrothermal Oxidation of Zr-Mg Coatings

Hydrothermal oxidation tests of pure zirconium (dimensions 2 cm x 2 cm) substrates, Zr-rich (Mg: 25 at%) and Mg-rich (Mg:53 at%) coatings that were sputter co-deposited on both zirconium and stainless steel substrates were performed with deionised water in an autoclave at 360°C for 3 days at a saturation pressure of 18.7 MPa in accordance with ASTM G2-06 [104] (performed at The University of Manchester). The pure zirconium substrates were polished according to the micropreparation regime described in Chapter 2, Section 2.1 prior to hydrothermal oxidation and were used as control reference samples which were compared to the hydrothermally oxidised Zr-rich and Mg-rich coatings. After 3 days, the autoclave was cooled (at a rate of 10°C per minute) and then the samples were removed. Another set of sputter co-deposited samples (that had similar elemental composition as the Zr-rich and Mg-rich coatings previously mentioned) were placed in the autoclave with hydrothermal oxidation performed under the same conditions but the duration was extended to 7 days. This was performed to analyse oxidation behaviour of the coatings at these conditions and to determine if the inclusion of magnesium in the coatings was successful in driving the formation of a stabilised tetragonal or cubic phase zirconia that might stabilise the coating over a wide temperature range during normal operating conditions and a loss of coolant accident in a nuclear reactor. Due to time limitations, only the hydrothermally oxidised Zr-rich and Mg-rich coatings were analysed.

5.2.1 SEM Analysis of Hydrothermally Oxidised Zr-rich and Mg-rich Coatings

The SEM micrographs of the pure zirconium substrates hydrothermally oxidised for 3 and 7 days are presented in Figure 5.15. The SEM micrograph of the pure Zr substrate hydrothermally oxidised for 3 days in Figure 5.15(a) shows mostly a smooth surface and no evidence of microcracks or porous regions. EDX spectrum of the surface shows a high zirconium and oxygen content suggesting that the surface had oxidised. The SEM micrograph also shows scattered artefacts which could be redeposited material on the oxidised surface. The SEM micrograph of the pure Zr substrate hydrothermally oxidised for 7 days in Figure 5.15(b) shows a coarser morphology and scratch defects as well as greater concentration of redeposited material on the oxidised surface (compared to the 3 days sample in Figure 5.15(a)) which suggests material spallation had taken place. Evidence of material spallation could be seen upon closer observation from the micrograph of the dark regions which were identified as craters where material had spalled. EDX spectrum of the surface shows predominantly zirconium but also significant magnesium and oxygen content which could be spalled material from the Mg-rich coating.

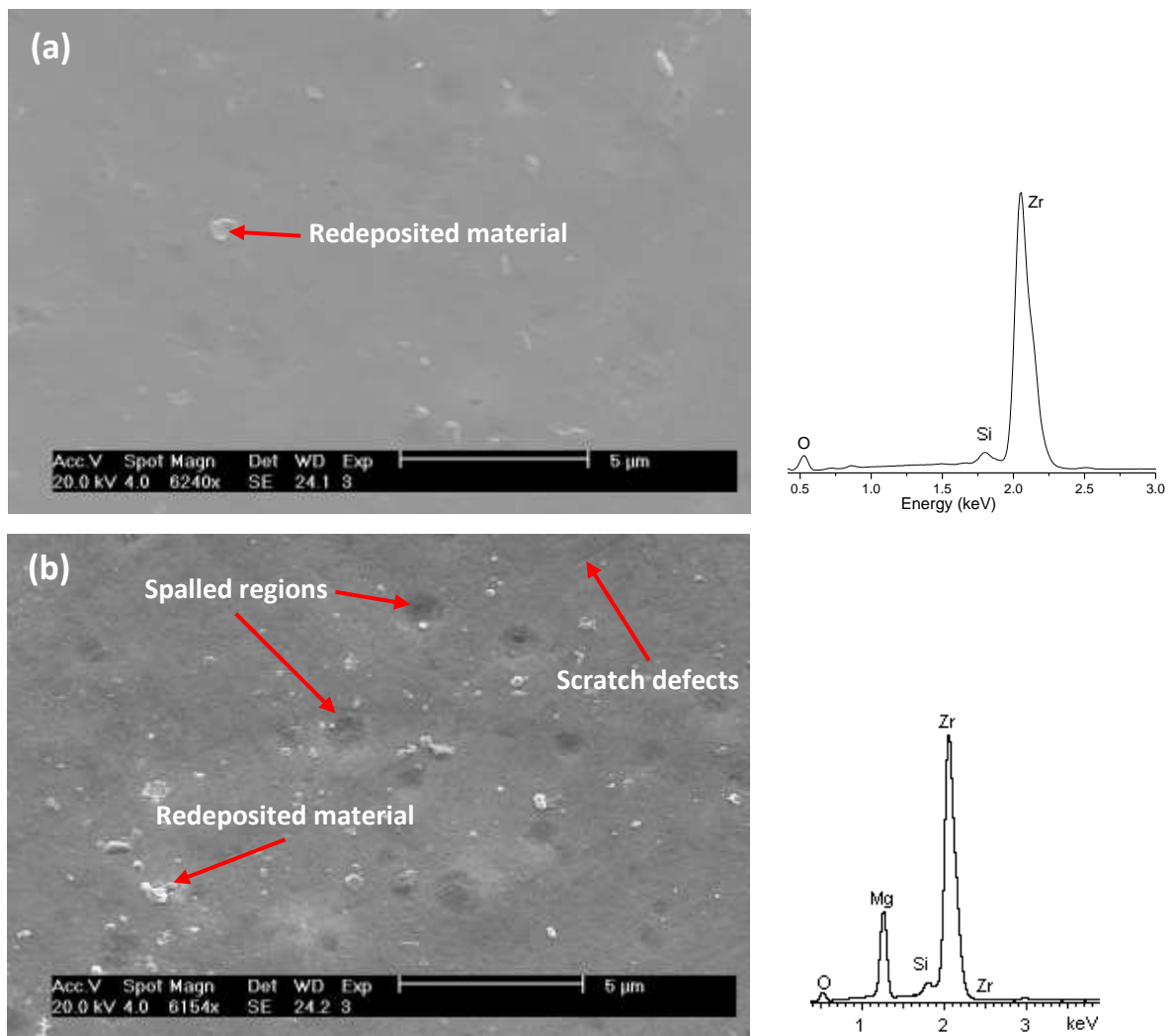


Figure 5.15: SEM micrographs and the associated EDX spectra of the surface of pure Zr following hydrothermal oxidation after (a) 3 days and (b) 7 days.

The SEM micrographs of the Zr-rich (Mg: 25 at%) samples (on zirconium substrates) hydrothermally oxidised for 3 and 7 days are presented in Figure 5.16. The SEM micrograph of the Zr-rich sample hydrothermally oxidised for 3 days in Figure 5.16(a) shows a few long scratch defects on the oxidised surface - probably as a result of residual scratches from the original sample polishing process rather than loose material or debris interaction with the sample in the autoclave under high pressure. EDX spectroscopic analysis of the surface showed a significant oxygen peak from the spectrum in Figure 5.16(a) whereby the elemental composition comprised approximately of zirconium: 50 at%, magnesium: 10 at% and oxygen: 40 at%. Furthermore, the morphology of the Zr-rich coating which showed irregularly-shaped grains (from the SEM micrograph in Figure 5.5(a) following sputter co-deposition is not evident and can be seen to show a largely smooth morphology following

hydrothermal oxidation. The oxidised surface also does not appear to show indications of spallation, porous regions, microcracks or craters.

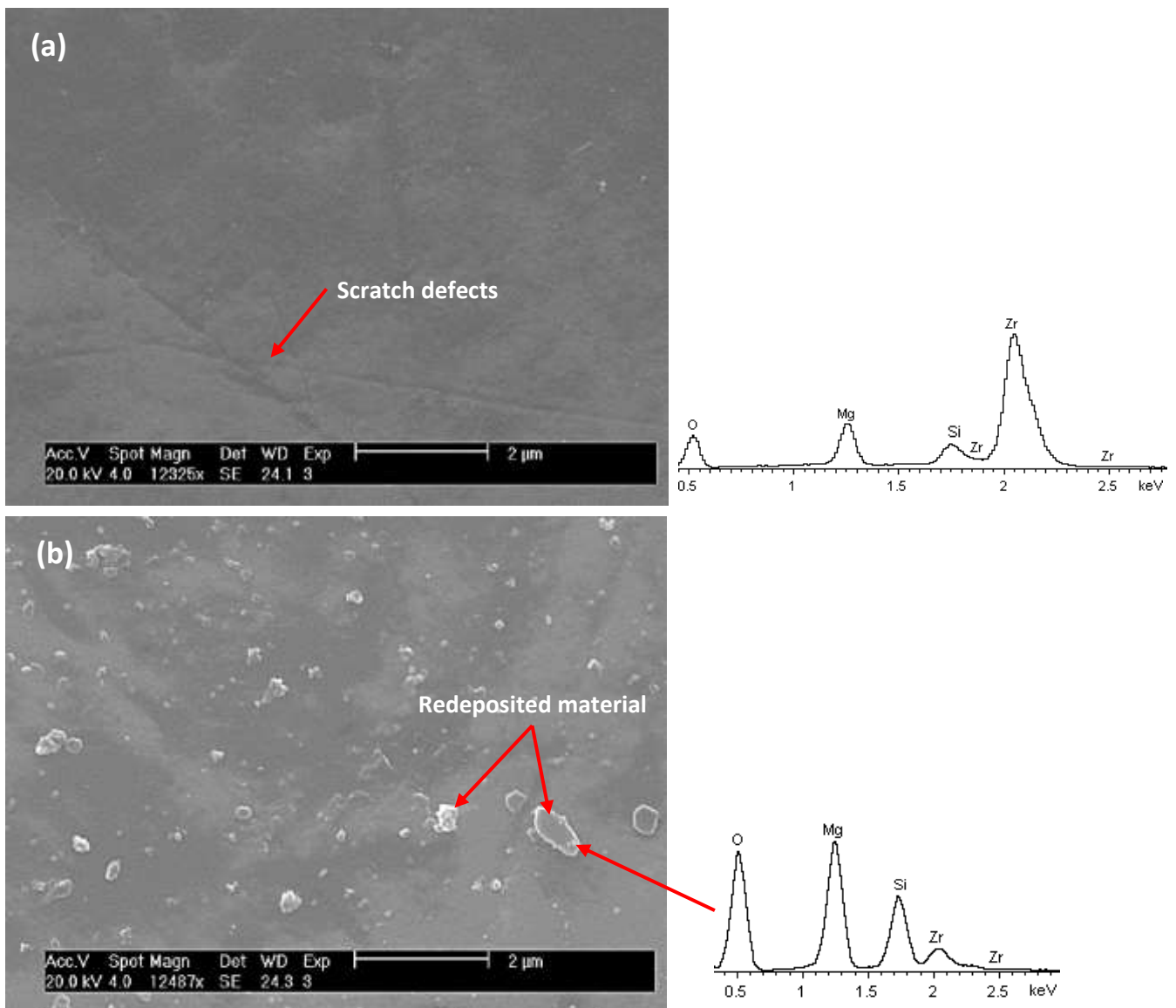


Figure 5.16: SEM micrographs and EDX spectra of the surface of the Zr-rich coatings (Mg: 25 at%) following hydrothermal oxidation after (a) 3 days and (b) 7 days.

The SEM micrograph of the Zr-rich sample hydrothermally oxidised for 7 days in Figure 5.16(b) shows many regions where foreign artefacts could be seen on the surface. EDX spectrum on one of these artefacts in Figure 5.16(b) revealed a high magnesium, silicon and oxygen content. Since the Mg-rich coating and the Zr-rich coating were placed in the same autoclave, this would suggest that the Mg-rich coating and possibly some regions of the growing oxide that had formed on the Mg-rich sample may have spalled and redeposited onto the oxidised surface of the Zr-rich sample. A similar observation was noted for the hydrothermally oxidised pure zirconium samples in Figure 5.15(b)

which showed redeposited material on the oxidised surface and EDX spectrum that showed a high magnesium and oxygen content for the redeposited material. Other than the possible cross-contamination of the spalled Mg-rich coating and oxide from the Mg-rich samples, the oxidised surface of the Zr-rich samples did not exhibit defects such as microcracks or porous regions.

The SEM micrographs of the Mg-rich (Mg: 53 at%) samples (on zirconium substrates) hydrothermally oxidised for 3 and 7 days are presented in Figure 5.17. The SEM micrograph of the Mg-rich sample hydrothermally oxidised for 3 days in Figure 5.17(a) exhibited mostly a smooth surface with a few scratch defects (similar to the findings of the oxidised Zr-rich coatings in Figures 5.16(a)). EDX spectrum of the redeposited material (inset spectrum of Figure 5.17(a)) which (again) revealed a high zirconium, magnesium and oxygen content suggesting that this is the spalled coating and possibly oxide material.

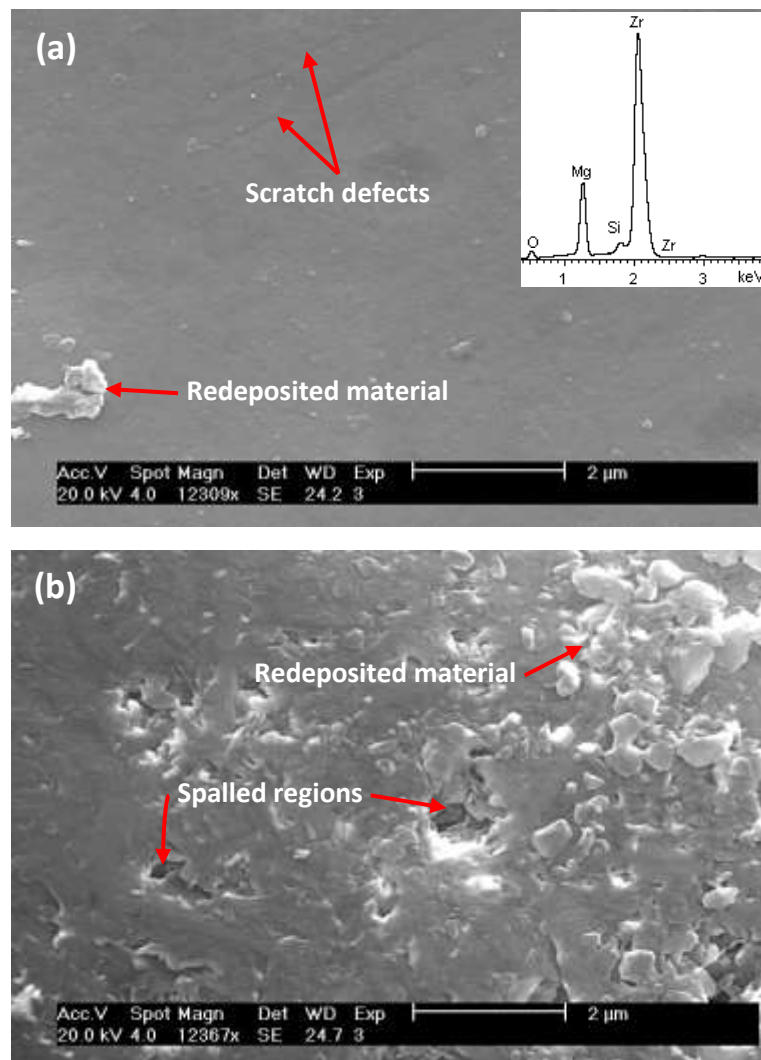


Figure 5.17: SEM micrographs of the surface of the Mg-rich coatings (Mg: 53 at%) following hydrothermal oxidation after (a) 3 days (with the EDX spectrum of the redeposited material) and (b) 7 days.

It is likely that hydrothermal oxidation of the Zr-rich and Mg-rich coatings, even after 3 days could have resulted in spallation of material of some regions which may have redeposited on another area of the same sample. This was previously evidenced from the SEM micrographs in Figures 5.15(b) and 5.16(b) which showed redeposited material on the oxidised surface. The Mg-rich coating hydrothermally oxidised for 7 days in Figure 5.17(b) shows a very different morphology compared to the Zr-rich coating hydrothermally oxidised for the same duration. The surface can be seen to be rough, coarse and porous, and showed craters where spallation of material had taken place. The concentration of redeposited material can also be seen to be greater compared to the Zr-rich coating hydrothermally oxidised for the same duration (Figure 5.16(b)).

The extent of material spallation of the Mg-rich coating hydrothermally oxidised for 7 days can be seen from the SEM micrograph in Figure 5.18. The micrograph shows extensive cracking across the oxidised surface and severe spallation revealing another layer underneath. The region where material had spalled could be seen to exhibit globular-like artefacts (measuring approximately 30 μm in diameter) that appear to have been redeposited on the oxidised surface. These artefacts are likely to be spalled coatings or oxide. Furthermore, numerous regions where material had spalled could be clearly identified from the hydrothermally oxidised Mg-rich sample (in Figure 5.17(b)) which may indicate there could have been a higher volume of redeposited material from the spalled regions of the oxidised Mg-rich sample.

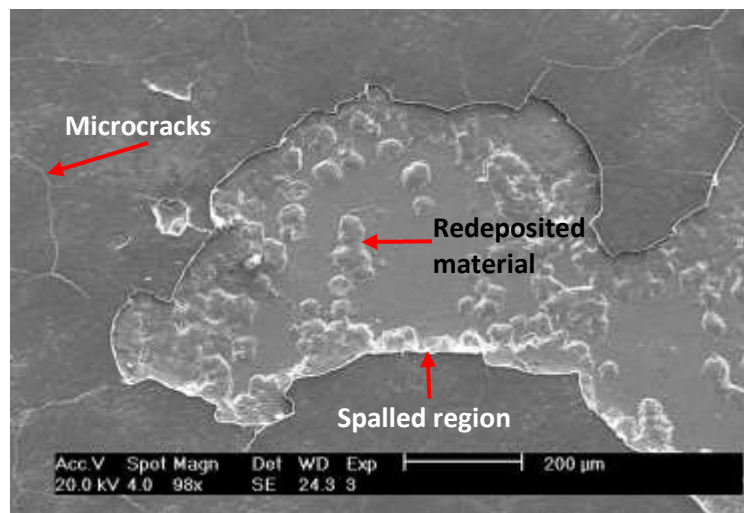


Figure 5.18: SEM micrograph of the Mg-rich coating hydrothermally oxidised for 7 days showing regions of spallation, microcracks are redeposited material on the oxidised surface.

Cross-sectional SEM micrographs of the pure zirconium substrate, Zr-rich (Mg: 25 at%) and Mg-rich (53 at%) coatings hydrothermally oxidised for 3 and 7 days are presented in Figure 5.19. The hydrothermally oxidised pure zirconium (which as mentioned earlier was used as a control reference sample) after 3 days in Figure 5.19(a) shows an oxide scale thickness of $13.1 \pm 0.5 \mu\text{m}$. However, the thickness of the oxide scale can be seen to increase significantly to $19.0 \pm 0.5 \mu\text{m}$ following hydrothermal treatment for 7 days (Figure 5.19(b)). What is also evident from these micrographs is the presence of lateral microcracks which increased in severity with distance from the oxide/metal interface region. Evidence of oxide spallation near the pre-formed outer oxide scale was also observed which indicates that the oxide scale is highly stressed and/or brittle. Importantly, this shows how easily oxide material is lost through spallation, and so the actual oxide scale thickness may have been higher than measured due to the spallation of the oxide scale at the conditions used during hydrothermal oxidation. A similar finding was observed in Chapter 4, Section 4.2.1. Furthermore, the oxide scale at the interface region was characterised as a wavy undulating appearance - possibly indicating a cyclic oxide growth pattern [94].

The Zr-rich (Mg: 25 at%) sample hydrothermally oxidised for 3 days in Figure 5.19(c) shows an oxide scale thickness of $3.2 \pm 0.5 \mu\text{m}$ which is significantly less than the oxide scale grown on pure Zr ($13.1 \mu\text{m}$) at the same duration. It was deduced earlier from the cross-sectional SEM micrograph in Figure 5.7 that the thickness of the Zr-rich (Mg: 25 at%) coating was measured to be $25.2 \pm 0.5 \mu\text{m}$. This suggests that much of the coating had spalled. There is likely to have been some regions of the coating that may have completely spalled resulting in the oxidation of the underlying pure Zr substrate as suggested in Figure 5.19(c), however the EDX spectrum in Figure 5.16(a) shows the detection of Zr and Mg which suggests that there are regions of the coating that remain and had not completely spalled. Thus, the oxidation of the sputter co-deposited Zr-Mg coating cannot be entirely ruled out, but this would require further research. Furthermore, the fact that the oxide scale developed was $3.2 \pm 0.5 \mu\text{m}$ (compared to the thickness of the oxide scale of $13.1 \mu\text{m}$ for pure Zr after 3 days) suggests a gradual spallation of the coating within 3 days and the start of the growth of an oxide scale on the zirconium substrate which continues to grow with increased duration. Furthermore, the oxide scale at the oxide/metal interface region exhibited an undulating 'wavy' appearance which is similar to the oxide scales formed (at the interface) on the pure zirconium substrates seen from the micrographs in Figure 5.19(a) and (b). Evidence of material spallation could also be seen at various regions along the preformed outer oxide scale. The cross-sectional SEM micrograph in Figure 5.19(d) of the hydrothermally oxidised Zr-rich coated sample after 7 days revealed an oxide scale thickness of $7.7 \mu\text{m}$. As before, regions where material had spalled could be seen near the preformed outer scale which suggests that the oxide scale formed could have been higher than was measured due to the

spallation of the oxide during the hydrothermal oxidation test. The thickness of the oxide scale developed after 7 days for the Zr-rich sample was found to be much less when compared to the thickness grown on the oxide scale of pure Zr substrate ($19.0 \pm 0.5 \mu\text{m}$) at the same duration. This supports our earlier proposition that spallation of the Zr-rich coating during hydrothermal oxidation was a gradual process. Even though much of the Zr-rich coating had undergone spallation, the coating appears to have been successful in delaying the onset of oxidation of the zirconium substrate (via gradual spallation of the Zr-rich coating) and subsequent corrosion of the metal when compared to pure zirconium.

The sectional SEM micrograph of the Mg-rich (Mg: 53 at%) sample hydrothermally oxidised for 3 days is presented in Figure 5.19(e) and shows an oxide scale thickness of $7.4 \pm 0.5 \mu\text{m}$. This is more than double the thickness of the oxide scale grown on the Zr-rich coated sample ($3.2 \pm 0.5 \mu\text{m}$) but slightly more than half (~56%) of the oxide scale thickness of the pure Zr substrate at the same duration. As with the Zr-rich coated sample, the Mg-rich coating following hydrothermal oxidation was not observed. Furthermore, the oxide scale at the oxide/metal interface region exhibited an undulating 'wavy' appearance which is consistent with the oxide scales formed (at the interface) on the pure zirconium substrates seen from the micrographs in Figure 5.19(a) and (b). The severity of the lateral microcracks for the oxide scale grown on the Mg-rich coated sample appeared to be similar to the oxide scale on the pure Zr substrate but was found to be higher when compared to the oxide scale on the Zr-rich coated sample.

Upon closer inspection, regions of the preformed outer oxide scale were found to have spalled indicating that the oxide is highly stressed and/or brittle. One potential method to confirm this would be to perform indents at several points of the oxide surface and then carry out AFM imaging to observe if there is cracking of the oxide where the indents have been made. The oxide scale grown on the Mg-rich sample hydrothermally oxidised for 7 days in Figure 5.19(f) showed a significant increase in thickness of $19.2 \pm 0.5 \mu\text{m}$. This is comparable to the oxide scale thickness of the pure Zr substrate at the same duration. The micrograph of the oxide scale showed extensive microcracks which may facilitate easier diffusion pathways for the ingress of oxygen to the zirconium substrate resulting in further oxidation. Furthermore, the severe spallation of the oxide that was seen from both the micrographs in Figure 5.19(e) and (f) indicates that the actual oxide scale thickness may have been higher than measured which is consistent with previous findings for the oxide scale formed on pure zirconium substrate and the Zr-rich coated sample. Overall, the high magnesium content of the Mg-rich coating does little to impede spallation of the coating during hydrothermal oxidation (compared to the Zr-rich coating) for the reasons mentioned previously. These results suggest that increased magnesium content in the Mg-rich coating may have accelerated the spallation of the coating during

hydrothermal oxidation resulting in an oxide scale forming earlier on the zirconium substrate of the Mg-rich coated sample compared to the Zr-rich coated sample. This finding is further corroborated from nanoindentation hardness and scratch adhesion tests performed earlier in Sections 5.1.4 and 5.1.5 respectively that showed a lower hardness of $(0.81 \pm 0.12 \text{ GPa})$ and lower critical loads to failure (determined from scratch adhesion tests) for the Mg-rich (Mg: 53 at%) coating compared to the Zr-rich (Mg: 25 at%) coating (which showed a much higher hardness of $4.32 \pm 0.10 \text{ GPa}$). Magnesium inclusion of 25 at% within the Zr-rich coating shows evidence of a higher resistance to spallation compared to the Mg-rich coating (with magnesium inclusion of 53 at%) during hydrothermal oxidation. For future work, it would be useful to perform hydrothermal oxidation for the other magnesium-containing Zr coatings with a range of Mg concentrations to study the resistance to spallation at these conditions.

On closer inspection of the cross-sectional micrographs showing the hydrothermally oxidised Zr-rich and Mg-rich samples in Figures 5.19(c) to (f), the evidence suggests extensive spallation of areas of the Zr-Mg coating, possibly leading to the oxidation of the zirconium substrate. For instance, the undulating 'wavy' appearance at the interface region is similar to the interface of the oxide scale formed on pure Zr in Figure 5.19(a) and (b) whereas the interface of the Zr- and Mg-rich coatings (in Figure 5.7) following sputter co-deposition did not exhibit this feature. The presence of lateral microcracking which appears to increase in severity with distance away from the interface region is consistent with the characteristics of a growing oxide scale deduced earlier in Chapter 4 (Figure 4.3(a) and 4.4) as well as the hydrothermally oxidised pure Zr presented in Figure 5.19(a) and (b). Interestingly, the irregularly-shaped columnar morphology of the Zr- and Mg-rich coating identified from SEM micrographs of the surface in Figure 5.5(a) and 5.6(a) was not observed from the SEM micrographs of the surface following hydrothermal oxidation. However, as mentioned previously, there are regions of the sample where the coating had not completely spalled as shown by the EDX spectrum in Figure 5.16(a) of the Zr-rich sample which shows that significant Mg content persists. On the balance of the evidence presented in this study, the SEM micrographs and EDX analysis would suggest that there are regions of the coating that remain adhered to the substrate (and possibly had oxidised) - and regions where the coating had spalled resulting in the oxidation of the underlying zirconium substrate.

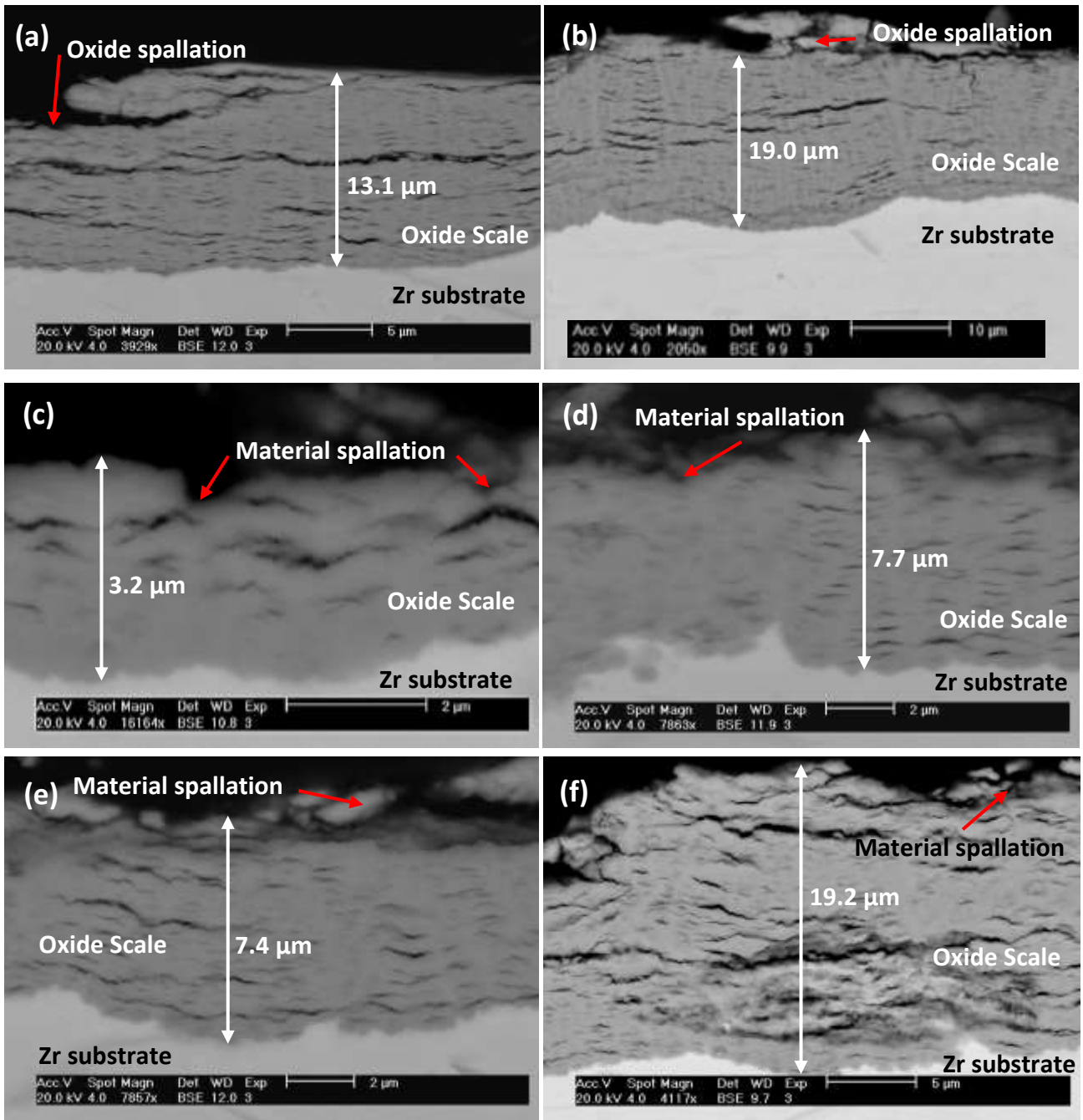


Figure 5.19: Cross-sectional SEM micrographs of hydrothermally-oxidised (a) pure Zr after 3 days; (b) pure Zr after 7 days; (c) Zr-rich coating after 3 days (d) Zr-rich coating after 7 days; (e) Mg-rich coating after 3 days and (f) Mg-rich coating after 7 days.

5.2.2 GAXRD Analysis of the Hydrothermally Oxidised Zr-rich and Mg-rich Sputter-deposited Coatings

The phase determination of the pure Zr, Zr-rich (Mg: 25 at%) and Mg-rich (53 at%) Zr-Mg coatings following hydrothermal oxidation with deionised water in an autoclave at 360°C for 3 and 7 days were performed using X-ray diffraction study using a Philips X'Pert³ (Panalytical) diffractometer (CuK α radiation), operated in glancing-angle configuration (Seeman-Bohlin geometry) at incident angles of 2°, 4° and 6° with a step size of 0.02 and a time step of 5 seconds in the 20° to 80° range of 2 θ . The results are presented in this section.

5.2.2.1 Glancing-Angle XRD Analysis of the Hydrothermally Oxidised Pure Zr Samples

The GAXRD patterns of the pure zirconium sample (used as a control reference sample) hydrothermally oxidised at 360°C for 3 and 7 days are presented in Figure 5.20. The patterns show that monoclinic zirconia (m-ZrO₂) phase was the predominant phase detected indicating that a zirconium oxide scale had formed following hydrothermal oxidation. Some of the m-ZrO₂ peaks such as those in the ($\bar{1}11$), (002), (20 $\bar{2}$) and (221) reflections exhibited lower intensity peaks with increased incident angle whilst others showed strong intensities even at 6° incident angle. The cross-sectional SEM micrograph of the pure zirconium sample hydrothermally oxidised for 3 days in Figure 5.19(a) shows that the thickness of the oxide scale to be 13.1 μm which is 'deeper' than the X-ray Penetration Depth of 6.24 μm (see Table 5.3) into the oxide layer at an incident angle of 6°. Thus, the X-rays do not penetrate to the zirconium substrate (at this incident angle) and only the oxide scale is detected. A similar pattern was observed for the 7 day hydrothermally oxidised pure Zr sample. One peak indexed to tetragonal zirconia was detected at an incident angle of 2° in the (020) reflection at a 2 θ angle of 50.5° which could be seen to decrease with increasing incident angle and at 6° incident angle, this phase can be seen to be negligible. On closer inspection of the peaks, the m-ZrO₂ peaks for both the 3 and 7 days samples show a slight shift to lower angles of 2 θ indicating an increase in the lattice parameters of the monoclinic zirconia structure due to interstitial diffusion of oxygen during hydrothermal oxidation.

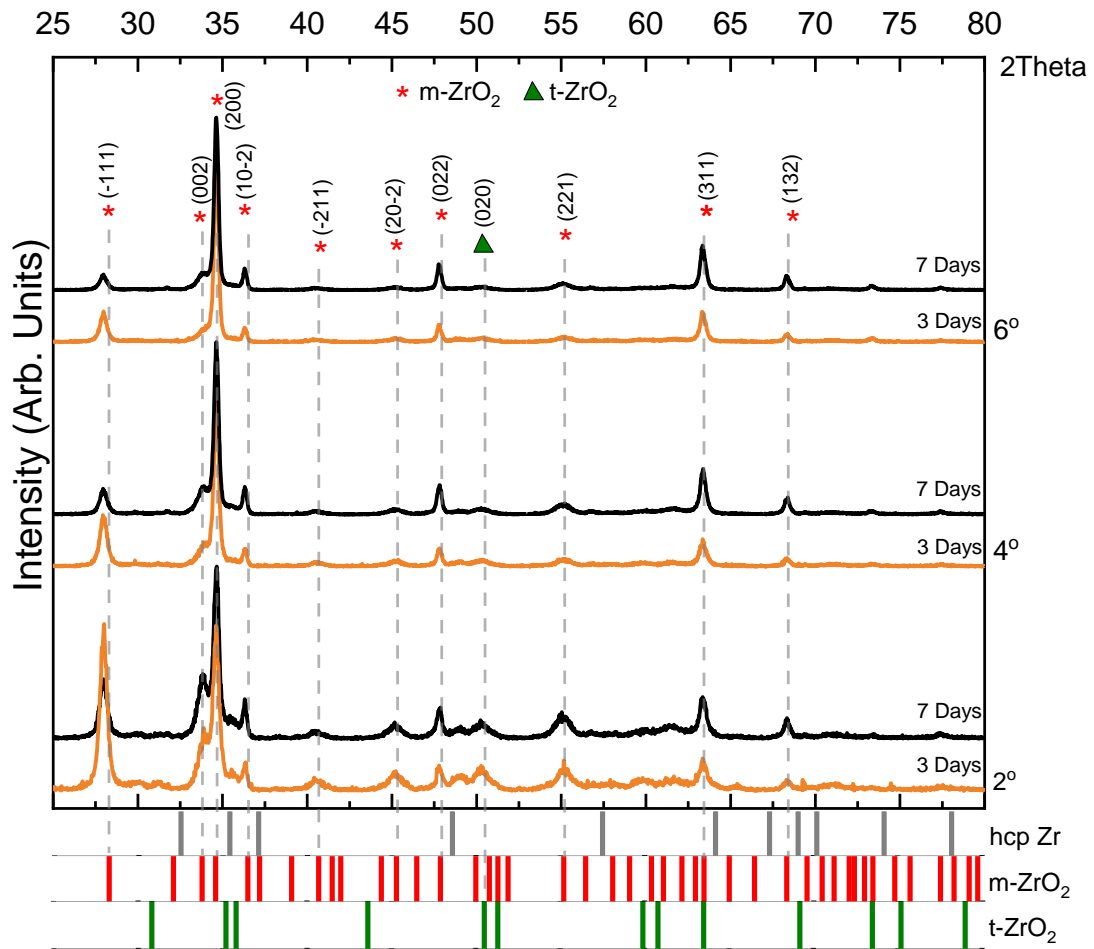


Figure 5.20: GAXRD patterns of pure zirconium hydrothermally oxidised for (a) 3 days and (b) 7 days. The phases formed and peak positions were compared with HCP α -Zr [59], m-ZrO₂ [56] and t-ZrO₂ [57].

Table 5.3: X-ray Penetration Depths into ZrO₂ at incident angles 2, 4 and 6° determined from AbsorbDX software.

ZrO ₂	
Incident angle (°)	X-ray Penetration Depth (μm)
2	2.01
4	4.11
6	6.24

5.2.2.2 Glancing-Angle XRD Analysis of the Hydrothermally Oxidised Zr-rich Coated Samples

The GAXRD patterns of the Zr-rich (25 at%) coated sample after hydrothermal oxidation at 360°C for 3 and 7 days are presented in Figure 5.21. The Zr-rich coated sample hydrothermally oxidised for 3 days in Figure 5.21(a) shows that the monoclinic zirconia (m-ZrO₂) phase was the predominant phase detected which confirms that a zirconium oxide scale had formed following hydrothermal oxidation. The highest peak intensity for m-ZrO₂ at the incident angle of 2° was in the (200) reflection. Other peaks attributable to the m-ZrO₂ phase in the ($\bar{1}11$), (20 $\bar{2}$) ($\bar{2}11$), (20 $\bar{2}$), (221) and (20 $\bar{3}$) reflections can be seen to decrease with increased incident angle (i.e. greater depth into the oxide layer), indicating that the highest concentration of m-ZrO₂ is found near the outer preformed oxide layer. At an incident angle of 6°, where X-ray Penetration Depth into ZrO₂ is 6.2 μm (Table 5.3), peaks attributable to the α-Zr phase (for the 3 days sample) were found to exhibit high peak intensities in the (200) and (013) reflection. Since the X-ray Penetration Depth at an incident angle of 6° is 'deeper' than the thickness of the oxide scale of 3.2 μm formed after 3 days (shown in Figure 5.19(c)), this would suggest the X-rays are starting to penetrate the bulk zirconium substrate.

The GAXRD pattern for the Zr-rich coated sample hydrothermally oxidised for 7 days in Figure 5.21(b) revealed a similar pattern to the 3 days sample in Figure 5.21(a). Monoclinic zirconia was found to be the predominant phase with the highest intensity in the (200) reflection. At an incident angle of 6°, peaks attributable to the m-ZrO₂ phase could still be seen in the pattern. Given the knowledge that the X-ray Penetration Depth at an incident angle of 6° is 6.2 μm (Table 5.3), this falls within the range of the oxide scale thickness of 7.7 μm determined from cross-sectional SEM micrograph in Figure 5.19(d). Peaks attributable to α-Zr phase could also be seen at an incident angle of 6° which suggests the detection of the zirconium substrate. Indeed, the oxide formed after 7 days (from Figure 5.19(d)) can be seen to be characterised by a wavy undulated appearance at the oxide/substrate interface region, so it is reasonable to deduce that given the thickness of the oxide, that the peaks indexed to the α-Zr phase would indicate the detection of the bulk zirconium metal. Careful observation of the m-ZrO₂ peaks for the 3 and 7 days exposed samples reveals a slight shift (~0.4°) to lower angles of 2θ compared to the ICDD standard m-ZrO₂ phase positions, [56] indicating an increase in lattice parameters of the monoclinic zirconia structure due to interstitial diffusion of oxygen in the Zr-lattice during hydrothermal oxidation.

The GAXRD patterns also showed three peaks indexed to tetragonal zirconia (t-ZrO₂) phase in the (011), (020), (110) and the (004) reflections. The peak intensities for the tetragonal phase was shown to be highest at an incident angle of 2° and decreased with increasing angle of incidence. This suggests that the highest concentration of the tetragonal phase was detected near the pre-formed outer oxide

scale. This is an interesting finding because the concentration of the tetragonal phase is typically highest near the metal/oxide interface region where it is stabilised by the compressive stresses and is lowest near the pre-formed outer oxide scale. This is due to the diminishing compressive stress with increased distance away from the interface whereby the t-ZrO₂ phase no longer be elastically constrained - allowing the transformation to monoclinic zirconia. However, the results presented in this study suggest that the inclusion of magnesium is possibly having an effect in elastically constraining the tetragonal phase as the oxide scale grows during hydrothermal oxidation and this is likely stabilising the tetragonal zirconia phase across the oxide scale that is shown by the detection of tetragonal zirconia peaks at higher angles of incidence. This is a promising result but would need further investigation since the tetragonal zirconia peaks are small.

As a recommendation for future work, it would be useful to carry out hydrothermal oxidation of the coatings with the range of Mg concentrations (Table 5.1) for 3 and 7 days and to perform GAXRD on the samples over a range of angles of incidence (i.e. 1-8°) to see if t-ZrO₂ phase could be detected. The volume fraction of t-ZrO₂/m-ZrO₂ could then be deduced to investigate the extent to which the t-ZrO₂ phase could be stabilised with the growing oxide scale thickness. As a further extension to this study, hydrothermal oxidation of the Zr-Mg coatings should be performed for much longer treatment times (i.e. 50 days) to determine the weight gain which could be used to measure corrosion resistance when compared to corrosion of Zr alloys reported in the literature.

It is interesting to note that from the GAXRD trace of the Zr-rich coatings (Mg: 25 at%) shown earlier in Figure 5.9 from which broad peaks were identified (which indicated that zirconium and magnesium in the coating were in substitutional solid solution with each other as mentioned in Section 5.1.3) were not detected from the GAXRD pattern of the hydrothermally oxidised Zr-rich sample at 2° or 4° angle of incidence. Furthermore, despite the X-ray Penetration Depth at an incident angle of 6° being 'deeper' than the thickness of the oxide scale of 3.2 μm formed on the Zr-rich sample following hydrothermal oxidation for 3 days, peaks attributable to the Zr and Mg phases (which would otherwise have again been characterised by several broad peaks) were not detected from the GAXRD pattern in Figure 5.21(a). This finding is consistent with the earlier proposition of oxidation of the coating as well as a gradual spallation of the Zr-rich coating and the formation of zirconium oxide on the substrate during hydrothermal oxidation which grows with treatment time.

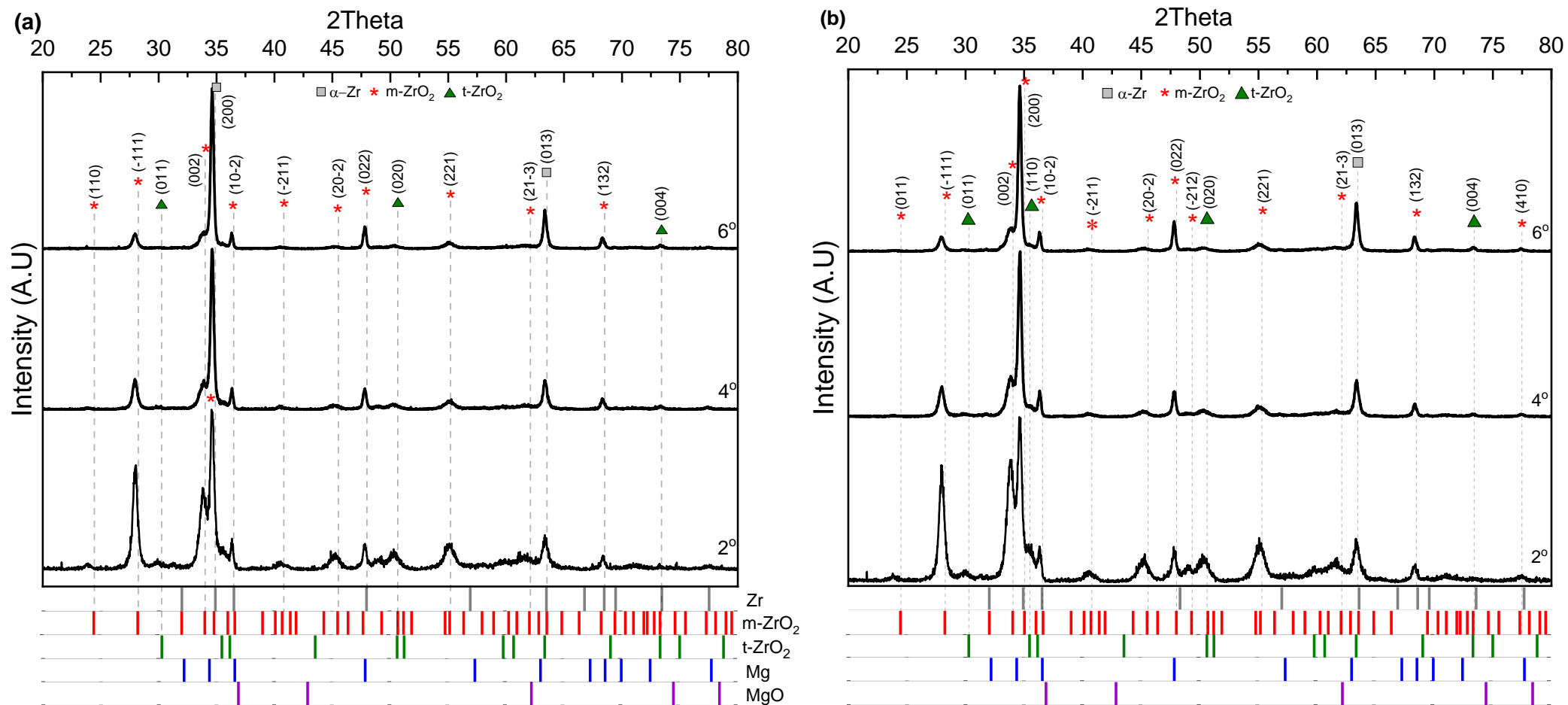


Figure 5.21: GAXRD patterns of Zr-rich coatings hydrothermally oxidised for (a) 3 days and (b) 7 days. The phases formed and peak positions were compared with HCP α -Zr [59], m-ZrO₂ [56] and t-ZrO₂ [57], Mg [213] and MgO [313].

5.2.2.3 Glancing-Angle XRD Analysis of Mg-rich Coatings

The GAXRD patterns of the Mg-rich (53 at%) coated sample after hydrothermal oxidation at 360°C for 3 and 7 days are presented in Figure 5.22. The Mg-rich coated sample hydrothermally oxidised for 3 days in Figure 5.22(a) shows that the monoclinic zirconia ($m\text{-ZrO}_2$) phase was the predominant phase detected at incident angles of 2, 4 and 6° which confirms that a zirconium oxide scale had formed following hydrothermal oxidation. The highest peak intensity for $m\text{-ZrO}_2$ at the incident angle of 2° was in the (200) reflection at a 2θ angle of 35.1°. Other peaks attributable to the $m\text{-ZrO}_2$ phase in the ($\bar{1}11$), (002), ($\bar{2}11$), ($20\bar{2}$), (221) and ($21\bar{3}$) reflections can be seen to decrease with increased incident angle (i.e. greater depth into the oxide layer), whereas peaks attributable to the $m\text{-ZrO}_2$ phase in the (200), ($10\bar{2}$), (022), (311) and (132) reflections show strong intensity peaks with increased incident angle. A similar pattern was seen for the Mg-rich coated sample hydrothermally oxidised for 7 days in Figure 5.22(b).

Tetragonal zirconia peaks were also identified (for the samples oxidised for 3 and 7 days) at the (011), (020) and (121) reflections up until an incident angles of 4° where the X-ray Penetration Depth is 4.11 μm . At an incident angle of 6°, the $t\text{-ZrO}_2$ phase can be seen to be negligible. The GAXRD trace of the Mg-rich coatings (53 at%) shown earlier in Figure 5.9 from which broad peaks were identified (which indicated that zirconium and magnesium in the coating might be in substitutional solid solution with each other as mentioned in Section 5.1.3) were not detected from the GAXRD pattern of the hydrothermally oxidised Mg-rich sample at 2° or 4° angle of incidence (as was the finding from the GAXRD patterns of the hydrothermally oxidised Zr-rich coated sample in Figure 5.21).

On closer inspection of the GAXRD patterns for the hydrothermally oxidised Mg-rich samples, the $m\text{-ZrO}_2$ peaks for both the 3 and 7 days samples show a slight shift to lower angles of 2θ by $\sim 0.4^\circ$ possibly indicating an increase in the lattice parameters of the monoclinic zirconia structure due to interstitial diffusion of oxygen in the Zr-lattice during hydrothermal oxidation. The Mg-rich coating also exhibited significant spallation (compared to the Zr-rich coating) during hydrothermal treatment resulting in oxidation of the zirconium substrate (where regions of the coating that had spalled off), resulting in the formation of an oxide scale comprising predominantly of monoclinic zirconia detected in the patterns (Figures 5.22(a) & (b)). However, since the oxide scale formed on the Mg-rich sample was thicker (7.4 μm after 3 days and 19.2 μm after 7 days as shown in Figures 5.19(e) and (f)) than the X-ray Penetration Depth of X-rays at an incident angle of 6° (6.2 μm), the region that is detected is still the oxide layer – as the X-rays do not penetrate to the bulk zirconium substrate and hence no peaks are indexed to the $\alpha\text{-Zr}$ phase. The available evidence presented in this study suggests that the conditions used during hydrothermal oxidation results in the oxidation and gradual spallation of the

Zr-rich (Mg: 25 at%) coating and the complete spallation of the Mg-rich (Mg: 53 at%) coating from the substrate.

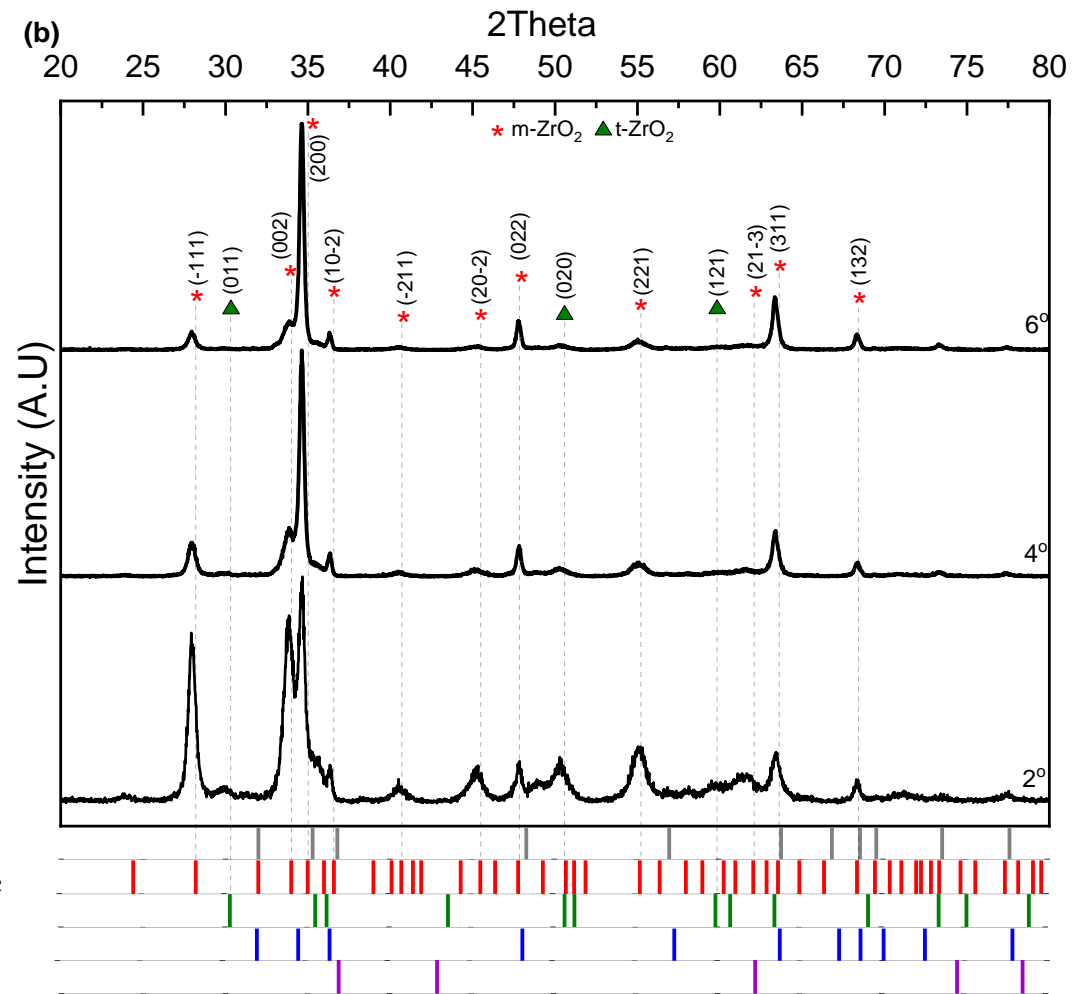
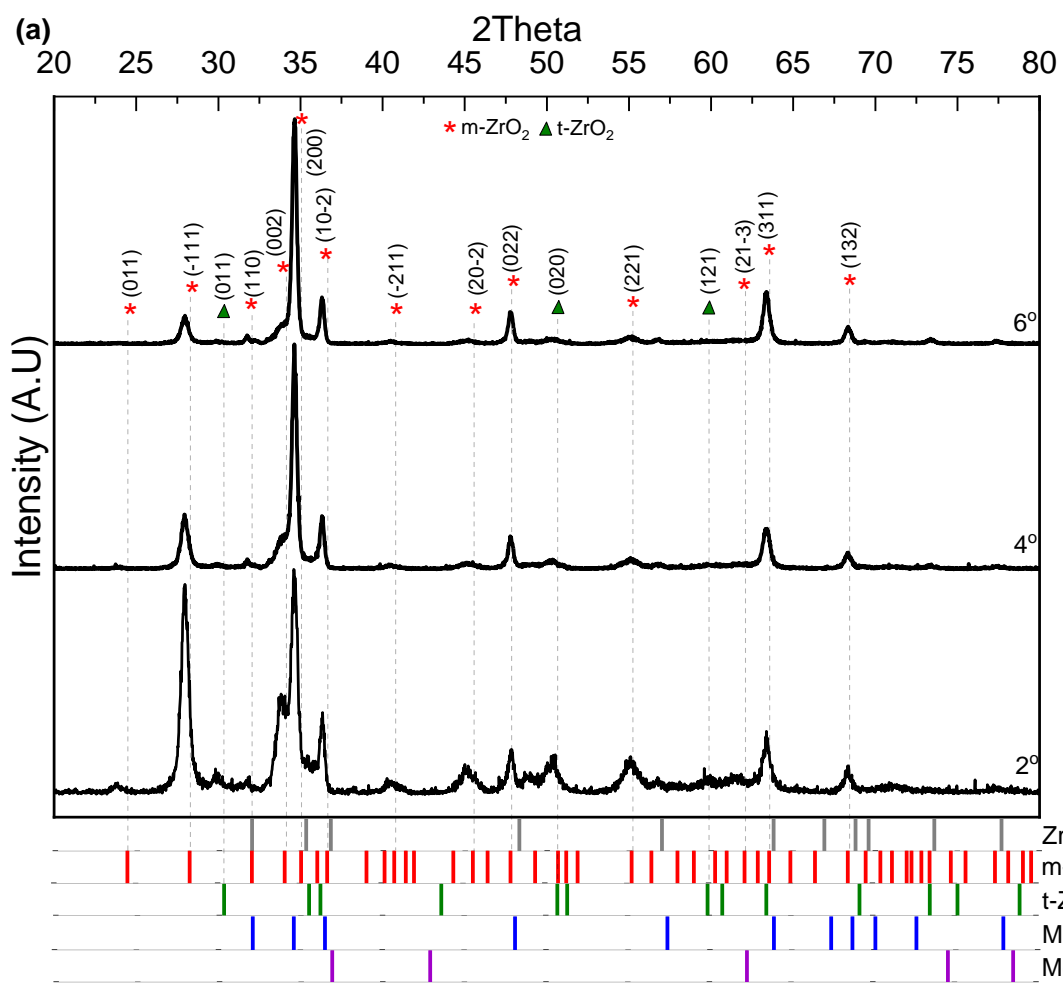


Figure 5.22: GAXRD patterns of Mg-rich coatings hydrothermally oxidised for (a) 3 days and (b) 7 days. The phases formed and peak positions were compared with HCP α -Zr [59], m-ZrO₂ [56] and t-ZrO₂ [57], Mg [213] and MgO [313].

Hydrothermal oxidation of the co-deposited Zr-Mg coating results in the oxidation and gradual spallation of the Zr-rich coating and a significant spallation of the Mg-rich coating. In both instances, the results indicate that the coating remains adhered to the substrate. It was determined that the Mg-rich coating was found to have undergone spallation at a faster rate compared to the Zr-rich coating. This is shown by the thicker oxide scales developed on the Mg-rich coated sample on the Zr substrate in Figure 5.19(c) to (f). On the balance of evidence presented in this section, the Zr-rich coatings had a higher resistance to spallation during hydrothermal oxidation compared to the Mg-rich coatings. Nanoindentation results showed the Zr-rich coating (25 at%) exhibited a much higher hardness of 4.32 ± 0.10 GPa compared to 0.81 ± 0.09 GPa for the Mg-rich coating. Scratch adhesion tests showed that the Zr-rich coating exhibited higher critical loads to failure compared to the Mg-rich coating – the latter was shown to have undergone a greater degree of spallation (via chipping damage) indicating that the Mg-rich coating is more brittle. Furthermore, the cross-sectional SEM micrographs of the Zr-Mg coatings in Figure 5.7 showed that the Mg-rich coating exhibited a greater concentration of microcracks and intercolumnar voids (compared to the Zr-rich coating) which facilitates crack propagation and oxygen migration through the coatings during hydrothermal oxidation (at 360°C for 3 and 7 days). Based on these results, the Zr-rich sample exhibited a higher resistance to spallation during hydrothermal oxidation compared to the Mg-rich coating.

The growth of the zirconium oxide layer during the oxidation process is described in Chapter 4, Section 4.2.2 but a brief summary is presented here. In addition to oxidation of the coatings, regions where the coating that had completely spalled results in oxide growth by inward diffusion of interstitial oxygen and the resulting oxide layer at the metal-oxide interface is elastically constrained. Majority of the oxide is composed monoclinic zirconia (by volume fraction) but a small fraction (~5 vol% - see section 4.2.2) is comprised of (metastable) tetragonal zirconia which was detected from the GAXRD patterns in Figures 5.21 and 5.22. Tensile stress is generated in the HCP α -Zr metal substrate as a reaction to the compressive stress created by the P-B ratio of the tetragonal zirconia to the substrate. Thus, tensile stress in the substrate may have a tendency to expand the metal lattice structure and enhance the inward diffusion of oxygen through the oxide scale and into the metal. The compressive stress in the oxide is therefore, highest at the Zr-ZrO₂ interface and continues to be elastically constrained with distance from the oxide/metal interface [102] due to the addition of magnesium that acts to stabilise the tetragonal zirconia phase with increased oxide thickness. The monoclinic zirconia phase that forms is still the predominant phase since the temperature and pressure conditions used is thermodynamically favourable allow for its formation (i.e. below 1170°C). The compressive stress generated as a result of the co-deposition of Mg and Zr to form a PVD coating and the indications of Mg and Zr being in substitutional solid solution is likely to play an important role in stabilising the t-

ZrO₂ phase (seen in the GAXRD patterns in Figures 5.21 and 5.22) in the oxide scale but as stated previously this would require research and opens an avenue for further investigation.

However, the volume fraction of t-ZrO₂ formed is small compared to m-ZrO₂ which is the main phase detected in the oxide scale. As oxide growth continues with treatment time, the compressive stress in the oxide continues to diminish and is associated with a volume expansion of about 3-5 vol% [64, 108] of the oxide. This is likely the main cause of the network of microcracks seen in the oxide scales from the cross-sectional SEM micrographs in Figure 5.19. The volume expansion results in existing cracks/pores present within the oxide scale to grow or multiply and creates additional compressive stress that would lead to the oxide scale to spall - severely limiting the overall load-bearing capacity of the oxide scale under mechanical strain.

5.3 Summary

Magnesium and zirconium were sputter co-deposited onto stainless steel and zirconium substrates using unbalanced magnetron sputtering with a range of magnesium concentrations from 8 at% to 60 at%. The microstructure and mechanical properties of Mg-containing Zr coatings – principally the Zr-rich (Mg:25 at%) and Mg-rich (Mg: 53 at%) coatings have been characterised using optical microscopy, GAXRD, SEM/EDX, nanoindentation and scratch adhesion tests. The GAXRD patterns indicated that the inclusion of Mg and Zr to form a Zr-Mg coating resulted in a coating that is likely to be highly stressed and showed possible indications that they could be in a single mutual substitutional solid solution with each other (though this would require further investigation). The results show no evidence of phase separation or ‘unmixing’ of these phases for the range of Mg concentrations in the Zr-Mg coatings. This is an interesting result since magnesium and zirconium have widely different melting temperatures and so do not typically exist (as an alloy) as well as differences in co-efficient of thermal expansion.

Nanoindentation hardness revealed the Zr-rich coating exhibited a higher hardness compared to the Mg-rich coating. Scratch adhesion tests showed that the Zr-rich coating exhibited a higher critical load to failure compared to the Mg-rich coating, indicating a higher load-bearing capacity for the Zr-rich coating (compared to the Mg-rich coating). The Mg-rich coating was shown to have undergone a greater degree of spallation (via chipping damage), indicating that the Mg-rich coating is more brittle.

Cross-sectional SEM micrographs revealed oxidation of both the Zr-rich and Mg-rich coatings as well as material loss due to the effects of spallation. The Zr-rich coating showed indications of a gradual spallation of some regions of the coating, whereas the Mg-rich coating was found to have undergone spallation at a faster rate compared to the Zr-rich coating resulting in much thicker oxide scales on the Mg-rich coated sample. On the balance of evidence presented in this section, the Zr-rich coating had a higher resistance to spallation during hydrothermal oxidation compared to the Mg-rich coatings.

Chapter 6 – Conclusions and Recommendations for Future Work

6.1 Conclusions

Waterside corrosion of zirconium and its alloys was identified as one of the principal issues that led to the meltdown at Fukushima following a loss of coolant accident. Following the accident, the nuclear industry has focused much of its efforts into enhancing safety of its current fleet of reactors and improving safety of future designs. A promising approach that has generated considerable research interest is to fabricate a protective coatings or surface-treated layers that would improve/enhance the oxidation resistance of the Zr-alloy cladding to be more damage-tolerant during LOCA conditions, such cladding failure is delayed and the accident response time to allow external intervention/solutions is increased.

In this study, Triode Plasma Nitriding treatments and sputter co-deposition on pure zirconium was performed to investigate whether oxidation resistance could be improved. Multiple characterisation tools permitted a comprehensive analysis of the surface-treated layers and coatings as well as performance following hydrothermal oxidation.

Based on the experimental work and analyses carried out in this PhD study, the following conclusions can be drawn:

- Triode plasma diffusion treatments of α -Zr at 700°C led to the formation of a surface-treated layer consisting of a thin nitrided compound layer consisting of a ZrN phase (likely to be hundreds of nanometers) and a much thicker nitrogen diffusion zone ($\sim 23 \mu\text{m}$) comprising of interstitial nitrogen in solid solution. The finer degree of etching using Ion polishing was found to be an important micropreparation step which revealed the nitrogen diffusion zone when studied using an optical microscope. The use of ion polishing permits for a safer and efficient micropreparation method of the sample compared to using toxic HF etching methods.
- Surface hardness values following TPN diffusion treatment were found to be significantly improved for all treatment durations (ranging between 10 to 12 GPa) compared to untreated bulk HCP α -Zr surface ($4.40 \pm 0.20 \text{ GPa}$). However, the hardness of the TPN-treated surface was found to decrease with contact depth into the nitrogen diffusion zone to the base of the zirconium substrate.
- Scratch adhesion profiles revealed that increased TPN-treatment duration resulted in an increased load-bearing capacity of the treated layer. The 4 hr nitrided sample showed higher resilience to failure before critical loads were reached compared to the 2 hr and 3 hr nitrided

samples. This is due to the 'deep' nitrogen diffusion zone allowing sufficiently high loads to be reached before failure occurs.

- Longer nitriding times were found to increase the surface roughness of the diffusion-treated layers. Results from AFM analysis revealed the growth of protuberances which generate a rougher topography with increased treatment times.
- Hydrothermal oxidation tests of the TPN-treated samples revealed a slight improvement in the oxidation resistance compared to untreated pure zirconium. The oxide scale formed on the TPN-treated samples was measured to be $10 \pm 0.5 \mu\text{m}$ and exhibited similar weight gain for all TPN-treated samples. However, the oxide scale was also shown to contain microcracks, which increase in severity with distance away from the oxide/metal interface, and the SEM micrographs appear to show material loss due to spallation during hydrothermal oxidation. This indicates that the oxide scale may have been thicker than measured.
- GAXRD patterns of the hydrothermally oxidised TPN-treated samples showed that the oxide scale comprises mostly of monoclinic zirconia and a small volume fraction of tetragonal zirconia. The ZrN compound layer was not detected suggesting that this layer is entirely consumed and as the oxide grows into the nitrogen-containing diffusion zone.
- The hydrothermal oxidation of pure zirconium was found to offer poor oxidation resistance when compared to the oxidation performance of Zr alloys under similar conditions reported in the literature. This is because of the oxidation resistance (of Zr alloys) offered by the elements that form intermetallic precipitates such as tin, iron and chromium provide increased mechanical strength by hindering dislocation movement, thereby improving the durability of the oxide during oxidation and resulting in a negligible deleterious effect on corrosion of the alloy.
- The GAXRD patterns of the hydrothermally oxidised TPN-treated samples revealed that the nitrogen diffusion zone provides a sustained resistance to oxygen ingress whereby the nitrogen in the interstitial sites suppressing oxygen migration into the diffusion zone and thereby delaying oxidation compared to pure zirconium.
- Scratch adhesion loading profiles and associated micrographs of the oxide scale formed on TPN-treated Zr samples revealed extensive chipping damage and tensile cracking along the scratch track indicating that the oxide layer is brittle which supports the findings from SEM micrographs of the surface and cross-sections of the oxide scale (which also show extensive microcracks). Thus, the monoclinic polymorph of the zirconia (which the oxide scale is mostly comprised) does not offer suitable oxidation resistance, necessary for the stabilisation of the

oxide layers formed in high pressure autoclave conditions and hence, unsuitable for reactor environments.

- Surface hardness values of the oxide scale were shown to be much lower compared to the TPN-treated samples and were found to decrease with increased depth towards the substrate interface.
- Magnetron sputter-deposition PVD technique was used to co-deposit magnesium and zirconium onto stainless steel and zirconium substrates with a range of magnesium concentrations from 8 at% to 60 at%. GAXRD patterns showed that the sputter co-deposited magnesium and zirconium (that form the coating) are highly stressed and indicate that they are in single mutual substitutional solid solution with each other. The results show no evidence of phase separation or 'unmixing' of these phases for the range of Mg concentrations in the Zr-Mg coatings. This is an interesting result because magnesium and zirconium do not typically co-exist (as an alloy) as they have widely different melting temperatures as well as the boiling point of Mg being much lower than the melting point of Zr. However, considering that PVD permits direct conversion from solid, to (ionised) gas, to solid (avoiding the liquid state), it is possible to co-deposit atomistically the two elements in solid solution with each other, whereby they might be expected to co-exist in the solid state as shown in the GAXRD patterns.
- SEM micrographs of the sputter co-deposited surface of the Zr-rich (Mg: 25 at%) and Mg-rich (Mg: 53 at%) samples showed irregularly-shaped columnar grain-like morphology with column sizes that ranged from 2 μm to about 15 μm in diameter (although it is likely that the actual column diameters are hundreds of nanometers). This is likely due to competitive grain growth which initially occurs by nucleation, followed by island growth then coalescence to form larger grains which grow as a columnar structure as the coating thickness increases. The faceted morphology is consistent with Zone 2 of the Structure Zone Model whereby surface diffusion is the dominant process during film growth leading to the formation of wide columns and well-defined grain boundaries.
- Cross-sectional SEM micrographs of the Zr-rich and Mg-rich samples revealed uniform coating thicknesses of 25.2 and 26.5 μm respectively, but the Mg-rich coating exhibited a higher concentration of microcracks in the coating and inter-columnar voids (compared to the Zr-rich coating).
- SEM micrographs of the surface of the hydrothermally oxidised Zr-rich and Mg-rich coated samples at 360°C for 3 and 7 days showed material that had spalled and redeposited on the

surface. Cross-sectional SEM micrographs revealed that the oxide scale thickness formed on the Zr-rich coated samples was much lower than the Mg-rich coated samples.

- The higher hardness (determined from nanoindentation) and higher critical load to failure (determined from scratch adhesion tests) of the Zr-rich coating compared to the Mg-rich coating suggests that the Zr-rich coating exhibits a higher resistance to coating spallation compared to the Mg-rich coating. The oxide scales on both the Zr-rich and Mg-rich coated samples exhibited microcracks which would permit oxygen ingress into the layer and to the substrate causing further oxidation, as well as contributing to spallation of the oxide scale. The oxide scale formed on the Mg-rich coated sample however, exhibited severe spallation whereby the oxide scale thickness was comparable to the oxide scale formed on the pure Zr substrate following hydrothermal oxidation for 7 days.
- GAXRD patterns of the oxide scales formed on the Zr-rich and Mg-rich coated samples following hydrothermal oxidation revealed monoclinic zirconia was the predominant phase detected which confirmed that a zirconium oxide scale had formed following hydrothermal oxidation. The patterns showed tetragonal zirconia to have also formed which was detected over a range of incident angles of 2θ which indicates that magnesium and zirconium inclusion has had an effect in stabilising the tetragonal zirconia phase at the conditions used.

6.1.2 Concluding Remarks

The work carried out in this thesis has led to materials being identified that have ideal properties for the development of accident tolerant coatings/barriers. Plasma nitriding diffusion treatments have shown that nitriding can be achieved in as little as 1.5 hours at 700°C to form an effective barrier against hydrogen ingress. The treatments resulted in significantly improved hardness and higher load-bearing capacity of the nitrided layers compared to untreated bulk HCP α -Zr samples. Overall, TPN treatment resulted in nitrided layers that successfully mitigated the formation of zirconium hydride precipitates in the bulk Zr lattice during hydrothermal oxidation testing but did not measurably improve (or worsen) the oxidation resistance compared to the pure zirconium at the conditions used.

Sputter co-deposited magnesium-containing zirconium coatings were produced with a range of magnesium concentrations. The Zr-rich (Mg: 25 at%) coatings exhibited a higher resistance to spallation compared to the Mg-rich coatings during hydrothermal oxidation due to the higher hardness and adhesion of the Zr-rich coating. The Mg-rich coating exhibited higher concentration of microcracks and inter-columnar voids that would facilitate crack propagation and oxygen ingress during hydrothermal oxidation, hence resulting in a thicker oxide scale. Although the Zr-rich coating

was shown to exhibit useful properties such as higher resistance to spallation during hydrothermal oxidation, it would be useful to investigate the spallation resistance of the Mg-containing Zr coatings with Mg concentrations below 25 at% at hydrothermal conditions and see whether this might induce a greater proportional of tetragonal zirconia phase that might be stabilised over a wide oxide thickness and temperature range.

6.2 Recommendations for Future Work

This research has thrown up a number of aspects for further research and investigation.

- Following successful trials, these should be replicated on reactor-grade zirconium alloys (on the exterior of the fuel rod cladding) and compared against the results obtained in this study for pure zirconium. Thus, the surface-treated layer/coating will act as an intermediary barrier between the coolant water and the fuel cladding to suppress hydrogen evolution and prevent migration of oxidative species to the underlying bulk metal.
- Electron backscatter diffraction (EBSD) should be performed on the TPN-treated layers to produce “colour-coded” maps that would show the distribution of crystal phases and orientation of individual grains (which is not obtained using conventional XRD). This important study would help distinguish grains attributed to the Zr_3N_4 top layer; nitride compound layer and nitrogen diffusion zone, (the phases and microstructure of which were also identified via XRD patterns and optical micrographs). This would provide important insights into oxidation behaviour of the nitride phases whereby the processing conditions can be altered to influence grain orientation and formation.
- Glow-discharge optical emission spectroscopy (GDOES) is a technique used for multi-element depth profiling (from nanometer scale to tens of microns and can detect from a few ppm to 100 at% of an element within a few minutes) commonly used for through-thickness composition analysis. This technique should be used for TPN diffusion treated samples to investigate the depth profile of nitrogen in the nitrated layers to obtain a more accurate representation of nitrogen concentration as a function of depth.
- Although cross-sectional optical micrograph of the diffusion-treated Zr did show the nitrogen diffusion zone, it was clear that mounting a single sample this way resulted in edge rounding which limited the observation and detection of the nitride compound layer. To mitigate this, a two-sample mounting technique should be adopted in which the treated surfaces would be mounted face to face (in cross-section) which can then be coated with carbon/gold prior to

mounting before being ion polished and would increase the probability of observing the nitrated layer.

- Although the ZrN phase was detected using GAXRD at an incident angle as low as 2° in Section 3.6 and from the Raman spectra in Section 3.7 which strongly indicates the formation of a nitride compound layer, it was challenging to measure the cross-sectional thickness of this layer using SEM alone. Thus, focused ion beam (FIB) and TEM should be used to determine the nitride compound layer thickness. Furthermore, TEM could be used to analyse the extent of the lattice distortion as a result of interstitial nitrogen diffusion in forming the nitrogen diffusion zone and investigate how the lattice distortion changes with depth into the bulk metal.
- A study should be carried out to investigate optimum hardness and adhesion properties that could be obtained using TPN diffusion treatments. This could be performed by carrying out TPN treatments for a longer duration (i.e. 8 hr) at low substrate negative bias (i.e. 200 V) to achieve a sufficiently 'deep' nitrogen diffusion zone case depth. This should be followed by a higher substrate negative bias (i.e. 600 or 800 V) for a short duration (i.e. 1 hr) to achieve a thick nitride compound layer. This step could introduce greater surface defects due to higher energies of nitrogen ions bombarding the substrate so the short 'burst' durations may need to be adjusted. The treated layer should be characterised using GAXRD, (cross-sectional) SEM/EDX to confirm the thickness of the nitride compound layer and nitrogen diffusion zone. It would be further useful to carry out mechanical testing such as nanoindentation to measure hardness and scratch adhesion tests to understand whether this might increase the critical load to failure when compared to the treatments carried out in this work.
- A point of further research would be to investigate the effects on the ZrN microstructure when extending treatment times to 8 hr and 12 hr whilst keeping the treatment temperature constant at 700°C . The study should attempt to address how hardness and surface roughness is affected as well as variability in thickness of the nitride compound layer and nitrogen diffusion zone and how this might affect the critical load to failure during scratch adhesion tests.
- Another recommendation is to use different substrate bias including -150 V, -250 V and -300 V or higher (i.e. -1000 V) whilst keeping the treatment temperature of 700°C constant. This would attempt to investigate how variation in substrate bias affects surface roughness and adhesion of the nitrated layer to the substrate after plasma-nitriding of α -Zr.
- GAXRD analysis of the magnesium-containing Zr coatings revealed narrower peaks with increased magnesium content possibly indicating larger crystallite size. It should also be noted

that for these traces (Mg: 53 at%, 56 at%), oxygen contamination (detected from EDX analysis) was higher than the coatings with magnesium content less than 45 at%. TEM investigation should be carried out to investigate how crystallite size varies with magnesium content and whether oxygen contamination/impurities might influence nucleation, island growth and column structures of the coatings.

- One of the other recommendations is to investigate the effects of increasing treatment temperature of 800, 900, 1000°C for 4 hr, 8 hr and 12 hr. The study would analyse how mechanical behaviour of the nitrated layer would be affected in the BCC β -phase region of Zr (above $\sim 900^\circ\text{C}$). Furthermore, it would be interesting to observe if grain growth had taken place and to what extent the oxidation behaviour is affected when oxidation-tested in hydrothermal conditions compared to the nitrated results obtained in the HCP α -Zr region. Following TPN treatment at 700°C , the bulk microstructure remained virtually unchanged. However, it has been reported that strength, ductility and fatigue properties degrade with increasing grain size for Ti alloys but would be an interesting avenue of research for bulk zirconium. It would also be interesting to investigate thickness variations of the compound layer formation during TPN treatment at 800°C whilst keeping the duration constant at 4 hr, since the extent of compound layer formation is related to the degree of roughening. Cassar et al [281] for instance found that TPN treatment of Ti-6Al-4V resulted in a considerable increase in surface roughness when diffusion-treated at 800°C , which also increase the nitride compound layer thickness from $0.25\ \mu\text{m}$ to $1.65\ \mu\text{m}$ between 700 and 800°C following a 4 hr treatment.
- Yttria-stabilised zirconia (YSZ) is widely used as the ceramic topcoat in thermal barrier coatings (TBCs) on turbine components which thermally insulate them against high temperature environments. Yttria typically comprises about 8 mol%, stabilises zirconia via the tetragonal phase (8YSZ). Yttrium has an atomic radius of $0.18\ \text{nm}$ comparable to Zr ($0.15\ \text{nm}$) and would likely be in substitutional solid solution with Zr. The success of YSZ coatings is well documented but has not been applied in the nuclear context for application on fuel rod cladding. This is mostly because of the low thermal conductivity of the $\text{Y}_2\text{O}_3\text{-ZrO}_2$ system ($2.0\text{-}2.3\ \text{W/mK}^{-1}$ at 1000°C) which could detrimentally limit energy transfer from the UO_2 fuel pellets to the coolant. This could however potentially be offset if the layers were tens of microns thick (rather than hundreds of microns thick - as is the case with aerospace coatings). Yttria-stabilised zirconia treated layers of a range of thicknesses should be developed using triode plasma oxidation diffusion treatment. The thickness of the treated layers can be deduced from cross-sectional SEM and EDX spectroscopic analysis can be used to determine the elements

present. GAXRD should be used to identify the formation of a tetragonal zirconia phase (and to what extent of the treated surface thickness which can be inferred by using higher incident angles during GAXRD experiments). Thermal conductivity measurements should be carried out to determine if there is a significant change in the thermal conductivity as a function of treated layer thickness. Magnetron sputtering should also be used to develop yttria-stabilised zirconia coatings and a similar process of characterisation described previously should be carried out. It would be useful to compare adhesion of the YSZ treated layers and coatings developed from these techniques using scratch adhesion tests. Finally, hydrothermal oxidation tests should be performed on YSZ treated layers and coatings to investigate oxidation resistance, phase analysis and indications of spallation effects.

- Ceria-stabilised zirconia coating (CSZ) could also be another potential avenue of exploration. CSZ has been investigated as an alternative to YSZ for use as the top coat in thermal barrier coatings. This is because CSZ has a lower thermal conductivity (~ 2.0 W/m.K) and a higher thermal expansion coefficient ($12.0 \times 10^{-6} \text{ K}^{-1}$ [316]) compared to YSZ (thermal conductivity: ~ 2.3 W/m.K; thermal expansion coefficient: $10.5 \times 10^{-6} \text{ K}^{-1}$ [317]). The atomic radius of Ce is 0.185 nm and density of 6.69 gcm^{-3} and has a low neutron absorption cross-section (0.63 barns), although this is slightly higher than Zr (0.184 barns). The ceria-doped coating has a better thermal shock resistance than YSZ due to: 1) A low propensity to undergo phase transition between monoclinic and tetragonal phase; 2) Higher thermal expansion coefficient and 3. Lower stresses generated in the oxide layer. Furthermore, Park et al [318] reported fewer microcracks and open pores in the CSZ coating (when oxidation tested in an aqueous solution of sodium metavanadate (NaVO_3)), which restricts access to penetrating salts from the corrosive medium and this was concluded as a marked improvement in oxidation resistance of CSZ compared to YSZ. However, the low thermal conductivity of CSZ coatings may be an obstacle for application on Zr alloy fuel rods and requires further investigation to improve heat transfer efficiency between cladding and water. A similar characterisation and testing methodology should be followed as mentioned in the previous bullet point to determine the viability
- Titanium is also another alloying element considered to stabilise the tetragonal or cubic phase of zirconia. It is a refractory element with a high melting point (1668°C [319]) and has a high strength-to-weight ratio which can be alloyed with a wide variety of other elements to produce lightweight alloys for aerospace, automotive, medical implants and industrial processes. Titanium has a HCP crystal structure at RT known as α -phase and phase transition to BCC structure occurs at 882°C [264] known as β -phase. This is similar to the transition

temperature of HCP α -phase to BCC β -phase of zirconium (865°C). Furthermore, the atomic radius of titanium (1.48 Å [216]) is similar to that of zirconium (1.64 Å [216]) and so substitutional diffusion of Ti atoms into random Zr sites without significantly altering the lattice parameters may limit lattice mismatch. Although titanium has quite a high neutron cross-section (6.09 barns [39]) relative to zirconium (0.184 barns [39]), it is potentially interesting to investigate further because although Ti and Zr have complete solid solubility in each other and their atom sizes are about 14% different (with Ti being smaller), so there might be some benefit from small additions of titanium (via substitutional diffusion in a PVD coating comprising of Ti and Zr), in reducing the oxide lattice parameter (to control stress), and in reducing the grain size of the crystalline oxide.

- $\text{Al}_2\text{O}_3/\text{YSZ}$ is another coating system that has been reported to show promise in improving corrosion resistance compared to YSZ alone. Similar to Ce_2O_3 , Zhu et al [320] suggested that Al_2O_3 reduces the infiltration of molten salts into the coating, but the added advantage is that Al_2O_3 has the potential to improve the phase stability of YSZ due to its presence at the grain boundaries of YSZ where tetragonal phase is present. The low neutron absorption cross-section of aluminium (0.230 barns) can provide good oxidation resistance without detrimentally effecting neutron economy which has been previously used as fuel cladding (magnesium with small amounts of aluminium) in MAGNOX reactors.
- Pyrochlores ($\text{A}_2\text{B}_2\text{O}_7$ structure) are of interest because of the close relationship with fluorite structures and offer attractive properties comparable to YSZ which include excellent thermal stability, attributed to the positions of cations in the crystal lattice. Yttrium-doped zirconia ($\text{Y}_2\text{Zr}_2\text{O}_7$) is unstable in the fluorite structure, but when Y^{3+} is replaced with a larger ion, for instance La^{3+} , the resultant lanthanum zirconate ($\text{La}_2\text{Zr}_2\text{O}_7$) pyrochlore structure is more stable to at least 1500°C [321]. This is particularly interesting because $\text{La}_2\text{Zr}_2\text{O}_7$ could be used to stabilise the oxide layer over a wide temperature range from normal operating conditions (300-330°C) to LOCA temperatures (~900°C). This indicates a low propensity to phase transformation from tetragonal to monoclinic oxide structure compared to 8YSZ. A limitation however, is the lower thermal conductivity (1.5 W/mK^{-1}) compared to YSZ ($2.0\text{-}2.3 \text{ W/mK}^{-1}$ at 1000°C). Although this is a disadvantage in the context of energy transfer in a nuclear reactor environment, it is an advantage when used as TBCs compared to 8YSZ. Notwithstanding, layer thicknesses of around tens of microns may offset this effect and may have limited impact. Likewise, replacing Zr^{4+} ion (0.15 nm) with a smaller ion such as Ti (0.14 nm) also stabilises the pyrochlore structure. Pyrochlores are an interesting avenue of research because many refractive elements can be included that have thermal stability in excess of 1500°C.

Furthermore, they can be formed from a wide range of cations, since the *A* site can have a charge of 3+ or 2+ and the *B* site cation have a valence of either 4+ or 5+. Thus, there can be extensive intermixing of different ions on the same crystallographic sites. It would be interesting to investigate whether this could be used to increase the stability of tetragonal zirconia in the oxide scale.

- TiN is a versatile hard ceramic which has become ubiquitous due to its proven wear resistance under high feed rates. Furthermore, the overall surface hardness has been reported to be higher compared to untreated Ti [322] due to the resulting ϵ -Ti₂N precipitates from nitrogen concentration greater than 12 wt% in Ti. However, Ti has a higher neutron absorption cross-section (6.09 barns) compared to Zr (0.184 barns) which should be taken into account during material selection as a potential candidate coating. Notwithstanding, hydrothermal testing of TiN coatings at hydrothermal reactor conditions has scarcely been reported and would thus be an interesting avenue of research for oxidation behaviour and adhesion properties.
- Titanium-aluminium-nitride (TiAlN) could be considered as a potential candidate coating for high temperature oxidation resistance and improved wear/abrasion resistance and toughness under demanding environments. It has been reported that for Ti_{1-x}Al_xN where 0.6 < x < 0.7 results in a significantly improved hardness and Young's modulus of the material compared to untreated Ti, and further improves oxidation resistance (upwards of 800-1000°C), improves thermal stability, improves toughness and wear/abrasion resistance. The increased oxidation resistance is due to the outward diffusion of Al to form an Al-rich oxide layer (Al₂O₃) at the outer surface and inward diffusion of oxygen to form a Ti-rich oxide layer at the substrate surface. In principle, during oxidation at high temperature, aluminium diffuses to the surface and reacts with oxygen to form a thin protective oxidation barrier (Al₂O₃) which significantly improves the oxidation performance as oxygen diffusion through aluminium oxide is several orders of magnitude slower than through zirconium oxide. Furthermore, Munz et al [323] also showed that oxidation initiation decreased with increased aluminium content of the TiAlN coating. However, there is some evidence of poor stability of Al₂O₃ under hydrothermal conditions compared to 'dry' high temperature oxidation but this would need to be studied further. Nonetheless, this provides an interesting avenue for further research which could be extended to TiCrAlN and TiCrAlYN coatings.
- The success of PVD TiAlN coatings in cutting tool applications has prompted further development of Ti-based coatings. For instance, the incorporation of 3 at% chromium in TiAlN has been shown to improve the oxidation resistance of the coating up to 920°C, which represents a 50°C increase above the oxidation resistance of TiAlN (870°C) [324]. Harris et al

[325] reported a higher average tool life for the TiAlCrN coatings compared to TiAlN coatings which was attributed to the multi-layered structure of the TiAlCrN coatings. Wear resistance was carried out by drilling holes into cast iron and using SEM to analyse the effect of wear on the coated drill bits. However, it has not been fully investigated how this coating might behave in high temperature aqueous conditions.

- The fraction of tetragonal zirconia found in an oxide scale is not constant but rather decreases with increased distance from the metal/oxide interface. Thus, the Garvie-Nicholson expressions in Equation 1.6 do not consider how the phases '*grades*' with oxide thickness. A few methods have been suggested to get around this. One is to mechanically remove the oxide, then grinding it to homogenise the mixture and then carry out X-ray diffraction analysis to obtain fractional quantities of the tetragonal and monoclinic phases formed. The issue here would be to ensure that all the oxide is removed and to ensure that as few impurities as possible are introduced from the mechanical grinding process. Another method might be to use synchrotron X-rays probing individual grains at different sampling depths within the oxide scale.

References

- [1] M. Hirano and T. Yonomoto, "Insights from review and analysis of the Fukushima Dai-ichi accident: Fukushima NPP accident related," *Journal of Nuclear Science and Technology*, vol. 49, no. 1, pp. 1-17, 2012.
- [2] S.-I. Tanaka, "Accident at the Fukushima Dai-ichi Nuclear Power Stations of TEPCO—Outline & lessons learned—," *Proceedings of the Japan Academy. Series B, Physical and biological sciences*, vol. 88, no. 9, p. 471, 2012.
- [3] O. Masson and A. Baeza, "Tracking of airborne radionuclides from the damaged Fukushima Dai-ichi nuclear reactors by European networks," *Environmental science & technology*, vol. 45, no. 18, pp. 7670-7677, 2011.
- [4] J. M. Schwantes, C. R. Orton, and R. A. Clark, "Analysis of a nuclear accident: fission and activation product releases from the Fukushima Daiichi Nuclear Facility as remote indicators of source identification, extent of release, and state of damaged spent nuclear fuel," *Environmental science & technology*, vol. 46, no. 16, pp. 8621-8627, 2012.
- [5] A. R. West, *Solid State Chemistry and its Applications*, 2nd ed. John Wiley & Sons Ltd, 2014.
- [6] L. Sepold, S. Hagen, P. Hofmann, and G. Schanz, "Behavior of BWR-type fuel elements with B4C/steel absorber tested under severe fuel damage conditions in the CORA facility," Forschungszentrum Karlsruhe GmbH Technik und Umwelt (Germany). Inst. fuer ..., 2009.
- [7] P. Hofmann, M. E. Markiewicz, and J. L. Spino, "Reaction behavior of B4C absorber material with stainless steel and zircaloy in severe light water reactor accidents," *Nuclear Technology*, vol. 90, no. 2, pp. 226-244, 1990.
- [8] F. Nagase, H. Uetsuka, and T. Otomo, "Chemical interactions between B4C and stainless steel at high temperatures," *Journal of nuclear materials*, vol. 245, no. 1, pp. 52-59, 1997.
- [9] M. Steinbrück, "Degradation and oxidation of B4C control rod segments at high temperatures," *Journal of Nuclear Materials*, vol. 400, no. 2, pp. 138-150, 2010.
- [10] M. Steinbrück, "Influence of boron carbide on core degradation during severe accidents in LWRs," *Annals of Nuclear Energy*, vol. 64, pp. 43-49, 2014.
- [11] "Fukushima Daiichi Accident." World Nuclear Association. <https://www.world-nuclear.org/information-library/safety-and-security/safety-of-plants/fukushima-accident.aspx> (accessed 08/10/2019, 2019).
- [12] J. PL and P. JE, "The Role of Nuclear Power After Fukushima," 2012.
- [13] A. J. González, "The recommendations of the ICRP vis-à-vis the Fukushima Dai-ichi NPP accident aftermath," *Journal of Radiological Protection*, vol. 32, no. 1, p. N1, 2012.
- [14] V. Vivoda, "Japan's energy security predicament post-Fukushima," *Energy Policy*, vol. 46, pp. 135-143, 2012, doi: <http://dx.doi.org/10.1016/j.enpol.2012.03.044>.
- [15] E. a. Department for Business, "New Direction for UK Energy Policy," ed. Whitehall, 2016.
- [16] L. Stevens, B. Anderson, C. Cowan, K. Colton, and D. Johnson, "The Footprint of Energy: Land Use of US Electricity Production," *Strata*, June, 2017.
- [17] J. Liman, "Small modular reactors: Methodology of economic assessment focused on incremental construction and gradual shutdown options," *Progress in Nuclear Energy*, vol. 108, pp. 253-259, 2018.
- [18] R. Adamson, F. Garzarolli, B. Cox, A. Strasser, and P. Rudling, "Corrosion mechanisms in zirconium alloys," *ZIRAT12 Special Topic Report*, 2007.
- [19] T. R. Allen, R. J. M. Konings, A. T. Motta, and R. J. M. Konings, "5.03 - Corrosion of Zirconium Alloys," in *Comprehensive Nuclear Materials*. Oxford: Elsevier, 2012, pp. 49-68.
- [20] B. Lustman and F. Kerze, *The metallurgy of zirconium*. McGraw-Hill Book Company, 1955.
- [21] C. Krenn, D. Roundy, J. Morris Jr, and M. L. Cohen, "Ideal strengths of bcc metals," *Materials Science and Engineering: A*, vol. 319, pp. 111-114, 2001.
- [22] *ASTM B353-12 Standard Specification for Wrought Zirconium Alloy Seamless and Welded Tubes for Nuclear Service*, A. International, United States, 2017.

- [23] P. Thomas, "21 - Nuclear reactors," in *Simulation of Industrial Processes for Control Engineers*. Oxford: Butterworth-Heinemann, 1999, pp. 268-281.
- [24] C. R. F. Azevedo, "Selection of fuel cladding material for nuclear fission reactors," *Engineering Failure Analysis*, vol. 18, no. 8, pp. 1943-1962, 2011, doi: <http://dx.doi.org/10.1016/j.engfailanal.2011.06.010>.
- [25] C. R. Gregson, D. T. Goddard, M. J. Sarsfield, and R. J. Taylor, "Combined electron microscopy and vibrational spectroscopy study of corroded Magnox sludge from a legacy spent nuclear fuel storage pond," *Journal of Nuclear Materials*, vol. 412, no. 1, pp. 145-156, 2011, doi: <http://dx.doi.org/10.1016/j.jnucmat.2011.02.046>.
- [26] C. Anwyl, C. Boxall, R. Wilbraham, D. Hambley, and C. Padovani, "Corrosion of AGR fuel pin steel under conditions relevant to permanent disposal," *Procedia Chemistry*, vol. 21, pp. 247-254, 2016.
- [27] R. Lobb and R. Jones, "The influence of iodine vapour on creep rupture properties of 20% Cr/25% Ni/Nb stabilised stainless steel," *Journal of Nuclear Materials*, vol. 59, no. 3, pp. 280-292, 1976.
- [28] R. H. Bogaard, P. D. Desai, H. H. Li, and C. Y. Ho, "Thermophysical properties of stainless steels," *Thermochimica Acta*, vol. 218, no. 0, pp. 373-393, 1993, doi: [http://dx.doi.org/10.1016/0040-6031\(93\)80437-F](http://dx.doi.org/10.1016/0040-6031(93)80437-F).
- [29] Y. Kim, J. Park, and J. Cleveland, "Thermophysical properties database of materials for light water reactors and heavy water reactors," IAEA, Vienna, 2006.
- [30] *Laser and Optics User's Manual. Material Expansion Co-efficients; Chapter 17*. Agilent Technologies, 2002.
- [31] M. T. Simnad, "A brief history of power reactor fuels," *Journal of Nuclear Materials*, vol. 100, no. 1-3, pp. 93-107, 1981.
- [32] R. Krishnan and M. Asundi, "Zirconium alloys in nuclear technology," *Proceedings of the Indian Academy of Sciences Section C: Engineering Sciences*, vol. 4, no. 1, pp. 41-56, 1981.
- [33] K. Linga Murty and I. Charit, "Texture development and anisotropic deformation of zircalloys," *Progress in Nuclear Energy*, vol. 48, no. 4, pp. 325-359, 2006, doi: <http://dx.doi.org/10.1016/j.pnucene.2005.09.011>.
- [34] M. Steinbrück and M. Böttcher, "Air oxidation of Zircaloy-4, M5[®] and ZIRLO[™] cladding alloys at high temperatures," *Journal of Nuclear Materials*, vol. 414, no. 2, pp. 276-285, 2011, doi: <http://dx.doi.org/10.1016/j.jnucmat.2011.04.012>.
- [35] Y. Yan, B. E. Garrison, M. Howell, and G. L. Bell, "High-temperature oxidation kinetics of sponge-based E110 cladding alloy," *Journal of Nuclear Materials*, vol. 499, pp. 595-612, 2018.
- [36] H. Lely and H. Hamburger, "Z. anorg, u. allgem," *Chem*, vol. 87, p. 269, 1914.
- [37] W. Kroll, "The production of ductile titanium," *Transactions of the Electrochemical Society*, vol. 78, no. 1, pp. 35-47, 1940.
- [38] W. Kroll, C. T. Anderson, H. Holmes, L. Yerkes, and H. Gilbert, "Large-Scale Laboratory Production of Ductile Zirconium," *Journal of The Electrochemical Society*, vol. 94, no. 1, pp. 1-20, 1948.
- [39] V. F. Sears, "Neutron scattering lengths and cross sections," *Neutron news*, vol. 3, no. 3, pp. 26-37, 1992.
- [40] O. Takeda, T. Uda, and T. H. Okabe, "Rare Earth, Titanium Group Metals, and Reactive Metals Production," in *Treatise on process metallurgy*: Elsevier, 2014, pp. 995-1069.
- [41] D. Charquet, "Improvement of the uniform corrosion resistance of Zircaloy-4 in the absence of irradiation," *Journal of Nuclear Materials*, vol. 160, no. 2, pp. 186-195, 1988.
- [42] A. Yilmazbayhan, O. Delaire, A. T. Motta, R. Birtcher, J. Maser, and B. Lai, "Determination of the alloying content in the matrix of Zr alloys using synchrotron radiation microprobe X-ray fluorescence," *Journal of Nuclear Materials*, vol. 321, no. 2-3, pp. 221-232, 2003.

- [43] C. Degueldre, J. Raabe, G. Kuri, and S. Abolhassani, "Zircaloy-2 secondary phase precipitate analysis by X-ray microspectroscopy," *Talanta*, vol. 75, no. 2, pp. 402-406, 2008.
- [44] P. Chemelle, D. Knorr, J. Van Der Sande, and R. Pelloux, "Morphology and composition of second phase particles in zircaloy-2," *Journal of Nuclear Materials*, vol. 113, no. 1, pp. 58-64, 1983.
- [45] D. Pickman, "Properties of zircaloy cladding," *Nuclear Engineering and Design*, vol. 21, no. 2, pp. 212-236, 1972.
- [46] G. Vesterlund, "Method of manufacturing cladding tubes of a zirconium-based alloy for fuel rods for nuclear reactors," ed: Google Patents, 1984.
- [47] E. Hillner, D. G. Franklin, and J. D. Smee, "Long-term corrosion of Zircaloy before and after irradiation," *Journal of Nuclear Materials*, vol. 278, no. 2-3, pp. 334-345, 2000, doi: [http://dx.doi.org/10.1016/S0022-3115\(99\)00230-5](http://dx.doi.org/10.1016/S0022-3115(99)00230-5).
- [48] A. T. Motta, A. Couet, and R. J. Comstock, "Corrosion of zirconium alloys used for nuclear fuel cladding," *Annual Review of Materials Research*, vol. 45, pp. 311-343, 2015.
- [49] B. Cox, "Effects of irradiation on the oxidation of zirconium alloys in high temperature aqueous environments: a review," *Journal of Nuclear Materials*, vol. 28, no. 1, pp. 1-47, 1968.
- [50] T. Arima, K. Moriyama, N. Gaja, H. Furuya, K. Idemitsu, and Y. Inagaki, "Oxidation kinetics of Zircaloy-2 between 450 C and 600 C in oxidizing atmosphere," *Journal of nuclear materials*, vol. 257, no. 1, pp. 67-77, 1998.
- [51] M. N. Cinbiz, D. A. Koss, and A. T. Motta, "The influence of stress state on the reorientation of hydrides in a zirconium alloy," *Journal of Nuclear Materials*, vol. 477, pp. 157-164, 2016.
- [52] D. R. Lide, *CRC handbook of chemistry and physics*. CRC press, 2004.
- [53] B. Cox *et al.*, "Waterside corrosion of zirconium alloys in nuclear power plants," *IAEA TECDOC*, vol. 996, 1998.
- [54] J. Abriata, J. Garces, and R. Versaci, "The O-Zr (oxygen-zirconium) system," *Bulletin of Alloy Phase Diagrams*, vol. 7, no. 2, pp. 116-124, 1986.
- [55] M. Salavati-Niasari, M. Dadkhah, and F. Davar, "Synthesis and characterization of pure cubic zirconium oxide nanocrystals by decomposition of bis-aqua, tris-acetylacetonato zirconium (IV) nitrate as new precursor complex," *Inorganica Chimica Acta*, vol. 362, no. 11, pp. 3969-3974, 2009.
- [56] Y. Kudoh, H. Takeda, and H. Arashi, "In situ determination of crystal structure for high pressure phase of ZrO₂ using a diamond anvil and single crystal X-ray diffraction method," *Physics and Chemistry of Minerals*, vol. 13, no. 4, pp. 233-237, 1986.
- [57] B. Bondars, "Powder diffraction investigations of plasma sprayed zirconia," *Journal of Materials Science*, vol. 30, no. 6, pp. 1621-1625, 1995.
- [58] P. Bouvier, E. Djurado, G. Lucazeau, and T. Le Bihan, "High-pressure structural evolution of undoped tetragonal nanocrystalline zirconia," *Physical Review B*, vol. 62, no. 13, p. 8731, 2000.
- [59] B. Lichter, "Precision lattice parameter determination of zirconium-oxygen solid solution," *Trans. Met. Soc. AIME*, vol. 218, 1960.
- [60] S. Shukla and S. Seal, "Mechanisms of room temperature metastable tetragonal phase stabilisation in zirconia," *International materials reviews*, vol. 50, no. 1, pp. 45-64, 2005.
- [61] D. Fettle, S. Bouvier, J. Favergeon, and L. Kurpaska, "Residual stresses in high temperature corrosion of pure zirconium using elasto-viscoplastic model: Application to the deflection test in monofacial oxidation," *Applied Surface Science*, vol. 357, pp. 777-786, 2015.
- [62] W. Harlow, H. Ghassemi, and M. L. Taheri, "Determination of the initial oxidation behavior of Zircaloy-4 by in-situ TEM," *Journal of Nuclear Materials*, vol. 474, pp. 126-133, 2016.
- [63] A. Yilmazbayhan, A. T. Motta, R. J. Comstock, G. P. Sabol, B. Lai, and Z. Cai, "Structure of zirconium alloy oxides formed in pure water studied with synchrotron radiation and optical

- microscopy: relation to corrosion rate," *Journal of Nuclear Materials*, vol. 324, no. 1, pp. 6-22, 2004.
- [64] H. F. Garces, B. S. Senturk, and N. P. Padture, "In situ Raman spectroscopy studies of high-temperature degradation of thermal barrier coatings by molten silicate deposits," *Scripta Materialia*, vol. 76, pp. 29-32, 2014.
- [65] S.-W. Yang, K.-H. Park, T.-G. Yoo, S.-J. Lee, and S.-D. Kim, "High Temperature Oxidation of a Zirconium Base Alloy in Steam," in *Proceedings of the Korean Nuclear Society Conference*, 2005: Korean Nuclear Society, pp. 326-327.
- [66] J. Godlewski, "How the Tetragonal Zirconia is Stabilized in the Oxide Scale that is Formed on a Zirconium Alloy Corroded at 400 C in steam," in *Zirconium in the nuclear industry: Tenth international symposium*, 1994: ASTM International.
- [67] R. Purohit, S. Saha, and A. Tyagi, "Combustion synthesis of nanocrystalline ZrO₂ powder: XRD, Raman spectroscopy and TEM studies," *Materials Science and Engineering: B*, vol. 130, no. 1, pp. 57-60, 2006.
- [68] S. Xie, E. Iglesia, and A. T. Bell, "Water-assisted tetragonal-to-monoclinic phase transformation of ZrO₂ at low temperatures," *Chemistry of materials*, vol. 12, no. 8, pp. 2442-2447, 2000.
- [69] J. Godlewski, J. Gros, M. Lambertin, J. Wadier, and H. Weidinger, "Raman Spectroscopy Study of the Tetragonal-to-monoclinic Transition in Zirconium Oxide Scales and Determination of Overall Oxygen Diffusion by Nuclear Microanalysis of O 1s," in *Zirconium in the Nuclear Industry: Ninth International Symposium*, 1991: ASTM International.
- [70] E. Polatidis, P. Frenkel and M. Preuss, "Residual stresses and tetragonal phase fraction characterisation of corrosion tested Zircaloy-4 using energy dispersive synchrotron X-ray diffraction," *Journal of Nuclear Materials*, vol. 432, no. 1, pp. 102-112, 2013.
- [71] A. Maroto, R. Bardoni and P. Koenig, "Growth and characterization of oxide layers on zirconium alloys," *Journal of nuclear materials*, vol. 229, pp. 79-92, 1996.
- [72] P. Barberis, T. Merle-Méjean, and P. Quintard, "On Raman spectroscopy of zirconium oxide films," *Journal of Nuclear Materials*, vol. 246, no. 2, pp. 232-243, 1997.
- [73] D. Pecheur, J. Godlewski, P. Billot, and J. Thomazet, "Microstructure of oxide films formed during the waterside corrosion of the Zircaloy-4 cladding in lithiated environment," in *Zirconium in the Nuclear Industry: Eleventh International Symposium*, 1996: ASTM International.
- [74] J. Wei, P. Frenkel and M. Preuss, "The effect of Sn on autoclave corrosion performance and corrosion mechanisms in Zr-Sn-Nb alloys," *Acta Materialia*, vol. 61, no. 11, pp. 4200-4214, 2013.
- [75] J. S. Moya, M. Diaz, J. F. Bartolomé, E. Roman, J. L. Sacedon, and J. Izquierdo, "Zirconium oxide film formation on zircaloy by water corrosion," *Acta Materialia*, vol. 48, no. 18-19, pp. 4749-4754, 2000, doi: [http://dx.doi.org/10.1016/S1359-6454\(00\)00267-6](http://dx.doi.org/10.1016/S1359-6454(00)00267-6).
- [76] A. Garner, A. Gholinia, P. Frankel, M. Gass, I. MacLaren, and M. Preuss, "The microstructure and microtexture of zirconium oxide films studied by transmission electron backscatter diffraction and automated crystal orientation mapping with transmission electron microscopy," *Acta Materialia*, vol. 80, pp. 159-171, 2014.
- [77] N. Petigny, P. Barberis, C. Lemaignan, C. Valot, and M. Lallemand, "In situ XRD analysis of the oxide layers formed by oxidation at 743 K on Zircaloy 4 and Zr-1NbO," *Journal of Nuclear Materials*, vol. 280, no. 3, pp. 318-330, 2000.
- [78] J. Lin, H. Li, C. Nam, and J. A. Szpunar, "Analysis on volume fraction and crystal orientation relationship of monoclinic and tetragonal oxide grown on Zr-2.5 Nb alloy," *Journal of nuclear materials*, vol. 334, no. 2, pp. 200-206, 2004.
- [79] I. Idarraga, M. Mermoux, C. Duriez, A. Crisci, and J. Mardon, "Raman investigation of pre-and post-breakaway oxide scales formed on Zircaloy-4 and M5® in air at high temperature," *Journal of Nuclear Materials*, vol. 421, no. 1, pp. 160-171, 2012.

- [80] U. Martin, H. Boysen, and F. Frey, "Neutron powder investigation of tetragonal and cubic stabilized zirconia, TZP and CSZ, at temperatures up to 1400 K," *Acta Crystallographica Section B: Structural Science*, vol. 49, no. 3, pp. 403-413, 1993.
- [81] R. Henry, T. Blay and S. Meille, "Local fracture toughness measurements in polycrystalline cubic zirconia using micro-cantilever bending tests," *Mechanics of Materials*, p. 103086, 2019.
- [82] H.-J. Beie, A. Mitwalsky, F. Garzarolli, H. Ruhmann, and H.-J. Sell, "Examinations of the corrosion mechanism of zirconium alloys," in *Zirconium in the nuclear industry: Tenth international symposium*, 1994: ASTM International.
- [83] C. Rosa, "Oxidation of zirconium—A critical review of literature," *Journal of the Less Common Metals*, vol. 16, no. 3, pp. 173-201, 1968.
- [84] I. Dickson, H. Evans, and K. Jones, "A comparison between the uniform and nodular forms of zircaloy corrosion in water reactors," *Journal of Nuclear Materials*, vol. 80, no. 2, pp. 223-231, 1979.
- [85] G. P. Sabol, R. J. Comstock, R. A. Weiner, P. Larouere, and R. N. Stanutz, "In-reactor corrosion performance of ZIRLO™ and zircaloy-4," in *Zirconium in the nuclear industry: Tenth International Symposium*, 1994: ASTM International.
- [86] K. Hauffe and J. Hinrichs, "Oxidation of metals and alloys," *New York*, 1965.
- [87] B. Cox and J. Pemsler, "Diffusion of oxygen in growing zirconia films," *Journal of Nuclear Materials*, vol. 28, no. 1, pp. 73-78, 1968.
- [88] J. Wei, P. Frenkel, R. Comstock and M. Preuss, "Autoclave study of zirconium alloys with and without hydride rim," *Corrosion Engineering, Science and Technology*, vol. 47, no. 7, pp. 516-528, 2012.
- [89] B. Cox, "Pore structure in oxide films on irradiated and unirradiated zirconium alloys," *Journal of Nuclear Materials*, vol. 148, no. 3, pp. 332-343, 1987.
- [90] B. Cox, "Some thoughts on the mechanisms of in-reactor corrosion of zirconium alloys," *Journal of Nuclear materials*, vol. 336, no. 2, pp. 331-368, 2005.
- [91] R. Patil and E. Subbarao, "Axial thermal expansion of ZrO₂ and HfO₂ in the range room temperature to 1400° C," *Journal of Applied Crystallography*, vol. 2, no. 6, pp. 281-288, 1969.
- [92] H. Boysen, F. Frey, and T. Vogt, "Neutron powder investigation of the tetragonal to monoclinic phase transformation in undoped zirconia," *Acta Crystallographica Section B: Structural Science*, vol. 47, no. 6, pp. 881-886, 1991.
- [93] A. Donaldson and H. Evans, "Oxidation-induced creep in Zircaloy-2: I. Basic observations," *Journal of Nuclear Materials*, vol. 99, no. 1, pp. 38-46, 1981.
- [94] J. Bryner, "The cyclic nature of corrosion of Zircaloy-4 in 633 K water," *Journal of nuclear materials*, vol. 82, no. 1, pp. 84-101, 1979.
- [95] P. Bouvier, J. Godlewski, and G. Lucazeau, "A Raman study of the nanocrystallite size effect on the pressure–temperature phase diagram of zirconia grown by zirconium-based alloys oxidation," *Journal of Nuclear Materials*, vol. 300, no. 2, pp. 118-126, 2002.
- [96] P. Barberis, "Zirconia powders and Zircaloy oxide films: tetragonal phase evolution during 400 C autoclave tests," *Journal of Nuclear Materials*, vol. 226, no. 1, pp. 34-43, 1995.
- [97] E. Djurado, P. Bouvier, and G. Lucazeau, "Crystallite Size Effect on the Tetragonal-Monoclinic Transition of Undoped Nanocrystalline Zirconia Studied by XRD and Raman Spectrometry," *Journal of Solid State Chemistry*, vol. 149, no. 2, pp. 399-407, 2000, doi: <http://dx.doi.org/10.1006/jssc.1999.8565>.
- [98] X. Iltis and H. Michel, "Transmission Electron Microscopy Study of a Locally Ordered Zr--O Solid Solution Obtained by an Oxidation Treatment of a Zircaloy-4 Alloy," *Journal of Alloys and Compounds(Switzerland)*, vol. 177, no. 1, pp. 71-82, 1991.
- [99] A. Heuer and M. Rühle, "Overview no. 45: on the nucleation of the martensitic transformation in zirconia (ZrO₂)," *Acta metallurgica*, vol. 33, no. 12, pp. 2101-2112, 1985.

- [100] R. A. Causey, D. F. Cowgill, and R. H. Nilson, "Review of the oxidation rate of zirconium alloys," Sandia National Laboratories, 2005.
- [101] N. Lakshmi, H.-I. Yoo, and M. Martin, "Oxidation Kinetics of Zirconium Examined by In Situ X-ray Diffraction," *Journal of The Electrochemical Society*, vol. 160, no. 3, pp. C136-C141, 2013.
- [102] M. Preuss, R. Comstock and M. Blat-Yrieix, "Studies regarding corrosion mechanisms in zirconium alloys," in *Zirconium in the Nuclear Industry: 16th International Symposium*, 2012: ASTM International.
- [103] H.-I. Yoo, B.-J. Koo, J.-O. Hong, I.-S. Hwang, and Y.-H. Jeong, "A working hypothesis on oxidation kinetics of Zircaloy," *Journal of Nuclear Materials*, vol. 299, no. 3, pp. 235-241, 2001.
- [104] *G2-06 Standard Test Method for Corrosion Testing of Products of Zirconium, Hafnium, and Their Alloys in Water at 680°F (360°C) or in Steam at 750°F (400°C)* ASTM, 2011.
- [105] M. Suzuki and S. Kawasaki, "Oxidation of Zircaloy cladding in air," *Journal of Nuclear Materials*, vol. 140, no. 1, pp. 32-43, 1986.
- [106] R. Garvie, "Stabilization of the tetragonal structure in zirconia microcrystals," *The Journal of Physical Chemistry*, vol. 82, no. 2, pp. 218-224, 1978.
- [107] P. Platt, D. Lunt, E. Polatidis, M. Wenman, and M. Preuss, "In-situ digital image correlation for fracture analysis of oxides formed on zirconium alloys," *Corrosion Science*, vol. 111, pp. 344-351, 2016.
- [108] A. Piosik, K. Żurowski, Z. Pietralik, W. Hędzielek, and M. Kozak, "Structural studies of degradation process of zirconium dioxide tetragonal phase induced by grinding with dental bur," *Nuclear Instruments and Methods in Physics Research Section B: Beam Interactions with Materials and Atoms*, vol. 411, pp. 85-93, 2017.
- [109] A. Arata, R. N. Tango, "Quantitative phase analysis from X-ray diffraction in Y-TZP dental ceramics: a critical evaluation," *Journal of dentistry*, vol. 42, no. 11, pp. 1487-1494, 2014.
- [110] "Fukushima: Background on Reactors." World Nuclear Association. <https://www.world-nuclear.org/information-library/safety-and-security/safety-of-plants/appendices/fukushima-reactor-background> (accessed).
- [111] M. Esmaily, J.E. Svensson and L.G. Johansson, "Fundamentals and advances in magnesium alloy corrosion," *Progress in Materials Science*, vol. 89, pp. 92-193, 2017.
- [112] H. Rickover, L. Geiger, and B. Lustman, "History of the development of zirconium alloys for use in nuclear reactors," Energy Research and Development Administration, Washington, DC (USA). Div. of Naval Reactors, 1975.
- [113] N. Pilling, "The oxidation of metals at high temperature," *J. Inst. Met.*, vol. 29, pp. 529-582, 1923.
- [114] W. Barker, F. Bailey, and W. Garrett, "A high-temperature neutron diffraction study of pure and scandia-stabilized zirconia," *Journal of Solid State Chemistry*, vol. 7, no. 4, pp. 448-453, 1973.
- [115] G. B. Skinner and H. L. Johnston, "Thermal expansion of zirconium between 298 K and 1600 K," *The Journal of Chemical Physics*, vol. 21, no. 8, pp. 1383-1384, 1953.
- [116] M. Mishra *et al.*, "Thermal stability and thermal expansion behaviour of ZrO₂/Y₂O₃ multilayers deposited by pulsed laser deposition technique," *Materials Chemistry and Physics*, vol. 162, pp. 592-607, 2015.
- [117] J. E. Jaffe, R. A. Bachorz, and M. Gutowski, "Low-temperature polymorphs of Zr O₂ and Hf O₂: A density-functional theory study," *Physical Review B*, vol. 72, no. 14, p. 144107, 2005.
- [118] D. Wang, Y. Guo, K. Liang, and K. Tao, "Crystal structure of zirconia by Rietveld refinement," *Science in China Series A: Mathematics*, vol. 42, no. 1, p. 80, 1999.
- [119] G. Katz, "X-Ray Diffraction Powder Pattern of Metastable Cubic ZrO₂," *Journal of the American Ceramic Society*, vol. 54, no. 10, pp. 531-531, 1971.

- [120] A. Couet, A. T. Motta, R. J. Comstock, and R. L. Paul, "Cold neutron prompt gamma activation analysis, a non-destructive technique for hydrogen level assessment in zirconium alloys," *Journal of Nuclear Materials*, vol. 425, no. 1, pp. 211-217, 2012.
- [121] L. Van Swam, A. Strasser, J. Cook, and J. Burger, "Behaviour of Zircaloy-4 and Zirconium Liner Zircaloy-4 Cladding at High Burn-up," in *ANS Topical Meeting on Light Water Reactor Fuel Performance, Portland, Oregon, 1997*, pp. 2-6.
- [122] A. Garde, G. Smith, and R. Pirek, "In-PWR irradiation performance of dilute tin-zirconium advanced alloys," in *Zirconium in the Nuclear Industry: Thirteenth International Symposium, 2002*: ASTM International.
- [123] J. Kearns, "Terminal solubility and partitioning of hydrogen in the alpha phase of zirconium, Zircaloy-2 and Zircaloy-4," *Journal of Nuclear Materials*, vol. 22, no. 3, pp. 292-303, 1967.
- [124] A. McMinn, E. C. Darby, and J. S. Schofield, "The terminal solid solubility of hydrogen in zirconium alloys," in *Zirconium in the Nuclear Industry: Twelfth International Symposium, 2000*: ASTM International.
- [125] R. Daum, S. Majumdar, D. Bates, A. Motta, D. Koss, and M. Billone, "On the embrittlement of Zircaloy-4 under RIA-relevant conditions," *ASTM SPECIAL TECHNICAL PUBLICATION*, vol. 1423, pp. 702-718, 2002.
- [126] T. Maimaitiyili and F. Ribeiro, "Observation of the δ to ϵ Zr-hydride transition by in-situ synchrotron X-ray diffraction," *Crystal Research and Technology*, vol. 51, no. 11, pp. 663-670, 2016.
- [127] R. Daum, Y. Chu, and A. Motta, "Identification and quantification of hydride phases in Zircaloy-4 cladding using synchrotron X-ray diffraction," *Journal of Nuclear Materials*, vol. 392, no. 3, pp. 453-463, 2009.
- [128] K. Barraclough and C. Beevers, "Some observations on the phase transformations in zirconium hydrides," *Journal of Nuclear Materials*, vol. 34, no. 2, pp. 125-134, 1970.
- [129] X. Yang, N. Takeichi, K. Shida, H. Tanaka, N. Kuriyama, and T. Sakai, "Novel Mg-Zr-A-H (A= Li, Na) hydrides synthesized by a high pressure technique and their hydrogen storage properties," *Journal of Alloys and Compounds*, vol. 509, no. 4, pp. 1211-1216, 2011.
- [130] B. Nath, G. Lorimer, and N. Ridley, "Effect of hydrogen concentration and cooling rate on hydride precipitation in α -zirconium," *Journal of Nuclear Materials*, vol. 58, no. 2, pp. 153-162, 1975.
- [131] W. M. Mueller, J. P. Blackledge, and G. G. Libowitz, *Metal hydrides*. Elsevier, 2013.
- [132] J. Bailey, "Electron microscope observations on the precipitation of zirconium hydride in zirconium," *Acta metallurgica*, vol. 11, no. 4, pp. 267-280, 1963.
- [133] C. Ells, "Hydride precipitates in zirconium alloys (a review)," *Journal of Nuclear Materials*, vol. 28, no. 2, pp. 129-151, 1968.
- [134] S. Wang, F. Giuliani, and T. B. Britton, "Microstructure and formation mechanisms of δ -hydrides in variable grain size Zircaloy-4 studied by electron backscatter diffraction," *Acta Materialia*, vol. 169, pp. 76-87, 2019.
- [135] J.-S. Kim, S.-D. Kim, and J. Yoon, "Hydride formation on deformation twin in zirconium alloy," *Journal of Nuclear Materials*, vol. 482, pp. 88-92, 2016.
- [136] D. Westlake, "Precipitation strengthening in crystals of zirconium-hydrogen alloys containing oxygen as an impurity," *Acta Metallurgica*, vol. 12, no. 12, pp. 1373-1380, 1964.
- [137] J. Bradbrook, G. Lorimer, and N. Ridley, "The precipitation of zirconium hydride in zirconium and Zircaloy-2," *Journal of Nuclear Materials*, vol. 42, no. 2, pp. 142-160, 1972.
- [138] Y. Yan, A. S. Blackwell, L. K. Plummer, B. Radhakrishnan, S. B. Gorti, and K. T. Clarno, "OBSERVATION AND MECHANISM OF HYDRIDE IN ZIRCALOY-4 AND LOCAL HYDRIDE RE-ORIENTATION INDUCED BY HIGH PRESSURE AT HIGH TEMPERATURES," Oak Ridge National Laboratory (ORNL), 2013.
- [139] B. Cox and H. Sheikh, "Redistribution of the alloying elements during Zircaloy-2 oxidation," *Journal of Nuclear Materials*, vol. 249, no. 1, pp. 17-32, 1997.

- [140] J. Sarkar, "Chapter 2 - Sputtering and Thin Film Deposition," in *Sputtering Materials for VLSI and Thin Film Devices*. Boston: William Andrew Publishing, 2014, pp. 93-170.
- [141] J. F. Wager, B. Yeh, R. L. Hoffman, and D. A. Keszler, "An amorphous oxide semiconductor thin-film transistor route to oxide electronics," *Current Opinion in Solid State and Materials Science*, vol. 18, no. 2, pp. 53-61, 2014, doi: <http://dx.doi.org/10.1016/j.cossms.2013.07.002>.
- [142] M. F. Morks, I. Cole, and A. Kobayashi, "Plasma forming multilayer ceramics for ultra-high temperature application," *Vacuum*, vol. 88, no. 0, pp. 134-138, 2013, doi: <http://dx.doi.org/10.1016/j.vacuum.2012.03.045>.
- [143] A. F. Renteria, B. Saruhan, U. Schulz, H. J. Raetzer-Scheibe, J. Haug, and A. Wiedenmann, "Effect of morphology on thermal conductivity of EB-PVD PYSZ TBCs," *Surface and Coatings Technology*, vol. 201, no. 6, pp. 2611-2620, 2006, doi: <http://dx.doi.org/10.1016/j.surfcoat.2006.05.003>.
- [144] J. Meneve, K. Vercammen, E. Dekempeneer, and J. Smeets, "Thin tribological coatings: magic or design?," *Surface and Coatings Technology*, vol. 94, pp. 476-482, 1997.
- [145] J.-E. Sundgren, "Structure and properties of TiN coatings," *Thin solid films*, vol. 128, no. 1, pp. 21-44, 1985.
- [146] E. Santecchia, A. M. S. Hamouda, F. Musharavati, E. Zalnezhad, M. Cabibbo, and S. Spigarelli, "Wear resistance investigation of titanium nitride-based coatings," *Ceramics International*, vol. 41, no. 9, Part A, pp. 10349-10379, 2015, doi: <http://dx.doi.org/10.1016/j.ceramint.2015.04.152>.
- [147] M. Mikula *et al.*, "Toughness enhancement in highly NbN-alloyed Ti-Al-N hard coatings," *Acta Materialia*, vol. 121, pp. 59-67, 2016, doi: <http://dx.doi.org/10.1016/j.actamat.2016.08.084>.
- [148] D. Batory, W. Szymanski, M. Panjan, O. Zabeida, and J. E. Klemberg-Sapieha, "Plasma nitriding of Ti6Al4V alloy for improved water erosion resistance," *Wear*, vol. 374-375, pp. 120-127, 2017, doi: <http://dx.doi.org/10.1016/j.wear.2017.01.041>.
- [149] E. De Las Heras, G. Ybarra, D. Lamas, A. Cabo, E. L. Dalibon, and S. P. Brühl, "Plasma nitriding of 316L stainless steel in two different N₂-H₂ atmospheres - Influence on microstructure and corrosion resistance," *Surface and Coatings Technology*, vol. 313, pp. 47-54, 2017, doi: <http://dx.doi.org/10.1016/j.surfcoat.2017.01.037>.
- [150] B. Engers and H. U. Bauer, "Cost-effective PVD coatings in batch systems," *Surface and Coatings Technology*, vol. 116-119, pp. 705-710, 1999, doi: [http://dx.doi.org/10.1016/S0257-8972\(99\)00119-X](http://dx.doi.org/10.1016/S0257-8972(99)00119-X).
- [151] N. C. Reger, V. K. Balla, M. Das, and A. K. Bhargava, "Wear and corrosion properties of in-situ grown zirconium nitride layers for implant applications," *Surface and Coatings Technology*, vol. 334, pp. 357-364, 2018.
- [152] B. S. Yilbaş and M. Sami, "Plasma nitriding of Ti-6Al-4V alloy to improve some tribological properties," *Surface and Coatings Technology*, vol. 80, no. 3, pp. 287-292, 1996.
- [153] A. Zhecheva, S. Malinov, and W. Sha, "Titanium alloys after surface gas nitriding," *Surface and Coatings Technology*, vol. 201, no. 6, pp. 2467-2474, 2006, doi: <https://doi.org/10.1016/j.surfcoat.2006.04.019>.
- [154] T. Spalvins, "Plasma assisted surface coating/modification processes: An emerging technology," 1986.
- [155] J. García and R.J. Rodriguez, "Nitrogen ion implantation on group IVb metals:: chemical, mechanical and tribological study," *Vacuum*, vol. 64, no. 3, pp. 343-351, 2002.
- [156] A. Leyland, K. Fancey, A. James, and A. Matthews, "Enhanced plasma nitriding at low pressures: a comparative study of dc and rf techniques," *Surface and Coatings technology*, vol. 41, no. 3, pp. 295-304, 1990.
- [157] W. Yang and C. Sun, "Enhancement of mechanical property and corrosion resistance of 316 L stainless steels by low temperature arc plasma nitriding," vol. 298, pp. 64-72, 2016.

- [158] D. M. Mattox, "Fundamentals of ion plating," *Journal of Vacuum Science & Technology*, vol. 10, no. 1, pp. 47-52, 1973.
- [159] W. Davis and T. Vanderslice, "Ion energies at the cathode of a glow discharge," *Physical Review*, vol. 131, no. 1, p. 219, 1963.
- [160] J. Richards, "Energies of particles at the cathode of a glow discharge," *Vacuum*, vol. 34, no. 5, pp. 559-562, 1984.
- [161] K. Fancey and A. Matthews, "Some fundamental aspects of glow discharges in plasma-assisted processes," *Surface and Coatings Technology*, vol. 33, pp. 17-29, 1987.
- [162] A. Korhonen, E. Sirvio, and M. Sulonen, "Plasma nitriding and ion plating with an intensified glow discharge," *Thin Solid Films*, vol. 107, no. 4, pp. 387-394, 1983.
- [163] K. Fancey and A. Matthews, "Process effects in ion plating," *Vacuum*, vol. 41, no. 7-9, pp. 2196-2200, 1990.
- [164] A. Brokman and F. R. Tuler, "A study of the mechanisms of ion nitriding by the application of a magnetic field," *Journal of Applied Physics*, vol. 52, no. 1, pp. 468-471, 1981.
- [165] G. G. Tibbetts, "Role of nitrogen atoms in ion-nitriding," *Journal of Applied Physics*, vol. 45, no. 11, pp. 5072-5073, 1974.
- [166] V. Fouquet, L. Pichon, M. Drouet, and A. Straboni, "Plasma assisted nitridation of Ti-6Al-4V," *Applied Surface Science*, vol. 221, no. 1, pp. 248-258, 2004.
- [167] E. Meletis, C. Cooper, and K. Marchev, "The use of intensified plasma-assisted processing to enhance the surface properties of titanium," *Surface and Coatings Technology*, vol. 113, no. 3, pp. 201-209, 1999.
- [168] H. F. Winters, "The growth of nitrided surface layers by ion bombardment," *Journal of Applied Physics*, vol. 43, no. 11, pp. 4809-4811, 1972.
- [169] J. A. Thornton, "High rate thick film growth," *Annual review of materials science*, vol. 7, no. 1, pp. 239-260, 1977.
- [170] A. Adjaottor, E. Ma, and E. Meletis, "On the mechanism of intensified plasma-assisted processing," *Surface and Coatings Technology*, vol. 89, no. 3, pp. 197-203, 1997.
- [171] H. Winters, "Ionic adsorption and dissociation cross section for nitrogen," *The Journal of Chemical Physics*, vol. 44, no. 4, pp. 1472-1476, 1966.
- [172] K. S. Fancey, "An investigation into dissociative mechanisms in nitrogenous glow discharges by optical emission spectroscopy," *Vacuum*, vol. 46, no. 7, pp. 695-700, 1995, doi: [https://doi.org/10.1016/0042-207X\(94\)00146-4](https://doi.org/10.1016/0042-207X(94)00146-4).
- [173] A. Smith, E. Caplinger, R. Neynaber, E. W. Rothe, and S. Trujillo, "Electron impact ionization of atomic nitrogen," *Physical Review*, vol. 127, no. 5, p. 1647, 1962.
- [174] T. Czerwicz, H. Michel, and E. Bergmann, "Low-pressure, high-density plasma nitriding: mechanisms, technology and results," *Surface and Coatings Technology*, vol. 108, pp. 182-190, 1998.
- [175] A. Davison, J. Avelar-Batista, A. Wilson, A. Leyland, A. Matthews, and K. Fancey, "Investigation of interactions between inert gases and nitrogen in direct current triode discharges," *Journal of Vacuum Science & Technology A: Vacuum, Surfaces, and Films*, vol. 21, no. 5, pp. 1683-1687, 2003.
- [176] A. Raveh, A. Bussiba, A. Bettelheim, and Y. Katz, "Plasma-nitrided α - β Ti alloy: layer characterization and mechanical properties modification," *Surface and Coatings Technology*, vol. 57, no. 1, pp. 19-29, 1993.
- [177] L. Pichon, T. Girardeau, A. Straboni, F. Lignou, J. Perrière, and J. M. Frigério, "Ion beam assisted deposition of zirconium nitrides for modulated optical index structures," *Nuclear Instruments and Methods in Physics Research Section B: Beam Interactions with Materials and Atoms*, vol. 147, no. 1-4, pp. 378-382, 1999, doi: [http://dx.doi.org/10.1016/S0168-583X\(98\)00567-9](http://dx.doi.org/10.1016/S0168-583X(98)00567-9).

- [178] J.-D. Zhang and K. Yang, "Theoretical study of the thermodynamic properties of cubic Zr₃N₄ and Hf₃N₄ under high pressures," *Journal of Alloys and Compounds*, vol. 608, pp. 90-94, 2014.
- [179] A. Zhecheva, W. Sha, S. Malinov, and A. Long, "Enhancing the microstructure and properties of titanium alloys through nitriding and other surface engineering methods," *Surface and Coatings Technology*, vol. 200, no. 7, pp. 2192-2207, 2005.
- [180] T. Muraleedharan and E. Meletis, "Surface modification of pure titanium and Ti-6Al-4V by intensified plasma ion nitriding," *Thin Solid Films*, vol. 221, no. 1-2, pp. 104-113, 1992.
- [181] N. Kashaev, H.-R. Stock, and P. Mayr, "Assessment of the application potential of the intensified glow discharge for industrial plasma nitriding of Ti-6Al-4V," *Surface and Coatings Technology*, vol. 200, no. 1, pp. 502-506, 2005.
- [182] G. Cassar, J. A.-B. Wilson, S. Banfield, J. Housden, A. Matthews, and A. Leyland, "A study of the reciprocating-sliding wear performance of plasma surface treated titanium alloy," *Wear*, vol. 269, no. 1, pp. 60-70, 2010.
- [183] A. Wilson, A. Leyland, and A. Matthews, "A comparative study of the influence of plasma treatments, PVD coatings and ion implantation on the tribological performance of Ti-6Al-4V," *Surface and coatings technology*, vol. 114, no. 1, pp. 70-80, 1999.
- [184] A. Matthews, K. Fancey, A. James, and A. Leyland, "Ionization in plasma-assisted physical vapour deposition systems," *Surface and Coatings Technology*, vol. 61, no. 1-3, pp. 121-126, 1993.
- [185] A. Leyland, K. Fancey, and A. Matthews, "Plasma nitriding in a low pressure triode discharge to provide improvements in adhesion and load support for wear resistant coatings," *Surface Engineering*, vol. 7, no. 3, pp. 207-215, 1991.
- [186] D. Wu, Z. Zhang, D. Fu, W. Fan, and H. Guo, "Structure, electrical and chemical properties of zirconium nitride films deposited by dc reactive magnetron sputtering," *Applied Physics A: Materials Science & Processing*, vol. 64, no. 6, pp. 593-595, 1997.
- [187] Z. Qi, P. Sun, F. Zhu, Z. Wang, D. Peng, and C. Wu, "The inverse Hall-Petch effect in nanocrystalline ZrN coatings," *Surface and Coatings Technology*, vol. 205, no. 12, pp. 3692-3697, 2011.
- [188] C. Wang, S. Akbar, W. Chen, and V. Patton, "Electrical properties of high-temperature oxides, borides, carbides, and nitrides," *Journal of materials science*, vol. 30, no. 7, pp. 1627-1641, 1995.
- [189] U. Wiiala, I. Penttinen, A. Korhonen, J. Aromaa, and E. Ristolainen, "Improved corrosion resistance of physical vapour deposition coated TiN and ZrN," *Surface and Coatings Technology*, vol. 41, no. 2, pp. 191-204, 1990.
- [190] P. Johnson and H. Randhawa, "Zirconium nitride films prepared by cathodic arc plasma deposition process," *Surface and Coatings Technology*, vol. 33, pp. 53-62, 1987.
- [191] D. Jianxin, L. Jianhua, Z. Jinlong, S. Wenlong, and N. Ming, "Friction and wear behaviors of the PVD ZrN coated carbide in sliding wear tests and in machining processes," *Wear*, vol. 264, no. 3, pp. 298-307, 2008.
- [192] R. W. Harrison and W. E. Lee, "Mechanism and kinetics of oxidation of ZrN ceramics," *Journal of the American Ceramic Society*, vol. 98, no. 7, pp. 2205-2213, 2015.
- [193] M. Pukari, M. Takano, and T. Nishi, "Sintering and characterization of (Pu, Zr) N," *Journal of Nuclear Materials*, vol. 444, no. 1, pp. 421-427, 2014.
- [194] K. A. Gruss, T. Zheleva, R. F. Davis, and T. R. Watkins, "Characterization of zirconium nitride coatings deposited by cathodic arc sputtering," *Surface and Coatings Technology*, vol. 107, no. 2-3, pp. 115-124, 1998, doi: [http://dx.doi.org/10.1016/S0257-8972\(98\)00584-2](http://dx.doi.org/10.1016/S0257-8972(98)00584-2).
- [195] R. Russell, "Coefficients of thermal expansion for zirconium," *JOM*, vol. 6, no. 9, pp. 1045-1052, 1954.

- [196] B. Zhang, B. Wang, and C. Zhao, "Microstructural effect on the radiative properties of YSZ thermal barrier coatings (TBCs)," *International Journal of Heat and Mass Transfer*, vol. 73, pp. 59-66, 2014.
- [197] C. Howard, R. Hill, and B. Reichert, "Structures of ZrO₂ polymorphs at room temperature by high-resolution neutron powder diffraction," *Acta Crystallographica Section B: Structural Science*, vol. 44, no. 2, pp. 116-120, 1988.
- [198] D. Hasselman, L. F. Johnson, L. D. Bentsen, R. SYED, H. Lee, and M. V. SWAIN, "Thermal diffusivity and conductivity of dense polycrystalline ZrO," *Am. Ceram. Soc. Bull*, vol. 66, no. 5, pp. 799-806, 1987.
- [199] http://www.rolls-royce.com/about/technology/material_tech/coatings.jsp (accessed 10th June, 2014).
- [200] W. Fan and B.Q. Li, "Microstructural design and properties of supersonic suspension plasma sprayed thermal barrier coatings," *Journal of Alloys and Compounds*, vol. 699, pp. 763-774, 2017, doi: <http://dx.doi.org/10.1016/j.jallcom.2016.12.356>.
- [201] F. Stott and G. Wood, "Growth and adhesion of oxide scales on Al₂O₃-forming alloys and coatings," *Materials Science and Engineering*, vol. 87, pp. 267-274, 1987.
- [202] N. P. Padture, M. Gell, and E. H. Jordan, "Thermal barrier coatings for gas-turbine engine applications," *Science*, vol. 296, no. 5566, pp. 280-284, 2002.
- [203] S.-C. Li, S.-C. Kim, and C.-S. Kang, "Recovery of scandium from KOH sub-molten salt leaching cake of fergusonite," *Minerals Engineering*, vol. 137, pp. 200-206, 2019.
- [204] Z. Liu, Y. Zong, H. Li, and Z. Zhao, "Characterization of scandium and gallium in red mud with Time of Flight-Secondary Ion Mass Spectrometry (ToF-SIMS) and Electron Probe Micro-Analysis (EPMA)," *Minerals Engineering*, vol. 119, pp. 263-273, 2018.
- [205] S. Lukich, C. Carpenter, and N. Orlovskaya, "Temperature and stress induced changes of the vibrational response of cubic and rhombohedral 10 mol% Sc₂O₃-1 mol% CeO₂-ZrO₂ ceramics," *Journal of Power Sources*, vol. 195, no. 8, pp. 2301-2309, 2010.
- [206] Y. Arachi *et al.*, "Electrical Conductivity of ZrO₂ Sc₂ O₃ Doped with HfO₂, CeO₂, and Ga₂ O₃," *Journal of the Electrochemical Society*, vol. 148, no. 5, pp. A520-A523, 2001.
- [207] D. McWhan, "Structure of Cerium above 50 kbar," *Physical Review B*, vol. 1, no. 6, p. 2826, 1970.
- [208] J. Zhang, Q. Liu, Q. He, and Y. Nozaki, "Rare Earth Elements and Their Isotopes in the Ocean," 2018.
- [209] Y. Zhang, C. Yan, F. Wang, H. Lou, and C. Cao, "Study on the environmentally friendly anodizing of AZ91D magnesium alloy," *Surface and Coatings Technology*, vol. 161, no. 1, pp. 36-43, 2002.
- [210] G. Makar and J. Kruger, "Corrosion of magnesium," *International materials reviews*, vol. 38, no. 3, pp. 138-153, 1993.
- [211] F. Hollstein, R. Wiedemann, and J. Scholz, "Characteristics of PVD-coatings on AZ31hp magnesium alloys," *Surface and Coatings Technology*, vol. 162, no. 2, pp. 261-268, 2003.
- [212] N. I. Z. Abidin, M.C. Morris and A. Atrens, "The in vivo and in vitro corrosion of high-purity magnesium and magnesium alloys WZ21 and AZ91," *Corrosion Science*, vol. 75, pp. 354-366, 2013.
- [213] H. E. Swanson, M. C. Morris, R. P. Stinchfield, and E. H. Evans, "Standard X-ray diffraction powder patterns," National Bureau of Standards, Washington, DC, 1962.
- [214] W. Kroll, A. Schlechten, and L. Yerkes, "Ductile zirconium from zircon sand," *Transactions of The Electrochemical Society*, vol. 89, no. 1, pp. 263-276, 1946.
- [215] G. L. Song and A. Atrens, "Corrosion mechanisms of magnesium alloys," *Advanced engineering materials*, vol. 1, no. 1, pp. 11-33, 1999.
- [216] W. M. Haynes, *CRC handbook of chemistry and physics*. CRC press, 2014.

- [217] E. Śniezek, P. Stock and E. Burkel, "Structural properties of MgO–ZrO₂ ceramics obtained by conventional sintering, arc melting and field assisted sintering technique," *Materials & Design*, vol. 99, pp. 412-420, 2016.
- [218] I. Polmear, "Light alloys- Metallurgy of the light metals", *London and New York, Edward Arnold, 1989, 288*, 1989.
- [219] P. Medvedev, S. Frank, T. O'Holleran, and M. Meyer, "Dual phase MgO–ZrO₂ ceramics for use in LWR inert matrix fuel," *Journal of Nuclear Materials*, vol. 342, no. 1, pp. 48-62, 2005.
- [220] A. Atrens, G.-L. Song, F. Cao, Z. Shi, and P. K. Bowen, "Advances in Mg corrosion and research suggestions," *Journal of Magnesium and Alloys*, vol. 1, no. 3, pp. 177-200, 2013.
- [221] D. Orlov, K. Ralston, N. Birbilis, and Y. Estrin, "Enhanced corrosion resistance of Mg alloy ZK60 after processing by integrated extrusion and equal channel angular pressing," *Acta Materialia*, vol. 59, no. 15, pp. 6176-6186, 2011.
- [222] J.-c. Zhang *et al.*, "Effect of Zr addition on microstructure and properties of Al–Mn–Si–Zn-based alloy," *Transactions of Nonferrous Metals Society of China*, vol. 24, no. 12, pp. 3872-3878, 2014.
- [223] J. Schaum and H. Burnett, "Magnesium-rich side of the magnesium-zirconium constitution diagram," *J. Res. Nat. Bur. Stand*, vol. 49, no. 3, 1952.
- [224] J. Lawal, P. Kiryukhantsev-Korneev, A. Matthews, and A. Leyland, "Mechanical properties and abrasive wear behaviour of Al-based PVD amorphous/nanostructured coatings," *Surface and Coatings Technology*, vol. 310, pp. 59-69, 2017.
- [225] A. Prasad, P. J. Uggowitzer, Z. Shi, and A. Atrens, "Production of high purity magnesium alloys by melt purification with Zr," *Advanced engineering materials*, vol. 14, no. 7, pp. 477-490, 2012.
- [226] W. Hume-Rothery, G. Mabbott, W. and K. Channel Evans, "The freezing points, melting points, and solid solubility limits of the alloys of silver and copper with the elements of the b sub-groups," *Philosophical Transactions of the Royal Society of London. Series A, Containing Papers of a Mathematical or Physical Character*, vol. 233, no. 721-730, pp. 1-97, 1934.
- [227] A. L. Allred, "Electronegativity values from thermochemical data," *Journal of inorganic and nuclear chemistry*, vol. 17, no. 3-4, pp. 215-221, 1961.
- [228] B. Movchan and A. Demchishin, "STRUCTURE AND PROPERTIES OF THICK CONDENSATES OF NICKEL, TITANIUM, TUNGSTEN, ALUMINUM OXIDES, AND ZIRCONIUM DIOXIDE IN VACUUM," *Fiz. Metal. Metalloved. 28: 653-60 (Oct 1969)*. 1969.
- [229] E. Kusano, "Homologous substrate-temperature dependence of structure and properties of TiO₂, ZrO₂, and HfO₂ thin films deposited by reactive sputtering," *Journal of Vacuum Science & Technology A: Vacuum, Surfaces, and Films*, vol. 37, no. 5, p. 051508, 2019.
- [230] E. Kusano, "Structure-Zone Modeling of Sputter-Deposited Thin Films: A Brief Review," *Applied Science and Convergence Technology*, vol. 28, no. 6, pp. 179-185, 2019.
- [231] J. A. Thornton, "Influence of apparatus geometry and deposition conditions on the structure and topography of thick sputtered coatings," *Journal of Vacuum Science and Technology*, vol. 11, no. 4, pp. 666-670, 1974.
- [232] R. Messier, A. Giri, and R. Roy, "Revised structure zone model for thin film physical structure," *Journal of Vacuum Science & Technology A: Vacuum, Surfaces, and Films*, vol. 2, no. 2, pp. 500-503, 1984.
- [233] A. Anders, "A structure zone diagram including plasma-based deposition and ion etching," *Thin Solid Films*, vol. 518, no. 15, pp. 4087-4090, 2010.
- [234] M. González, P. M. Alarcón-Elbal, J. Valle-Mora, and A. Goldarazena, "Comparison of different light sources for trapping *Culicoides* biting midges, mosquitoes and other dipterans," *Veterinary parasitology*, vol. 226, pp. 44-49, 2016.
- [235] G. Cassar, A. Matthews, and A. Leyland, "Triode plasma diffusion treatment of titanium alloys," *Surface and Coatings Technology*, vol. 212, pp. 20-31, 2012.
- [236] J. Schemel, *ASTM manual on zirconium and hafnium*. ASTM International, 1977.

- [237] D. Depla, S. Mahieu, and J. Greene, "Sputter deposition processes," in *Handbook of deposition technologies for films and coatings*: Elsevier, 2010, pp. 253-296.
- [238] P. J. Kelly and R. D. Arnell, "Magnetron sputtering: a review of recent developments and applications," *Vacuum*, vol. 56, no. 3, pp. 159-172, 2000, doi: [http://dx.doi.org/10.1016/S0042-207X\(99\)00189-X](http://dx.doi.org/10.1016/S0042-207X(99)00189-X).
- [239] A. H. Simon, "Sputter processing," in *Handbook of Thin Film Deposition*: Elsevier, 2018, pp. 195-230.
- [240] V. K. Pecharsky and P. Y. Zavalij, *Fundamentals of powder diffraction and structural characterization of materials*. Springer, 2009.
- [241] A. R. West, *Solid state chemistry and its applications*. John Wiley & Sons, 2007.
- [242] P. D. F. ICDD, "International Centre for Diffraction Data," *Powder Diffraction File, Newtown Square, Pennsylvania, USA*, 1997.
- [243] W. C. Oliver and G. M. Pharr, "An improved technique for determining hardness and elastic modulus using load and displacement sensing indentation experiments," *Journal of materials research*, vol. 7, no. 06, pp. 1564-1583, 1992.
- [244] W. C. Oliver and G. M. Pharr, "Measurement of hardness and elastic modulus by instrumented indentation: Advances in understanding and refinements to methodology," *Journal of materials research*, vol. 19, no. 1, pp. 3-20, 2004.
- [245] S. Bull, "Failure modes in scratch adhesion testing," *Surface and Coatings Technology*, vol. 50, no. 1, pp. 25-32, 1991.
- [246] K. G. Budinski, "Tribological properties of titanium alloys," *Wear*, vol. 151, no. 2, pp. 203-217, 1991.
- [247] A. Standard, "C1624-05," *Standard Test Method for Adhesion Strength and Mechanical Failure Modes of Ceramic Coatings by Quantitative Single Point Scratch Testing*, ASTM, West Conshohocken, PA, pp. 201-213, 1999.
- [248] B. EN, "1071-3: 2005," *Advanced technical ceramics-Methods of test for ceramic coatings: Part 3: Determination of adhesion and other mechanical failure modes by a scratch test*.
- [249] A. Leyland, D. Lewis, P. Stevenson, and A. Matthews, "Low temperature plasma diffusion treatment of stainless steels for improved wear resistance," *Surface and Coatings Technology*, vol. 62, no. 1, pp. 608-617, 1993.
- [250] A. Matthews and A. Leyland, "The Future of Plasma-Based Surface Engineering Techniques in Tribology (Keynote)," in *World Tribology Congress III, 2005: American Society of Mechanical Engineers*, pp. 297-298.
- [251] A. Wilson, A. Matthews, J. Housden, R. Turner, and B. Garside, "A comparison of the wear and fatigue properties of plasma-assisted physical vapour deposition TiN, CrN and duplex coatings on Ti-6Al-4V," *Surface and Coatings Technology*, vol. 62, no. 1-3, pp. 600-607, 1993.
- [252] D. Nolan, S. W. Huang, V. Leskovsek, and S. Braun, "Sliding wear of titanium nitride thin films deposited on Ti-6Al-4V alloy by PVD and plasma nitriding processes," *Surface and Coatings Technology*, vol. 200, no. 20, pp. 5698-5705, 2006.
- [253] P. Walker and W. H. Tarn, *CRC handbook of metal etchants*. CRC press, 1990.
- [254] A. Standard, "E112: Standard Test Methods for Determining Average Grain Size," *West Conshocken*, 1996.
- [255] X. Tao, X. Liu, A. Matthews, and A. Leyland, "The influence of stacking fault energy on plasticity mechanisms in triode-plasma nitrided austenitic stainless steels: Implications for the structure and stability of nitrogen-expanded austenite," *Acta Materialia*, vol. 164, pp. 60-75, 2019.
- [256] G. Cassar, S. Banfield, J. A.-B. Wilson, J. Housden, A. Matthews, and A. Leyland, "Tribological properties of duplex plasma oxidised, nitrided and PVD coated Ti-6Al-4V," *Surface and Coatings Technology*, vol. 206, no. 2, pp. 395-404, 2011.
- [257] J. A. Davidson, "Zirconium oxide and zirconium nitride coated stents," ed: Google Patents, 1997.

- [258] A. Yetim, A. Alasaran, I. Efeoglu, and A. Çelik, "A comparative study: The effect of surface treatments on the tribological properties of Ti–6Al–4V alloy," *Surface and Coatings Technology*, vol. 202, no. 11, pp. 2428-2432, 2008.
- [259] D. Prokoshkina, V. Esin, G. Wilde, and S. Divinski, "Grain boundary width, energy and self-diffusion in nickel: effect of material purity," *Acta Materialia*, vol. 61, no. 14, pp. 5188-5197, 2013.
- [260] Y. Zeng, Q. Li, and K. Bai, "Prediction of interstitial diffusion activation energies of nitrogen, oxygen, boron and carbon in bcc, fcc, and hcp metals using machine learning," *Computational Materials Science*, vol. 144, pp. 232-247, 2018.
- [261] G. Cassar, J. A.-B. Wilson, S. Banfield, J. Housden, A. Matthews, and A. Leyland, "Surface modification of Ti–6Al–4V alloys using triode plasma oxidation treatments," *Surface and Coatings Technology*, vol. 206, no. 22, pp. 4553-4561, 2012.
- [262] S. Ma, K. Xu, and W. Jie, "Wear behavior of the surface of Ti–6Al–4V alloy modified by treating with a pulsed dc plasma-duplex process," *Surface and Coatings Technology*, vol. 185, no. 2, pp. 205-209, 2004.
- [263] A. N. CHRISTENSEN, "A NEUTRON DIFFRACTION INVESTIGATION ON SINGLE CRYSTALS OF TITANIUM CARBIDE TITANIUM NITRIDE, AND ZIRCONIUM NITRIDE," *Chemischer Informationsdienst*, vol. 6, no. 47, 1975.
- [264] N. Clément, A. Lenain, and P. Jacques, "Mechanical property optimization via microstructural control of new metastable beta titanium alloys," *Jom*, vol. 59, no. 1, pp. 50-53, 2007.
- [265] A. Fragiél, M. H. Staia, J. Muñoz-Saldaña, E. S. Puchi-Cabrera, C. Cortes-Escobedo, and L. Cota, "Influence of the N₂ partial pressure on the mechanical properties and tribological behavior of zirconium nitride deposited by reactive magnetron sputtering," *Surface and Coatings Technology*, vol. 202, no. 15, pp. 3653-3660, 2008, doi: <http://dx.doi.org/10.1016/j.surfcoat.2008.01.001>.
- [266] Z. Zhiguo, L. Tianwei, X. Jun, D. Xinlu, and D. Chuang, "N-rich Zr–N films deposited by unbalanced magnetron sputtering enhanced with a highly reactive MW-ECR plasma," *Surface and Coatings Technology*, vol. 200, no. 16, pp. 4918-4922, 2006.
- [267] Q. Meng, M. Wen, C. Qu, C. Hu, and W. Zheng, "Preferred orientation, phase transition and hardness for sputtered zirconium nitride films grown at different substrate biases," *Surface and Coatings Technology*, vol. 205, no. 8-9, pp. 2865-2870, 2011.
- [268] J. Song, C. Yang, H. Hu, X. Dai, C. Wang, and H. Zhang, "Penetration Depth at various Raman excitation wavelengths and stress model for Raman spectrum in biaxially-strained Si," *Science China Physics, Mechanics and Astronomy*, vol. 56, no. 11, pp. 2065-2070, 2013.
- [269] W. Spengler and R. Kaiser, "First and second order Raman scattering in transition metal compounds," *Solid State Communications*, vol. 18, no. 7, pp. 881-884, 1976.
- [270] X.-J. Chen, V. V. Struzhkin, S. Kung, H.-k. Mao, R. J. Hemley, and A. N. Christensen, "Pressure-induced phonon frequency shifts in transition-metal nitrides," *Physical Review B*, vol. 70, no. 1, p. 014501, 2004.
- [271] C. Constable, J. Yarwood, and W.-D. Münz, "Raman microscopic studies of PVD hard coatings," *Surface and Coatings Technology*, vol. 116, pp. 155-159, 1999.
- [272] A. Singh *et al.*, "Tribological properties of sputter deposited ZrN coatings on titanium modified austenitic stainless steel," *Wear*, vol. 280–281, no. 0, pp. 22-27, 2012, doi: <http://dx.doi.org/10.1016/j.wear.2012.01.013>.
- [273] M. Kuroda, D. Setoyama, M. Uno, and S. Yamanaka, "Nanoindentation studies of zirconium hydride," *Journal of alloys and compounds*, vol. 368, no. 1-2, pp. 211-214, 2004.
- [274] K. Kese, A.-M. Alvarez, J.-H. Karlsson, and K. Nilsson, "Experimental evaluation of nanoindentation as a technique for measuring the hardness and Young's modulus of Zircaloy-2 sheet material," *Journal of Nuclear Materials*, vol. 507, pp. 267-275, 2018.
- [275] *Standard Specification for Zirconium and Zirconium Alloy Sheet, Strip and Plate for Nuclear Application (B352/B352M-17)*, ASTM, 2017.

- [276] Z. Lu, A. Chernatynskiy, M. J. Noordhoek, S. B. Sinnott, and S. R. Phillpot, "Nanoindentation of Zr by molecular dynamics simulation," *Journal of Nuclear Materials*, vol. 467, pp. 742-757, 2015.
- [277] A. Rico, M. Martin-Rengel, J. Ruiz-Hervias, J. Rodriguez, and F. Gomez-Sanchez, "Nanoindentation measurements of the mechanical properties of zirconium matrix and hydrides in unirradiated pre-hydrated nuclear fuel cladding," *Journal of Nuclear Materials*, vol. 452, no. 1, pp. 69-76, 2014.
- [278] H. Dong, A. Bloyce, P. Morton, and T. Bell, "Surface engineering to improve tribological performance of Ti-6Al-4V," *Surface engineering*, vol. 13, no. 5, pp. 402-406, 1997.
- [279] D. Pilloud, A. Dehlinger, J. Pierson, A. Roman, and L. Pichon, "Reactively sputtered zirconium nitride coatings: structural, mechanical, optical and electrical characteristics," *Surface and Coatings Technology*, vol. 174, pp. 338-344, 2003.
- [280] Z. Wu, Z. Qi, D. Zhang, and Z. Wang, "Nanoindentation induced plastic deformation in nanocrystalline ZrN coating," *Materials Letters*, 2015.
- [281] G. Cassar, S. Banfield, J. A.-B. Wilson, J. Housden, A. Matthews, and A. Leyland, "Impact wear resistance of plasma diffusion treated and duplex treated/PVD-coated Ti-6Al-4V alloy," *Surface and Coatings Technology*, vol. 206, no. 10, pp. 2645-2654, 2012.
- [282] V. V. Shanbhag, B. F. Rolfe, J. M. Griffin, N. Arunachalam, and M. P. Pereira, "Understanding galling wear initiation and progression using force and Acoustic Emissions sensors," *Wear*, vol. 436, p. 202991, 2019.
- [283] I. Milošev, H.-H. Strehblow, and B. Navinšek, "Comparison of TiN, ZrN and CrN hard nitride coatings: Electrochemical and thermal oxidation," *Thin Solid Films*, vol. 303, no. 1, pp. 246-254, 1997.
- [284] L. Krusin-Elbaum and M. Wittmer, "Oxidation kinetics of ZrN thin films," *Thin Solid Films*, vol. 107, no. 1, pp. 111-116, 1983.
- [285] P. Moseley and B. Hudson, "Phases involved in the corrosion of zircaloy by hot water (350° C)," *Journal of Nuclear Materials*, vol. 99, no. 2, pp. 340-344, 1981.
- [286] C. Duriez, T. Dupont, B. Schmet, and F. Enoch, "Zircaloy-4 and M5® high temperature oxidation and nitriding in air," *Journal of Nuclear Materials*, vol. 380, no. 1, pp. 30-45, 2008.
- [287] H. Yueh *et al.*, "Improved ZIRLO™ Cladding Performance through Chemistry and Process Modifications," in *Zirconium in the Nuclear Industry: Fourteenth International Symposium*, 2005: ASTM International.
- [288] H. H. Kim, J. H. Kim, J. Y. Moon, H. S. Lee, J. J. Kim, and Y. S. Chai, "High-temperature oxidation behavior of Zircaloy-4 and Zirlo in steam ambient," *Journal of Materials Science & Technology*, vol. 26, no. 9, pp. 827-832, 2010.
- [289] S. Kass, "The development of the zircaloys," in *Corrosion of Zirconium Alloys*: ASTM International, 1964.
- [290] M. Takahashi, G.-C. Lai, K. Ohta, and F. Kanamaru, "Bond strength and thermal stability of transition metal nitrides," in *Advances in quantum chemistry*, vol. 29: Elsevier, 1998, pp. 253-268.
- [291] H.-G. Kim, J.-H. Baek, S.-D. Kim, and Y.-H. Jeong, "Microstructure and corrosion characteristics of Zr-1.5 Nb-0.4 Sn-0.2 Fe-0.1 Cr alloy with a β -annealing," *Journal of Nuclear Materials*, vol. 372, no. 2-3, pp. 304-311, 2008.
- [292] A. R. Massih, M. Dahlbäck, M. Limbäck, T. Andersson, and B. Lehtinen, "Effect of beta-to-alpha phase transition rate on corrosion behaviour of Zircaloy," *Corrosion science*, vol. 48, no. 5, pp. 1154-1181, 2006.
- [293] A. Rizzo *et al.*, "Sputtering deposition and characterization of zirconium nitride and oxynitride films," *Thin Solid Films*, vol. 520, no. 9, pp. 3532-3538, 2012.
- [294] R. H. Hannink, P. M. Kelly, and B. C. Muddle, "Transformation toughening in zirconia-containing ceramics," *Journal of the American Ceramic Society*, no. 83, pp. 461-487, 2000.

- [295] D. K. Smith and W. Newkirk, "The crystal structure of baddeleyite (monoclinic ZrO₂) and its relation to the polymorphism of ZrO₂," *Acta Crystallographica*, vol. 18, no. 6, pp. 983-991, 1965.
- [296] R. Hill and L. Cranswick, "International Union of Crystallography. Commission on Powder Diffraction. Rietveld refinement round robin. II. Analysis of monoclinic ZrO₂," *Journal of applied crystallography*, vol. 27, no. 5, pp. 802-844, 1994.
- [297] A. Patterson, "The Scherrer formula for X-ray particle size determination," *Physical review*, vol. 56, no. 10, p. 978, 1939.
- [298] W. Small, J. Root, and D. Khatamian, "Observation of kinetics of γ zirconium hydride formation in Zr–2.5 Nb by neutron diffraction," *Journal of nuclear materials*, vol. 256, no. 2-3, pp. 102-107, 1998.
- [299] B. Cox, "Some factors which affect the rate of oxidation and hydrogen absorption of Zircaloy-2 in steam," United Kingdom Atomic Energy Authority. Research Group. Atomic Energy Research Establishment, Harwell, Berks, England, 1963.
- [300] Z. Qi, Z. Wu, H. Liang, D. Zhang, J. Wang, and Z. Wang, "In situ and ex situ studies of microstructure evolution during high-temperature oxidation of ZrN hard coating," *Scripta Materialia*, vol. 97, pp. 9-12, 2015.
- [301] P. K. Rao, P. Jana, M. I. Ahmad, and P. Roy, "Synthesis and characterization of zirconia toughened alumina ceramics prepared by co-precipitation method," *Ceramics International*, 2019.
- [302] R. Garvie, R. Hannink, and R. Pascoe, "Ceramic steel?," *Nature*, vol. 258, no. 5537, pp. 703-704, 1975.
- [303] C. Piconi and G. Maccauro, "Zirconia as a ceramic biomaterial," *Biomaterials*, vol. 20, no. 1, pp. 1-25, 1999.
- [304] B. Panicaud, J.-L. Grosseau-Poussard, D. Retraint, M. Guérain, and L. Li, "On the mechanical effects of a nanocrystallisation treatment for ZrO₂ oxide films growing on a zirconium alloy," *Corrosion Science*, vol. 68, pp. 263-274, 2013.
- [305] L. Kurpaska *et al.*, "Raman spectroscopy analysis of air grown oxide scale developed on pure zirconium substrate," *Journal of Nuclear Materials*, 2015.
- [306] Y. Cheng, E. Matykina, P. Skeldon, and G. Thompson, "Characterization of plasma electrolytic oxidation coatings on Zircaloy-4 formed in different electrolytes with AC current regime," *Electrochimica Acta*, vol. 56, no. 24, pp. 8467-8476, 2011, doi: <http://dx.doi.org/10.1016/j.electacta.2011.07.034>.
- [307] I. Zlotnikov, I. Gotman, and E. Gutmanas, "Characterization and nanoindentation testing of thin ZrO₂ films synthesized using layer-by-layer (LbL) deposited organic templates," *Applied Surface Science*, vol. 255, no. 5, pp. 3447-3453, 2008.
- [308] M. Reyes, A. Aryanfar, S. W. Baek, and J. Marian, "Multilayer interface tracking model of zirconium clad oxidation," *Journal of Nuclear Materials*, vol. 509, pp. 550-565, 2018.
- [309] R. Luthier and F. Levy, "Magnetron sputtered TiAlON composite thin films. I. Structure and morphology," *Journal of Vacuum Science & Technology A: Vacuum, Surfaces, and Films*, vol. 9, no. 1, pp. 102-109, 1991.
- [310] F. Cverna, *ASM ready reference: thermal properties of metals*. ASM International, 2002.
- [311] X. Liu, J. Kavanagh, A. Matthews, and A. Leyland, "The combined effects of Cu and Ag on the nanostructure and mechanical properties of CrCuAgN PVD coatings," *Surface and Coatings Technology*, vol. 284, pp. 101-111, 2015.
- [312] J. Robson and C. Paa-Rai, "The interaction of grain refinement and ageing in magnesium–zinc–zirconium (ZK) alloys," *Acta Materialia*, vol. 95, pp. 10-19, 2015.
- [313] S. SASAKI, K. FUJINO, and Y. TAKÉUCHI, "X-ray determination of electron-density distributions in oxides, MgO, MnO, CoO, and NiO, and atomic scattering factors of their constituent atoms," *Proceedings of the Japan Academy, Series B*, vol. 55, no. 2, pp. 43-48, 1979.

- [314] J. C. Slater, "Atomic radii in crystals," *The Journal of Chemical Physics*, vol. 41, no. 10, pp. 3199-3204, 1964.
- [315] J. Murray, "The Ti– Zr (Titanium-Zirconium) system," *Bulletin of Alloy Phase Diagrams*, vol. 2, no. 2, pp. 197-201, 1981.
- [316] J. Brandon and R. Taylor, "Thermal properties of ceria and yttria partially stabilized zirconia thermal barrier coatings," *Surface and Coatings Technology*, vol. 39, pp. 143-151, 1989.
- [317] H. Hayashi, T. Saitou, N. Maruyama, H. Inaba, K. Kawamura, and M. Mori, "Thermal expansion coefficient of yttria stabilized zirconia for various yttria contents," *Solid state ionics*, vol. 176, no. 5-6, pp. 613-619, 2005.
- [318] S. Park, J. Kim, M. Kim, H. Song, and C. Park, "Microscopic observation of degradation behavior in yttria and ceria stabilized zirconia thermal barrier coatings under hot corrosion," *Surface and Coatings Technology*, vol. 190, no. 2-3, pp. 357-365, 2005.
- [319] M. Donachie, "Titanium: a technical guide. 2nd," *Materials Park, OH, ASM International*, 2000.
- [320] C. Zhu, A. Javed, P. Li, F. Yang, G. Liang, and P. Xiao, "A study of the microstructure and oxidation behavior of alumina/yttria-stabilized zirconia (Al₂O₃/YSZ) thermal barrier coatings," *Surface and Coatings Technology*, vol. 212, pp. 214-222, 2012.
- [321] J. Zhang, X. Guo, Y.-G. Jung, L. Li, and J. Knapp, "Lanthanum zirconate based thermal barrier coatings: A review," *Surface and Coatings Technology*, vol. 323, pp. 18-29, 2017.
- [322] S. Malinov, A. Zhecheva, and W. Sha, "Modelling the nitriding in titanium alloys," in *1 st ASM International Surface Engineering Conference and the 13 th IFHTSE Congress*, 2002, pp. 344-352.
- [323] W. D. Münz, "Titanium aluminum nitride films: A new alternative to TiN coatings," *Journal of Vacuum Science & Technology A: Vacuum, Surfaces, and Films*, vol. 4, no. 6, pp. 2717-2725, 1986.
- [324] L. Donohue, I. Smith, W.-D. Münz, I. Petrov, and J. Greene, "Microstructure and oxidation-resistance of Ti_{1-x-y-z}Al_xCr_yY_zN layers grown by combined steered-arc/unbalanced-magnetron-sputter deposition," *Surface and Coatings Technology*, vol. 94, pp. 226-231, 1997.
- [325] S. Harris, E. Doyle, A. Vlasveld, J. Audy, J. Long, and D. Quick, "Influence of chromium content on the dry machining performance of cathodic arc evaporated TiAlN coatings," *Wear*, vol. 254, no. 1-2, pp. 185-194, 2003.

Appendix 1

The AbsorbDX software uses the Beer-Lambert law to determine the Penetration Depth of X-rays in a material at a given angle of incidence. The X-rays are absorbed mainly by photo-electric effect, but also scattered by elastic diffusion (or Rayleigh Diffusion) and inelastic diffusion (or Compton diffusion); the total attenuation follows the Beer-Lambert law for a given wavelength λ :

$$I(d) = I_0 \cdot e^{-\mu \cdot \rho \cdot d}$$

Where d is the length of the path of the X-rays into the material ("distance"), μ is the mass attenuation (absorption) co-efficient (how easily the material can be penetrated by X-rays), which depends on λ , and ρ is the specific mass of the material (Appendix I).

The mass absorption coefficient is computed from the composition of the material:

$$\mu = \sum_i c_i \cdot \mu_i$$

Where i is the chemical element, c_i is its mass proportion, and μ_i is the absorption co-efficient. The μ_i depends on the wavelength.

Considering the specific geometry of the diffractometer, and assuming a homogenous sample, the path of the X-rays analysing the depth x of the sample is:

$$d = x \cdot \left(\frac{1}{\sin \gamma} + \frac{1}{\sin(2\theta - \gamma)} \right)$$

With γ the angle between the incident beam and the surface of the sample and 2θ is the deviation of the beam.

Thus, the intensity of the X-rays diffracted by the surface layer which thickness x is equal to:

$$I(x) = I_1 \left[1 - \exp \left(-\mu \cdot \rho \cdot x \cdot \left(\frac{1}{\sin \gamma} + \frac{1}{\sin(2\theta - \gamma)} \right) \right) \right]$$

I_1 is the total intensity collected by the detector. The analysed thickness corresponds to the layer which gives a fraction p of the signal $\left(\frac{I(x)}{I_1} = p \right)$. p which is taken equal to 0.9 (90% of the signal).

The analysed depth is then estimated by:

$$x = -\ln(1 - p) \cdot \left(\mu(\lambda) \cdot \rho \cdot \left(\frac{1}{\sin \gamma} + \frac{1}{\sin(2\theta - \gamma)} \right) \right)^{-1}$$

